Dynamic Analysis, identification and Control studies of Aero-engine model rotor-bearing Systems

Dissertation submitted to the

National Institute of Technology Rourkela

in partial fulfilment of the requirements

for the degree of

Doctor of Philosophy

in

Mechanical Engineering

by

M. Rajasekhar

(Roll Number: 510ME810)

Under the supervision of

Prof. J. Srinivas

and

Dr. C.V. Gopinath

May 2016

Department of Mechanical Engineering

National Institute of Technology Rourkela

Certificate of Examination

Roll Number: <u>510ME810</u>

Name: <u>M.RAJASEKHAR</u>

Title of Dissertation: <u>Dynamic Analysis, Identification and Control studies of Aero-engine model rotor-bearing systems</u>

We the below signed, after checking the dissertation mentioned above and the official record book (s) of the student, hereby state our approval of the dissertation submitted in partial fulfilment of the requirements for the degree of Doctor of Philosophy in Mechanical Engineering at National Institute of Technology Rourkela. We are satisfied with the volume, quality, correctness, and originality of the work.

Dr.C.V.Gopinath
Co-Supervisor

J Srinivas
Principal Supervisor

D.R.K. Parhi
Member (DSC)

R.K.Behera
Member (DSC)

S. Jayanthu
Member (DSC)

<Name of Examiner>
Examiner

S.K. Acharya
Chairman (DSC)

November 10, 2016

Supervisor's Certificate

This is to certify that the work presented in this dissertation entitled **"Dynamic Analysis, identification and Control studies of Aero-engine model rotor-bearing systems"** by **"M.RAJASEKHAR "**, Roll Number **510ME810**, is a record of original research carried out by him under our supervision and guidance in partial fulfilment of the requirements for the degree of *Doctor of Philosophy* in *Mechanical Engineering*. Neither this dissertation nor any part of it has been submitted for any degree or diploma to any institute or university in India or abroad.

Dr. C.V. Gopinath   *Prof. J. Srinivas*
Co-Supervisor   Principal Supervisor

Dedicated

To

My family members

Declaration of Originality

I, **M.RAJASEKHAR**, Roll Number **510ME810** hereby declare that this dissertation entitled **"Dynamic Analysis, identification and Control studies of Aero-engine model rotor-bearing systems"** represents my original work carried out as a doctoral student of NIT Rourkela and, to the best of my knowledge, it contains no material previously published or written by another person, nor any material presented for the award of any other degree or diploma of NIT Rourkela or any other institution. Any contribution made to this research by others, with whom I have worked at NIT Rourkela or elsewhere, is explicitly acknowledged in the dissertation. Works of other authors cited in this dissertation have been duly acknowledged under the section "Bibliography". I have also submitted my original research records to the scrutiny committee for evaluation of my dissertation.

I am fully aware that in the case of any non-compliance detected in future, the Senate of NIT Rourkela may withdraw the degree awarded to me on the basis of the present dissertation.

November 10, 2016

M. Rajasekhar

NIT Rourkela

Acknowledgment

The research reported here has been carried out in the **Dept. of Mechanical Engineering, Natioal Institute of Technology Rourkela.** I am greatly indebted to many persons for helping me complete this dissertation.

First and foremost, I would like to express my sense of gratitude and indebtedness to my supervisor **Prof. J. Srinivas** for his inspiring guidance, encouragement, and untiring effort throughout the course of this work. His timely help and painstaking efforts made it possible to present the work contained in this thesis. I consider myself fortunate to have worked under his guidance. Also, I am indebted to him for providing all official and laboratory facilities.

I would like to express my sense of gratitude and indebtedness to my co-supervisor **Dr. C.V.Gopinath** for his continuous encouragement and guidance and untiring effort throughout the course of this work.

I am grateful to Director, **Prof. Animesh Biswas** and **Prof. S.S. Mahapatra**, Head of Mechanical Engineering Department, National Institute of Technology, Rourkela, for their kind support and concern regarding my academic requirements.

I am grateful to my Doctoral Scrutiny Committee members, **Prof. S.K. Acharya, Prof. D.R.K. Parhi, Prof. R.K. Behera** and **Prof. S. Jayanthu,** for their valuable suggestions and comments during this research period. I express my thankfulness to the faculty and staff members of the Mechanical Engineering Department for their continuous encouragement and suggestions.

I am especially indebted to my colleagues in the Machine Design and Analysis group. First, I would like to thank my co-scholars **Mrs. K.V.Vara Lakshmi, Mr. D. Koteswara Rao, Mr.Jakir Hussain, Mr. M. Rajasekhar Reddy** and **Mr Puneet Kumar** who helped me in my research work. We shared each other a lot of knowledge in the field of rotordynamics and vibrations.

I express my deep sense of gratitude and reverence to my beloved wife **Sulakshana**, son **Joseph**, parents and my brothers and sisters who supported and encouraged me all the time, no matter what difficulties I encountered. I would like to express my greatest admiration to **all my family members** and **relatives** for their positive encouragement that they showered on me throughout this research work. Without my family's sacrifice and support, this research work would not have been possible. It is a great pleasure for me to

acknowledge and express my appreciation to all **my well-wishers** for their understanding, relentless supports, and encouragement during my research work. Last but not the least, I wish to express my sincere thanks to all those who helped me directly or indirectly at various stages of this work.

Above all, I would like to thank **The Almighty God** for the wisdom and perseverance that he has been bestowed upon me during this research work, and indeed, throughout my life.

I would like to dedicate this thesis to my parents.

November 10, 2016   *M.Rajasekhar*

NIT Rourkela   Roll Number: 510ME810

Abstract

Aero-engines have high speed rotors carrying multi-stage turbine and compressor discs. Such systems need continuous monitoring during the operating regime. These rotors are mounted on ball bearings supported with squeeze film dampers and connected to stator casings. The motions of bearings and rotor are influenced by each other and therefore such a system requires structural dynamic studies. These rotors involve several nonlinear factors including contact forces, varying compliance vibration of ball bearing, nonlinear oil-film force of squeeze film damper etc Solving such nonlinear dynamic problems using the traditional transfer matrix method, modal synthesis approach, finite element method or impedance coupling technique is therefore a challenging task.

Present work focuses on modelling of rotors using ball bearing nonlinearities along with nonlinear secondary transient excitations using finite element modelling. In order to validate the finite element model, preliminary dynamic analysis is carried out using linear spring-damper bearing elements. Results are illustrated both for LP rotor model and twin-spool rotor. Initially, the natural frequencies obtained from the computer program based on Timoshenko beam elements are validated with ANSYS results. Further, the results are also validated with those obtained from impact hammer tests on a scaled dual disk rotor-bearing system. To utilize this finite element model, the time and frequency-domain response studies are conducted with double-row ball bearing forces, rub-impact forces, Muszynska's gas transients along with squeeze-film forces. In all the cases, differences from simple rotor supported by single-row ball bearings with only unbalance excitations have been reported. Using the fundamental frequency and its amplitude, an inverse modelling approach is applied to predict the parameters of rotor bearing system such as increased bearing clearance, changes in disc unbalances and the centralizing spring constants in squeeze-film damper. In this regard, a trained model of 3-layer perceptron neural network model is employed. In the second study, changes in dynamic response due to waviness and race-way defects in ball-bearings are first studied using modified contact force relations. Using this data, type of bearing fault is estimated from the statistical parameters of the time-domain signal by training an unsupervised Kohenen's neural network model. Here, the simulated data is collected from the rotor over an operating speed range. In the third study, the additional stiffness of rotor due to rub-impact forces is identified from optimization modelling. Such identification of rotor stiffening effect using finite element modelling is a new concept.

Two types of control studies are proposed to minimize the amplitudes of rotor during the critical operating conditions. Semi active electromagnetic damper design helps in reducing vibration amplitudes of the LP rotor over a frequency range of interest. Here,

the damper comprises of an electro-magnet and a spring. The required current and spring stiffness are identified from the basic relations and the results of control are illustrated with a two-disc LP rotor model. In active controller design, an electromagnetic actuator model is employed. The nominal gap maintained between the rotor and actuator coils is used in computing the actuator force. A proportional derivative (PD) control strategy is used to estimate the required forces. A neural network based alternate control scheme also proposed to compute the required actuator forces.

In overall, the work focussed on the dynamic analysis of dual disc rotor model subjected to parametric nonlinear bearing loads under the action of various external forces and some controller design aspects applicable to this rotor.

Contents

List of Figures

List of Tables

Nomenclature

A	waviness configuration constant
$A(z)$	cross section of the shaft
A_0 and A_j^i	the unloaded and loaded relative distances between inner and outer race centre of curvatures
a_i	inner raceway groove curvature center
A_m	amplitude of harmonics-outer race
A_n	amplitude of harmonics-inner race.
a_o	outer raceway groove curvature center
c	radial clearance of SFD
C_b	Hertzian contact stiffness
c_s	seal clearance
$d(\phi_j)$	defect depth at the ball angular position ϕ_j,
D_b	ball diameter
D_p	bearing pitch diameter
e	eccentricity
E	Young's modulus
f	friction coefficient between rotor and stator
F_b	bearing forces
F_N	radial impact force
F_T	tangential rub force
F_{xb} and F_{yb}	total restoring force components in X and Y directions
g	gravitational acceleration
G	shear modulus

g_e	non-dimensional displacement
h	defect depth of square- shaped outer raceway, varying film thickness as a function of θ.
$H(\delta_j^i)$	Heaviside function
$I(z)$	moment of inertia
I_1, I_2 and I_3	bearing integrals
J_{di}	diametral moments of inertia
J_{pi}	polar moments of inertia
k_c	radial stiffness of the stator
K_g, D_g and m_g	fluid stiffness, damping and mass coefficients
L	land length of SFD, rotor total length
m	order of harmonic of waviness in the inner race
m_d	mass of the disk
M_x and M_y	static moment loads in x and y axes
N	order of harmonic of waviness in the inner race
N_1, N_2,.. and D_1, D_2,..	shape functions
N_b	number of balls
$N_j(Z)$	arbitrary shape functions
N_w	Number of waves
p	instantaneous oil pressure distribution
q	displacement vector
q^e	nodal displacements
Q_j	Hertz's contact force
r	radius of inner race
R	radius of outer race

R_s	radius of SFD
r_0	radial clearance
r_{ci}	radial clearance between inner race and ball
r_{co}	radial clearance between outer race and ball
T	kinetic energy
t_1 and t_2	time intervals in the dynamic trajectory
T_d	disk kinetic energy
U	potential energy
u_b	relative displacements of inner races along X direction
v_b	relative displacements of outer races along Y direction
VC	varying compliance frequency
W	axial displacement
W_d	external work done at disk
w_j	wave at the contact angle corresponding to j^{th} ball
w_o	initial wave amplitude
w_p	maximum amplitude of the wave
α_0	unloaded contact angle
α_j	contact angle
ε	non-dimensional eccentricity ratio
θ_j	angle location of the jth ball
μ	dynamic viscosity of oil
ω_{cage}	angular velocity of the cage
u, v and w	relative displacements in the x ,y and z direction
$\alpha(Z,t)$	rotational displacement
κ	shear coefficient

ρ	density
$J_z^{'}$	axial moment of inertia
$J_T^{'}$	lateral moment of inertia
γ	shear correction factor
λ	wavelength of roughness
Ω	speed of the shaft
δ	variational operator
θ and ϕ	two rotational degree of freedoms
ζ	damping ratio
ε	relative eccentricity at the seal
ϕ_j	cage angular position (attitude angle)
δ_j	contact deformation of jth ball
θ_x, θ_y and θ_z	rotations with respect to x,y and z axes
$\dot{\phi}$	angular velocity of SFD
ϕ_c	cage angular position
ϕ_f	defect location
λ^i	dimensionless constant coefficient
ϕ_j	angular position of jth ball
$(\delta_r)_j^i$ and $(\delta_z)_j^i$	radial and axial displacements
$(\delta_r)_j^i$	radial deflections
$(\delta_z)_j^i$	axial deflections
$(\delta_{zo})^i$	axial preload displacement on the ith row
$\dot{\theta}_z$	rotational speed of the beam

Δ_i	additional deformation in the contact deformation
Δ_r	additional deflection, when the ball passes over the defect location
F_x , F_y and F_z	static force loads in the radial (x,y) and axial (z) directions
K_{bi}, K_{bo}	ball-inner, ball-outer races contact stiffness
Q_{bj}	restoring force
d_z^i	axial distance between the bearing center and bearing i[th] row
v^i	dimensionless constant depending on ball configuration
α_j^i	loaded contact angle
α_o	unloaded contact angle
δ_{rj} and δ_{zj}	displacement of jth ball in the radial and axial directions
[C$_r$]	viscous damping matrices
[G$_d$]	gyroscopic matrix of disc
[m$_d$]	Mass matrix of disc
[M$_r$], [G$_r$] and [K$_r$]	reduced mass, gyroscopic and stiffness matrices respectively

Chapter 1

Introduction

1.1 Background

A jet engine system basically contains an impeller for suction of outside air, a single/multistage compressor for pressurizing the air, a combustion chamber for burning the fuel and mixing with pressurized air, a single/multi stage turbine for expanding the gases to drive the compressor and a nozzle to generate the thrust power. The engine rotor system is a very lengthy component carrying the impeller and compressor at one end and turbine at the other end. These rotor systems are mounted on multiple bearings supported over the engine casing. In real practice, there are two rotors in the system: (i) a low pressure (LP) rotor (ii) high pressure (HP) rotor. Both carry the compressor and turbine discs separately and are connected to each other by intermediate bearings. Both these rotors have different speeds of rotation. Further, in construction, LP rotor is a solid rotor passes through the hollow HP rotor system. This set-up is known as twin-spool rotor configuration. Figure 1.1 shows a twin spool rotor configuration of aero-engine with low and high speed rotors.

High pressure compressor High pressure turbine

Low pressure compressor   Low pressure turbine
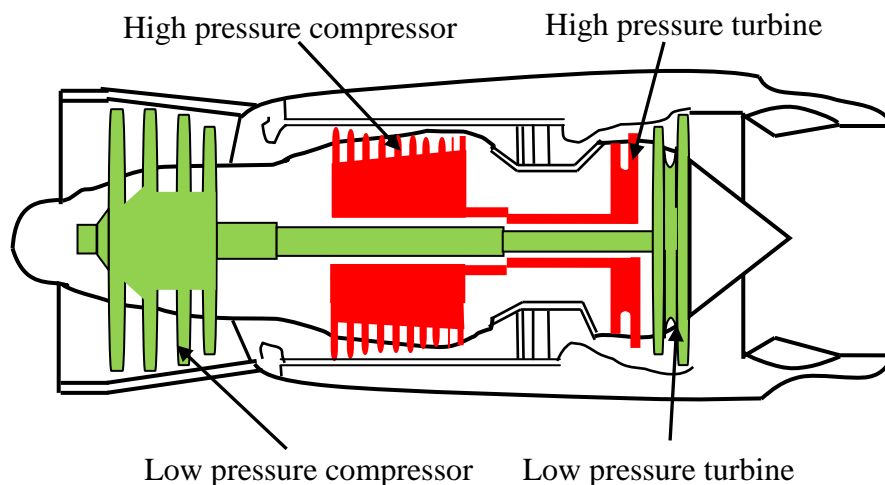
Figure 1.1: Twin Spool Turbojet

Aero-engine rotor consists of several components having distinct functions with different materials, such as the fan disk, the compressor drum, the connecting shaft, and the turbine drum. The misalignment of mass centre axis to rotor rotating axis is often referred as unbalance. When the principal inertia axis of the rotor does not coincide with its

geometrical axis, it results in synchronous vibrations and significant undesirable forces are transmitted to the mechanical elements and supports. These excessive forces will lead to malfunctioning of the rotating machine and results in rotor-stator contact events known as rub impact phenomenon. In a rotor, unbalance may not be nullified fully to zero level. Unbalance occurs due to the repetitive operation of rotors. For example, in aero-engine rotors, a diffuser blade loss event occurring from a bird impact raises the unbalance drastically. Unbalance increases with the rotor speed. Although the controlled imbalance response measurements commonly performed during shop testing provide information about the critical speed and the amplification factors, it is often desirable to confirm the support rotor dynamic properties in the test stand and in the field.

Hydrodynamic bearings have been used extensively in almost all aircraft turbines designed since 1970 to dampen imbalance response and are probably a major contributor to the rarity of rotor dynamic instability encountered in these engines. The main disadvantages of these bearings are its passive nature, instability and very sensitive variability of performance with raise in temperatures and frequencies of the rotors. These bearings are now-a-days replaced with rolling contact bearings. Ball bearings as one of such simple alternative are extensively used for their load supporting ability in high speeds in combination with squeeze film dampers providing the necessary damping for vibration reduction. Both single-row and double-row bearing configurations are found frequently. Other forces include the rub-impact occurring at unbalancing disks and oil seals. There is a lubricating fluid-solid interaction in very close clearances of rotor/stator may cause seal forces, these forces are responsible for self-excited motion of the rotor. These seal forces sometimes help in supporting the rotor in the radial direction but in some occasions they may act in tangential direction and lead to severe vibrations in the system. Apart from bearing reactions and seal forces, aero-engine rotor is subjected to external excitations due to gas pressures and thermal effects in addition to unbalance and gravity.

The faulty and damaged rolling element bearings plays a key role in the machinery breakdown, which leads to significant economic loses and even many human lives in some cases, such as aero-engine failures due to seizure of a bearing. Many research works are carried out in the field of ball bearings to understand the vibration generating mechanisms in the rolling element bearings.

Numerous vibration generation mechanisms in rolling element bearings have been investigated by researchers. These mechanisms include varying compliance and defects in the bearings. The varying compliance is due to varying stiffness due to continuous movement of the balls in the bearings and the defects include due to fatigue of old bearings and manufacturers errors even in the new bearings. Fatigue of bearings leads to

cracks, pits, dents and spills. The manufacturer errors include distributed defects of waviness in the bearings.

The effects of ball bearing dynamics on the overall dynamics of the system are ignored in low speed applications in the the previous studies due to presense of major contributions turbines and compressor dynamics. In simplified modeling of bearing systems these bearing dynamics are ignored. But these bearing dynamic forces are cosiderable as the unloaded rolling elements strike the bottom of the defect.

The bearing fault modeling is very much useful in measuring and analysing the nonlinear behaviour of bearing dynamics. Many authors are working to present a faulty model of a bearing system. Standard condition monitoring techniques are available to monitor the health of the bearings by measuring acceleration response at bearing nodes and conducting the time and frequency domain analysis and finding the faults at the peak impulses. The study of vibration generating mechanisms and understanding the mechanisms in designing of a new bearing system are very much useful for quality inspection and condition monitoring. To avoid catastrophic failures, the reliable and accurate identification of faults in the rotor bearing systems are very much necessary. Figure 1.2 shows the condition monitoring concept of rotor system using vibration signature.

Test input → | Rotor bearing system | → Vibration data from the rotor → | Rotor modal identification | → System parameters
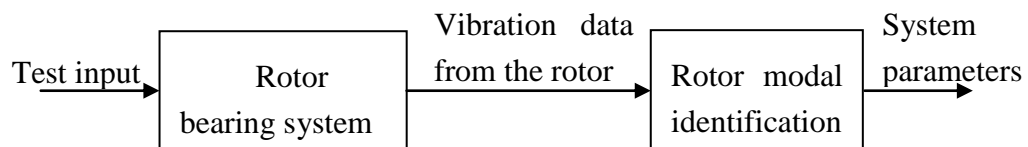
Figure 1.2: Condition monitoring strategy of rotor system

Production and development of supercritical turbines in aerospace applications is helpful for energy economization, environmental protection, rise in efficiency and cost-effectiveness. As an important component, a rotor-bearing assembly in such turbines requires a detailed study to understand several effects and instability states. An accurate model of the rotor assembly is essential in this regard. Accurate prediction and control of the dynamic behaviour (unbalance response, critical speeds and instability) is therefore, a vital requirement.

The reduction of vibration amplitudes at critical operating speeds is important part. In addition to the safety requirement of avoiding rotor bend critical speeds within the engine running range, the response at many other modes of the rotors and engine structure system must be controlled to ensure acceptable levels of vibration. Control of vibration is essential in respect of the bearing loads, structural fatigue loads, rotor/casing tip clearances, casing and engine external responses, and transmission of vibration to the

frame. The concept of magnetic bearings is one of the developments in control of rotor vibrations. In these bearings, electromagnetic suspension system will provide the required force to levitate the rotor in the air by maintaining a constant air gap between the rotor and the stator. The currents in the electromagnetic coils produce the required time varying force in the system. The perfect way of levitation depends on the efficient positioning of the rotor in the electromagnetic field. Several passive and semi-active vibration control concepts are also famous in rotors. For example, use of electro and magneto-rheological fluids, electromagnetic, piezoelectric techniques come under the regional semi-active control approaches. The inverse principle of electromagnetic exciter via a power amplifier is in fact the concept of active control approach. A perfect understanding of all these concepts helps in condition monitoring and diagnostic studies of real time aero-engine rotor systems.

1.2 Objectives and Scope

Analysis of rotors mounted on rolling element bearings subjected to various nonlinear excitations is one of the important issues in the rotor design. Following are the important objectives of proposed work:

The first task is to predict the natural frequencies, mode shapes and dynamic response of the rotordynamic models of LP and twin-spool systems. The rotor system is modelled by finite element analysis by employing the linear bearing elements with springs. In the next step, Hertzian bearing contact force model is used to obtain the dynamic response from the rotors. Upon validating it with experimental modal analysis results, effects of double-row bearing forces, squeeze-film damper forces, rub-impact forces and Muszynska transient model forces are predicted on the dynamic response of rotor. By considering three parameters of rotor-bearing system, viz., disk unbalance eccentricity, bearing radial clearance and squeeze-film damper central stiffness, the natural frequencies of rotor are recorded and this data is further used to train a neural network model inversely so as to predict the unknown system information from frequency and amplitude data. In next stage, different bearing faults are accounted and corresponding changes in Hertzian contact models are used to obtain the dynamic response from finite element model. The statistical data corresponding to these time-domain graphs are used to distinguish the various fault states in bearing. The additional stiffness during rub-impact event is predicted by minimizing the difference of frequency responses of system with and without rub forces. The additional stiffness in each element is identified and reported using particle swarm optimization scheme.

In order to reduce the resonant amplitudes at critical speed of operation, the rotor system requires some control strategy. Passive methods are straight forward and are being implemented at several rotors. However, the situations where the requirement of vibration control over a specified frequency ranges with available power amplifiers and other sources in an automatic manner, semi-active and active control techniques are required. In present task, it is planned to implement two control strategies: semi-active and active. In semi-active control approach, electromagnetic damper system is designed to minimize the vibration amplitude within the required frequency band. Results are presented for LP model rotor.

Following are the principal objectives of the present work.

- To study the effect of bearing clearance, disc eccentricity and centralizing spring stiffness of SFD on the dynamic response of rotor and experimental validation.
- To model the rubbing of the rotor with the stator as nonlinear excitation force model.
- To incorporate the nonlinear Muszynska's gas excitation forces in the system modelling at disk locations.
- To distinguish different neural network models used for bearing fault identification.
- To conduct studies on the shaft stiffening identification due to rub impact by proposing an optimization technique.
- To design the semi-active and active control methodologies for reduction of amplitudes at critical speeds of operation.
- To develop user-friendly programs with the nonlinear bearing forces to study further insights in the system and validate the solution obtained using the 3-D modelling of the system.

1.3 Organization of thesis

This thesis is organized into seven chapters.

Chapter-2 presents the literature review on the dynamic analysis of aero-engine rotors. Here, the literature is grouped into following heads: (a) rolling element bearing issues, (b) rotor modelling considerations, (c) external forces, (d) rub-impact loads and (e) rotor vibration control studies.

In chapter 3, the mathematical modelling of general rotor-bearing systems with associated nonlinear forces is presented.

Chapter 4 explores on the various solution methods employed in the present work for solving the dynamic equations including their interactive computer programs. Also the description of scaled rotor model fabrication and experimental work carried-out is briefly presented.

In chapter 5, the mathematical modelling of semi-active and active control methods to reduce amplitudes of response are described.

In chapter 6, the results of the numerical simulations are presented in following sequence: (i) Linear bearing model (preliminary studies) (ii) Rotor dynamic analysis with Hertzian contact force model subjected to unbalance, squeeze film forces, rub-impact excitations and transient Muszynska forces. (iii) Identification studies for bearing faults and rub-impact stiffening of rotor. (iv) Program outputs from semi-active and active controller for the model rotors as frequency-domain plots.

In chapter 7 concluding remarks and recommendations for future research scope are written.

Chapter 2

Literature Review

Typically aero-engine rotors are affected by exogenous or endogenous vibrations produced by unbalance, misalignment, resonances, material imperfections and cracks. Vibration caused by mass unbalance is a common problem in rotating machinery. Rotor unbalance leads to synchronous vibrations and significant undesirable forces transmitted to the mechanical elements and supports. Several works have been reported during the last two decades on the dynamic instability of rotors mounted on ball/roller bearings subjected to other nonlinear excitations. The literature on the dynamic analysis of these rotors is classified into the following headings and described in detail.

2.1 Rolling element bearing issues

Ball/ roller bearings play a vital role in the field of high speed rotating machineries like, aircraft engines and rocket turbopumps and so on. Ball bearing identification and defects have attracted considerable attention, due to the demand of high rotational speeds of the rotor systems. Ball bearings produce considerable undesired noise and vibration. Even though the ball bearings are geometrically and elastically perfect, due to the application of external load on them and involvement of numerous balls in the ball bearing lead to noise and vibration.

Early in 1980, Sunnersjo [1] analyzed radial vibrations of radially loaded bearings having a positive radial clearance. Examples of theoretical solutions obtained through digital simulation were presented and made comparisons with experiments.

Fukata et al. [2] used computer simulation to analyze the radial vibrations of ball bearings to overcome the experimental and theoretical difficulties. The results show that superharmoic, subharmonic, beat and chaos-like vibrations appear, in addition to harmonic vibration which synchronizes with ball passage.

Hertizian contact stress theory defines the basic load deflection relation [3], [4] and the relative location of the rolling element is responsible for the load experienced by it. Lim and Singh [5]–[8] developed a first mathematical model for rolling element bearings from basic concepts.

The radial clearance also plays key role in the system stability. The loss of contact between balls and raceways occurs in ball bearings and the radial internal clearance in the ball bearings [9]–[14] leads to varying bearing stiffness; this is the main parameter of ball loads along with the angular position of the cage, both of which leads to varying compliance [15]. The stiffness was presented for angular- contact bearings using neural network method [16].

The rolling element bearing consists of different members like the rolling elements, inner and outer rings and the spacer and they are in contact under very high speeds and severe dynamic loads. The defects in the bearings are investigated by Kiral and Karagulle [17]. Many other authors e.g. [18]–[21] analyzed the translational and angular displacement of the rotor supported over ball bearings as a function of waviness.

Preloading is very much useful in reduce the clearance and obtain the correct dynamic requirements of the rolling element bearings and is the expression for a restoring force [22]. Sinou [23] in his studies obtained non-linear dynamic response of a flexible rotor supported by ball bearings. Finite element model composed of a shaft with one disk, two flexible bearing supports and a ball bearing element was employed. Non-linear behaviour of the bearing rotor was illustrated with the harmonic balance method. Non-linear unbalance responses and the associated orbits of the bearing rotor were investigated. Villa et al. [24] modelled rolling bearing using harmonic balance method by considering the internal clearance and the Hertzian contact forces with kinematics of rolling elements.

Shen et al. [25] studied the nonlinear dynamics and stability of the rotor–bearing–seal system using Muszynska nonlinear seal force model and short bearing theory. The experimental system was simplified as a Jeffcott rotor.

Cao and Xiao [26] developed a spherical roller bearing model by considering the speeds and the surface profiles of inner/ outer race and rollers contacting surfaces and also the contact surface waviness. Bonello and Hai [27] introduced an impulsive receptance method for the time domain analysis of structures. This approach was tested on a realistic twin spool aero-engine, and this method was faster around 40 times than a conventional implicit integration scheme.

Wenhuia et al. [28] studied the rotor bearing system dynamic behaviour and the stability analysis was carried out with dual disk rotor imbalance.

Bonello and Hai [29] proposed a receptance harmonic method for a whole engine for the first time to analyze frequency domain of such a structure. The twin spool engine was also simulated in this method and it was shown an excellent correlation. Chen [30] modelled an unbalanced rotor supported over ball bearings by considering the nonlinear

factors like the clearance of bearing, nonlinear Hertzian contact forces and the varying compliance vibrations.

Chen [31] established a dynamic rotor ball bearing stator coupling system model to simulate the real aero-engine vibration. Rubbing effects were also considered in this model. Figure 2.1 shows a coupled model of rotor-bearing-stator system proposed here.
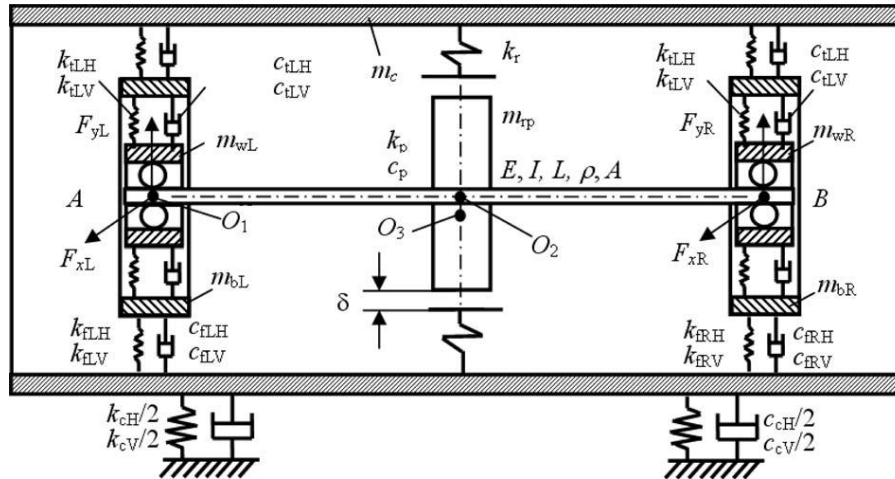
Figure 2.1: Rotor-bearing-stator coupled model [31]

Jacome et al. [32] developed a model with the finite element method for mechanical event simulations with the AlgorTM code to provide the spatial and time distributions of stress and stain values and nodal displacement at each time step.

Rafsanjania et al. [33] proposed a model to analyze the nonlinear dynamic behaviour of rolling element bearing system including the surface defects due to local imperfections on raceways and rolling elements. Ricci [34] introduced an iterative computational procedure to calculate internal normal ball loads in statically loaded single-row, angular-contact ball bearings, subjected to a known thrust load.

Bai et al. [35] investigated the nonlinear dynamic behaviour of a flexible rotor supported over ball bearings system. An experimental test rig was prepared to analyze the nonlinear dynamic performance of the system and employed a finite element method and two degree of freedom dynamic model of a ball bearing to model the flexible rotor system.

Ghafari et al. [36] investigated the balanced fault-free ball bearings vibrations by considering the lumped mass damper-spring model. Patil et al. [37] predicted the effects of a localized defect on the ball bearing vibrations using an analytical model. Non-linear spring considerations were used to design the contacts between the ball and the races. Tomovic et al. [38] proposed a vibration model of a rigid rotor supported by rolling

element bearing. The internal clearance value and number of rolling elements influence was analyzed on the system stability.

Abbes et al. [39] studied the dynamic behaviour of ball bearing waviness effect using time integration techniques. Ashtekar and Sadeghi [40] investigated the dynamics of an angular ball bearing rotor system in a   high speed turbocharger test rig and developed a coupled dynamic model to correlate the experimental and analytical results.

Aram et al. [41] presented a nonlinear model to show the effect of contact stress in the vibration behaviour of rotating components. The mass and nonlinear springs were used to model the system and the equations of motion were solved by using Lindstedt-Poincare method. Gupta et al. [42] investigated the instability and chaos were of a flexible rotor supported on two deep groove ball bearings system by developing a Timoshenko beam finite element formulation.

Kankar et al. [43], [44] diagnosed the faults of a high speed rotor supported over rolling ball bearings by using artificial neural network, support vector machine methods. Various localized defects like spalls on rolling elements, inner and outer races considered.

Kappaganthu and Nataraj [45] developed a rolling element bearing model for internal clearances between the races and deflections in different angular positions to identify the chaotic frequencies of the machine.

Nataraj [46] reviewed the state of art in rolling element bearing defects and condition based maintenance through fault identification and estimation methods. The data collected from the experiments is very useful in identification of the system. Li et al. [47] proposed a model of nonlinear model of rotor / bearing / seal system based on the Hamilton principle for steam turbine systems in power plants. The nonlinear steam excitation and oil film forces were derived from Musznyska and unsteady bearing oil-film force models. Nakhaeinejad and Bryant [48] modelled a multibody dynamics of rolling element bearings using bond graphs by considering the localized faults, centrifugal and gyroscopic effects, bearing clearance forces and contacts slip and separations.

Randall and Antoni [49] reviewed rolling element bearing to analyze the acceleration signals to diagnosis the health of bearings used in very high speed machinery. Sawahli and Randall [50] investigated the vibration signals of rolling element bearings at entry and exit of the spall. The life of the bearing might be extended by tracking spall position and by taking primitive actions.

Zapomel and Ferfecki [51] studied the dynamic behaviour of a rotor by altering the parameters like operating speeds and the stiffness of supports. Chen [52] studied the bearing design parameters to suggest the optimal values of stability of the rotordynamic system.

Gunduz et al. [53] studied the importance of bearing preloads on the modal characteristics of a rotor supported over bearing system with a double row angular contact ball bearing. Initially, an analytical model was developed to study the effects of preload on the system characteristics.

Kankar et al. [54] studied the effects of inner and outer races surface waviness and analyzed the rotor supported on ball bearing system nonlinear dynamic responses and modelled the system by considering stiffnesses of different elements of a bearing.

Xin et al. [55], [56] presented a methodology to analyze the planar multibody system containing deep groove ball bearings with clearance by introducing a constraint force system by considering the contact stiffness point of raceways and rolling balls and bearing kinematics.

Cong et al. [57] proposed a ball bearing fault signal model by considering the dynamic load analysis of a rotor supported over ball bearing system. The system was analyzed by dividing the surface of the bearing where load is actually applied as alternate and determinate loads.

Groves and Bonello [58] presented the squeeze film damper identification technique by using neural networks with a trained the experimental data to give the required information of the SFD clearance.

Gunduz and Singh [59] proposed an analytical approach to analyze the double row ball bearings by taking the Hertzian theory for different arrangements like face to face and back to back and tandem positions. Five dimensional stiffness matrixes for double row ball bearing were compared with a commercial code.

Kankar et al. [60] presented ball bearing fault diagnosis feature-recognition system by using the auto correlated the raw vibration signals and also a artificial neural network is used to classify the fault features.

Lahriri and Santos [61] measured the contact bearing forces in two types of backup bearings during the impacts of the ball bearings. The whip and whirling motion were also studied. Muruganatham et al. [62] proposed a singular spectrum analysis method to deduce the bearing fault features in a rotor bearing system and one more method was proposed by considering energy of the principal components. Two methods were compared by using an artificial neural network method.

Takabi and Khonsari [63] developed a mathematical model to analyze the ball bearing with provision for frictional heat generation, heat transfer processes and thermal expansion of bearing components. Tian et al. [64] investigated the influence of unbalance

on the nonlinear dynamic characteristics of turbocharger rotor-floating ring bearing system with the aid of run-up and run-down simulation method.

Ye et al. [65] analyzed the rolling element bearing load distribution and contact stresses by using quasi-dynamic and FEA methods by considering inner and outer rings tilted misalignment effects. There may be impact on the number of balls in the bearing to increase the loading properties of the bearing.

Zhang et al. [66] presented a Jones-Harris stiffness model to understand the stiffness of the rolling element bearings considering five degrees of freedom. The stiffness is a time varying feature due to unbalance force and finite number of balls.

Harrer et al. [67] investigated bearing system used in pharmaceutical and food industries, which are made up of ceramic materials. The ceramic bearing consists of Zro_2 rings and silicon nitrate balls. A premature wear was identified in the bearing system.

Jacobs et al. [68] investigated the deep groove ball bearing system dynamics, when the system was supported on deep groove ball bearings and the effects of lubricant film formation were studied and also, the stiffness and damping properties of the bearing in the static bearing load direction were identified. The dynamic behaviour of the lubricant oil film in the bearing was measured by using an electrical resistance. There was an increase in the stiffness by 3.2% and damping by 24% due to the effective formation of the lubricant film was observed.

Kogan et al. [69] proposed a three-dimensional rolling element bearing dynamic model to simulate the contact between the rolling elements and the cases by using classic dynamic and kinematic equations of Hertzian contact theory. The frictional force was determined with a hyperbolic-tangent function and also allows in simulating different faults in the bearing. Korolev et al. [70] developed a methodology to calculate the maximum load dependence on the balls at different contact positions of the balls and the races.

Nonato and Cavalca [71] presented a deep groove ball bearing model, in which the lateral vibrations of elastohydrodynamic film effects were included as a set of equivalent nonlinear viscous damper and spring. The proposed model and the finite difference results were compared. A finite element model of the rotor accounting for the lubricated bearing formulation adequately portrayed the frequency content of the bearing orbits observed on the test rig.

Petersen and Howard [72] presented a method to estimate the bearing raceway defects size that are bigger than angular spacing between the adjacent balls. There was an effect of varying stiffness of the ball bearings due to re and de stresses in the entrance and exiting of the balls in these defects of the ball bearings.

Shah and Patel [73] reviewed the rolling element bearing dynamics due to presence and absence of different defects of the bearing and summarized the fault identification techniques. The presence of tiny defects in the bearings will leads to failure of even very high speed machinery with economical and personal losses. The health monitoring of bearings was very useful to prevent such dangerous conditions.

Sheng et al. [74] explained the variation in the stiffnesses due to varying the speed of a rolling element bearing system by using Jones and Harris efforts and also proposed a model based on differentiation of implicit function to measure the speed varying stiffness of the system. The results of the proposed and literature methods were compared.

Singh et al. [75] presented a physical mechanism by which defect-related impulsive forces, and consequently, vibrations were generated in defective rolling element bearings. A dynamic nonlinear finite element model of a rolling element bearing with an outer race way defect was numerically solved using the explicit dynamics finite element software package, LS-DYNA. The dynamic contact forces between the rolling elements and the raceways of a bearing were reported.

Zhou et al. [76] studied the two different floating ring squeeze film dampers, one has a single oil film, which was referred as floating ring squeeze film dampers, and the other has a double layer oil film, which is referred to as FSFDD. The dynamic characteristics of FSFDS and FSFDD of two rotor dynamic models were investigated and the coupling effect between rotor, ball bearing and FSFDS/FSFDD were considered.

Zhuo et al. [77] established a three degrees of freedom model for a double-row self-aligning ball bearing system and studied the dynamic behaviour of the system during starting process and constant speed rotating process. A mathematical model was developed to account the effects of damping, stiffness of the bearing, three dimensional applied load, centrifugal force of the rotor, etc.

Han and Chu [78] proposed a three-dimensional nonlinear dynamic model to predict the skidding behaviour of angular contact ball bearings under combined load condition. The centrifugal and gyroscopic effects induced by ball rotation and revolution, Hertz contact between the ball and inner/outer races, discontinuous contact between the ball and cage and elastohydrodynamic lubrication were considered in the model.

Ahmadi et al. [79] presented a nonlinear dynamic model of defective ball bearings to generate contact forces and vibration responses. In this model accounts the responses of the line spall defects, when the ball enters the defect zone.

Kurvinen et al. [80] presented guidelines for the appropriate selection of a suitable bearing model for three case studies and two ball bearing models were implemented. One considers high-speed forces, and the other neglects them. Both models were used to study

three structures, and the simulation results were compared. The bearing behaviour is studied at different shaft rotation speeds and the simulation results are used to determine when the model containing the centrifugal and gyroscopic forces should be used.

Li et al. [81] proposed a general dynamic modelling method of ball bearing–rotor systems. Gupta's bearing model was applied to predict the rigid body motion of the system considering the three- dimensional motions of each part (i.e., outer ring, inner ring, ball, and rotor), lubrication tractions, and bearing clearances. The finite element method was used to model the elastic deformation of the rotor. The dynamic model of the whole ball bearing–rotor system was proposed by integrating the rigid body motion and the elastic vibration of the rotor. This proposed model may provide guidance for structural optimization, fault diagnosis, dynamic balancing, and other applications.

Petersen et al. [82] presented a method for calculating and analyzing the quasi-static load distribution and varying stiffness of a radially loaded double row bearing with a raceway defect of varying depth, length, and surface roughness. The method was applied to ball bearings on gearbox and fan test rigs seeded with line or extended outer raceway defects. When balls pass through the defect and lose all or part of their load carrying capacity, the load was redistributed between the loaded balls.

Zhang et al. [83] proposed a five-degree- of-freedom load distribution model by considering the bearing preload and the loads due to the rotor imbalance. Utilizing this model, the variation of the bearing contact angle was investigated thoroughly. The comparisons of the obtained contact angle against the results from literature validate that the proposed load distribution model was effective. The main resonance regions for the rotor-bearing system shift to the lower speed ranges when the variation of contact angle was taken into account.

2.2 Rotor modelling considerations

Rotor modelling is one of the major issues before its fabrication. Both one and three dimensional models have become famous. Early literature on modelling of rotors has started with famous Jeffcott rigid models.

Nelson [84] established the shape functions of transverse shear effects by using the Timoshenko beam theory. The effects of rotatory inertia, gyroscopic moments, axial load, and internal damping are already included in the literature, but have not included shear deformation or axial torque effects. This was the first work recorded in this area. After Nelson proposed the finite element model for a flexible rotor using Timoshenko beam theory, several authors [eg.,[85], [86]] employed the concept of finite element modelling for several rotors.

Muszynska and Bently [87] described the perturbation techniques used for identification of rotating system dynamic characteristics. A comparison between two periodic frequency-swept perturbation methods applied in identification of fluid forces of rotating machines was presented. Kim and Noah [88] developed a alternating frequency time method to obtain quasi-periodic responses of a horizontal Jeffcott rotor with a bearing clearance. Two truncated double harmonic expansions were used for calculating accurate quasi-periodic responses. Mao and Qin [89] developed an approach for calculating the dynamic response of multi-spool rotor systems with several inter shaft bearings using the combined methodologies of the finite element method, transfer matrices and impedance methods. Mao and Qin [90] developed a new shaft element model with 10 degrees of freedom for coupled torsional - flexural vibration of rotor systems. The model was based on an extended Hamilton's principle and includes the effects of translational and rotational inertia, gyroscopic moments, bending, shear and torsional deformations, internal viscous and hysteretic damping, and mass eccentricity. Figure 2.2 shows a virtual model of the rotor assembly within the engine.
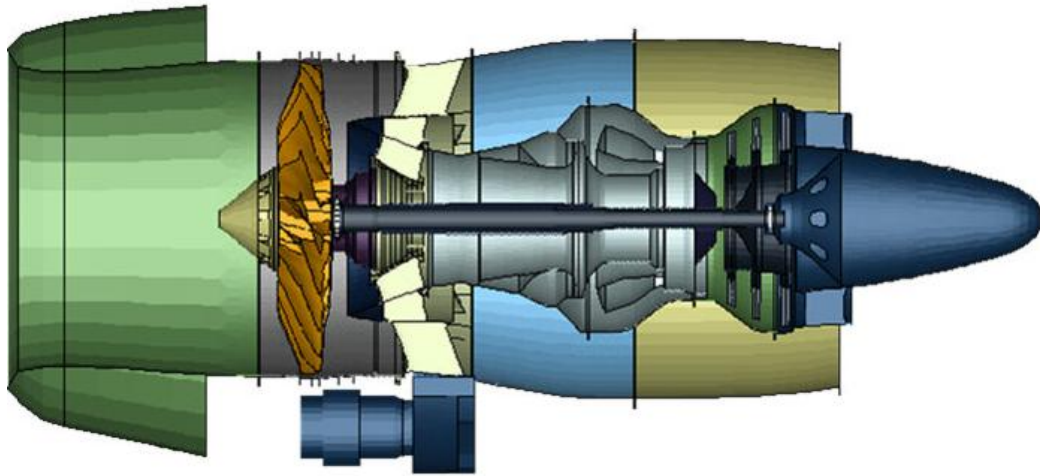
Figure 2.2: Schematic of Aero-Engine rotor

Tiwari and Vyas [91] described a procedure for extraction of the linear and nonlinear stiffness parameters in rotors with multiple discs, supported in rolling element bearings. The analysis puts forth a technique, which could be employed on-line, for processing the rotor vibrations picked up at the bearing caps, as it does not require an a priori knowledge of the excitation force. The problem was formulated for a multi-degree, nonlinear, balanced rotor system experiencing random excitations from the bearings, caused due to imperfections and deterioration of the rolling surfaces as well as from the other random sources, like inaccuracies in alignment, etc.

Nagasaka et al. [92] studied nonlinear phenomena caused by both of the nonlinear spring characteristics and an initial axial force in the vicinity of the major critical speed and twice in a very slender continuous rotor. When the rotor was supported horizontally, the difference in support stiffness and the asymmetrical non- linearity appear as a result of shifting from the equilibrium position. Tiwari et al. [93] studied effect of radial internal clearance of the ball bearing on the dynamic response of the rotor. The response of a balanced horizontal rigid motor rotor supported by a deep groove ball bearing was theoretically simulated.

Ganguli [94] developed a fuzzy logic system for ground based health monitoring of a helicopter rotor blade. Structural damage was modelled as a loss of stiffness at the damaged location that can result from delimitation. A finite element model of the rotor blade was used to calculate the change in blade frequencies (both rotating and non-rotating) because of structural damage.

Zhou and Shi [95] presented an on-line estimation method that can simultaneously estimate the parameters and determine the significance of the non-linear and time variant effects in the rotor-bearing dynamic system is presented. This method is based on an order down dating algorithm, which can deal with all linear-in-the-parameter non-linear and time variant effects, such as the unsymmetrical shaft, the structural internal damping, and the non-linear elastic restoring force of the bearing.

Zhou et al. [96] presented an active balancing method to offset the imbalance of the rotor system during acceleration by using an electromagnetic balancer. Qiu and Rao [97] presented a methodology for the fuzzy analysis of nonlinear rotor-bearing systems along with numerical results to demonstrate the computational feasibility of the methodology. Yang and Suh [98] presented results of applying instantaneous frequency to the interpretation and characterization of bifurcation and evolution of instability for a comprehensive rotor-journal bearing model incorporating translational and rotational inertia, bending stiffness, gyroscopic moments, shear deformation and disk imbalance.

Lou et al. [99] presented a finite - element formulation of a Timoshenko beam subjected to a moving mass. The beam was discretized into a number of simple elements with four degrees of freedom each. The inertial effects of the moving mass were incorporated into a finite-element model. Shanmugam and Padmanabhan [100] developed a fixed–free interface component mode synthesis method for carrying out rotordynamic analysis with the gyroscopic effects being considered. This model was used to combine the advantages of the fixed interface method, known as the Craig–Bampton approach.

Cheng et al. [101] investigated the non-linear dynamic behaviours of a rotor–bearing–seal coupled system. The influence of parameters, such as the rotation speed, seal

clearance and eccentricity of rotor were analyzed. Peters et al. [102] developed a test rig for the rotor dynamic behaviour investigation and optimisation of the supercritical low-Pressure Spool. The test rig was built up to investigate mainly the non-linear behaviour of the rotor-bearing-system under extreme operating conditions like out of balance of the shaft and the turbine, oil of conditions, gyroscopic effects and additional tests.

Santiago and Andres [103] presented an identification procedure that is suitable for implementation in the field and that relies on measurements of rotor synchronous response to calibrated imbalance. The method was extended to the typical case when the displacement measurements occur away from the bearing locations in flexible rotor systems. Mei et al. [104] investigated the non-linear dynamic behaviours of a rotor-bearing-seal coupled system and to analyze the influence of the seal and bearing on the nonlinear characteristics of the rotor system. Sun et al. [105] presented an approach for blade loss simulation including thermal growth effects for a dual-rotor gas turbine engine supported on bearing and squeeze film damper. A nonlinear ball bearing model using the Hertzian formula predicts ball contact load and stress, while a simple thermal model estimates the thermal growth so bearing components during the blade loss event.

Yao et al. [106] studied the complicated dynamical behaviour of a flexible rotor-bearing system. The unsteady oil-film force model described by three functions was considered. Kankar et al. [107] focused on accurate performance prediction, which is essential to the design of high performance rotor bearing system. It considers distributed defects such as internal radial clearance and surface waviness of the bearing components. In the mathematical formulation the contacts between the rolling elements and the races were considered as nonlinear springs, whose stiffnesses were obtained by using Hertzian elastic contact deformation theory.

Lees et al. [108] gave an overview of the developments in this field of condition monitoring, which has considerable practical importance. Lu et al. [109] analysed the non-linear coupling dynamic behaviour of a hydrodynamic bearing- flexible rotor system and proposed a method, the iterations were executed only on non-linear degrees of freedom. The iteration process shown that, improved convergence by taking the prediction value as the initial value.

Bai et al. [110] studied non-linear dynamic response of a flexible rotor supported by ball bearings. The finite element rotor system was composed of a shaft with one disk, two flexible bearing supports and a ball bearing element where the non-linearities were due to both the radial clearance and the Herztian contact between races and rolling elements.

Ying et al. [111] investigated the effect of foundation excitation on the dynamical behaviour of a turbocharger, a dynamic model of a turbocharger rotor-bearing system was

established which includes the engine's foundation excitation and nonlinear lubricant force. The rotor vibration response of eccentricity was simulated by numerical calculation.

Taplak et al. [112] investigated the rotor bearing system behaviour and also implemented the vibration analysis of the vertical system. The spectrum graphs are used to diagnosis the health of the system. by using vibration monitoring with trend analysis and spectrum graphs.

Genta et al. [113] developed an annular finite element for the computation of second and higher order harmonics modes of bladed rotating discs. The elements take into account gyroscopic effect and stiffening due to centrifugal and thermal stresses. The displacement field was expressed by a truncated Fourier series along the angle and by polynomial shape functions in the radial direction. Karlberg [114] derived analytical expressions for such approximated pedestal stiffness coefficients by using such approximated pedestals in simple rotordynamical models; it was found that the eigen frequencies decrease significantly with clearance.

Moore et al. [115] presented two approaches, including development of transfer functions of the casing and foundation, as well as a fully coupled rotor-casing-foundation model. The effect of bearing support compliance was captured, as well as the influence of casing modes on the rotor response.

Sheng et al. [116] developed a rigid-flexible dynamic simulation software based on the available commercial software MSC.ADAMS/ SOLVER and simulated an aero-engine main-shaft high speed cylindrical bearing's working dynamic performance by taking the cage's flexibility into consideration. The bearing's dynamic equations was established using a modified Craig-Bampton substructure mode synthesis method.

Wang and Jiang [117] developed enhanced and robust prognostic methods for aircraft engine including wavelet based method for weak signature enhanced for adaptive de-noising and correlation dimension based for incipient fault diagnosis. Gupta et al. [118] analysed two sources of excitations rotating imbalance and self excitation due to varying compliance effect of ball bearing in a rotor bearing system.

Hai and Bonello [119] applied impulsive receptance and the harmonic balance receptance methods are applied to a realistic three-spool engine and the aims are twofold: (i) to present some preliminary results of a parametric study into a three-spool aero-engine assembly and (ii) to propose a technique that makes use of both in producing the speed responses under multifrequency unbalance excitation (from all three rotors) with a realistic speed relation between the rotors.

Jansson et al. [120] discussed the effects of inertia and the rotational energy of the fluid in the turbine on lateral transversal shaft vibrations of hydraulic generator units. There was a lack of agreement among engineers upon how fluid inertia of the turbine should be included in rotor models. The rotational energy of the fluid has a potential risk of feeding self- excited vibrations. A fluid-rotor model was presented that captures the effect of inertia and angular momentum of a fluid annulus on vibrations of an inner rigid cylinder.

Li et al. [121] established a new dynamic model of a rotor system based on the Hamilton principle and the finite element method and analyzed the dynamic behaviour of the rotor system with the coupled effects of the nonlinear oil film force, the nonlinear seal force, and the mass eccentricity of the disk. The equations of the motion were solved effectively using the fourth order Runge-Kutta method in MATLAB.

Cheng et al. [122] analysed the nonlinear model of rotor / bearing / seal system by considering the Muszynska's non-linear seal fluid dynamic force model and non-linear oil film forces.

Rodrigues et al. [123] investigated a single-plane automatic balancer that was fitted to a rigid rotor. Two balls, which were free to travel around a circular race, were used to compensate for the mass imbalance in the plane of the device. The experimental rig possesses both cylindrical and conical rigid body modes and the performance of the automatic balancer is assessed for a variety of different levels of imbalance.

Sawicki et al. [124] investigated the modelling and analysis of machines with breathing cracks, which open and close due to the self-weight of the rotor, producing a parametric excitation. After reviewing the modelling of cracked rotors, the paper analysed the use of auxiliary excitation of the shaft, often implemented using active magnetic bearings to detect cracks. Sudhakar and Sekhar [125] applied equivalent loads minimization and vibration minimization methods for the identification of unbalance fault in a rotor system. Unbalance fault was identified using proposed methods by measuring transverse vibrations at only one location.

Babu et al. [126] presented a nonlinear vibration analysis of angular contact ball bearings supporting a rigid rotor by considering the frictional moments (load dependent and load independent components of frictional moments) in the bearings. Six degrees of freedom of rigid rotor was considered in the dynamic modelling of the rotor-bearings system. Moreover, waviness on surfaces of inner race, outer race, and ball were considered in the model by representing it as sinusoidal functions with waviness orders of 6, 15, and 25.

Bai and Zhang [127] presented the modelling of rotor systems subjected to stochastical axial loads as stochastically excited and dissipated Hamiltonian systems. The

stochastic averaging method for quasi-integrable – Hamiltonian systems was applied to obtain the averaged equations and the expression for the largest Lyapunov exponent was formulated. The necessary and sufficient conditions for the almost sure asymptotic stability of the rotor system were presented approximately.

Barad et al. [128] presented a Neural Network based approach for executing this task of combined health monitoring viz. mechanical and performance, with an example case study pertaining to a developmental power turbine. The various parameters used along with the trending methodologies both for steady state and transient operations were brought out.

Didier et al. [129] investigated the quantification of uncertainty effects on the variability of the nonlinear response in rotor systems with multi-faults (such as unbalance, asymmetric shaft, bow, parallel and angular misalignments). To take account all uncertainties in this kind of nonlinear problem by using the Harmonic Balance Method with a polynomial chaos expansion is very much important.

Lal and Tiwari [130] developed an identification algorithm to estimate parameters of multiple faults in a turbine – generator system model based on the forced response information. A simple discrete model of the system has been developed with the assumption of the rigid- rotor, flexible-bearings and the flexible-coupling. This was capable of describing the vibration resulting from coupling misalignments and rotor unbalances.

Siqueira et al. [131] presented a linear parameter varying control design for a flexible shaft supported by plain journal bearings. The model used in the LPV control design was updated from unbalance response experimental results and dynamic coefficients for the entire range of rotating speeds were obtained by numerical optimization.

Taplak et al. [132] performed the passive balancing of a rotating mechanical system having multi-discs. Reducing the bearing vibrations was considered an optimization problem, and the Genetic Algorithm approach was used for solving it under the appropriate constraints. Therefore, bearing amplitudes are formulated as an objective function, and the eccentricity directions of 2nd, 3rd... nth discs were defined as design variables relative to the first one.

Wan et al. [133] investigated the dynamic response of a multi-disk rotor system with coupling misalignment theoretically and experimentally, considering the nonlinear oil film force. The rotor was simplified to a lumped mass model and the governing equations were derived considering the gyroscopic effect. The reacting forces and moments caused by misalignment were treated as excitations to the rotor system.

Han and Chu [134] studied the dynamic response of cracked rotor-bearing system under time-dependent base movements. Three base angular motions, including the rolling, pitching and yawing motions, were assumed to be sinusoidal perturbations superimposed upon constant terms. Both the open and breathing transverse cracks were considered in the analysis. The finite element model was established for the base excited rotor-bearing system with open or breathing cracks.

Reimann et al. [135] focused on a strategy that uses the m-synthesis control technique to attenuate the oil whip instability effect of flexible hydrodynamically supported rotors and allows the rotor to operate in higher speeds. For the identified rotor model and the synthesized controller applied on a magnetic actuator, the control system stability and performance specifications were analyzed with regard to the model uncertainties and m-synthesis controlled vibration levels are compared to PID controller in vertical and horizontal directions. Sinha and Elbhbah [136] adopted conventional practice uses a number of vibration sensors at a bearing pedestal of a rotating machine for the vibration based condition monitoring. The number of bearings in a machine is likely to be very high hence increasing sensors to a large number and reduced the number of sensors per bearing pedestals by enhancing the computational effort in signal processing.

Sopanen et al. [137] investigated the complex rotor-bearing system of a tube roll of a paper machine supported by a hard-bearing-type balancing machine. Non-idealities of the rotor- bearing system were measured from the existing structure and the parameters of the real structure were emulated as accurately as possible in the simulation model.

Taplak et al. [138] investigated the dynamic behaviour of a direct coupled rotor-bearing system. Experimental vibration analyses in the vertical direction of the system were implemented.

Vanini et al. [139] developed fault detection and isolation scheme for an aircraft jet engine and was based on the multiple model approach and utilizes dynamic neural networks to accomplish this goal.

Jalili et al. [140] carried out the full dynamic analysis of a high speed rotor with certain geometrical and mechanical properties using 3D finite element model, one-dimensional beam-type model and experimental modal test.

Lee et al. [141] reviewed prognostics and health management field, followed by an introduction of a systematic prognostics and health management design methodology, 5S methodology, for converting data to prognostics information. This methodology includes procedures for identifying critical components, as well as tools for selecting the most appropriate algorithms for specific applications.

Li et al. [142] analyzed the stability of periodic motion of a rotor-bearing system with two unbalanced disks based on a multi-degree of freedom finite element model. Nonlinear effects of supporting oil-film and inertia distributions as well as shearing effect were taken into account.

Ozsahin et al. [143] presented an analytical modelling and an analysis approach for asymmetric multi-segment rotor–bearing systems. Timoshenko beam model which includes the effect of gyroscopic moments was employed for modelling rotor segments. Cui et al. [144] presented a method for calculating and analyzing the quasi-static load distribution and varying stiffness of a bearing with a raceway defect of varying depth, length, and surface roughness.

Tang et al. [145] proposed a mode separation method to separate the first and the second bending modes in rotor displacement and reconstruct the displacement signal nearby the first bending mode. Then, the original rotor displacement signal used by the digital controller was substituted by the reconstructed displacement signal and the amplifier current was reduced a lot when the rotor passes the first bending critical speed. Ghalamchi et al. [146] proposed model to describe the contact forces between bearing rolling elements and race surfaces as nonlinear Hertzian contact deformations, taking radial clearance into account.

2.3 External forces

Apart from unbalance force and bearing reactions, rotors are subjected to various forces including seal forces or harmonic loads. Exhaustive literature is available and some of them are summarized below.

Kim et al. [147] developed a structural model of a rotor system and integrated with the turbine flow model to examine the effects of the aerodynamic forces on the structural stability of the rotor system. Effects of the Alford force, and analytical/numerical methods had been chosen as methods for investigation.

Li et al. [148] established the nonlinear model of rotor-labyrinth seal system using Muszynska's nonlinear seal forces. We deal with dynamic behaviours of the unbalanced rotor-seal system with sliding bearing based on the adopted model and Newmark integration method. The influence of the labyrinth seal on the nonlinear characteristics of the rotor system was analyzed.

Nataraj and Harsha [149] presented an analytical model to investigate the non-linear dynamic behaviour of an unbalanced rotor bearing system due to cage run-out. Due to run-out of the cage, the rolling elements no longer stay equally spaced. The mathematical model takes into account the sources of non-linearity such as Hertzian contact forces and

cage run-out, and the resulting transition from a state of no contact to contact between the rolling elements and the races. The contact between the rolling elements and races is treated as nonlinear springs and the system was analyzed for varying number of balls.

Wang and Wang [150] presented the nonlinear coupling vibration and bifurcation of a high-speed centrifugal compressor with a labyrinth seal and two air-film journal bearings. The rotary shaft and disk were modelled as a rigid Jeffcott rotor. Muszynska's model was used to express the seal force with multiple parameters.

Mei Cheng et al. [151] investigated the nonlinear dynamic behaviours of an unbalanced rotor system supported on ball bearings with Alford force. In the rotor model, the rotor unbalance that varied with rotating speed, ball bearing clearance, nonlinear Hertzian contact force, varying compliance vibration, contact angle and Alford force were considered. Tiwari and Chakravarthy [152] proposed algorithm has the flexibility to incorporate any type and any number of bearings including seals.

Jing Liu et al. [153] proposed a dynamic simulation method to study ball bearing with local defect based on the coupling of the piecewise function and the Hertzian contact mechanism at the edge of the local defect. The ball bearing was modelled as a two-degree of freedom system. The impulse force was determined by the ratio of the ball size to the defect size and the contact deformation at the edge of the local defect was included.

Moazenahmadi et al. [154] presented a nonlinear dynamic model of the vibrations generated and contact forces in bearings due to a rectangular shape surface defect in a raceway. Singh et al. [155] explained the mechanisms of damaged bearing produced impacts from the numerical modelling using finite element analysis software.

2.4 Rub – impact loads

Due to extremely small clearances between the rotor and stator often provided by the designers to have a better efficiency, the rotor in course of time will be in contact with stator. This rub impact phenomenon will lead to rotor instability.

Chu and Zhang [156] investigated non-linear vibration characteristics of a rub-impact in Jeffcott rotor. The system is two-dimensional, non-linear and periodic. Fourier series analysis and the Floquet theory were used to perform qualitative global analysis on bifurcation and stability. After the rub-impact, three kinds of routes to chaos were found, that is, from a stable periodic motion through period doubling bifurcation, grazing bifurcation and a sudden transition from periodic motion to chaos. Quasi- periodic motions were also found.

Chu and Lu [157] considered the rotor stiffness as a variable and the rub-impact effect was included in the dynamic stiffness. Based on simulation data the least-square

method was used to identify the dynamic stiffness at different positions along the rotor. It was found that the dynamic stiffness at the position where the rub-impact occurs increases. This method was found to be very effective in detecting the rubbing position.

Lu et al. [158] considered the existence of rub-impact periodic motions in an eccentric rotor system. A criterion for the periodicity condition of n-periodic impacts was derived and other conditions for real rub-impacts were also discussed. A method consisting of analytical and numerical techniques was presented to solve the existence problem of rub-impact periodic motions.

Wan et al. [159] investigated the vibration of a cracked rotor sliding bearing system with rotor–stator rubbing using harmonic wavelet transform. Three non-linear factors, non-linear oil film forces, rotor–stator rubbing and the presence of crack, were taken into account. So the non-linear behaviour of the rotor will be much more complex. According to Newmark method, the dynamic response of the rotor was calculated. The effect of these non-linear factors is analyzed simultaneously in both time and frequency domain. Han et al. [160] proposed a quantitative identification procedure for local rubbing fault in rotor systems based on a hybrid model. The hybrid model combines finite element model of rotor and rigid discs, online identified oil film stiffness and elastic supports. The identification algorithm of oil film parameters was stated. The hybrid model based diagnosis process for local rubbing fault was described with assumption of periodic rubbing forces. These approaches have been tested on a test rig with single rotor double discs.

Hua et al. [161] established the nonlinear model of the rotor–seal system using Muszynska's nonlinear seal forces. An efficient and high-precision direct integration scheme was presented based on the 2 type algorithm for the computation of exponential matrices. The nonlinear phenomena in the unbalanced rotor–seal system were investigated using the adopted model and numerical integration method.

Inoue and Ishida [162] investigated the dynamic characteristics of nonlinear phenomena, especially chaotic vibration, due to the 1 to (-1) type internal resonance at the major critical speed and twice the major critical speed. The Hopf-bifurcation and consecutive period doubling bifurcations possible route to chaos occur from harmonic resonance at the major critical speed and from subharmonic resonance at twice the major critical speed, and chaotic vibration from the combination resonance occurs at twice the major critical speed were studied theoretically and experimentally.

Cheng et al. [163] investigated non-linear phenomena compressing periodic and quasi-periodic motion in the rotor–bearing–seal system and mathematical model and experimental results were compared. Jian and Chen [164] studied the dynamic analysis of

the rotor-bearing system supported by oil film journal bearings. An observation of a nonlinearly supported model and the rub-impact between rotor and stator was needed for more precise analysis of rotor-bearing systems. The periodic, quasi-periodic, sub-harmonic and chaotic motion were demonstrated.

Pennacchi and Vania [165] presented an actual case history of a large turbogenerator unit that was subjected to partial arc rubs. The results were discussed along with the model-based diagnostic strategy employed to identify the fault severity and the location of the shaft cross-sections where the heaviest rubs occurred. Comparisons between experimental data and simulated vibrations caused by the identified fault were identified to validate the proposed methodology.

Patel and Darpe [166] examined the vibration response of the cracked rotor in presence of common rotor faults such as unbalance and rotor stator rub. Numerical and experimental investigations were carried out and steady-state vibration analysis was presented. The investigation focused on directional nature of the higher harmonics for identification of rub in the cracked rotor. Shen and Zhao [167] investigated the stability and nonlinear behaviour of a rotor-bearing-seal system both numerically and experimentally. Wang and Chen [168] modelled rotor-support-casing structural features by using finite element beam method and the supports are modelled as lumped- mass models. Figure 2.3 shows the model rig employed in their work.
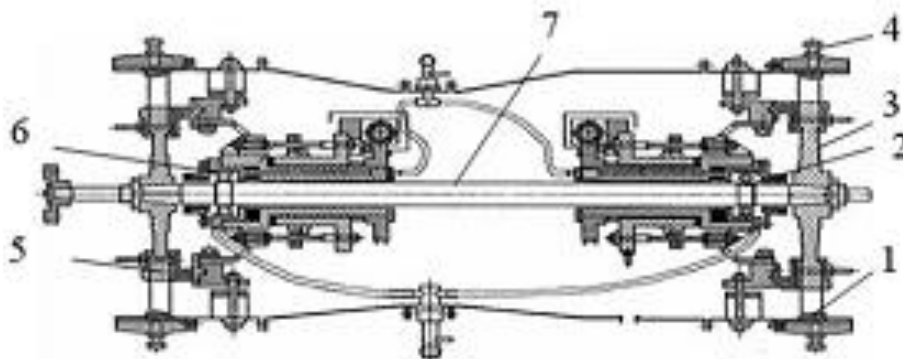
Figure 2.3: Profile of aero-engine rotor test rig [168]

Jeng et al. [169] introduced an alternative Poincare section method to analyze the dynamic behaviour of a rotor in rubbing. The response integration for analyzing high-order harmonic and chaotic responses was used to integrate the distance between state trajectory and the origin in the phase plane during a specific period. The integration process was based on the fact that the integration value would be constant if the integration interval was equal to the response period.

Patel and Darpe [170] investigated the coast-up lateral vibration response of the rotor–stator rub. Rub detection at its initiation stage was attempted. Shift in resonance speed and the directional nature of the rub fault were observed. Potential of Hilbert–Huang transform over wavelet transform was examined.

Patel and Darpe [171] modelled and attempted the vibration signature analysis of rotor with rotor – stator rub, transverse fatigue crack and unbalance. The rotor–stator interaction effects on the response of a rotor were investigated in the presence/absence of a transverse crack. The torsional vibrations were investigated for their sensitivity to rubbing using finite element model that also accounts for cross coupling of stiffness introduced due to crack.

Chen at al. [172] established a rotor-ball bearings-support-stator coupling system dynamic model with rubbing coupling faults for practical aeroengine. In the model, the rubbing fault was modelled, the stator motion was considered, the flexible support and squeeze film damper were established, and the nonlinear factors of ball bearing, such as the clearance of the bearing, the nonlinear Hertzian contact force between balls and races, and the varying compliance vibration because of the periodical variety of the contact position between balls and races, were modelled.

Chu and Lu [173] investigated the dynamic model of the rubbing rotor system was established and the dynamics of the rubbing rotor. The parameter identification was used to process the vibration data obtained by numerical simulation and experimental test. The change in the transient stiffness of the rotor was analyzed and the stiffening effect of the rotor was investigated quantitatively. It was found that the change of the transient stiffness could effectively reflect the severity of the rub–impact.

Ma et al. [174] investigated the nonlinear dynamic characteristics of a single span rotor system with two discs under fixed-point and local arc rub-impact conditions. A twenty-degree- of- freedom model considering the gyroscopic effect was developed, the simple Coulomb friction model and piecewise linear spring model to describe the contact between the rotor and the stator. The vibration characteristics of the rotor system with two types of rub-impact forms were analyzed. Rad et al. [175] studied the effects of shaft rub on a rotating system's vibration response with emphasis on heat generation at the contact point. A 3D heat transfer code, coupled to a 3D vibration code, was developed to predict the dynamic response of a rotor in the time domain. The shaft bow was represented by an equivalent bending moment and the contact forces by rotating external forces. The seal ring was modelled as a linear spring, which exerts a normal force to the rotor.

Roques et al. [176] introduced a rotor–stator model of a turbogenerator investigate speed transients with rotor-to-stator rubbing caused by an accidental blade-off imbalance.

In order to assess the angular deceleration of the rotor due to rubbing, the angular position of its cross-section was considered as an unknown of the problem. Displacement fields are discretized through a finite element formulation.

Shang [177] studied the global response characteristics of a general rotor/stator rubbing system, which takes into account the dominant factors in the process of rotor /stator rubbing, and the dry friction effect.

Cao et al. [178] investigated the nonlinear dynamic characteristics of rub-impact rotor system with fractional order damping. The model of rub- impact comprises a radial elastic force and a tangential Coulomb friction force. The fractional order damped rotor system with rubbing malfunction was established. Various complicated dynamic behaviours and types of routes to chaos were found, including period doubling bifurcation, sudden transition and quasi-periodic from periodic motion to chaos.

Cong et al. [179] installed an experimental setup which can simulate the rotor-to-stator rub in a rotor system. A rub screw was used to simulate the condition of local rub–impact fault. Based on the theory of elastic collision and energy conservation, an Impact Energy Model was proposed to evaluate the probability or severity of rub–impact fault. Hammer test and rub– impact fault validation were conducted to prove the model.

Khanlo et al. [180] studied the chaotic vibration analysis of a rotating flexible continuous shaft-disk system with rub impact. The system was modelled as a continuous shaft with a rigid disk in its mid- section with Coriolis and centrifugal effects included. The governing partial differential equations of motion were extracted based on the Euler–Bernoulli beam theory.

Zhou et al. [181] proposed nonlinear model of a double disc rotor seal system based on the finite element method and the Lagrange equation with the coupled effects of the gravity force of the discs.

Zapomel and Ferfecki [182] developed a mathematical model by considering the shaft as flexible and the disks as rigid bodies and the model also includes the hydrodynamic bearings impacts and the nonlinear forces of couplings.

Lahriri at al. [183] proposed a new unconventional backup bearing design in order to reduce the rub related severity in friction and centre the rotor at impact events. The analysis showed that the rotor at impacts was forced to the centre of the backup bearing and the lateral motion was mitigated. As a result, the rotor spin was kept constant. Lahriri and Santos [184] dealt with the theoretical study of a horizontal shaft, partially levitated by a passive magnetic bearing, impacting its stator. Rigid body dynamics were utilised in order to describe the governing nonlinear equations of motion of the shaft interacting with

a passive magnetic bearing and stator. Theoretical and experimental studies were compared.

Ma et al. [185] established a lumped mass model of a rotor-bearing-seal system considering the gyroscopic effect. The graphite self-lubricating bearing and the sliding bearing were simulated by a spring-damping model and a nonlinear oil-film force model based on the assumption of short bearings, respectively. The seal was simulated by Muszynska nonlinear seal force model. Effects of the seal force and oil-film force on the first and second mode instabilities were investigated under two loading conditions.

Olgac et al. [186] presented an alternative pathway in studying the ubiquitous blade/casing rub problem in turbomachinery. Bladed disks interfere with the stationary shroud (casing) for a variety of reasons, such as axial offsets, thermal expansions. Both components being compliant, time-varying interface characteristics, nonlinearities and uncertainties in the rub forces make this dynamics very complex to model and analyze.

Ma et al. [187] studied the dynamic characteristics of a rotor rubbing with circular stator and four pin shape stators based on contact dynamics theory. Based on finite element method, the rotor system attached with two disks and pin shape stators were simulated by Timoshenko beam. The circular stator was simulated by a lumped mass model, and the rotor and stator were connected by one or more point–point contact elements to establish the dynamic model of the rotor–stator coupling system.

Ma et al. [188] derived a rubbing model between a rotating blade and elastic casing based on the law of conservation of energy. In this model, the bending deflection of blade and the casing deformation during rubbing were taken into account and the influences of the penetration depth, casing stiffness, friction coefficient, blade physical dimensions (thickness, width and length) on the quasi-static normal rubbing forces were analyzed.

Weaver et al. [189] examined a three-disk rotor analytically for nonlinear rotordynamic behaviour due to an unbalance driven rub. The rotordynamic solution was obtained using nonlinear and steady state finite element models to demonstrate the effect of the rub impact on the dynamic response of the machine[190]. A thermoelastohydrodynamic model of tilting pad journal bearing performance was also used to study the possible removal of the rub impact by making minor adjustments to bearing parameters including preload, clearance, pad orientation, and lubricant properties.

2.5 Control studies

Vibration control system of rotor dynamic system is very essential. Passive, semi-active and active control methods are available in this regard. Active magnetic bearings are very

appropriate in this line. However, due to cost economy requirements several alternative actuators systems are proposed.

Rezvani and Hahn [191] analyzed the attenuation and stabilization of high speed rotating machinery with the aid of a squeeze film damper and also studied flexible horizontal rotor theoretically and experimentally. Khajepour and Golnaraghi [192] studied free and forced vibration suppression in a piezoceramic actuated flexible beam via the nonlinear modal coupling control.

Chinta and Palazzolo [193] studied nonlinear forced response using imbalance force and non imbalance harmonic force. They have investigated the regimes of nonlinear behaviour such as jumps and subharmonic motion with the aid of different parameters i.e. rotor speed\ imbalance eccentricity\ forcing amplitude\ rotor weight\ and geometric coupling. Smith [194] developed a nonlinear optimal control methodology for magnetostrictive actuators. At moderate to high drive levels, the output from these actuators was highly nonlinear and contains significant magnetic and magneto-mechanical hysteresis.

Yu et al. [195] presented a description of the electromagnetic actuator for active vibration control of a flexible rotor bearing system. The transfer characteristics of the electromagnetic actuator were investigated theoretically and experimentally. The linearized relationship of the electromagnetic force/input control voltage could be achieved by employing the analogue square root control circuits. A control algorithm which allows the control force of the actuator to be computed to minimize the synchronous rotor vibration is discussed.

Elmadany and Abduljabbar [196] developed an optimal control law design for the lateral vibration suppression and stabilization of a rotor system with anisotropic fluid-film bearings and fluid leakage. Evaluation of the degree of controllability and observability and synthesis of the optimal control law using linear quadratic regulator theory accompanied by an asymptotic state observer are performed.

Vance et al. [197] described the requirements for bearing dampers to be used in an aircraft engine and discussed the pros and cons of various types of dampers that were considered for active control in aircraft engines.

Fung et al. [198] formulated the rotating flexible-Timoshenko-shaft/flexible-disk coupling system by applying the assumed-mode method into the kinetic and strain energies, and the virtual work done by the eddy-current damper. From Lagrange's equations, the resulting discretized equations of motion could be simplified as a bilinear system.

Ji [199] investigated the effect of time delays on the non-linear dynamical behaviour of a Jeffcott rotor with an additional magnetic bearing locating at the disc. The time delays were presented in the proportional and derivative feedback, respectively.

Ahn et al. [200] investigated the performance of the squeeze film damper experimentally. When the applied current increased, the whirling amplitude greatly reduced at the critical speeds and damping ratio increased. Stability of a rotor system with a squeeze film damper using an electromagnet derived.

Bonello et al. [201] modelled a rotor running in unsupported squeeze-film dampers housed in a flexible support structure using an integrated analytical technique. A modal-based approach was then used for the analysis of the stability and bifurcation of these solutions, as well as the analysis of a periodic motion. The simulation correctly predicts the overall performance, including subharmonic motion, combination frequencies and subcritical superharmonic resonances.

Clark et al. [202] discussed the advancement of gas turbine engines and the vitality of magnetic bearings, a brief comparison between magnetic bearings and other bearing technologies in both their advantages and limitations, and an examination of foreseeable solutions to historically perceived limitations to magnetic bearing.

Horst And Wolfel [203] developed a structural model of a high speed rotor for the examination of active vibration control in rotor dynamics. Suppression of lateral bending vibrations of the elastic shaft is realized by means of surface-bonded piezoceramic actuator patches on the shaft surface. Models for actuator implementation were derived.

Inthra and Gandhi [204] studied the potential of using a semi-active controllable damper, whose damping coefficient can be modulated in real time, for tonal vibration isolation applications. A frequency-domain control algorithm was developed for determining the damping coefficient variation (at twice the disturbance frequency) that minimizes the force transmitted to the support at the disturbance frequency.

Kasarda et al. [205] proposed an active control solution utilizing active magnetic bearing technology in conjunction with conventional support bearings. The active magnetic bearing is utilized as an active magnetic damper at rotor locations inboard of conventional support bearings. Presented here were initial proof-of-concept experimental results using an active magnetic damper for vibration control of subsynchronous rotor vibrations in a high-speed single-disk laboratory rotor.

Chen et al. [206] investigated a three-pole active magnetic bearing system with and without a motor. For the system without a motor designed and implemented three controllers: a linear state feedback controller, feedback linearization with a linear state feedback controller, and feedback linearization with an integral sliding mode controller.

Shin et al. [207] developed a system identification methodology for a linear time-periodic system and applied to an experimental setup of an integrally twist-actuated helicopter rotor blade. Identification was conducted for a controller design, which alleviates vibratory loads induced in forward flight.

Zhu [208] studied the dynamic behaviour of the disk-type MR fluid damper for attenuating rotor vibration under AC sinusoidal magnetic fields on a flexible rotor. It was shown that as the frequency of AC sinusoidal magnetic field increases, the capability of the disk-type MR fluid damper to attenuate rotor vibration significantly reduces.

Changsheng [209] studied the controllability of the disk-type magnetorheological grease damper on the dynamic behaviour of a rotor system, the effectiveness of the disk-type magnetorheological grease damper for attenuating the rotor's vibration, and the suitability of the magnetorheological grease damper for a feedback vibration control of rotor systems in a flexible rotor.

He et al. [210] proposed a pseudo self-optimizing support system for a rotor-bearing system based on shape memory alloy. A numerical simulation was given to verify the theoretical model.

Hussain [211] investigated the response of an imbalanced rigid rotor supported by active magnetic bearing system. The mathematical model of the rotor-bearing system used in this study incorporates nonlinearity arising from the electromagnetic force-coil current-air gap relationship, and the effects of geometrical cross-coupling. The response of the rotor is observed to exhibit a rich variety of dynamical behaviour including synchronous, sub-synchronous, quasi-periodic and chaotic vibrations.

Tonoli [212] modelled the dynamic behaviour of eddy current dampers and couplers and, by extension, of resistively shunted synchronous motors with permanent magnets. The modelling approach used Faraday's law for the computation of the eddy current; the torque was then computed from the Lorentz force acting on the conductors. The electromechanical model was valid under rather general conditions and can be interfaced to the model of a mechanical structure to describe the coupled behaviour.

Amati et al. [213] presented a model of electrodynamic bearings. The model takes into account the R-L dynamics of the eddy currents on which this type of bearing was based, making it valid for both quasistatic and dynamic analyses. Das et al. [214] proposed an active vibration control scheme for controlling transverse vibration of a rotor shaft due to unbalance and presented a theoretical study. The technique uses electromagnetic exciters mounted on the stator at a plane, in general away from the conventional support locations, around the rotor shaft for applying suitable force of actuation over an air gap to control transverse vibration. Electromagnets used for

vibration control do not levitate the rotor and facilitate the bearing action, which was provided by conventional bearings. Figure 2.4 shows the controller mounted on rotor system.
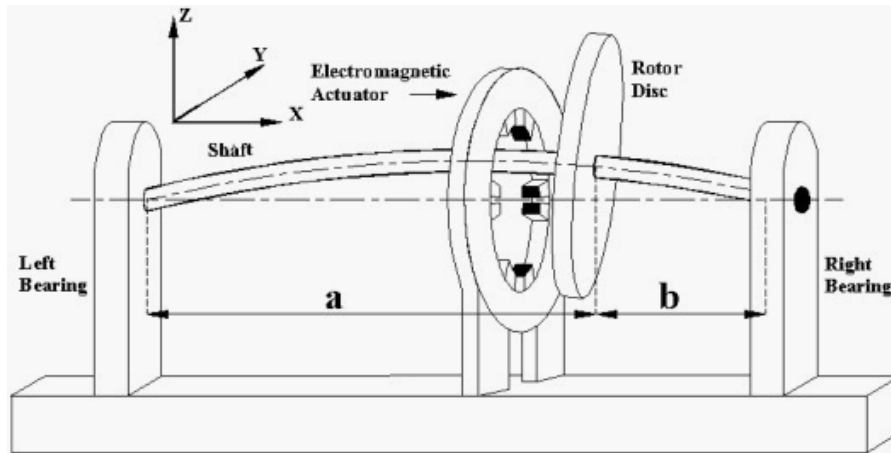

Figure 2.4: EM actuator for control of rotor vibrations [214]

Ji et al. [215] reviewed on the nonlinear dynamics of magnetic bearing systems and it provides background information on analytical methods, nonlinear vibrations resulting from a rotor contacting auxiliary bearings, and other active topics of research involving the nonlinear properties of magnetic bearing systems, such as nonlinear self-sensing magnetic bearings and nonlinear control of magnetic bearings.

Lallart [216] studied Converging Input, Converging Output stability and robustness. This method was almost as effective as active techniques, but might generate instabilities and deals with instability problems.

Tonoli et al [217] investigated the dynamic behaviour of transformer eddy current dampers integrated in a mechanical structure. The electromechanical system was modelled using the Lagrange approach in terms of the magnetic flux linkages in the electromagnets.

Bonfitto et al. [218] investigated the potential of a self-sensing strategy in the case of an electromagnetic damper for the vibration control of flexible structures and rotors and studied performed in the case of a single degree of freedom mechanical oscillator actuated by a couple of electromagnets. The self-sensing system was based on a Luenberger observer. Two sets of parameters have been used: nominal ones (based on simplifications on the actuator model) and identified ones.

Burrows et al. [219] reviewed the design of a smart rotating machine involves the integration of controllable bearings, actuators, and sensors to measure a defined set of physical variables, an on-line adaptive controller, a control algorithm to achieve the desired performance, and an algorithm to reconfigure the system in the event of faults.

Fan and Pan [220] presented a electromagnetic actuator technique to increase the stability regions in the fluid-film bearing by eliminating the oil and dry whips. Jiffri and Garvey [221] studied various actuation technologies such as piezoelectric, magneto-strictive, electromagnetic, shape memory alloys and ultrasonic motors. Some of these technologies were considered in more detail as they show more potential of being implemented in a relatively uncomplicated configuration, in the intended application.

Bouzidane and Thomas [222] studied the nonlinear dynamic behaviour of a flexible shaft supported by smart hydrostatic squeeze film dampers, which were filled with a negative electrorheological fluid (NERF). A new smart hydrostatic squeeze film damper was proposed to reduce the transient response of the shaft and transmitted forces by applying an electric field to the NER fluid, which results in modifying its viscosity.

2.6 Summary

This chapter has explored various developments in rotor dynamic analysis procedures especially for gas turbine and aero-engine rotors mounted on ball and roller bearings. Ball and journal bearing dynamics significantly influences the rotor stability. Single row, double row ball bearing analysis procedures were explained in detail. Also, various works illustrated the effects of localized faults such as inner race defect, outer race defect and ball defects on vibration response of rotor. The shaft modelling and its flexibility considerations are very important to realise the behaviour of actual rotor system. Several earlier works focused on finite element modelling and illustrated unbalance response as an aid to identify the system. Also, the modelling of external forces using Alford and Muszyska's models became a common issue in most of the literature. Several developments on modelling rub-impact analysis were summarised. The works related to control of rotor vibrations, have been classified into active, passive and semi-active techniques and several models were reported in a separate section. Present work focuses on the following broad issues relating to aero-engine rotors (i) Modelling experimental studies on LP and two spool rotor bearing systems with secondary faults including rub-impact excitations, gas transients, and ball bearing faults. (ii) Numerical studies on semi-active and active control of these rotors passing through critical speeds. The next chapter focuses on mathematical modelling of the proposed rotor bearing systems.

Chapter 3

Mathematical modelling

This chapter presents modelling of rotor-bearing system under consideration with various nonlinear forces involved in the system. Also, the analysis outcomes are implemented for identification of the entire rotor dynamic system.

3.1 Dynamic Equations of rotor

The rotor dynamic system, in the present study contains a generalized non-uniform shaft having cross section A (z) and moment of inertia I (z), with one or more disks having mass m_i and the diametral and polar moments of inertia J_{di} and J_{pi} supported over the rolling element bearings. Initially, the continuous systems of equations for shaft are described. Figure 3.1 shows the shaft configuration as a beam undergoing bending and torsional motions.
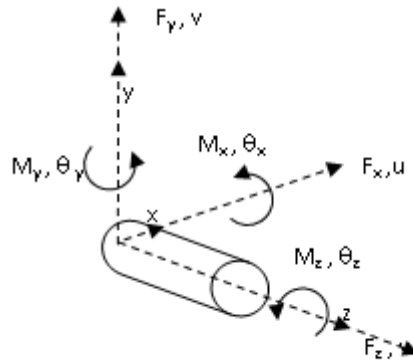

Figure 3.1: Rotating Timoshenko beam with generalized coordinates

Here w is the axial displacement, u and v are the lateral displacements and θ_x, θ_y and θ_z are the rotations with respect to x, y and z axes, respectively. Based on the generalized coordinates considered, the kinetic and potential energies, T and U, of the spinning beam are given by,

$$T = \frac{1}{2}\, \rho \int_o^L \left[A(z)(\dot{u}^2 + \dot{v}^2) + I_d \left(\dot{\theta}_x^2 + \dot{\theta}_y^2 \right) + I_p \left(\dot{\theta}_z^2 + \dot{\theta}_z(\dot{\theta}_x \theta_y + \dot{\theta}_y \theta_x) \right) \right] dz \tag{3.1}$$

$$U = \frac{1}{2} \int_o^L \left\{ EI(z) \left(\theta_x'^2 + \theta_y'^2 \right) + \kappa GA(z)[(\theta_y - u')^2 + (\theta_x + v')^2] \right\} dz \tag{3.2}$$

Substituting these energy expressions in the Hamilton principle in the usual notation

$\delta \int_{t_1}^{t_2}(T - U)dt = 0$, (where t_1 and t_2 are the time intervals in the dynamic trajectory and δ is the variational operator), the following set of equations are obtained:

$$\rho A(z)\frac{\partial^2 u}{\partial t^2} - \kappa A(z)G\left(-\frac{\partial \emptyset_y}{\partial z} + \frac{\partial^2 u}{\partial z^2}\right) = 0 \tag{3.3}$$

$$\rho A(z)\frac{\partial^2 v}{\partial t^2} - \kappa A(z)G\left(\frac{\partial \theta_x}{\partial z} + \frac{\partial^2 v}{\partial z^2}\right) = 0 \tag{3.4}$$

$$\rho I(z)\frac{\partial^2 \theta_x}{\partial t^2} + 2\Omega I(z)\rho\frac{\partial \theta_y}{\partial t} - EI(z)\frac{\partial^2 \theta_x}{\partial z^2} + \kappa A(z)G\left(\theta_x + \frac{\partial v}{\partial z}\right) = 0 \tag{3.5}$$

$$\rho I(z)\frac{\partial^2 \theta_y}{\partial t^2} - 2\Omega I(z)\rho\frac{\partial \theta_x}{\partial t} - EI(z)\frac{\partial^2 \theta_y}{\partial z^2} + \kappa A(z)G\left(\theta_y - \frac{\partial u}{\partial z}\right) = 0 \tag{3.6}$$

where, ρ is the density, E is Young's modulus, G is the shear modulus, κ is the shear coefficient, and $\dot{\theta}_z = \Omega$ is the rotational speed of the beam. The boundary conditions of the rotating

By eliminating the bending rotations θ_x and θ_y, equation of motion of the rotating Timoshenko beam in y directions will take the following form

$$EI(z)\frac{\partial^4 v}{\partial z^4} + \rho A(z)\frac{\partial^2 v}{\partial t^2} - \rho I(z)\left(1 + \frac{E}{\kappa G}\right)\frac{\partial^4 v}{\partial z^2 \partial t^2} + \frac{\rho^2 I(z)}{\kappa G}\frac{\partial^4 v}{\partial t^4}$$
$$+ 2\rho I(z)\Omega\left(\frac{\partial^2}{\partial z^2}\left(\frac{\partial u}{\partial t}\right) - \frac{\rho}{\kappa G}\frac{\partial^3 u}{\partial t^3}\right) = 0 \tag{3.7}$$

The same equation of motion can be written for the *x* direction as well.

It is seen that the motion in two orthogonal planes are coupled with the last term. This equation cannot be solved by classical solution methods. Unlike the shaft, disks can be considered as rigid and have kinetic energy given as

$$T_d = \frac{1}{2}m_d(\dot{u}^2 + \dot{v}^2) + \frac{1}{2}J_d(\dot{\theta}_x^2 + \dot{\theta}_y^2) + \frac{1}{2}J_p[\Omega^2 + \Omega(\dot{\theta}_x\theta_y - \dot{\theta}_y\theta_x)] \tag{3.8}$$

The external work done by unbalance forces at the disk (mass m_d and eccentricity- e) are given as

$$W_d = m_d e \Omega^2(u \cos\Omega t + v \sin\Omega t) \tag{3.9}$$

Likewise, gravity forces in Y-direction would also contribute to the work expression. Unlike synchronous rotor motions, where the precession and rotation speeds are equal, in flexible rotors, the rotor motion is stable and synchronous below certain operating speed. Above this speed, there is a sub-synchronous component to the rotor motion. This onset speed of instability always exceeds the rotor first critical speed. As rotor rotates above this onset speed, the sub-synchronous component diverges exponentially with time. This type of motion is referred to as whirling. Forward and backward whirls occur and most of the synchronous whirling is due to the forward mode. Therefore, the first study in rotor analysis is to predict the critical speeds of operation.

3.2 Bearing Dynamics

Apart from the disk and shaft inertia and stiffness, the rotor dynamic system is subjected to reactions at the bearing nodes. Earlier studies considered these reactions as linear time invariant forces. However, depending on the type of bearing, later on, it was realized that these forces are highly nonlinear functions of bearing displacements and time. In present context, the ball/roller bearing dynamic forces due to dry friction contacts are often used from Hertz's contact theory.

Ball bearing consists of inner race, outer race, and rolling balls and cages as shown in Figure 3.2. The outer race acts on the inner race by rolling balls, and their interaction force is a restoring force, which is generated by the contact deformation between balls and races.

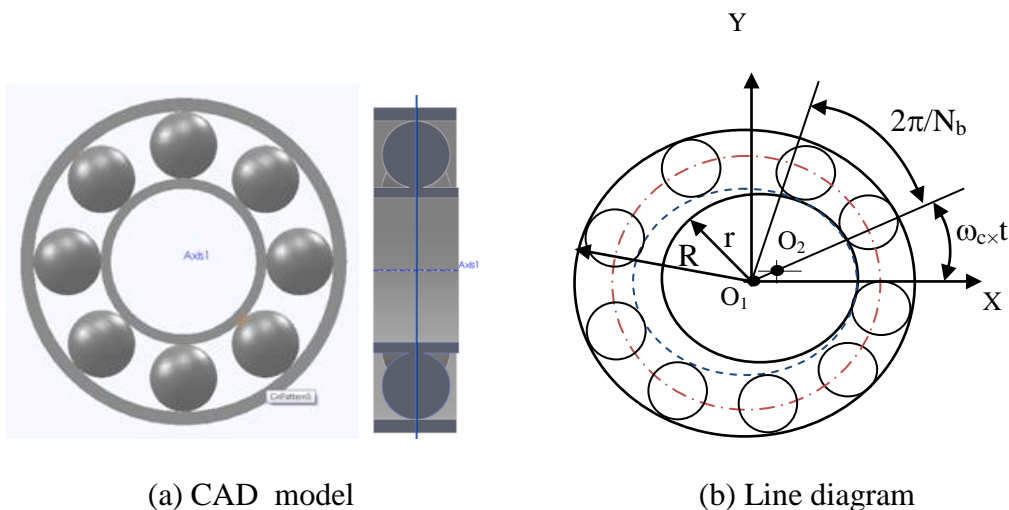(a) CAD model   (b) Line diagram

Figure 3.2: Schematic diagram of ball bearing system

In the rotor-ball bearing system, usually, the outer race of the ball bearing is fixed to the bearing housing and the inner race is rigidly fixed to the rotating shaft. During the working of ball bearing, the total stiffness and compliance of bearing vary periodically with variation in contact position between balls and races and the varying compliance

(VC) of bearing is a parametric excitation of the rotor-ball bearing coupling. This VC vibration is inherent and it always exists even if the bearing is newly installed and fault-free.

Due to these ball passing oscillations (VC), the frequency response of the rotor contains spikes at frequencies other than the critical operating modes of the rotor.

3.2.1 Hertz's contact deformation and forces

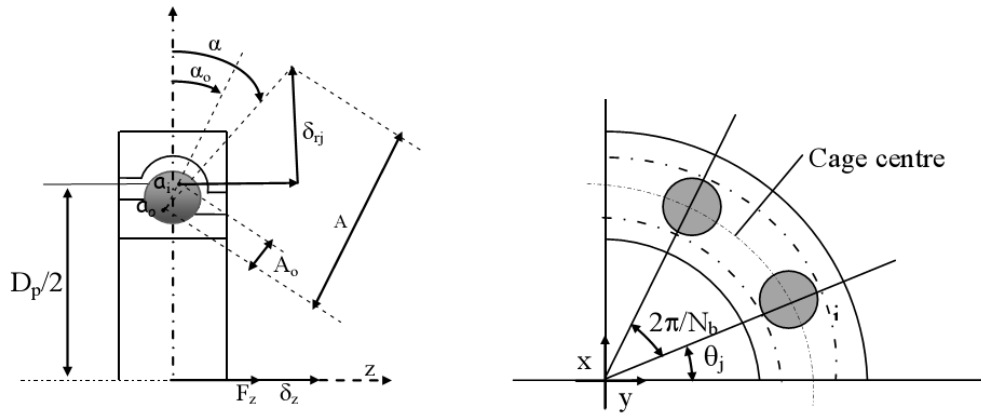Figure 3.3 shows the coordinate system of the ball bearing geometry for a deep groove ball bearing.

Figure 3.3: The coordinate system of the ball bearing geometry

The general displacement vector q is given by

$$\mathbf{q} = [\text{u v w } \theta_x\, \theta_y\,]^T \tag{3.10}$$

Where u, v and w are the relative displacements in the x, y and z direction, and θ_x and θ_y are the relative rotations around the x and y axes. The bearing forces are defined as

$$\mathbf{F} = [\text{F}_x\ \text{F}_y\ \text{F}_z\ \text{M}_x \text{M}_y\,]^T \tag{3.11}$$

where F_x, F_y and F_z are the static force loads in the radial (x,y) and axial (z) directions, and M_x and M_y are the static moment loads around the x and y axes. The rotational displacement about z-axis is not included, as the shaft is allowed to freely rotate about z-axis. For a bearing with pitch diameter D_p, an unloaded contact angle α_0, a ball diameter D_b, the resulting nominal cage speed ω_c is given by

$$\omega_c = \frac{\Omega}{2}\left(1 - \frac{D_b \cos\alpha_0}{D_p}\right) \tag{3.12}$$

The angular position ϕ_j of ball j is defined as

$$\phi_j = \phi_c + \frac{2\pi(j-1)}{N_b}, \quad j=1, 2 \dots N_b \tag{3.13}$$

where $\phi_c = \omega_c t$, is the cage angular position and N_b is the number of balls.

The Hertz's contact force Q_j associated with the contact deformation δ_j is defined by the load-deformation by the load-deflection relation

$$Q_j = K_b \delta_j^{1.5}, \tag{3.14}$$

where the load-deflection factor K_b (units of $N/m^{1.5}$) depends on the curvatures and material properties of the surfaces in contact defined as follows:

$$K_b = \left[\frac{1}{\left(\frac{1}{K_{bi}}\right)^{2/3} + \left(\frac{1}{K_{bo}}\right)^{2/3}} \right]^{3/2} \tag{3.15}$$

where K_{bi}, K_{bo} are ball-inner, ball-outer races contact stiffness values respectively.

The contact force Q_j acts along the loaded contact angle α_j which is defined as

$$\tan \alpha_j = \frac{\delta_{zj}^*}{\delta_{rj}^*}. \tag{3.16}$$

where

$$\delta_{rj}^* = A_o \cos\alpha_o + \delta_{rj} \tag{3.17a}$$

$$\delta_{zj}^* = A_o \sin\alpha_o + \delta_{zj}, \tag{3.17b}$$

are the components of loaded relative distance

$$A = \sqrt{\delta_{rj}^{*2} + \delta_{zj}^{*2}}. \tag{3.18}$$

Also, the effective displacement δ_{rj} and δ_{zj} of jth ball in the radial and axial directions are calculated from the relative bearing displacements vector $\{q\}$ as

$$\delta_{rj} = u\cos \phi_j + v\sin \phi_j - r_c \tag{3.19}$$

$$\delta_{zj} = w + r_d \left(\theta_y \sin \phi_j - \theta_y \cos \phi_j\right), \tag{3.20}$$

where r_c is the radial clearance and r_d is the radial distance of the inner raceway groove curvature centre.

The contact deformation δ_j for ball j is given by

$$\delta_j = \begin{cases} A - A_o, & \delta_j > 0 \\ 0, & \delta_j \le 0 \end{cases} \tag{3.21}$$

where A and A_o are the loaded and unloaded relative distance between the inner and outer raceway groove curvature centres a_i and a_o (Figure 3.3) respectively.

The loads carried by the ball are calculated by solving the following set of nonlinear algebraic equations as a function of the cage angular position ϕ_j.

$$\begin{bmatrix} F_x \\ F_y \\ F_z \\ M_x \\ M_y \end{bmatrix} = \Sigma_{j=1}^{N_b} Q_j \begin{bmatrix} \cos\alpha_j \cos\phi_j \\ \cos\alpha_j \sin\phi_j \\ \sin\alpha_j \\ r_d \sin\alpha_j \sin\phi_j \\ -r_d \sin\alpha_j \cos\phi_j \end{bmatrix} = \Sigma_{j=1}^{N_b} \begin{bmatrix} F_{xj} \\ F_{yj} \\ F_{zj} \\ M_{xj} \\ M_{yj} \end{bmatrix} \tag{3.22}$$

3.2.2 Simplified model with 2 degrees of freedom

Based on the above formulation with five displacement components, the expressions for first two forces are employed frequently. During simplification, the contact angle α_j is considered as zero leading to two contact forces only. This simplified contact forces are summarized below:

$$F_{xb} = -\Sigma_{j=1}^{N_b} K_b(\delta_j)^{1.5} H(\delta_j) \cos\phi_j \tag{3.23}$$

$$F_{yb} = -\Sigma_{j=1}^{N_b} K_b(\delta_j)^{1.5} H(\delta_j) \sin\phi_j \tag{3.24}$$

Where Heaviside function is defined as

$$H(\delta_j) = \begin{cases} 1, & \delta_j > 0 \\ 0, & \delta_j \le 0 \end{cases} \tag{3.25}$$

Here, δ_j is total elastic deformation, given as

$\delta_j = u_b \cos\phi_j + v_b \sin\phi_j - r_c$, with $r_c = r_{ci} + r_{co}$, is total radial clearance between inner and outer races and ball, u_b and v_b refers to the relative displacements of inner and outer races along X and Y directions respectively. Also, the attitude angle for each ball is given by $\emptyset_j = \frac{2\pi}{N_b}(j-1) + \Omega\left(\frac{r_i}{r_i + r_o}\right)$, where Ω is speed of rotation of shaft, N_b is number of balls, r_i and r_c are inner and outer race radii respectively.

3.2.3 Double-row ball bearing forces

Double-row bearings offer certain advantages over single-row bearings, as they are capable of providing higher axial and radial rigidity and carry bi-directional or combined loads. Consequently, double-row bearings are widely used in machine tool spindles, industrial pumps and air compressors, as well as in automotive, helicopter and aircraft applications such as gear boxes, wheel hubs and helicopter rotors. Compared to single-row ball bearings, in double-row bearings, shaft is subjected to alternating load vector

$$\boldsymbol{F} = [F_x \, F_y \, F_z \, M_x \, M_y \,]^T.$$ (3.26)

Figure 3.4 shows the back-to-back and face-to-face bearings configurations respectively.

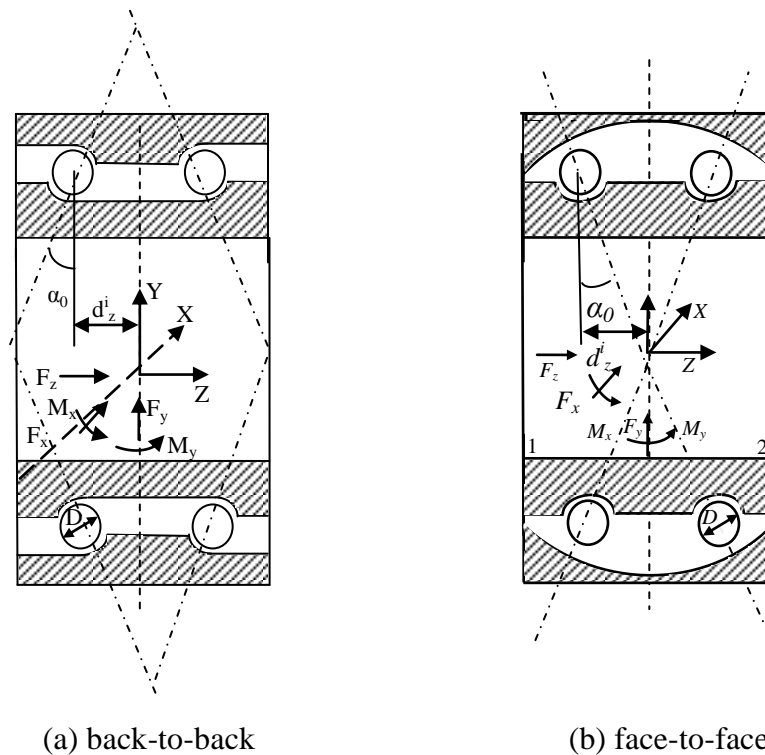(a) back-to-back   (b) face-to-face

Figure 3.4: Possible arrangements of double-row ball bearings

In former case, load lines (the lines that pass through the contact point of the balls) meet outside of the bearing, while in latter case; they converge toward the bore of the bearing. In general the effective load centre (spread) of the back-to-back arrangement is larger; thus, it has higher moment stiffness terms and a higher moment load carrying capacity. The vast majority of commercial double-row angular contact ball bearings are found in the back-to-back arrangement. It is considered that only the relative displacement between the bearing rings. Consider the jth rolling element of the ith row of a double-row angular contact ball bearing shown in Figure 3.5.

Here, A_0 and A_j^i are respectively the unloaded and loaded relative distances between inner and outer race centre of curvatures. Assuming the outer ring to be fixed, the total elastic deformation of each ball is first obtained by using kinematics of balls in the double-row ball bearing.

Figure 3.5: Schematic of double-row angular contact ball bearing

The components of the resultant radial load are given by following equation:

$$F_x = \sum_{i=1}^{2} \sum_{j=1}^{N_b} K_b [\delta(\phi_j^i)]^{1.5} H(\delta_j^i) \cos\phi_j^i \cos\alpha_j^i \tag{3.27}$$

$$F_y = \sum_{i=1}^{2} \sum_{j=1}^{N_b} K_b [\delta(\phi_j^i)]^{1.5} H(\delta_j^i) \sin\phi_j^i \cos\alpha_j^i \tag{3.28}$$

$$F_z = \sum_{i=1}^{2} \sum_{j=1}^{N_b} K_b [\delta(\phi_j^i)]^{1.5} H(\delta_j^i) \sin\alpha_j^i \tag{3.29}$$

$$M_x = \sum_{i=1}^{2} \sum_{j=1}^{N_b} K_b [\delta(\phi_j^i)]^{1.5} H(\delta_j^i) \, [R_p \sin\phi_j^i - \mu^i \, d_z^i \cos(\alpha_j^i)]\sin(\phi_j^i) \tag{3.30}$$

$$M_y = \sum_{i=1}^{2} \sum_{j=1}^{N_b} K_b [\delta(\phi_j^i)]^{1.5} H(\delta_j^i) \, [-R_p \sin\phi_j^i + \mu^i \, d_z^i \cos(\alpha_j^i)] \cos(\phi_j^i) \tag{3.31}$$

where $\mu^i = $ -1 for left row (i=1)and

$\qquad\qquad = +1$ for right row (i=2)

And d_z^i is the axial distance between the bearing centre and ith row of the bearing.

The elastic deformation δ is given by

$$\delta(\phi_j^i) = A_j^i - A_0 \tag{3.32}$$

Here, $H(\delta_j^i)$ is a Heaviside function similar to single-row case. The ball is unloaded, when A_0 is greater than A_j^i and elastic deformation is considered as zero. Further, A_j^i is defined

in terms of radial and axial displacements ($(\delta_r)_j^i$ and $(\delta_z)_j^i$) and unloaded contact angle (α_o) of the balls as follows:

$$A_j^i = \sqrt{\left((\delta_r^*)_j^i\right)^2 + \left((\delta_z^*)_j^i\right)^2} \tag{3.33}$$

where

$$(\delta_r^*)_j^i = (\delta_r)_j^i + A_o\cos(\alpha_o) \tag{3.34}$$

$$(\delta_z^*)_j^i = (\delta_z)_j^i + v^i\left(A_o\sin(\alpha_o) + (\delta_{zo})^i\right) \tag{3.35}$$

The radial and axial deflections are given by:

$$(\delta_r)_j^i = \left[u + \lambda^i d_z^i \theta_y\right]\cos\left(\phi_j^i\right) + \left[v - \lambda^i d_z^i \theta_x\right]\sin\left(\phi_j^i\right) - r_c \tag{3.36}$$

$$(\delta_z)_j^i = w + R_p[\theta_x\sin\left(\phi_j^i\right) - \theta_y\cos\left(\phi_j^i\right)] \tag{3.37}$$

The loaded contact angle is given by:

$$\alpha_j^i = \tan^{-1}\left(\frac{(\delta_z^*)_j^i}{(\delta_r^*)_j^i}\right) \tag{3.38}$$

where v^i is a dimensionless constant depending on ball configuration. For back-to-back configuration,

$\quad\quad v^i = +1$ for i=1(left row)

$\quad\quad\quad = -1$ for i=2(right row)

For face-to-face configuration,

$\quad\quad v^i = -1$ for i=1(left row)

$\quad\quad\quad = +1$ for i=2(right row).

The coefficient λ^i is a dimensionless constant equal to -1 for i=1 (left row) and equal to +1 for i=2 (right row) and $(\delta_{zo})^i$ defines an axial preload displacement on the ith row obtained by bringing the inner and outer race ways closer together. It can have a positive value only if the radial clearance is eliminated.

3.2.4 Ball bearing fault models

The geometric imperfections are classified into two categories (1) relating to local defect in the balls and inner and outer races, which generate vibrations in ball-race contact. (2) Relating to the distributed defects like, surface roughness, waviness of rolling contact surfaces, misaligned races or off sized balls etc. which give continuous fluctuations in bearing reactions. Localized bearing defects occur in different forms, such as spalls, pits

and dents. Corrosion and oxidation pits and hard particle contamination dents would cause fatigue failures of bearings due to repeated cyclic stresses on the race surfaces. The bearing faults generate a series of impact vibrations every time a running ball passes over the surface of the defect. These impacts reoccur at bearing characteristic frequencies, which are estimated based on geometry of bearing, location of defect and the running speed of the shaft. As the impact generated by the bearing fault distributes its energy over a wide frequency range, the bearing characteristic frequency has relatively low energy and is contaminated by high energy noise. Often, these localized faults appeared in three different components: (1) Outer raceway (2) Inner raceway and (3) Rolling elements. The ball looses the contact suddenly once it enters the dent region and regains its contact instantly when it exits the area. This results in large impulse force. When ball rolls over the defect, normal motions of all bearing components will be disturbed resulting in either of the following effects. (i) Additional deflection due to material absence will be introduced. (ii) Change of curvature radius of a raceway in a defect zone altering the Hertzian contact coefficients. The radial deformation of jth rolling element entering the spall is given as

$$\delta_j = (x_j \cos \phi_j + y_j \sin \phi_j - r_c - \beta_j \Delta_r) \tag{3.39a}$$

Here, β_j is a factor to be computed based on the type of fault and Δr is the depth of fault.

(a) Outer raceway defect

Figure 3.6 (a) shows the outer raceway defect and when the ball passes through the outer race defect.
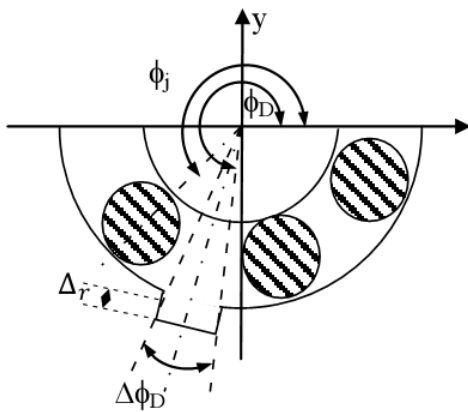
(a) Outer raceway defect (spall)   (b) Inner raceway defect (dent)
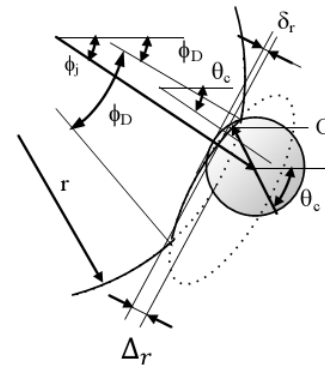
Figure 3.6: Outer and Inner race defects

Let the angle spanned by the defect be $\Delta\phi_D$ and the angular position of the defect is ϕ_D.

The switch value β_j here may be written as:

$$\beta_j \quad = 1, \text{ if } \phi_D < \phi_j < \phi_D + \Delta\phi_D$$

$$= 0, \text{ otherwise} \tag{3.39b}$$

It results in a characteristic frequency equal to

$$f_{obp} = \frac{N_b}{2} \left(\frac{\Omega}{2\pi}\right) \left(1 - \frac{D_b}{D_p} \cos\alpha_i\right) \tag{3.40}$$

Here, D_b and D_P are ball and pitch diameters.

(b) Inner raceway fault (dent)

When defect of depth Δ_r is on inner race as shown in Figure 3.6 (b) the defect angular position changes as

$$\phi_D = \Omega t + \phi_{Do} \tag{3.41a}$$

where, ϕ_{Do} is initial angular position of the defect.

Here ,

$$\beta_j \quad = 1, \text{ if } \phi_j \epsilon \ (\phi_D, \phi_D + \Delta\phi_D)$$

$$= 0, \text{ otherwise} \tag{3.41b}$$

When the ball passes through the inner race defect, it has following characteristic frequency:

$$f_{ibp} = \frac{N_b}{2} \left(\frac{\Omega}{2\pi}\right) \left(1 + \frac{D_b}{D_p} \cos\alpha_i\right) \tag{3.42}$$

(c) Ball defect

When a ball with spall rotates about an axis normal to the plane containing centres of inner race and outer race as shown in Figure 3.7, it comes in contact with inner and outer races at regular intervals. Assuming the response is different for contact on inner and outer races, there will be a periodicity based on rotation of the ball. The additional deflection Δ_r is obtained as a sum of deflections during contact of ball with inner and outer rings.

Here, $\beta_j = 1$, if $\left\{\left[\text{mod}\left(\phi_j, 2\pi\right) - \theta_{bd}\right] + \left[\text{mod}\left(\phi_j, 2\pi\right) - \pi - \theta_{bd}\right]\right\} \leq \theta_e \tag{3.43}$
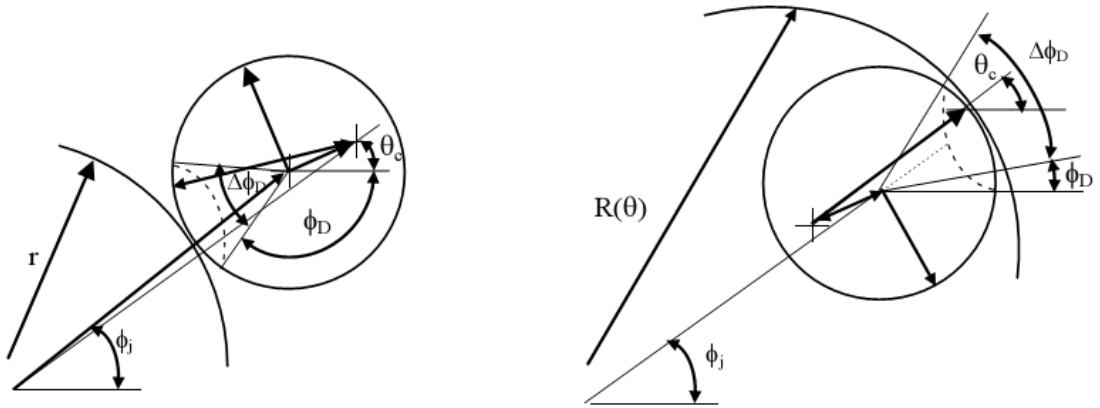
$$= 0 \text{ otherwise}$$

(a) Inner race and ball bent contact   (b) Outer race and ball bent contact

Figure 3.7: Dent on the rolling element

In summary, the additional deflection due to these three type of faults is given as $\Delta_r = \beta_j \times \Delta_D$. Where, $\beta_j(x) = 1$, if $|x| \leq \theta_e$

$$= 0, \text{ otherwise}$$

Where x is given from the Table 3.1 given below

Table 3.1: Types of faults

Type of fault	X
Outer race	$\text{mod}(\theta_{oj}, 2\pi) - \frac{2\pi}{z}(j-1) - \varphi_{od}$ where $\theta_{oj} = \frac{2\pi}{z}(j-1) + \omega_c \times t$
Inner race	$\text{mod}(\theta_{ij}, 2\pi) - \frac{2\pi}{z}(j-1) - \varphi_{id}$ where $\theta_{ij} = \frac{2\pi}{z}(j-1) + (\omega_c - \omega) \times t$
Ball fault	$\text{mod}(\theta_b, 2\pi) - \varphi_{bd} + \text{mod}(\theta_b, 2\pi) - \pi - \varphi_{bd}$

$\varphi_{od}, \varphi_{id}, \varphi_{bd}$ are initial angular offset of detect to first ball and initial angular offset of defect to inner race at $\theta_b = 0$.

The radial force of the jth ball, when it coincides with defect angle is given by

$$Q_j = K_b(u_b \cos \phi_j + v_b \sin \phi_j - r_c - \Delta_r)^{1.5} \tag{3.44}$$

The total restoring force components in X and Y directions can be computed as

45

$$F_{xb} = -\sum_{j=1}^{N_b} Q_j \cos \emptyset_j \tag{3.45}$$

$$F_{yb} = -\sum_{j=1}^{N_b} Q_j \sin \emptyset_j \tag{3.46}$$

3.2.5 Effects of waviness

Sometimes, the wavy surface on inner or outer races would also affect the contact forces. Surface peaks and valleys influence the rolling contact forces. This generated force due to surface texture is related to frequency of surface waves as shown in Figure 3.8 (waviness and roughness). Imperfection of waviness with varying amplitudes present across the circumference of the inner and outer races of the bearing surfaces. This waviness is the main source of vibration.
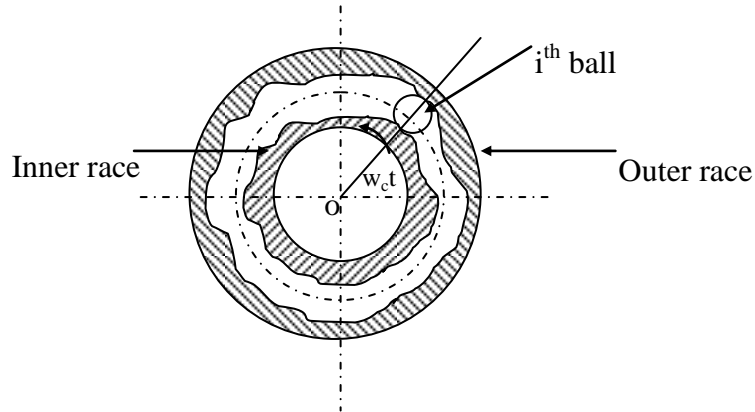
Figure 3.8: Schematic of waviness in bearing

The radial elastic deformation in the restoring force equation due to waviness is modified as

$$\delta_j = (x_j \cos \phi_j + y_j \sin \phi_j - r_c - w_j) \tag{3.47}$$

where w_j is the wave at the contact angle corresponding to j^{th} ball represented as

$$w_j = w_o + w_p \sin (N_w \phi_j) \tag{3.48}$$

Here, w_p is maximum amplitude of the wave, w_o is the initial wave amplitude. Number of waves $N_w = \pi D/\lambda$, where λ is the wave length of roughness, D is diameter of outer/inner race. The common wavelength, measured by bearing manufacturers is 0.8mm.

(a) Inner race waviness

When the ball is moving round the inner race, it follows the rolling surface contour continuously. It is assumed that there exists no slip condition, i.e., ball is always in

46

contact with inner race and also it is assumed that the inner race surface has a circumferential unevenness. The amplitude of uneven surface is often measured with respect to the central point at a certain angle from the reference axis.

Considering the waviness of inner race, an additional deformation in the contact deformation becomes

$$\Delta_i = \sum A_m \sin \left[m \left(\frac{2\pi}{N_b}(i-1) + (\omega_{cage} - \omega_{inner}) \times t \right) \right] \tag{3.49}$$

where m is the order of harmonic of waviness in the inner race, and A_m is the amplitude of these harmonics.

(b) Outer Race Waviness

The outer race unevenness is usually of the same order of magnitude as inner race unevenness. The outer race surface also has circumferential uneven surface. By assuming the outer race to be fixed, an additional term in the contact deformation becomes

$$\Delta_o = \sum A_n \sin \left[n \left(\frac{2\pi}{N_b}(i-1) + \omega_{cage} \times t \right) \right] \tag{3.50}$$

where n is the order of harmonic of waviness in the outer race, and A_n is the amplitude of these harmonics.

3.3 Squeeze film damper forces

Figure 3.9 shows the outer race of the bearing supported over a SFD with the help of centralizing springs. It is assumed that the outer race of ball bearing serves as a journal for the squeeze-film damper.
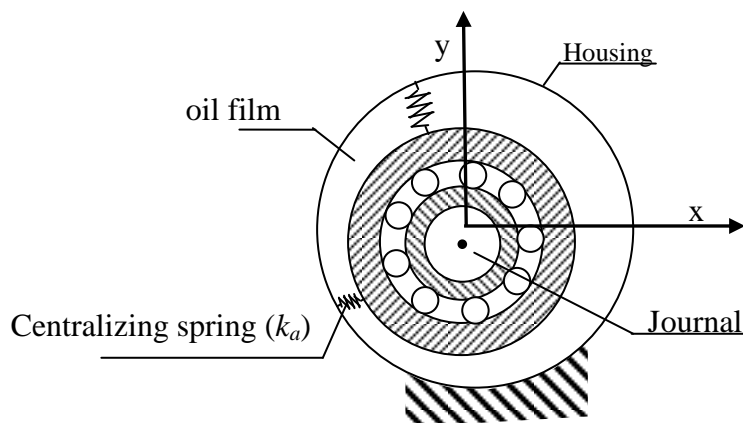
Figure 3.9: Schematic of SFD system

In obtaining additional forces due to SFD, a short bearing approximation based on Reynolds equation for incompressible flow is considered and the cavitation is modelled

as a π-film and therefore the contribution below ambient pressure to the oil-film force is negligible. The instantaneous oil pressure distribution *p* is given from the solution of the following incompressible Reynolds equation:

$$\frac{1}{R_s^2}\frac{\partial}{\partial\theta}\left\{h^3\left(\frac{\partial p}{\partial\theta}\right)\right\} + h^3\frac{\partial^2 p}{\partial z^2} = 12\mu\left(e\dot{\phi}\sin\theta + \dot{e}\cos\theta\right) \tag{3.51}$$

Here *h* is the varying film thickness as a function of θ. e and ė are the displacement and velocity of the journal in the radial direction respectively, θ is the angular coordinate measured from the position of maximum film thickness in the direction of rotor angular speed. Then the oil film force components are obtained explicitly with cavitated (π-film) short bearing approximation as:

$$F_x = F_r \cos\phi - F_t \sin\phi \tag{3.52a}$$

$$F_y = F_r \sin\phi + F_t \cos\phi \tag{3.52b}$$

where

$$F_r = -\frac{\mu R L^3}{c^2}\left[\dot{\varepsilon}I_1 + \varepsilon\dot{\phi}I_2\right] \tag{3.52c}$$

$$F_t = -\frac{\mu R L^3}{c^2}\left[\dot{\varepsilon}I_2 + \varepsilon\dot{\phi}I_3\right] \tag{3.52d}$$

$$\phi = \tan^{-1}\left(\frac{Y}{X}\right) \tag{3.52e}$$

where (*X,Y*) is the displacement of SFD in the fixed co-ordinate system, μ is the oil viscosity, R_s is the radius of SFD, *L* is the land length of SFD, *c* is the radial clearance of SFD, ε is the non-dimensional eccentricity ratio with *c,* that is: $\varepsilon = \frac{\sqrt{(X^2+Y^2)}}{c}$, $\dot{\phi}$ is the angular velocity of SFD, $\tan\phi = X/Y$.. As outer race of ball bearing is floating in the damper, the values of X and Y are respectively taken as x_0 and y_0 of the outer race.

The bearing integrals I_1, I_2 and I_3 are obtained from the Somerfield transform as follows:

$$I_1 = \int_{\theta_1}^{\theta_1+\pi}\frac{\cos^2\theta}{(1+\varepsilon\cos\theta)^3}d\theta \tag{3.53a}$$

$$I_2 = \int_{\theta_1}^{\theta_1+\pi}\frac{\sin\theta\cos\theta}{(1+\varepsilon\cos\theta)^3}d\theta \tag{3.53b}$$

$$I_3 = \int_{\theta_1}^{\theta_1+\pi}\frac{\sin^2\theta}{(1+\varepsilon\cos\theta)^3}d\theta \tag{3.53c}$$

$$\theta = \tan^{-1}\left(-\frac{\dot{\varepsilon}}{\varepsilon\dot{\phi}}\right) \tag{3.53d}$$

48

These are evaluated analytically in closed form. Further, in order to arrest outer-race rotation in the damper, a centralizing spring of stiffness k_a connecting outer race with the casing of damper is often employed as shown in the Figure 3.10.
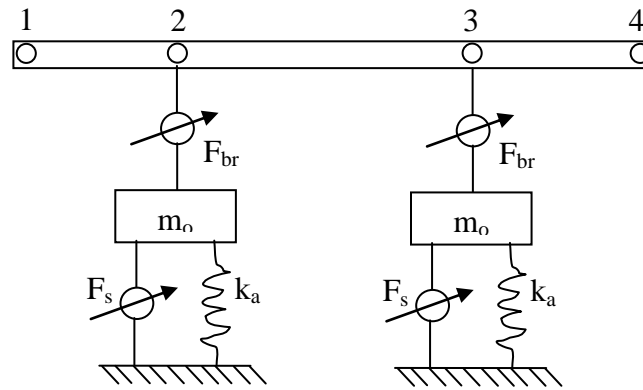

Figure 3.10: Rotor modelling with SFD forces (m_o is the outer race mass)

The stiffness of this spring affects the rotor response considerably. While modelling SFD forces with rotor model, a semi-finite element description of the system is employed in present work.

3.4 External loads

In addition to unbalance of the disk and bearing reactions, the rotordynamic system is subjected to various forces including rub-impact loads between rotor and stator, or between rotor and seals, the periodic excitations, transient gas forces etc.

3.4.1 Rub-impact excitation

It is assumed that there is an initial clearance of   between rotor and stator. Compared with one complete period of rotating, the time during rub-impact is very short; therefore, an elastic impact model is used. Also the Coulomb type of frictional relationship is assumed in the analysis. When rub happens as shown in Figure 3.11, the radial impact force F_N and the tangential rub force F_T can thus be expressed as

$$F_N(x, y) = \begin{cases} 0, & \text{(for } e < \delta) \\ (e - \delta)k_c, & \text{(for } e \geq \delta) \end{cases}$$

$$F_T = f F_N \qquad\qquad (3.54)$$
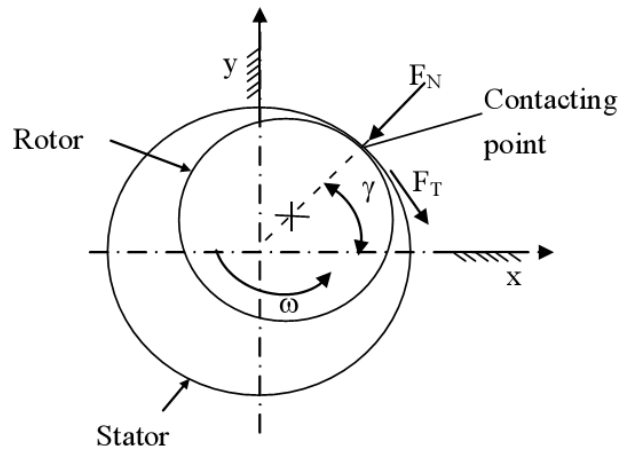
Figure 3.11: Schematic of rub and impact forces

where δ the initial static clearance between rotor and stator, f is is the friction coefficient between rotor and stator, k_c is the radial stiffness of the stator and $e = \sqrt{x^2 + y^2}$ is the radial displacement of the rotor. These two forces can be written in x–y co-ordinates as

$$F_x(x, y) = -F_N \cos \gamma + F_T \sin \gamma$$
$$F_y(x, y) = -F_N \sin \gamma - F_T \cos \gamma$$

$\qquad(3.55)$

(or)

$$\begin{Bmatrix} F_x \\ F_y \end{Bmatrix} = H(e - \delta) \frac{(e-\delta)k_c}{e} \begin{bmatrix} 1 & -f \\ f & -1 \end{bmatrix} \begin{Bmatrix} x \\ y \end{Bmatrix}$$

$\qquad(3.56)$

where H:IR⟶IR is the Heaviside function, that is,

$$H(x) = \begin{cases} 0, & x \leq 0 \\ 1, & x > 0 \end{cases}$$

$\qquad(3.57)$

This equation indicates that when the rotor displacement e is smaller than δ, there will be no rub-impact interaction and the rub-impact forces are zero while the rub-impacting will happen if the rotor displacement e is bigger than δ .

3.4.2 Muszynska's gas forces

Among various computing models, Muszynska's force model is widely recognized because it is able to describe the nonlinear characteristic of excitation force nicely. The nonlinear seal-fluid force expression is given as

$$\begin{Bmatrix} F_{gx} \\ F_{gy} \end{Bmatrix} = - \begin{bmatrix} k_g - m_g \gamma^2 \Omega^2 & \gamma \Omega d_g \\ -\gamma \Omega d_g & k_g - m_g \gamma^2 \Omega^2 \end{bmatrix} - \begin{bmatrix} d_g & 2\gamma \Omega m_g \\ -2\gamma \Omega m_g & d_g \end{bmatrix} \begin{Bmatrix} \dot{x} \\ \dot{y} \end{Bmatrix} - \begin{bmatrix} m_g & 0 \\ 0 & m_g \end{bmatrix} \begin{Bmatrix} \ddot{x} \\ \ddot{y} \end{Bmatrix}$$

$\qquad(3.58)$

Muszynska's model assumes that the fluid force which results from averaging the circumferential flow is rotating with angular velocity $\gamma\omega$, where ω is the shaft rotational speed and γ is the key variable of Muszynska's model, which represents the fluid average circumferential velocity ratio. In above Equation, k_g, D_g and m_g are fluid stiffness, damping and inertia coefficients respectively. The factors K_g, D_g and γ vary with increase in rotor eccentricity and can be written as:

$$k_g = k_0(1 - \varepsilon^2)^{-n_1}, d_g = d_0(1 - \varepsilon^2)^{-n_1} \tag{3.59}$$

Where

$n_1 = 0.5\text{-}3$, $\gamma = \gamma_0(1 - \varepsilon)^{n_2}$, where $0 < n_2 < 1$ and $\gamma_0 < 0.5$. Here, $\varepsilon = \dfrac{\sqrt{x^2 + y^2}}{c_s}$ is the relative

eccentricity at the seal; c_s is seal clearance, n_1, n_2 and γ_0 vary for different types of seal materials; Characteristic factors K_0, D_0 and m_g can be obtained from Childs equation.

$$m_g = \mu_2\mu_3 T_f^2, \tag{3.60}$$

$$k_o = \mu_3\mu_0,$$

$$d_o = \mu_3\mu_0 T_f$$

$$\mu_0 = \frac{2\sigma^2}{1 + \xi + 2\sigma} E_f(1 - m_0),$$

$$\mu_1 = \frac{2\sigma^2}{1 + \xi + 2\sigma}\left[\frac{E_f}{\sigma} + \frac{B}{2}\left(\frac{1}{6} + E_f\right)\right],$$

$$\mu_2 = \frac{\sigma}{1 + \xi + 2\sigma}\left(\frac{1}{6} + E_f\right),$$

$$\mu_3 = \frac{\pi R_f \Delta P}{\lambda},$$

$$T_f = \frac{l_f}{v}$$

$$\lambda = n_0(R_a)^{m_0}\left[1 + \left(\frac{R_v}{R_a}\right)^2\right]^{(1+m_0)/2}$$

$$\sigma = \frac{\lambda l_f}{c_f},$$

$$E_f = \frac{1+\xi}{2(1+\xi+2\sigma)},$$

$$B = 2 - \frac{(R_v/R_a)^2 - m_0}{(R_v/R_a)^2 + 1},$$

$$R_v = \frac{R_f \omega C_f}{v},$$

(3.61)

$$R_a = \frac{R_f \omega C_f}{v}$$

Here, the parameters of Eq. (3.61) are as follows:

$\xi=0.1$, $n_o=0.0079$, $m_o=-0.25$, $v=1.5\times10^{-5}$Pa S (dynamic viscous coefficient of air).

3.5 Finite element modelling of the rotor

3.5.1 Shaft model

The finite element model of the rotor/ ball bearing/seal system is established using two-node Timoshenko beam elements as shown in Figure 3.12. Viscous damping and gyroscopic effects are added in the element damping matrix. Each node has four Degrees of Freedom (DOF) including two rotations and two translations.
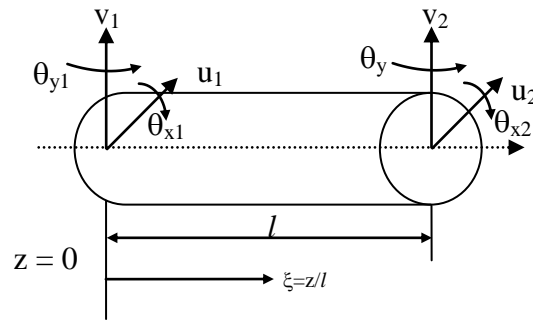
Figure 3.12: Timoshenko Beam element

According to the finite element method, the translations and rotational displacements of a typical cross section of the shaft unit can be approximated by the following equations:

$$\left\{ \begin{matrix} u \\ v \end{matrix} \right\} = [N]\{q_e\} = \begin{bmatrix} N_1 & 0 & 0 & N_2 & N_3 & 0 & 0 & N_4 \\ 0 & N_1 & -N_2 & 0 & 0 & N_3 & -N_4 & 0 \end{bmatrix}\{q_e\}$$

(3.62)

$$\left\{ \begin{matrix} \theta_x \\ \theta_y \end{matrix} \right\} = [D]\{q_e\} = \begin{bmatrix} 0 & -D_1 & -D_2 & 0 & 0 & -D_3 & -D_4 & 0 \\ D_1 & 0 & 0 & D_2 & D_3 & 0 & 0 & D_4 \end{bmatrix}\{q_e\}$$

(3.63)

Here, $\{q_e\}^T = \{u_1 \ v_1 \ \theta_{x1} \ \theta_{y1} \ u_2 \ v_2 \ \theta_{x2} \ \theta_{y2}\}$ is nodal displacement vector. The detailed expressions for shape functions $N_1, N_2,..$ and $D_1, D_2,..$ are given below with shear deformation consideration.

$$N_1 = \frac{1}{1+\phi}(1 + \phi - \phi\,\xi - 3\xi^2 + 2\xi^3) \qquad N_2 = \frac{1}{1+\phi}\left(\left(1 + \frac{\phi}{2}\right)\xi - \frac{4+\phi}{2}\xi^2 + \xi^3\right)$$

$$N_3 = \frac{1}{1+\phi}(\phi\,\xi + 3\xi^2 - 2\xi^3) \qquad N_4 = \frac{1}{1+\phi}\left(-\frac{\phi}{2}\xi - \frac{\phi-2}{2}\xi^2 + \xi^3\right) \qquad (3.64)$$

$$D_1 = -D_3 = -\frac{6}{(1+\phi)l}(\xi - \xi^2) \qquad D_2 = \frac{1}{1+\phi}[1 + \phi - (4 + \phi)\xi + 3\xi^2]$$

$$D_4 = \frac{1}{1+\phi}[(\phi - 2)\,\xi + 3\xi^2] \qquad \phi = \frac{12EI}{kAGl^2} \qquad (3.65)$$

These shape functions or interpolation functions are predetermined known functions of the independent variable ξ and these functions describe the variation of the field variables (bending displacements and slopes) within the element. For the beam element idealizing the shaft such a shape function is often a cubic polynomial as described above. More details of these shape functions are found in open literature [84].

Element mass matrix:-

$$M_e = \int_0^l \rho A N^T N dz + \int_0^l \rho I_D D^T D dz \qquad (3.66)$$

Element stiffness matrix:-

$$K_e = \int_0^l EI[D']^T[D']dz + \int_0^l kGA\left\{[N']^T[N'] + D^T D + 2[N']^T\begin{bmatrix} 0 & -1 \\ 1 & 0 \end{bmatrix}\right\}dz \qquad (3.67)$$

Gyroscopic matrix:

$$G_e = \int_0^l \rho I_p D^T \begin{bmatrix} 0 & -1 \\ 1 & 0 \end{bmatrix} D dz \qquad (3.68)$$

Equation for shaft element

$$M_e\ddot{q}_s + (C_e + \Omega G_e)\dot{q}_s + K_e q_s = F_e \qquad (3.69)$$

3.5.2 Modelling of a disk

Each disk node has four degrees of freedom, including two translations of mass centre (x, y) and two rotations of the plane of disk (θ_x, θ_y). The finite element formulation of disk is written as:

$$\mathbf{M}^d\ddot{\boldsymbol{q}}^d + \mathbf{G}^d\boldsymbol{q}^d = 0 \qquad (3.70)$$

The element mass and gyroscopic matrices corresponding to that disk node are written as:

$$\mathbf{M}^d = \begin{bmatrix} m_d & 0 & 0 & 0 \\ 0 & m_d & 0 & 0 \\ 0 & 0 & I_d & 0 \\ 0 & 0 & 0 & I_d \end{bmatrix}, \; \mathbf{G}^d = \begin{bmatrix} 0 & 0 & 0 & 0 \\ 0 & 0 & 0 & 0 \\ 0 & 0 & 0 & -I_p\Omega \\ 0 & 0 & I_p\Omega & 0 \end{bmatrix} \qquad (3.71)$$

Here, I_d and I_p are respectively diametral (about x and y axes) and polar (about z-axis) moments of inertia of disk, while m^d is mass of disk and Ω is the speed of rotor.

Matrix equations for whole rotor are

$$\mathbf{M}\ddot{q} + (\mathbf{C} + \Omega\mathbf{G})\dot{q} + \mathbf{K}q = F \qquad (3.72)$$

where $\mathbf{M}$, $\mathbf{C}$, $\mathbf{G}$ and $\mathbf{K}$ are assembled systems of matrices, q and F are global displacements and force vectors.

3.6 Concluding remarks

This chapter presented brief mathematical preliminaries of rotor modelling. Initially rotor was modelled by using Timoshenko beam theory. The bearing dynamics are imparted for the designed rotor by taking Hertz's contact deformations and forces. Then the model was extended for two row ball bearing system with the bearing forces afterwards the bearing faults are introduced into the system. The external forces like rub impact and Muszynska's forces are also included in the system.

Chapter 4

Solution Methodology

4.1 Introduction

The dynamic equations of the rotor bearing system are highly nonlinear and are difficult to solve by exact solution approaches. Numerical and approximate solution techniques are often employed. The effect of the bearing parameters, rub impact forces and nonlinear excitations on the natural frequencies and mode shapes cannot be predicted merely by solving eigenvalue equations. The dynamic response should be obtained by solving the equations in time-domain and the frequency domain responses are obtained from Fourier transforms. Approximate solution techniques reduce the partial differential equations into an equivalent ordinary differential equation /algebraic form, which can be conveniently solved for the response. This chapter explores on the various methods employed in the present work for solving the dynamic equations including their interactive computer programs. Also the experimental approach carried out to validate the natural frequencies and illustrate the rub impact effect on dynamic response.

4.2 Formulation of the rotor model

This section deals with modelling of two disk rotor system idealising an LP rotor considered in the present work using continuous system model, lumped parameter model and finite element model.

Figure 4.1 shows the proposed model of the LP rotor. Left and right disks respectively indicate compressor and turbine systems, while the rotor is supported over two ball bearings.
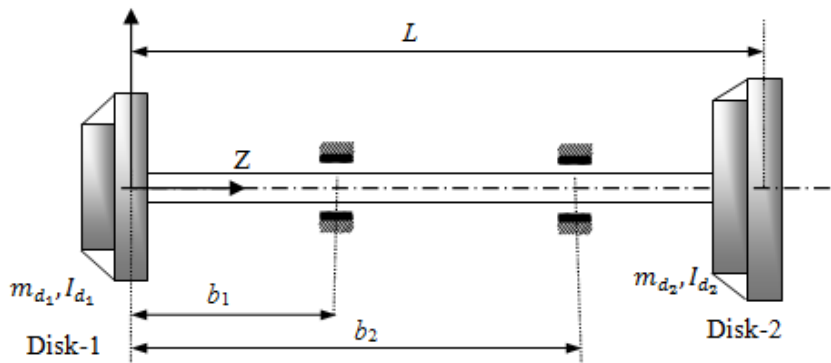
Figure 4.1: Distributed parameter model of the rotor

The formulation of equation of motion and boundary conditions of the rotor with disk and bearings as per the nomenclature given in the earlier chapter is first presented for each bending direction.

$$EI(z)\frac{\partial^4 u}{\partial z^4} + \rho A(z)\frac{\partial^2 u}{\partial t^2} + m_{d_1}\delta(z)\frac{\partial^2 u}{\partial t^2} + 2I_{d_1}(z)\Omega\left(\frac{\partial^2 v}{\partial z\,\partial t}\right)\delta'(z) + c_x\left(\frac{\partial u}{\partial t}\right)$$

$$+ m_{d_2}\delta(z-L)\frac{\partial^2 u}{\partial t^2} + 2I_{d_2}(z)\Omega\left(\frac{\partial^2 v}{\partial z\,\partial t}\right)\delta'(z-L) = P_x\delta(z) + Q_x\delta(z-L) \tag{4.1}$$

$$EI(z)\frac{\partial^4 v}{\partial z^4} + \rho A(z)\frac{\partial^2 v}{\partial t^2} + m_{d_1}\delta(z)\frac{\partial^2 v}{\partial t^2} - 2I_{d_1}(z)\Omega\left(\frac{\partial^2 u}{\partial z\,\partial t}\right)\delta'(z) + c_y\left(\frac{\partial v}{\partial t}\right)$$

$$+ m_{d_2}\delta(z-L)\frac{\partial^2 v}{\partial t^2} + 2I_{d_2}(z)\Omega\left(\frac{\partial^2 u}{\partial z\,\partial t}\right)\delta'(z-L) = P_y\delta(z) + Q_y\delta(z-L) \tag{4.2}$$

where

$$P_x = m_{d_1}\Omega^2 e_1\cos\Omega t \tag{4.3}$$

$$Q_x = m_{d_2}\Omega^2 e_2\cos\Omega t \tag{4.4}$$

$$P_y = m_{d_1}\Omega^2 e_1\sin\Omega t - m_{d_1}g \tag{4.5}$$

$$Q_y = m_{d_2}\Omega^2 e_2\sin\Omega t - m_{d_2}g \tag{4.6}$$

$\delta(z)$ is Dirac delta function for showing concentrated shear forces (due to two discs).

Its definition with derivative is given as

$$\int_{-\infty}^{\infty} f(x)\delta(z-a)dx = f(a) \tag{4.7}$$

$$\int_{-\infty}^{\infty} f(x)\delta'(z-a)dx = -f'(a) \tag{4.8}$$

δ' helps in defining the moment contribution term.

Boundary conditions

At z=b$_1$ and z= b$_2$:

$$\frac{\partial^2 u}{\partial t^2} = 0, \frac{\partial^2 v}{\partial t^2} = 0, EI\frac{\partial^3 u}{\partial z^3} = F_{xb}, EI\frac{\partial^3 v}{\partial z^3} = F_{yb} \tag{4.9}$$

where

F_{xb} and F_{yb} are the bearing force components in X and Y directions in terms of coordinates x and y. Also,

$$\frac{\partial^2 u}{\partial x^2}(L, t) = \frac{\partial^3 u}{\partial x^3}(L, t) = 0 , \frac{\partial^2 v}{\partial y^2}(L, t) = \frac{\partial^3 v}{\partial y^3}(L, t) = 0 \tag{4.10a}$$

$$\frac{\partial^2 u}{\partial x^2}(0, t) = \frac{\partial^3 u}{\partial x^3}(0, t) = 0 \; , \frac{\partial^2 v}{\partial y^2}(0, t) = \frac{\partial^3 v}{\partial y^3}(0, t) = 0 \tag{4.10b}$$

Most of the approximate solution techniques for solving the nonlinear dynamic equations are based on the mode summation approaches. Commonly, method of separation of variables (time and spatial) is employed. Here, the spatial terms are expressed in terms of mode shapes of the system based on the boundary conditions. Galerkin technique belongs to this category. The equations (4.1) and (4.2) have to be discretized in order to solve numerically. Assumed modes method can be used to do this discretization as follows.

Here, the bending displacements are written as

$$u(x, t) = \sum_{i=1}^{p} \emptyset_i(t)\, X_i(z) = X^T(z)\, \phi(t) \tag{4.11a}$$

$$v(x, t) = \sum_{i=1}^{p} \psi_i(t)\, Y_i(z) = = Y^T(z)\psi(t) \tag{4.11b}$$

where p is the number of modes considered for the discretization, ϕ and ψ are the generalized coordinate vectors. Also, X and Y are the basic functions or vectors of assumed mode often selected as mode shape functions which depend on the boundary conditions on the system. For example for simply-supported end condition $X_i(z)=C_i\sin\beta_i z$ and $Y_i(z)=D_i\sin\beta_i z$ with β_i as frequency parameter and z is axial coordinate. When *n* modes are considered, it forms *n* reduced equations in time domain.

By substituting the expression for u and v into the governing equations, the following coupled non-linear ordinary differential equations are obtained:

$$EI \sum_{i=1}^{p} X_i''''\phi_i(t) + m \sum_{i=1}^{p} X_i\ddot{\phi}_i(t) + m_{d_1} \sum_{i=1}^{p} X_i\ddot{\phi}_i(t)\, \delta(x - L)$$

$$+ 2\Omega I_{d_1} \sum_{i=1}^{p} Y_i'\psi_i(t)\, \delta'(x - L) + c_x \sum_{i=1}^{p} X_i\dot{\phi} = P_x(t)\delta(x - a) + Q_x\delta(x - L) \tag{4.12}$$

$$EI \sum_{i=1}^{p} Y_i''''\psi_i(t) + m \sum_{i=1}^{p} Y_i\ddot{\psi}_i(t) + m_{d_1} \sum_{i=1}^{p} Y_i\ddot{\psi}_i(t)\, \delta(x - L)$$

$$- 2\Omega I_{d_1} \sum_{i=1}^{p} X_i'\phi_i(t)\, \delta'(x - L) + c_y \sum_{i=1}^{p} Y_i\dot{\psi}_1 = P_y(t)\delta(x - a) + Q_y\delta(x - L) \tag{4.13}$$

Multiplying the above equation respectively by $X_i(x)$ and $Y_i(x)$ and integrating over x in the range [0, L] and employing the orthogonality conditions, a set of partially decoupled non-linear ordinary differential equations are obtained. For example, in X- direction we have

$$\ddot{\emptyset}_j(t) + \omega_j^2 \emptyset_j(t) + 2\Omega I_D \sum_{i=1}^{p} Y_i'(L)Y_j'(L)\dot{\psi}_i(t) + c_x \sum_{i=1}^{p} \left(\frac{\delta_{ij}}{m} - \frac{m_{d1}X_i(L)X_j(L)}{m}\right)\dot{\phi}(t)$$

$$= P_1(t)X_j(a) + Q_1(t)X_j(L) \tag{4.14}$$

4.2.1 Lumped parameter model

The three segments of the rotor shown in Figure 4.2 (a) are represented with three springs of stiffness k_{s1}, k_{s2} and k_{s3} respectively, whose magnitudes are predicted from the length and cross section of each segment. Figure 4.2 (b) shows the 3 segmented rotor simplified lumped parameter model considered in the present work. Here, the suffices b and d refer to the bearings and discs.

(a) 3-segmented rotor   (b) lumped parameter model
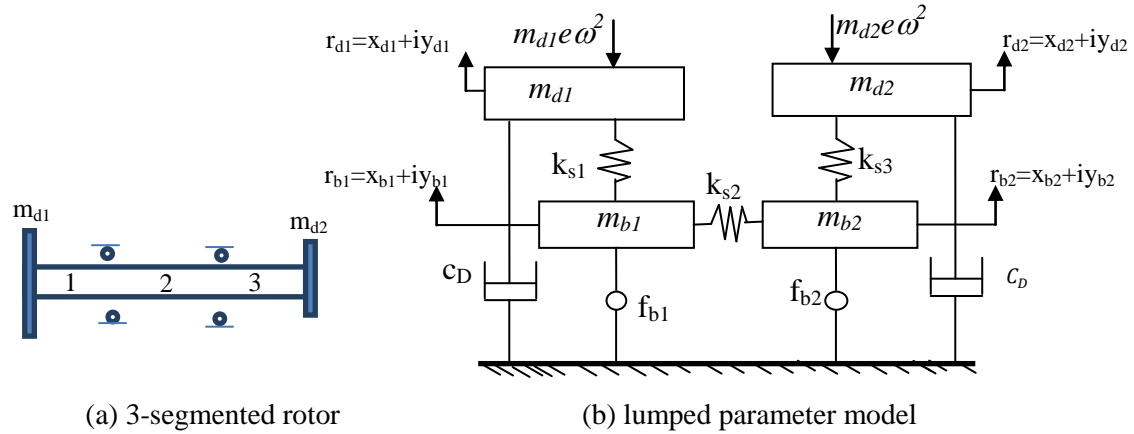
Figure 4.2: Simplified model

There are unbalance force and rub excitations at the disk masses m_{d1} and m_{d2}, while bearing forces f_{b1} and f_{b2} at the bearings act on journal portion of shaft. The masses m_{b1} and m_{b2} are equivalent masses at the bearings. The term c_D is aerodynamic damping due rotation. The equations of motion in terms of radial coordinates at each mass are given below:

$$m_{d1}\ddot{r}_{d1} + c_d\dot{r}_{d1} + k_{s1}(r_{d1} - r_{b1}) = m_{d1}e\omega^2 e^{i\omega t} \tag{4.15}$$

$$m_{b1}\ddot{r}_{b1} + k_{s1}(r_{b1} - r_{d1}) + k_{s3}(r_{b1} - r_{b2}) = f_{b1} \tag{4.16}$$

$$m_{d2}\ddot{r}_{d2} + c_d\dot{r}_{d2} + k_{s2}(r_{d2} - r_{b2}) = m_{d2}e\omega^2 e^{i\omega t} \tag{4.17}$$

$$m_{b2}\ddot{r}_{b2} + k_{s2}(r_{b2} - r_{d2}) + k_{s3}(r_{b2} - r_{b1}) = f_{b2} \tag{4.18}$$

These four equations have two components in two bending directions(r=x+iy) resulting in total 8 equations, which are represented in the form $M\ddot{X}+C\dot{X}+KX=F$. In y-direction, gravity loads also act. A computer program is developed to obtain the response at the

bearings, by solving the differential equations simultaneously using fourth-order Runge-Kutta method.

The squeeze film damper forces are considered by adding another mass (outer race mass m_o) to the above system along with a centralizing spring of stiffness k_a connecting outer race mass to the fixed casing. It results in the effective degrees of freedom of the system to be 12.

4.3 Finite element modelling

In finite element modelling the rotor in its simplest form has 4 nodes connected by 3 circular beam elements representing each segment stiffness and inertia. The disks are considered as rigid and rotor equations of motion are written as

$$[\mathbf{M}]\{\ddot{q}\} + [[\mathbf{C}] - \Omega\mathbf{G}]\{\dot{q}\} + [\mathbf{K}]\{q\} = \{F\} \tag{4.19}$$

where $\{q\} = \begin{bmatrix} u_1 \ v_1 \ \theta_{x1} \ \theta_{y1} \ ... . \ u_4 \ v_4 \ \theta_{x4} \ \theta_{y4} \end{bmatrix}$ is the displacement vector relating to the four nodes, $\mathbf{M}$, $\mathbf{C}$, $\mathbf{G}$ and $\mathbf{K}$ are respectively distributed symmetric mass matrix, system damping matrix, gyroscopic matrix of shaft and stiffness matrix of assembly. $\{F\}$ is external force vector consisting of gravity, unbalance and active force terms. Figure 4.3 shows the two models containing different number of elements.
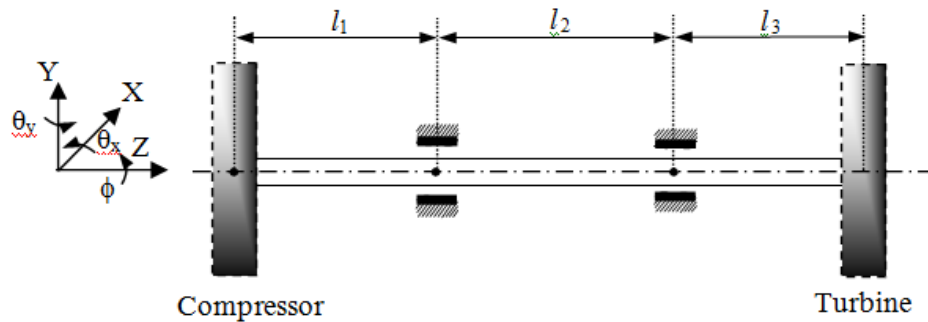
(a) Three element model
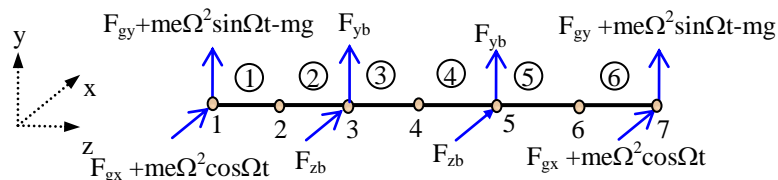
(b) Six element model with forces

Figure 4.3: Meshing of the rotor bearing system.

These matrices are assembled and using Guyan's reduction (static condensation scheme), the rotational degrees of freedom $\{\theta_{x1}, \theta_{y1}, \theta_{x2}, \theta_{y2}, \theta_{x3}, \theta_{y3} \dots\}$ are eliminated and the following governing equations of motion for the system are obtained:

$$[M_r]\{\ddot{q}\} + [C_r]\{\dot{q}\} - \Omega[G_r]\{\dot{q}\} + [K_r]\{q\} = \{F\} \tag{4.20}$$

where $\{q_e\}^T = \{u_1 \quad v_1 \quad u_2 \quad v_2 \dots\}$ are the overall translational degrees of freedom corresponding to four element model and $[M_r]$, $[C_r]$, $[G_r]$ and $[K_r]$ are reduced mass, viscous damping, gyroscopic and stiffness matrices respectively. For five element case the force vector can be written as:

$$\{F\} = \begin{bmatrix} F_{xb} & F_{yb} & 0 & 0 & F_{gx} + me\Omega^2 \cos\Omega t & F_{gy} + me\Omega^2 \sin\Omega t - mg & 0 & 0 & F_{xb} & F_{yb} \end{bmatrix}^T \tag{4.21}$$

4.3.1 Computation of global matrices

In the finite element analysis, assembly of matrices generally follows these steps

1. Set up $n \times n$ and $n \times 1$ null matrices (zero matrix), here n is the number of system nodal variables.
2. For one element, transform local element equations to global coordinates, if these two coordinates systems are not coincident.
3. Now, any necessary matrix operations can be performed.
4. Using the established correspondence between local and global numbering schemes, change to global indices.
5. Insert these terms into the corresponding $n \times n$ and $n \times 1$ master matrices in the locations designed by their indices. Each time a term is placed in a location where another term has already been placed, it is added to whatever value is there.
6. Return to step 2 and repeat this procedure for one element after another until all elements have been treated. The result will be an $n \times n$ master matrix **K** of stiffness coefficients and an $n \times 1$ column matrix $\{R\}$ of resultant nodal actions. The complete system equations are then

$$[K]_{n\times n}\{X\}_{n\times 1} = \{R\}_{n\times 1}$$

where $\{X\}$ is the column matrix of nodal unknowns for the assemblage.

The very definite advantage of this assembly process is, once a computer program for the assembly process has been developed for the solution of one particular class of problems by the finite element method, it may be useful for finite element solutions of other classes of problems. A part of the model program developed in the Matlab software is given below.

Model code: Assembly of global matrices

```
% Initializing global matrices as null matrices
Kf1=zeros(4*(n),4*(n));Mf1=zeros(4*(n),4*(n));Gf1=zeros(4*(n),4*(n));
for ii=1:8
    i=ne(ii);% nodal connectivity
  for jj=1:8
    j=ne(jj);% nodal connectivity
    Kf1(i,j)=Kf1(i,j)+ke(ii,jj);
    Mf1(i,j)=Mf1(i,j)+me(ii,jj);
    Gf1(i,j)=Gf1(i,j)+ge(ii,jj);
  end
 end
```

4.3.2 Matrix reduction scheme

In discretization process, it is necessary to divide the rotor into large number of elements. When these elements are assembled, the number of degrees of freedom becomes quite large, resulting in very large dimensional matrices. It makes difficulty in computing the natural frequencies and dynamic responses of such a system. It is desirable to reduce the sizes of matrices to obtain the solutions quite economically.

There are two schemes in this regard (i) Static condensation (ii) Dynamic condensation

The static condensation employed in present work is described below:

Static condensation eliminates certain degrees of freedom which are called slaves and **the** retained degrees of freedom are called masters. Generally retained degrees of freedom coincide with the bending deflections at various nodes including lumped disks, bearing locations and other external force locations. Slave degrees of freedom include degrees of freedom which are non-crucial or difficult to measure; like rotational degrees of freedom. Let the original equations of motion be written as:

$$\begin{bmatrix} \mathbf{M}_{pp} & \mathbf{M}_{ps} \\ \mathbf{M}_{sp} & \mathbf{M}_{ss} \end{bmatrix} \begin{Bmatrix} \ddot{q}_p \\ \ddot{q}_s \end{Bmatrix} + \begin{bmatrix} \mathbf{K}_{pp} & \mathbf{K}_{ps} \\ \mathbf{K}_{sp} & \mathbf{K}_{ss} \end{bmatrix} \begin{Bmatrix} q_p \\ q_s \end{Bmatrix} - \Omega_s \begin{bmatrix} \mathbf{G}_{pp} & \mathbf{G}_{ps} \\ \mathbf{G}_{sp} & \mathbf{G}_{ss} \end{bmatrix} \begin{Bmatrix} \dot{q}_p \\ \dot{q}_s \end{Bmatrix} = \begin{Bmatrix} F_p \\ F_s \end{Bmatrix} \tag{4.22}$$

where *p* and *s* are master and slave degree of freedoms respectively. By assuming, no external force is applied to slave degree of freedoms, the transfer matrix

$$\begin{Bmatrix} q_p \\ q_s \end{Bmatrix} = \begin{bmatrix} \mathbf{I} \\ -\mathbf{K}_{ss}^{-1}\mathbf{K}_{sp} \end{bmatrix} \{q_p\}$$

$$= [\mathbf{T}_s]\{q_p\} \tag{4.23}$$

where $[\mathbf{T}_s]$ is static transfer matrix between full degree of freedom vectors and reduced master degree of freedom vector. Therefore, we can write after static transformation:

$$[\mathbf{M}_R]\{\ddot{q}_p\} - \Omega_s[\mathbf{G}_R]\{\dot{q}_p\} + [\mathbf{K}_R]\{q_p\} = \{f_p\} \tag{4.24}$$

where $[\mathbf{M_R}] = [\mathbf{T_s}]^{\mathrm{T}}[\mathbf{M}][\mathbf{T_s}]$

$[\mathbf{G_R}] = [\mathbf{T_s}]^{\mathrm{T}}[\mathbf{G}][\mathbf{T_s}]$ (4.25)

$[\mathbf{K_R}] = [\mathbf{T_s}]^{\mathrm{T}}[\mathbf{K}][\mathbf{T_s}]$ (4.26)

$[\mathbf{f_p}] = [\mathbf{T_s}]^{\mathrm{T}}\{f\}$ (4.27)

are condensed matrices of rotor substructure.

4.4 Solution Techniques

Finite element method resolves the continuous system model described in the form of partial differential equations into a multi degree of freedom model in time-domain. In order to solve these equations, various numerical approaches are available. In present work, the free vibration analysis of rotor bearing system is employed for obtaining Campbell diagrams and for validation with experimental data. Subspace iteration scheme is employed for eigenvalue problems, which requires the reduced stiffness, resultant mass and gyroscopic matrices. The forward and backward whirl modes are obtained from complex conjugate eigenvalue sets at different speeds of operation. As presented in Chapter-3, the total stiffness of the rotor is sum of the stiffness of the shaft and bearings at common nodes. However, the bearing stiffness is found to be time varying and it is only approximate, if one considers the problem as a free vibration type. Static load bearing capacity is therefore different from dynamic load bearing conditions.

4.4.1 Eigenvalue analysis

The dynamic analysis of any rotordynamic system will starts from the finding out its natural frequencies and mode shapes. The natural frequency and mode shapes will characterize the dynamic behaviour of the rotor bearing system and also shows the response of system under dynamic loading. The natural frequency gives the vibrating tendency of the structure under applying external disturbances. Mode shapes and natural frequencies depend on the boundary conditions and the structural properties of the system. The main reason of determining natural frequencies is to estimate the dynamic stability of the system under different operating conditions.

The equation of motion of the rotating system for mode shapes and natural frequencies should in a reduced form of free vibration as follows.

$\mathbf{M}\ddot{x} + \mathbf{C}\dot{x} + \mathbf{K}x = 0$ (4.28a)

(or) $\dot{y} = \mathbf{A}y$ (4.28b)

with

$$A = \begin{bmatrix} \mathbf{0} & \mathbf{I} \\ -\mathbf{M}^{-1}\mathbf{K} & -\mathbf{M}^{-1}\mathbf{C} \end{bmatrix}, y = \begin{Bmatrix} x \\ \dot{x} \end{Bmatrix} \tag{4.28c}$$

The above matrix $\mathbf{A}$ is skew-symmetric when $\mathbf{C}$ is non-proportional damping matrix such as gyroscopic matrix and $\mathbf{A}$ has complex conjugate eigenvalues from which the natural frequencies and damping ratios are obtained.

For undamped system, the harmonic solution is assumed as

$$x = \emptyset \sin \omega t \tag{4.29}$$

where $\emptyset$ is the mode shapes or eigenvector set and ω is the natural frequency of the system. Campbell plot is constructed from the eigenvalue analysis at various operating speeds. It indicates critical speeds of operation at various engine harmonics.

4.4.2 The subspace iteration method

The generalized eigenvalue problem is as follows

$$\mathbf{K}\varphi = \lambda \mathbf{M}\varphi \tag{4.30}$$

The smallest eigenvalues λ_i, $i=1,2,\ldots,p$, and the respective eigenvectors φ_i, $i=1,2,\ldots,p$, with the ordering

$$0 < \lambda_1 \le \lambda_2 \le \ldots \le \lambda_p \tag{4.31}$$

which satisfy $\mathbf{K}\varphi_i = \lambda_i \mathbf{M}\varphi_i$, $i=1,\ldots,p$ and the Knonecker delta relationships

$$\varphi_i^T \mathbf{M}\varphi_i = \delta_{ij} , \varphi_i^T \mathbf{K}\varphi_i = \lambda_i \delta_{ij} \tag{4.32}$$

If the smallest value is zero, the shift can be used to reach the Eq. (4.31).

The basic equations used in the subspace iteration method are, for k=1, 2…,

$$\mathbf{K}\overline{X}_{k+1} = \mathbf{M}X_k \tag{4.33}$$

$$\mathbf{K}_{k+1} = \overline{X}_{k+1}^T \mathbf{K}\overline{X}_{k+1} \tag{4.34}$$

$$\mathbf{M}_{k+1} = \overline{X}_{k+1}^T \mathbf{M}\overline{X}_{k+1} \tag{4.35}$$

$$\mathbf{K}_{k+1}Q_{k+1} = \mathbf{M}_{k+1}Q_{k+1}\mathbf{\Lambda}_{k+1} \tag{4.36}$$

$$X_{k+1} = \overline{X}_{k+1}Q_{k+1} \tag{4.37}$$

In practice, it is effective to order the iteration vectors in X_k naturally from the first to the last columns such that these correspond to increasing eigenvalues. Then the first vector in X_k corresponds to the eigenvector approximation of φ_i and the qth vector to the eigenvector approximation of φ_q. The calculated approximations to the eigenvalues are given in Λ_{k+1}.

4.5 Dynamic response computations

Dynamic response in time-domain of a multi-degree of freedom system like rotor bearing assemblies is obtained in two different approaches: (i) Implicit time integration (ii) Explicit time integration. Optional time steps and computational procedure is the main contrast between explicit and implicit time integration methods. In explicit time integration methods, determining the unknown values at the present time step is based on the evaluated values of displacement, velocity and acceleration in the previous time step. Where as in the case of implicit time integration method, the unknown values of any time step is based on the value of the previous time step and the current time step values. Due to this reason, implicit solution algorithms need assembling and solution of algebraic equations.

In present work, both the approaches are implemented to validate response histories. As the dynamic forces are highly nonlinear, variable time steps are required during the solution. Under implicit time integration, Wilson theta and its variants are proposed for the present problem, while variable time step Runge-kutta fourth order method is considered under explicit method. A brief description will be provided first.

4.5.1 Wilson Theta method

The Wilson Theta method assumes that the acceleration of the system varies linearly between two instants of time as shown in Figure 4.4. The acceleration is assumed to be linear from time to time t between $t_i = i\Delta t$ to time $t_{i+\theta} = t_i + \theta\Delta t$, where $\theta \geq 1.0$.
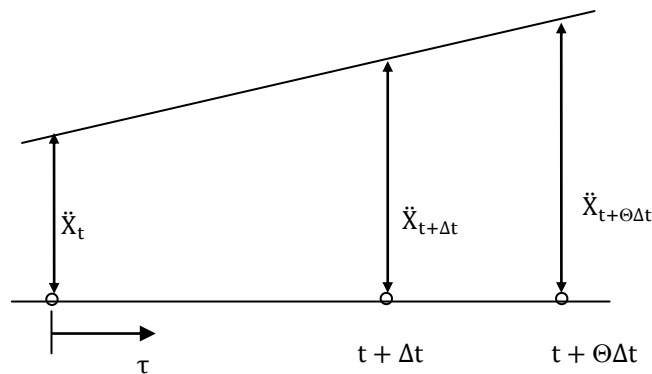
Figure 4.4: Linear variation of acceleration

If τ is the increase in time t between t and $t + \theta\Delta t$ ($0 \leq \tau \leq \theta\Delta t$), then for time interval t to $t_+ \theta\Delta t$, it can be assumed that

$$\ddot{X}_{t+\tau} = \ddot{X}_t + \frac{\tau}{\theta\Delta t}(\ddot{X}_{t+\theta\Delta t} - \ddot{X}_t) \tag{4.38}$$

Successive integration for above Eq. gives the following expressions for $\ddot{X}_{t+\tau}$ and $X_{t+\tau}$:

$$\dot{X}_{t+\tau} = \dot{X}_t + \ddot{X}_t\tau + \frac{\tau^2}{2\theta\Delta t}(\ddot{X}_{t+\theta\Delta t} - \ddot{X}_t) \tag{4.39}$$

$$X_{t+\tau} = X_t + \dot{X}_t\tau + \frac{1}{2}\ddot{X}_t\tau^2 + \frac{\tau^3}{6\theta\Delta t}(\ddot{X}_{t+\theta\Delta t} - \ddot{X}_t) \tag{4.40}$$

Substituting $\tau = \theta\Delta t$ into the above Eqs. (4.38) and (4.39), we obtain the following expressions for $\dot{X}$ and X at time $t + \theta\Delta t$:

$$\dot{X}_{t+\theta\Delta t} = \dot{X}_t + \frac{\theta\Delta t}{2}(\ddot{X}_t + \ddot{X}_{t+\theta\Delta t}) \tag{4.41}$$

$$X_{t+\theta\Delta t} = X_t + \theta\Delta t\dot{X}_t + \frac{\theta^2\Delta t^2}{6}(\ddot{X}_{t+\theta\Delta t} + 2\ddot{X}_t) \tag{4.42}$$

Solving the above two equations for $\ddot{X}_{t+\theta\Delta t}$ and $\dot{X}_{t+\theta\Delta t}$ in terms of $X_{t+\theta\Delta t}$, we get

$$\{\ddot{X}_{t+\theta\Delta t}\} = \frac{6}{\theta^2\Delta t^2}(\{X_{t+\theta\Delta t}\} - \{X_t\}) - \frac{6}{\theta\Delta t}\{\dot{X}_t\} - 2\{\ddot{X}_t\} \tag{4.43}$$

$$\{\dot{X}_{t+\theta\Delta t}\} = \frac{3}{\theta\Delta t}(\{X_{t+\theta\Delta t}\} - \{X_t\}) - 2\{\dot{X}_t\} - \frac{\theta\Delta t}{2}\{\ddot{X}_t\} \tag{4.44}$$

Since accelerations vary linearly, a linear projected force vector is used such that

$$\mathbf{M}\{\ddot{X}_{t+\theta\Delta t}\} + \mathbf{C}\{\dot{X}_{t+\theta\Delta t}\} + \mathbf{K}\{X_{t+\theta\Delta t}\} = \{F_{t+\theta\Delta t}\} \tag{4.45a}$$

where

$$\{F_{t+\theta\Delta t}\} = \{F_t\} + \theta(\{F_{t+\theta\Delta t}\} - \{F_t\}). \tag{4.45b}$$

By substituting the expressions for $\{\dot{X}_{t+\theta\Delta t}\}$ and $\{\ddot{X}_{t+\theta\Delta t}\}$ from above equations in equilibrium Eq.(4.45) and simplifying, we get

$$\overline{\mathbf{M}}\{\dot{X}_{t+\theta\Delta t}\} = \{\overline{F}_{t+\theta\Delta t}\} \tag{4.46}$$

Where the effective mass matrix $|\overline{\mathbf{M}}|$ and the effective force vector $\{\overline{F}_{t+\Delta t}\}$ are given by

$$\overline{\mathbf{M}} = \frac{6}{\theta^2\Delta t^2}\mathbf{M} + \frac{3}{\theta\Delta t}\mathbf{C} + \mathbf{K} \tag{4.47}$$

$$\{\overline{F}_{t+\theta\Delta t}\} = \{F_{t+\theta\Delta t}\} + \left(\frac{6}{\theta^2\Delta t^2}\mathbf{M} + \frac{3}{\theta\Delta t}\mathbf{C}\right)\{X_t\} + \left(\frac{6}{\theta\Delta t}\mathbf{M} + 2\mathbf{C}\right)\{\dot{X}_t\} + \left(2\mathbf{M} + \frac{\theta\Delta t}{2}\mathbf{C}\right)\{\ddot{X}_t\} \tag{4.48}$$

The solution of Eq.(4.46) gives $\{X_{t+\theta\Delta t}\}$ which is then substituted into the following relationships to obtain the displacements, velocities, and accelerations at time $t + \theta\Delta t$.

$$\{\ddot{X}_{t+\theta\Delta t}\} = \frac{6}{\theta^2\Delta t^2}(\{X_{t+\theta\Delta t}\} - \{X_t\}) - \frac{6}{\theta\Delta t}\{\dot{X}_t\} + \left(1 - \frac{3}{\theta}\right)\{\ddot{X}_t\} \tag{4.49}$$

$$\{\dot{X}_{t+\theta\Delta t}\} = \{\dot{X}_t\} + \frac{\Delta t}{2}(\{\ddot{X}_{t+\theta\Delta t}\} + \{\ddot{X}_t\}) \tag{4.50}$$

$${X_{t+\theta\Delta t}} = {X_t} + \Delta t\left({\dot{X}_t} + \frac{\Delta t^2}{6}{\ddot{X}_{t+\theta\Delta t}} + 2{\ddot{X}_t}\right) \tag{4.51}$$

When $\theta = 1.0$, the method reduces to the linear acceleration scheme (Newmark). The method is unconditionally stable for linear dynamic systems when $\theta \geq 1.37$ and a value of $\theta = 1.4$ is often used for nonlinear dynamic systems. It may also be noted that no special starting procedures are needed, since $X, \dot{X}$ and $\ddot{X}$ are expressed at time $t + \Delta t$ in terms of the same quantities at time t only. The summary of the algorithm used in the Wilson Theta method is given in the below

(a) Initial Computations:
1. Form stiffness **K**, mass **M** and damping **C** matrices
2. Initialize ${X_0}$, ${\dot{X}_0}$ and compute ${\ddot{X}_0}$ using
$${\ddot{X}_0} = \mathbf{M}^{-1}{F_0 - \mathbf{C}{\dot{X}_0} - \mathbf{K}{X_0}} \tag{4.52}$$
3. Select the time step Δt and set $\theta = 1.4$.
4. Form effective stiffness matrix:
$$\overline{\mathbf{K}} = \mathbf{K} + \frac{6}{(\theta\Delta t)^2}\mathbf{M} + \frac{3}{\theta\Delta t}\mathbf{C} \tag{4.53}$$

(b) For each time step:
1. Calculate effective force vector at time $t + \Delta t$:
$${F_{t+\theta\Delta t}} = {F_t} + \theta({F_{t+\Delta t}} - {F_t}) + \mathbf{M}\left(\frac{6}{(\theta\Delta t)^2}{X_t} + \frac{6}{(\theta\Delta t)}{\dot{X}_t} + 2{\ddot{X}_t}\right)$$
$$+\mathbf{C}\left(\frac{3}{\theta\Delta t}{X_1} + 2{\dot{X}_t} + \frac{\theta\Delta t}{2}{\ddot{X}_t}\right) \tag{4.54}$$
2. Solve displacements at time $t + \theta\Delta t$ according to the following
$${X_{t+\theta\Delta t}} = \overline{\mathbf{K}}^{-1}{F_{t+\theta\Delta t}} \tag{4.55}$$
3. Calculated ${X}$, ${\dot{X}}$ and ${\ddot{X}}$ at time $t + \Delta t$ as follows
$${\ddot{X}_{t+\Delta t}} = \frac{6}{\theta^3\Delta t^2}({X_{t+\theta\Delta t}} - {X_t}) - \frac{6}{\theta^2\Delta t}{\dot{X}_t} + \left(1 - \frac{3}{\theta}\right){\ddot{X}_t} \tag{4.56a}$$

$${\dot{X}_{t+\Delta t}} = {\dot{X}_t} + \frac{\Delta t}{2}\left({\ddot{X}_{t+\Delta t}} + {\ddot{X}_t}\right) \tag{4.56b}$$

$${X_{t+\Delta t}} = {X_t} + \Delta t{\dot{X}_t} + \frac{(\Delta t)^2}{6}\left({\ddot{X}_{t+\Delta t}} + 2{\ddot{X}_t}\right) \tag{4.56c}$$

A part of Matlab program developed is shown in Algorithm below:

Model code: Wilson theta solver

```
define X0=[1e-6;1e-6;0;0;0;0;0;0;1e-6;1e-6];
X0d=[0;0;0;0;0;0;0;0;0;0];
F0=[0;0;0;0;md*ecc*omega^2;-md*g;0;0;0;0];
X0dd=inv(Mr)*(F0-Cr*X0d-Kr*X0);
theta=1.4;
```

```
a0=6/(theta*dt)^2;a1=3/(theta*dt);a2=2*a1;
a3=2;a4=(1/2*theta*dt);a5=-a2/theta;
a6=1-3/theta;a7=dt/2;a8=dt^2/6;
Kb=Kr+a0*Mr+a1*Cr;
i=1;
for t=dt:dt:ti
   i=i+1;
   Ft=F0+Mr*(a0*X(:,i-1)+a2*Xd(:,i-1)+a3*Xdd(:,i-1))  +Cr*(a1*X(:,i-1)+a3*Xd(:,i-1)+a4*Xdd(:,i-
1))+theta*(F-F0);
   Xt(:,i)=inv(Kb)*Ft;
   Kb=Kr+a0*Mr+a1*Cr;
   Xdd(:,i)=(a0/theta)*(Xt(:,i)-X(:,i-1))+a5*Xd(:,i-1)+a6*Xdd(:,i-1);
   Xd(:,i)=Xd(:,i-1)+a7*(Xdd(:,i)+Xdd(:,i-1));
   X(:,i)=X(:,i-1)+dt*Xd(:,i-1)+a8*(Xdd(:,i)+2*Xdd(:,i-1));
   F0=F;
end
```

4.5.2 Fourth order Runge-Kutta method

In order to solve n second order differential equations, conventional Runge- Kutta method initially converts the problem into 2n state space (first order) equations which require 2n initial conditions. In the present work, the second order equations are solved as it is, using the following formulation. The matrix equations of motion are used to express the acceleration vector as

$$\ddot{X}(t) = \mathbf{M}^{-1}\left(F(t) - \mathbf{C}\dot{X}(t) - \mathbf{K}X(t)\right) \tag{4.57}$$

By treating the displacements as well as velocities as unknowns, a new vector, $Y(t)$ is defined as

$$\{Y(t)\} = \begin{Bmatrix} X(t) \\ \dot{X}(t) \end{Bmatrix} \tag{4.58}$$

So that

$$\{\dot{Y}\} = \begin{Bmatrix} \dot{X} \\ \ddot{X} \end{Bmatrix} = \begin{Bmatrix} \dot{X} \\ \mathbf{M}^{-1}(F - \mathbf{C}\dot{X} - \mathbf{K}X) \end{Bmatrix} \tag{4.59}$$

The above equation can be rearranged to obtain

$$\{\dot{Y}(t)\} = \begin{bmatrix} \mathbf{0} & \mathbf{I} \\ -\mathbf{M}^{-1}\mathbf{K} & -\mathbf{M}^{-1}\mathbf{C} \end{bmatrix} \begin{Bmatrix} X(t) \\ \dot{X}(t) \end{Bmatrix} + \begin{Bmatrix} 0 \\ \mathbf{M}^{-1}F(t) \end{Bmatrix}$$

$$= \mathbf{A}Y + G$$

$$= g(Y,t) \tag{4.60}$$

With this, the recurrence formula to evaluate $\{Y(t)\}$ at different grid points t_i can be obtained as follows

$$\{Y_{i+1}\} = \{Y_i\} + \frac{1}{6}[\{K_1\} + 2\{K_2\} + 2\{K_3\} + \{K_4\}] \tag{4.61}$$

where

$$K_1 = h\{g(Y_i, t_i)\} \tag{4.62}$$

$$K_2 = h\{g\left(Y_i + \frac{1}{2}K_1, t_i + \frac{1}{2}h\right)\} \tag{4.63}$$

$$K_3 = h\{g\left(Y_i + \frac{1}{2}K_2, t_i + \frac{1}{2}h\right)\} \tag{4.64}$$

$$K_4 = h\{g(Y_i + K_3, t_i + h)\} \tag{4.65}$$

where h=dt, is the step size,

A simple computer program can be developed for a given set of system matrices with initial conditions as follows:

Model code:**:** Fourth-order Runge-Kutta for multi-degree system

---

```
for t=0:h:T
  blade_dis(i)=Y(2);
  %X(:,i)=Y;
  %fprintf('%f\t%f\t%f\n',t,Y(1),Y(2));
  K1=h*f(Y,t);
  K2=h*f(Y+0.5*K1,t+h/2);
  K3=h*f(Y+0.5*K2,t+h/2);
  K4=h*f(Y+K3,t+h);
 Y=Y+(K1+2*K2+2*K3+K4)/6;
 i=i+1;
end
```

4.5.3 Fourier transforms

Fourier transforms convert the time-domain data into frequency domain signal. Often, Fourier series data contains the constants which are shown against frequency to form a histogram or frequency response. Here, number of sampling points is very important. Fourier series expression in exponential form is expressed as:

$$X(t)= \sum_{n=-\infty}^{\infty} C_n e^{in\omega t} \tag{4.66}$$

Where $\qquad C_n = \dfrac{i}{T}\int_0^T X(t)e^{-in\omega t}\,dt$ $\tag{4.67}$

When periodic function X(t) is supplied only at N equally spaced time-intervals ($\Delta t = T/N$), the integral may be approximated by the summation (discrete Fourier transform)

$$C_n = \frac{i}{N} \sum_{j=0}^{N-1} X(t_j) e^{-2\pi i (nj/N)} \quad , \text{n=0, 1, 2, ... (N-1)}. \tag{4.68}$$

These coefficients C_n have been limited to 0 to (N-1) in order to maintain symmetry of transforms. Here, the frequencies increase with increasing index n up to n=N/2. For n>N/2, the corresponding frequencies are equal to the negative of frequencies of order N=n. This fact restricts the harmonic components that may be represented in the series to a maximum of N/2. The frequency corresponding to the maximum order is known as Nyquist frequency. To avoid distortion in lower harmonic components of series, often number of sample points N should be at least twice the harmonic components present in the function.

Fast Fourier Transforms (FFT) is a numerical approach for increasing the speed of computations in discrete form of Fourier series. In 1965, Cooley and Tukey presented the FFT algorithm. Currently, the FFT has an important role in digital signal processing. In applying FFT, the expression for X may be written as:

$$X(j) = \sum_{n=0}^{N-1} X_0(n) W_N^{jn} \tag{4.69}$$

where $W_n = e^{\frac{2\pi i}{N}}$. Evaluation of sum will be efficient if the number of time increments N into which the period T is divided is a power of 2, viz., $N=2^M$, where M is the integer. Ex., if M=3, $N=2^3=8$, we write:

$$X(j) = \sum_{n_2=0}^{1} \sum_{n_1=1}^{1} \sum_{n_0=0}^{1} X^0(n) W_8^{(j_0+2j_1+4j_2)(n_0+2n_1+4n_2)} \tag{4.70}$$

A model program for computing FFT spectrum is given below:

Model code: FFT from time-domain

```
Fs =1/dt;                    % Sample frequency
L = length(xx(:,5));           % Length of time-domain signal
NFFT = 2^nextpow2(L); % Next power of 2 from length of fx
Xf1 = fft(xx(:,5),NFFT)/L;
fre = Fs/2*linspace(0,1,NFFT/2+1);
plot(fre,(2*abs(Xf1(1:NFFT/2+1))));
xlabel('frequency (Hz)');
ylabel('X_3 amplitude (m)');
```

4.6 Rotor Identification Schemes

In many instances, changes in rotor bearing parameters are to be obtained from the overall vibration response. Since, it is difficult procedure to identify these bearing parameters or rotor unbalance using conventional methods, often inverse-based approaches are used with the help of measured or simulated vibration responses.

Figure 4.5 shows the three different identification studies carried out in the present work. Here, both neural networks and the optimization schemes are employed during the procedure.
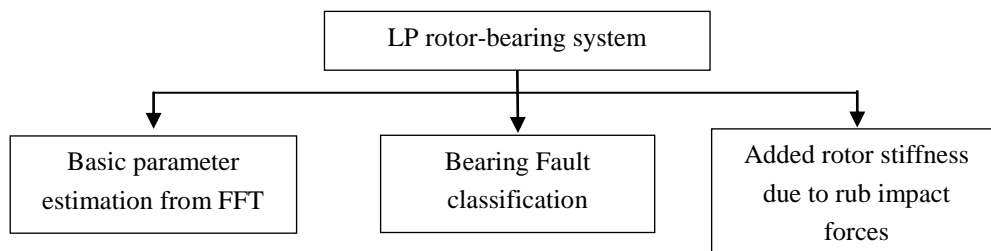
Figure 4.5: Identification studies carried out

4.6.1 Basic parameter identification

After validation of FE model using an experimental modal analysis, the model is employed to generate a set of frequency response data corresponding to different rotor bearing parameters of the system. Due to strong nonlinear relationship between the rotor bearing parameters, disc unbalance and squeeze-film damper parameters on the overall transient response of the system, it is planned to study the effect of commonly used parameters like: bearing radial clearances, disc eccentricities and centralizing spring stiffness of SFD on the fundamental frequencies and their amplitudes. Rotor is allowed to rotate at rated speed (2000 rpm) and the three input parameters are varied in three levels. The corresponding frequencies and amplitudes are recorded from FFT plots in each case.

For modelling inverse relationship, a 3-layer feed-forward neural network model is employed with frequencies and amplitudes as inputs and the corresponding bearing clearance, disc eccentricity and stiffness constant of centralized spring are obtained as outputs. Figure 4.6 shows the block diagram of neural network based system identification. In the neural network model under consideration, input or feedback delay concepts do not arise as this trained with error-back propagation algorithm for updating the weights and bias terms between the two layers.
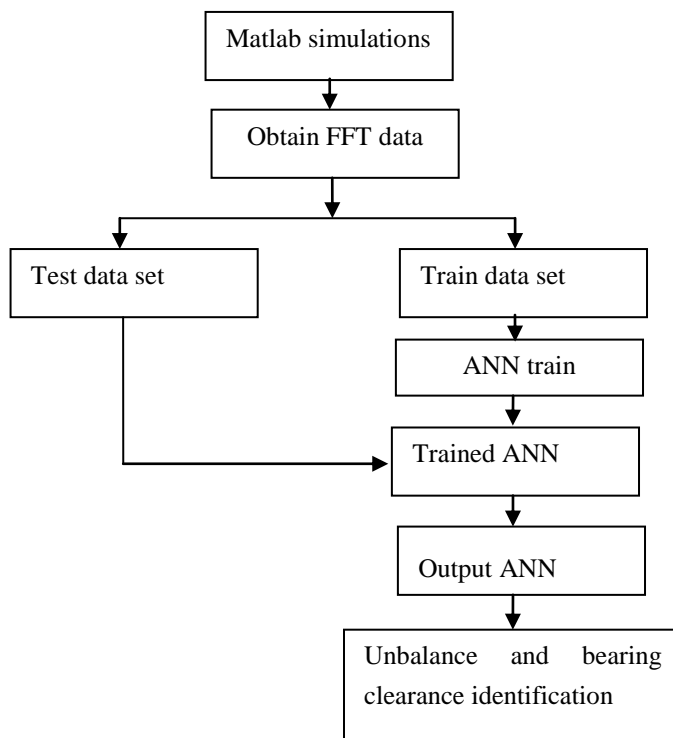
Figure 4.6: Neural network based parameter identification scheme

Brief introduction to the neural network models is given in this section: Artificial neural networks (ANN) are established by referring to the structure and characteristics of human brain, which is interconnected with a large number of simple processing units called neurons. And ANN is a nonlinear dynamical system to realize large-scale parallel distributed information processing. Compared with conventional information processing methods, ANN has some characteristics including structure variability, high nonlinearity, self-learning and self-organization, etc. Figure 4.7 shows the output computation step in between two layers of neurons.
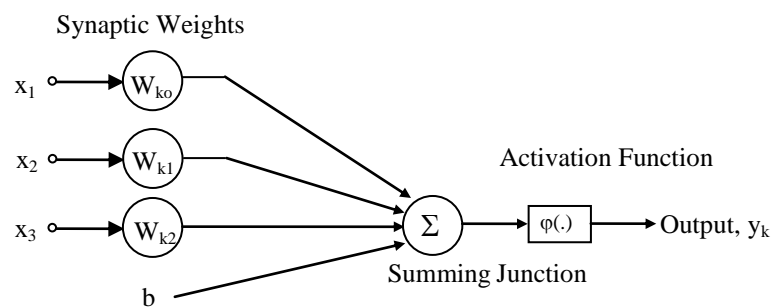
Figure 4.7: Nonlinear model of neuron

The connecting links, called synapses, specify the connection between a signal x_j at the input of the sample j, and a neuron k, through a weighing factor, w_{kj}. An adder sums up the input signals weighted by the respective synapses of the neuron. The operation is similar to that of a linear combiner. The activation function limits the amplitude of the output of the neuron. The, model includes an externally applied bias b that has the effect of lowering the net input of the activation function. The activation function, φ (.), defines the output of a neuron in terms of the activity level at its input. The sigmoid function is the most common activation function used in the construction of the artificial neural networks. It is defined as the logistic function.

$$\varphi(v) = 1/[1 + \exp(-av)] \tag{4.71}$$

where a is the slope parameter of the sigmoid function. Mathematically, the neuron has been described as

$$u_k = \sum_{i=1}^{p} w_{ki}x_i, \tag{4.72}$$

$$y_k = \varphi(u_k). \tag{4.73}$$

(a) Multi-layer perceptron neural network

In the year of 1986, Rumelhart et al. proposed back-propagation (BP) algorithm, which has been one of the most widely used network algorithm nowadays for feed-forward models. Error back-propagation divides the learning process to two stages. The first stage is forward propagation, where the input vectors reach the output layer via hidden (intermediate) layer. This results in an actual input in forward pass using randomly selected connection strengths known as weights. The second stage is back propagation. In the output layer these actual outputs are compared against the expected set and the error formed as the difference between the two outputs is calculated recursively for every new input set. Then this error is used to adjust the initial connection strengths or weights between the layers. The structure of BP neural network is shown in Figure 4.8
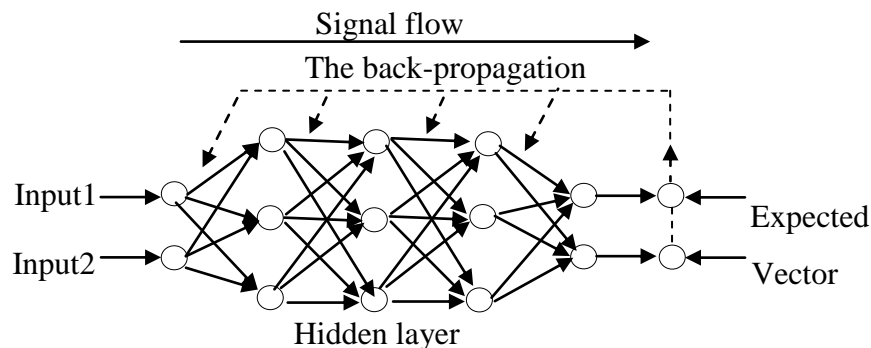
Figure 4.8: Structure of a BP neural network.

It is proved that a BP neural network with hidden layers can approximate any nonlinear continuous function with any accuracy. BP neural network is defined with L hidden layers and n units in each. Each unit just receives the outputs of previous layer and outputs to the units of the next layer. In order to simplify the network, assume there is one output y for the whole network. Define m samples (x_k, y_k) $(k = 1, 2 \ldots m)$, and the output o_i of any unit i. For an input x_k, the output of the unit is o_{ik} and the output of the network is y_k. Define unit j of layer l, and the input of unit j with k samples inputs is shown in the following equation:

$$P_{ij}^l = \sum_j w_{ij}^l o_{jk}^{l-l} \tag{4.74}$$

where w^l_{ij} is the weight coefficient, and o_{jk}^{l-1} represents the output of unit j on the layer i−1 with k input samples. Then the output of unit j on the layer i, o_{jk}^l can be calculated in the following equation:

$$o_{jk}^l = f\left(p_{jk}^l\right) \tag{4.75}$$

Here, f(x) is a called sigmoid function defined as $f(x)=1/(1+e^x)$ (known as logarithmic sigmoid function for target outputs to be between 0 to 1

Define the error function E_k in the following equation:

$$E_k = \frac{1}{2}\sum_l (y_{lk} - y_{lk}')^2 \tag{4.76}$$

where y_{lk}' is the real output of unit j on the layer l. Then the total mean error E_t is computed in the following equation:

$$E_t = \frac{1}{2m}\sum_{k=1}^m E_k \tag{4.77}$$

BP neural network algorithm is implemented in following steps:

(i)   Determine initial values of weight coefficients.

(ii)   Compute: o_{jk}^{l-1}, p_{jk}^l and y_k' for forward propagation are computed, while k = 2..., m.

(iii)   And λ_{jk}^l is calculated for back propagation from the layer $l − 1$ to layer 2.

(iv)   Then the weight coefficient is corrected by the following equation:

$$w_{ij} = w_{ij} - \eta \frac{\partial E}{\partial w_{ij}}, \eta > 0 \text{, where } \eta \text{ is learning rate}$$

Above steps repeated until the total error $E_t < \varsigma$, where ς is the specified precision. Figure 4.9 shows the input-output configuration of the neural network.
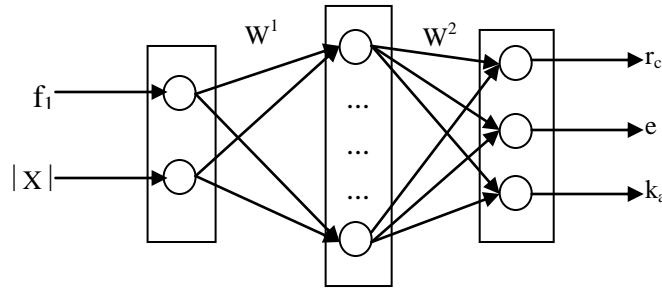
Figure 4.9: Three layer feed-forward neural network

A Matlab neural network toolbox program is shown below. The following statements are used to execute the above set of equations:

Model code: Neural network toolbox program

```
% let P be the input vector, T be the target vector
% n is number of hidden nodes, o is number of output nodes
mnet=newff(minmax(P),[n o], {'logsig','logsig'},'traingd');
mnet.trainParam.epochs=1000;
mnet.trainParam.goal=0;
mnet.trainParam.lr=0.4;
mnet.trainParam.show=25;
mnet=train(mnet,P,T);
```

(b) Radial Basis Function Neural Network

Radial basis function (RBF) network is another supervised model where, both input and target training vectors are supplied. Figure 4.10 shows the radial basis function neural network.
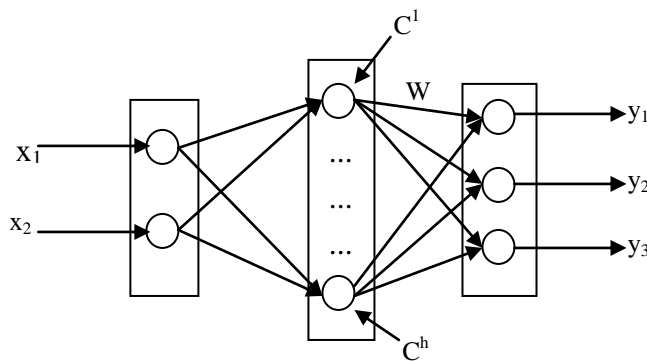
Figure 4.10: Structure of RBF neural network

Here, there are only three layers: (i) input (ii) hidden and (iii) output layers. The connections between input and hidden are not weighted, instead hidden nodes are supplied with central vectors C^i, which are subsets of input training vectors. Input is

denoted by vector x_i and neurons in the hidden layer implement the Gaussian activated function to extract the features from the input vector x_i. The output of the hidden layer is obtained as:

$$y_i = \exp\left(-\frac{\left\|x_i - c_{ij}\right\|^2}{\sigma^2}\right) \qquad (4.78)$$

The vector y_j is output of the jth neuron of the hidden layer (j=1, 2, ...h), c_{ij} is the central vector of the Gaussian function, σ is called width of the function. The output layer has output z obtained as linear combination of y_j as follows:

$$z_k = y_j\, w_{jk} + b_k \qquad (4.79)$$

where w_{jk} is the weight matrix of linear output layer and b_k is vector of bias. The values of C, σ, W and b are determined throughout the training.

4.6.2 Bearing fault identification

The concept of feature extraction for accurately assessing bearing performance degradations is a critical task towards realizing an online bearing condition monitoring platform. When a rotor has faulty ball bearing, its response has distinct properties compared to the original signal. The time-domain or frequency-domain signal obtained is very difficult to distinguish, in what form the signal is different from the baseline response. Therefore, often some statistical parameters are employed to define the signal features. Traditional statistic features are a powerful tool which characterizes the change of bearing vibration signals when faults occur. The benefits of these features are the simplicity of implementation and the low computational time. Heng and Nor defined six important statistical parameters of time-history:

(i) Waveform factor (X_w); It indicates the shift in time waveform and determined as:
$$X_w = \frac{RMS\ value}{mean\ value}$$

(ii) Crest factor: It shows the indication of peak height in time waveform and is determined as: $X_c = \frac{maximum\ peak}{RMS.value}$

(iii) Impulse factor: It shows indication of shock in time-waveform and is given as:
$$X_i = \frac{maximum\ peak}{mean\ value}$$

(iv) Allowance factor: It is defined as: $X_a = \frac{maximum\ peak}{X_r}$, where $X_r = \left(\frac{1}{N}\sum_{n=1}^{N} x^{0.5}(n)\right)^2$

(v) Skewness is the third moment, while kurtosis is fourth moment of signal distribution time-domain and both are sensitive indicators for the shape of the signal. Skewness is

defined as follows: $X_s = M_3/\sigma^s$, where $M_3 = \frac{1}{N}\sum_{n=1}^{N}(x(n) - \bar{x})^3$ and $\sigma = \left(\frac{1}{N}\sum_{n=1}^{N}(x(n) - \bar{x})^2\right)^{0.5}$. Likewise, Kurtosis is defined as: $X_k = M_4/\sigma^4$, where $M4 = \frac{1}{N}\sum_{n=1}^{N}(x(n) - \bar{x})^4$. For sine wave, the Kurtosis value is 1.5.

Table 4.1 shows the summary of these important statistical parameters. By considering the time-domain signals from rotor with five cases of bearing conditions: (a) no-fault (b)outer race waviness (c) outer race dent (d) inner race dent and (e) ball spall, a set of above statistical parameters are recorded. In each condition of the bearing, 201 sets are recorded by changing the speeds of operation of the rotor from 500 rpm to 2500 rpm

Table 4.1: Summary of time domain features

RMS	$\left(\frac{1}{N}\sum_{i=1}^{N} x_i^2\right)^{\frac{1}{2}}$	**Impulse Factor**	$\dfrac{\max\lvert x_i\rvert}{\frac{1}{N}\sum_{i=1}^{N}\lvert x_i\rvert}$
Mean	$\bar{x} = \dfrac{\sum_{i=1}^{N} x_i}{N}$	Margin Factor	$\dfrac{\max\lvert x_i\rvert}{\left(\frac{1}{N}\sum_{i=1}^{N}\lvert x_i\rvert^{\frac{1}{2}}\right)^2}$
Standard deviation (σ)	$\left(\frac{1}{N}\sum_{i=1}^{N}(x_i - \bar{x})^2\right)^{0.5}$	**Form factor**	$\dfrac{RMS}{\bar{x}}$
Skewness	$\frac{1}{N}\sum_{i=1}^{N}\dfrac{(x_i - \bar{x})^3}{\sigma^3}$	Peak to peak (P_P)	$x_{max} - x_{min}$
Kurtosis	$\frac{1}{N}\sum_{i=1}^{N}\dfrac{(x_i - \bar{x})^4}{\sigma^4}$	**Crest Factor**	$\dfrac{\max\lvert x_i\rvert}{RMS}$

Objective is to identify the class in which the given vibration signals fits-in. In this regard, two supervised neural network models and one unsupervised neural network model are employed to test the accuracy of classification result. In addition to 3-layer back propagation neural network, another neural network called probabilistic neural network (PNN) is also employed in this regard. It is first described below:

(a) Probabilistic Neural Network (PNN)

A PNN (Probabilistic neural network) is designed to fault diagnosis in ball bearing system and input/output nodes are same as in BP network. In PNN, weights do not alter with training samples. As number of hidden nodes represent the training samples. The connection between the input and hidden layers are initial weighing coefficients which indicates the symptom sets of training samples as shown in Figure 4.11.
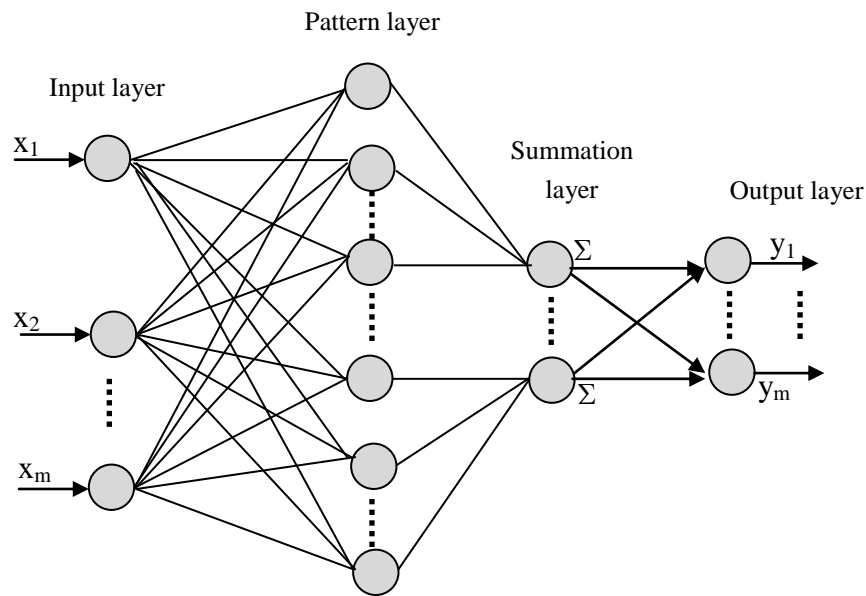
Figure 4.11: Architecture of probabilistic neural network

The connection between hidden and output layers indicates the fault sets of the training samples. The output neuron decision in hidden layer is expressed by [223]

$$f_A(X) = \frac{1}{(2\pi)^{p/2} \sigma^p} \frac{1}{m} \sum_{i=1}^{m} \exp\left(-\frac{(X-X_{Ai})^T(X-X_{Ai})}{2\sigma^2}\right) \tag{4.80}$$

where m is the total number of the training patterns, $X=(x_1,x_2,x_3....x_p)^T$ is the input pattern vector. X_{Ai} is the ith training pattern of the category A, P is the dimension of the metric space, σ is the smoothing factor (the standard deviation). The output layer is the decision layer which makes the final network decision.

It was proved that PNN is easy to train and it can be used in real-time applications. Compared with other classification methods, PNN has prominent advantages in timeliness. Furthermore, the relevant calculation of PNN is very simple and convenient. Above all, PNN can almost get the best classification effect if the training data is enough.

(b) Kohonen self organization model

Self-organization model (SOM) is a class of unsupervised neural networks that is trained to produce discretized representation of the input space of the training samples, called a map. Precisely, it is a nonlinear, ordered, smooth mapping of high dimensional input data onto the elements of a regular, low-dimensional array. SOM maps can be used for classification and visualizing of high-dimensional data.

Unlike many other types of NNs, the SOM doesn't need a target output to be specified. Instead, weights are selected close to the inputs at the end of training. From an initial

distribution of random weights and over much iteration, the SOM eventually settles into a map of stable zones. Each zone is effectively a feature classifier. The standard Kohonen learning algorithm is an unsupervised training process. It produces a vector quantizer by repeat updating the prototypes of the class- units. After initialization of: prototypes ($W_i(t)$), learning rate ($\eta(t)$) and neighbourhoods ($N_i(t)$), all patterns are presented to the SOM network. For each pattern X_p, the distances $d_i = \left\| W_i(t) - X_p \right\|$ to the prototypes of the class- units are computed and the winning class- unit j is chosen. The prototypes of the class- unit j and the class- units inside the neighbourhood $N_j(t)$ are then updated. Figure 4.12 shows the Kohonen's SOM network.
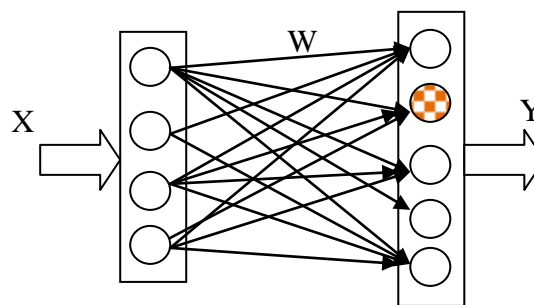
Figure 4.12: Kohonen's self-organization map (One of output node only fires at a time)

The basic steps in Kohonen algorithm are:

1. Initialize the network: number of class- units C, prototypes W_i, learning rate $\eta(t)$, neighbourhoods $N_i(t)$, i=1…C, maximum number of epochs T_{max} and accuracy ε
2. Present a pattern X_p to the network
3. Determine the winning class- unit j, the one closest to pattern X_p:

$$d_j = \min\left(d_i\right) = \min\left(\left\| W_i(t) - X_p \right\|\right), \forall i = 1...C \tag{4.81}$$

4. Update prototype of the winning class-unit j and class-units inside the neighbourhood $N_j(t)$ according to following formula:

$$W_i(t+1) = W_i(t) + \eta(t)\left[X_p - W_i(t)\right] i \in N_j(t), \tag{4.82}$$

5. Update the learning rate as $\eta(t)=0.9(1-t/t_{max})$ and the neighbourhoods $N_i(t+1)$, i=1…C
6. Repeat steps 2-5 until either the changes in prototypes in two consecutive epochs fall below ε, or the maximum number of epochs T_{max} is reached

To determine the best matching unit, one method is to iterate through all the nodes and calculate the Euclidean distance between each node's weight vector and the current input vector. The node with a weight vector closest to the input vector is tagged as the best matching unit. As the learning rate $\eta(t)$ reduces, the system cannot learn new patterns and

gives the results from already learnt patterns. Kohonen SOM is very well suited for classification applications.

In present context, SOM is provided with the four statistical parameters corresponding to 5 different types of bearing signals. As per the trends of these parameters for each type of fault, the outputs are categorized into one of the five classes.

4.6.3 Identification of transient stiffness due to rub

Due to rubbing of rotor during highly unbalanced conditions, the shaft stiffness tremendously increases along with speed. In order to identify this increased rotor stiffness, an optimization scheme is proposed in this work. The rotor dynamic equations of the system with unbalance, rub and gravity forces along with bearing nonlinear forces reproduced as

$$\mathbf{M}\ddot{X} + (\mathbf{C} - \Omega\mathbf{G})\dot{X} + \mathbf{K}X = F_u + F_r + F_g + F_b \tag{4.83}$$

where, F_u, F_r, F_g and F_b are respectively the unbalance, external rub-impact, gravity and bearing force vectors. Now, the effect of rub-impact on the rotor system is reflected by the transient stiffness. Therefore, the rotor system can be considered as a system without rub-impact interaction and differential equations describing the system may be written as:

$$\mathbf{M}\ddot{X} + (\mathbf{C} - \Omega\mathbf{G})\dot{X} + \mathbf{K^e}X = F_u + F_g + F_b \tag{4.84}$$

where $\mathbf{K^e}=\mathbf{K}+\mathbf{\Delta K}$ is effective stiffness of the system as a result of rubbing effect. Here, the objective is to obtain ΔK by knowing the experimental or simulated response of rotor with rub-impact on one or all the discs by suitable approach. In present formulation, the responses are converted into frequency-domain and with rub-impact forces, the FFT spectrums $X_i(\omega)$ are obtained at 5 different speeds of operation using finite element model. This data is considered as the required response data. With randomly selected stiffness coefficients of diagonal stiffness matrix $\mathbf{\Delta K}$ corresponding to all the elements, a response $X^e(\omega)$ is derived by solving eq.(4.94). The correct sets of elements of $\mathbf{\Delta K}$ are obtained by minimizing the average difference between the required response and derived response. That is

$$\text{Minimize } f(\Delta k_1, \Delta k_2, ...) = E = \frac{1}{Ns}\sum_{n=1}^{Ns}(X^e(n\omega) - X_i(n\omega))^2 \tag{4.85}$$

where, *Ns* is sampling points considered and this mean error in discrete domain is computed under the constraints of variables Δk_i. For this particle swarm optimization scheme is considered, which is described below:

Particle swarm optimization Scheme

Particle Swarm optimization (PSO) is a stochastic optimization method based on the simulation of the social behavior of bird flocks and was originally developed by Kennedy and Edberhart. In this algorithm, the system is initialized with a population of random solutions and each potential solution is also assigned a randomized velocity. The potential solutions, called particles, are then "flown" through hyperspace. And each particle will change the velocity toward its best previous value p_{best} and global best value g_{best} locations according to its own flying experience and its companion's flying experience. In a d-dimension space, the velocity and location of particle k are updated by following equations:

$$v_k^d(s+1) = wv_k^d(s) + C_1\xi\left(P_k^d - x_k^d(s)\right) + C_2\xi\left(P_g^d - x_k^d(s)\right) \tag{4.86}$$

$$x_k^d(s+1) = x_k^d - v_k^d(s) \tag{4.87}$$

where s is the iteration step of PSO; x_k^d and $v_k^d(s)$ are the position and velocity of the kth particle at s step; ξ is a random number uniformly distributing in the range [0, 1]; c_1 and c_2 represent the weighting of the stochastic acceleration terms that pull each particle toward its best previous value and overall best value positions; the inertia weight $w=(w_{max}-w_{min}*s/N)$ plays a role of balancing the global and local search, it can be a positive constant or a positive linear or nonlinear function of time; P_k^d is the best previous position of the kth particle and P_g^d is the swarm's best position. The steps for implementing PSO algorithm are simply shown in
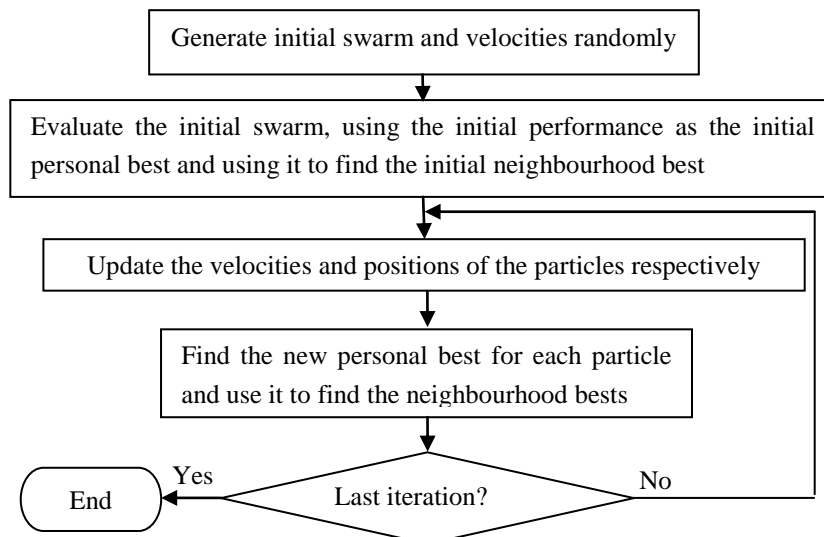
Figure 4.13: Basic steps of PSO.

Chapter 5

Design of Control system

5.1 Introduction

The reduction of vibrations of aero-engines is an important part of rotor dynamics. In addition to the safety requirement of avoiding rotor bend critical speeds within the engine running range, the response of the many other modes of the rotors and engine structural system must be controlled to ensure acceptable levels of vibration. Control of vibration is essential in respect of the bearing loads, structural fatigue loads, rotor/casing tip clearances, casing and engine external responses, and transmission of vibration to the airframe. Hydrodynamic bearings have been used extensively in almost all aircraft turbine designs since 1970 to dampen the imbalance response and are probably a major contributor to the rarity of rotor dynamic instability encountered in the engines. The main disadvantages of these bearings are their passive nature, instability, and very sensitive variability of performance with raise in temperatures and frequencies of the rotors. Rotor damping at the bearings is mostly needed near critical speeds and is relatively ineffective at other speeds. Use of smart synthetic fluids, which change their viscosity from liquid to semi-solid state within milliseconds, due to sufficiently strong electric or magnetic field have been employed as alternative to hydrodynamic bearings. But, such fluids are not also fit for resolving all the above mentioned drawbacks.

As a recent technology active/semi-active magnetic dampers have several advantages in respect of amplitude control. The difference between active magnetic bearings (AMBs) technology and active magnetic dampers (AMD) is rather small. In case of AMB, the shaft is completely supported by electromagnets, which achieve levitation and vibration control at the same time. In the latter case, the rotor is supported by mechanical means and the electromagnetic actuators are used only to control the shaft vibrations. In AMBs, both stiffness and damping forces must be provided by the electromechanical interactions increasing the mass of coils and hence the overall size of the system. Hence, they cannot be used in aeronautic applications.

Semi-active and active control methods are introduced to reduce or attenuate very high amplitudes of vibrations in any rotating machinery. Balancing is done with a proper adjustment of correction mass, stiffness and damping of rotating shaft of machinery is known as passive control. In this type of control the induced centrifugal forces and unbalance will be cancelled out due to correction masses like inertial disks.

The main objective of controller design is to identify the critical speeds of idealized low-pressure (LP) stage in aero-engine rotor shaft and design a damper mechanism that becomes active within the critical speed regions.

5.2 Semi- Active methods

Semi-active vibration control is very useful in different settings and being implemented and investigated. Semi-active devices make changes in the system properties like stiffness and damping in the running conditions only. This is an analysis of open loop response control scheme. These are very useful control schemes due to its adaptability of active control without of having very large sources of power and are very popular in the recent years. Semi-active methods to Control of vibrations at critical speeds are described below.

In order to minimize the vibration amplitudes at the critical speeds of operation of the rotor, it is proposed to design the electromagnetic dampers, which are to be laid at the two support bearing locations. Basically, these dampers have an electromagnet and a mechanical spring. In absence of electromagnet, it works as a hysteretic damper and damping action occurs with respect to the rotor speed. In a magnetic damper the reluctance of the magnetic circuit is influenced by the speed of the moving part in the circuit. This produces a flux variation and generates a back EMF and ultimately eddy currents in the coils. There are two effects of this eddy current:

1. Generating a force that increases with decrease in air gap, responsible for a negative stiffness.
2. Generation of damping force acting against the speed of the moving element.

In semi-active type of magnetic damper (SAMD) implemented in present work, voltage in the coil is kept constant and no closed loop position feedback is necessary as only current in the coil is monitored. Energy dissipation takes place in the stator. We can define the transfer function between the speed of rotor and electromagnetic force (F_{EM}) in terms of pole frequency ω_{RL} as:

$$\frac{F_{EM}}{\dot{q}} = \frac{k_{EM}}{s(1+\frac{s}{\omega_{RL}})} \qquad (5.1)$$

where $k_{EM} = -\dfrac{2V^2}{RG^2\omega_{RL}}$ is negative stiffness coefficient and pole frequency $\omega_{RL}=R/L_0$; here

$L_0 = \dfrac{\mu_0 N^2 A}{2G}$ is inductance of each electromagnet at nominal air gap G, 's' is Laplace variable, $\dot{q}$ is speed of the moving part of magnetic circuit. R is total resistance (coil resistance and additional resistance to tune the electric circuit pole). Also N_t is number of turns of each winding, A is area of magnetic circuit at the air gap and μ_0 is magnetic permeability of vacuum.

In semi-active magnetic damper a mechanical spring of stiffness k_m (where k_m is greater than $-k_{EM}$) is added in parallel to the electromagnet, driven by constant voltage. A better insight can be obtained by studying the mechanical impedance of the damper in parallel to the spring. i.e., for SAMD transfer function will become

$$\frac{F_{EM}}{\dot{q}} = \frac{1}{s}\left[\frac{k_{EM}}{(1+\dfrac{s}{\omega_{RL}})} + k_m\right] = \frac{k_{eq}}{s}\left[\frac{1+\dfrac{s}{\omega_z}}{1+\dfrac{s}{\omega_{RL}}}\right] \qquad (5.2)$$

where $k_{eq}=k_m+k_{EM}$ and $\omega_Z = \omega_{RL}(k_{eq}/k_m)$. It is possible to identify following three different frequency ranges:

1) Equivalent stiffness range ($\omega \ll \omega_Z$), where the system acts as a spring of stiffness k_{eq}
2) Damping range ($\omega_Z < \omega < \omega_{RL}$), where system behaves as a viscous damper with $c=k_m/\omega_{RL}$.
3) Mechanical stiffness range ($\omega \gg \omega_{RL}$), where system acts as a mechanical spring of stiffness k_m.

Figure 5.1shows the mechanical equivalent diagram of SAMD.
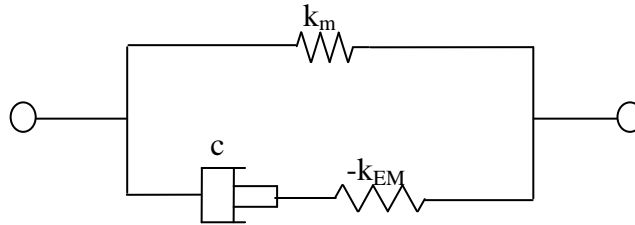
Figure 5.1: Mechanical Equivalent of eddy-current transformer damper

A sort of constant bandwidth product $k_m=c\omega_{RL}$ characterises damping range of the EM damper.

5.2.1 Specifications

The knowledge of the resonant frequencies at which the dampers should become effective and the maximum acceptable response, allows in specifying the needed value of the damping coefficient (c). The pole and zero frequencies (ω_{RL}, ω_Z) have to be decided so that the relevant resonant frequencies fall within the damping range of the damper. Additionally, tolerance and construction technology considerations impose the nominal air gap G. Electrical power supply considerations lead to the selection of the excitation voltage V.

5.2.2 Definition of the SAMD parameters

The mechanical stiffness can be obtained as $k_m=c\omega_{RL}$, once the pole frequency (ω_{RL}) and the damping coefficient (c) are given by the specifications. The electromechanical parameters of the damper viz., the electromechanical constant N_t^2A and the total resistance R can be determined as follows:

a. The required electrical power V^2/R is obtained from $V^2/R=0.5G^2\omega_{RL}\ k_m$ (1-ω_z/ω_{RL}). The knowledge of the available voltage V allows them to determine the resistance R.

b. The electromechanical constant N_t^2A is then found using $L_0=R/\omega_{RL}=\dfrac{\mu_0 N^2 A}{2G}$.

5.3 Active methods

In active control of vibrations, active devices or actuator are used to change the dynamical properties of the system by measuring instantaneous operating conditions with sensors. This system can be useful at different load conditions and configurations.

Piezoelectric actuators are used as a pusher in the rotating machines as an active vibration controller in 90's. Later, they are modelled as dampers and springs. Then, these piezoelectric actuators are developed as an adaptive hydrodynamic bearing to reduce the high frequency amplitudes of vibrations. Generally active magnetic bearings are used as active vibration controllers and are very extensively used in industrial applications. Active magnetic bearings are recently used as lubrication free and non-contact bearings with a feedback control.

5.3.1 Conventional PD controller

To minimize the vibration amplitude of system appropriate magnetic force should applied by the actuator force should act in the opposite direction of motion and should increase with displacement. The magnetic force, on the other hand, depends upon the pole winding current of an electromagnet, so by controlling pole winding currents, the system response can be controlled. Proportional-Derivative (PD) control is generally used for faster response. Proportional control increase the control input in proportion to the error e(t) within the acceptable range of error. Derivative control changes the control input in proportion rate of change of error. Equation of control output of PD controller can be given as

$$u(t) = K_p e(t) + K_d \dot{e}(t) \tag{5.3}$$

The controlled output is control currents and the error signal. Here x and y are the displacements in the two lateral directions at the LP compressor disk location. Hence, the control currents for pole pair in vertical direction (i1) and in the horizontal direction (i2) are:

$$i_1 = -K_p x - K_d \dot{x}$$
$$i_2 = -K_p y - K_d \dot{y} \tag{5.4}$$

5.4 Design of Electromagnetic Actuator

The control system has an actuator placed very close to the plane of the disks and oriented along two orthogonal radial directions. Due to the arrangement of poles in the actuator, the components of magnetic control force along X and Y directions are obtained independent of each other. The magnetic force is controlled by both the current and

displacement. Tuning of current varies the stiffness of the rotor. Figure 5.2 shows schematic of four-pole electromagnetic actuator. The magnetic flux f_n for each pole is given by:

$$\emptyset_n = \frac{\mu_0 A_g N I_n}{G - d\cos\alpha} \quad (n=1\text{-}4) \tag{5.5}$$

where μ_0 denotes the permeability of free space ($4\pi \times 10^{-7}$ H/m), A_g be the effective cross sectional area of air gap, N_t the number of turns of winding coil around a pole, I_n the control current through the coil, G is the nominal gap size of air, α is the half angle between the two adjacent poles (22.5^0) and d the displacement of shaft at the horizontal and the vertical directions. The magnetic force, F_n, can be obtained as follows

$$F_n = \frac{\mu_0 A_g N_t{}^2 I_n^2 \cos\alpha}{(G - d\cos\alpha)^2}, \quad (n=1\text{-}4) \tag{5.6}$$
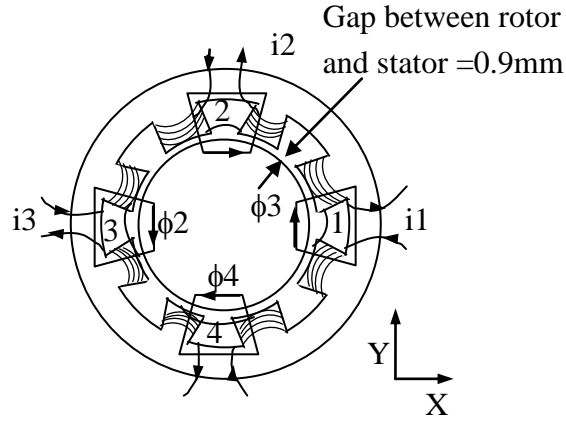
Figure 5.2: Schematic of four pole electromagnetic exciter

From this equation, it is seen that the magnetic force is proportional to the square of the control current of an electromagnetic exciter and inverse to the displacement of a rotor. F_n is nonlinear function. For the sake of controlling, it is linearized. The PD controller first provides a bias current and then adds a small variable control current. Therefore, it is defined as:

$$I_n = I_b + i_n \tag{5.7}$$

where I_b and i_n are the bias current and the control currents respectively. Replacing I_n (n=1 - 4) in Eq. (5.6)

$$F_n = \frac{\mu_0 A_g N^2 (I_b + i_n)^2 \cos\alpha}{(G - d\cos\alpha)^2}. \tag{5.8}$$

Let $i_1 = -i_3$ and $i_2 = -i_4$ (see Figure 5.2) and then the magnetic forces in the x- and the y- direction are obtained as:

$$F_x = F_1 - F_3 = \mu_0 A_g N^2 \cos\alpha \left[\frac{(I_b + i_1)^2}{(G - x\cos\alpha)^2} - \frac{(I_b + i_3)^2}{(G + x\cos\alpha)^2}\right] \tag{5.9a}$$

$$F_y = F_2 - F_4 = \mu_0 A_g N^2 \cos \alpha \left[\frac{(I_b+i_2)^2}{(G-y\cos\alpha)^2} - \frac{(I_b+i_4)^2}{(G+y\cos\alpha)^2} \right] \tag{5.9b}$$

The Taylor series is used to expand these equations. As the x- displacement and y-displacement and the control current i_n are small variances, the higher terms can be ignored in this equation. Consequently, the equation is obtained as

$$F_x = \frac{4\mu_0 A_g N^2 I_b \cos \alpha}{G^2} i_1 + \frac{4\mu_0 A_g N^2 I_b^2 \cos^2 \alpha}{G^3} x + \cdots \tag{5.10}$$

$$F_y = \frac{4\mu_0 A_g N^2 I_b \cos \alpha}{G^2} i_2 + \frac{4\mu_0 A_g N^2 I_b^2 \cos^2 \alpha}{G^3} y + \cdots \tag{5.11}$$

(or)

$$F_x = K_i i_1 + K_d x \tag{5.12}$$

$$F_y = K_i i_2 + K_d y \tag{5.13}$$

Where

$$K_i = \frac{4\mu_0 A_g N^2 I_b \cos \alpha}{G^2} \text{ , and } K_d = \frac{4\mu_0 A_g N^2 I_b^2 \cos^2 \alpha}{G^3} \ .$$

Here, the currents i_1 and i_2 are given by:

$$i_1 = -k_v \dot{x} - k_p x, \quad i_2 = -k_v \dot{y} - k_p y \tag{5.14}$$

where k_p and k_v as well as i_1 and i_2 are the proportional gains, the derivative gains and the currents of the controller in the x- and y-directions, respectively. Figure 5.3 shows the block diagram of control system logic.
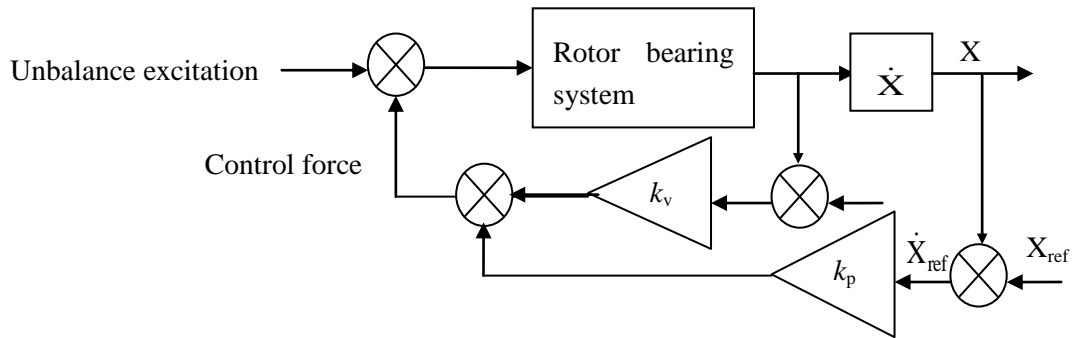
Figure 5.3: Proportional-Derivative control strategy for controlling vibrations at a disk

Here, the proportional and derivative gains k_p and k_v are selected as 10 and 0.1 respectively. Other parameters include: A_g=240 mm^2, N=106, α=22.5^o, G=0.9 mm and I_b=3 A. The instantaneous current components i_1 and i_2 depend on the displacements x and y at the disk node-1.

5.4.1 Neural network based controller

As seen from Eq.(5.9), it is observed that the control forces are nonlinear functions of the radial displacements and velocities of rotor. So, an inverse dynamic model of the system is used as a controller, by training a radial basis neural network with instantaneous transient response as inputs and corresponding currents and forces as outputs. Figure 5.4 shows the present methodology employed in this work.
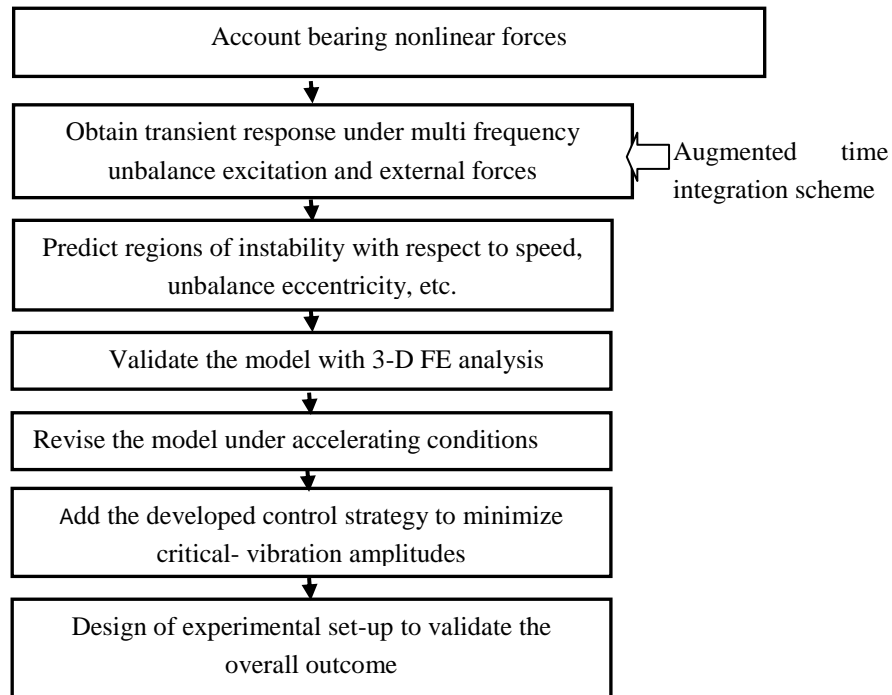
Figure 5.4: Flowchart of the methodology

Chapter 6

Results and Discussions

6.1 Introduction

Finite element analysis is employed initially to model the rotor. Effects of bearing stiffness, double-row ball bearing, squeeze film damper parameters, bearing faults, rub contact stiffness on unbalance response are studied. For identification and classification tasks, inverse modelling is employed to predict the parameters from given vibration response. Figure 6.1 shows the overall approach followed during the computer programming.
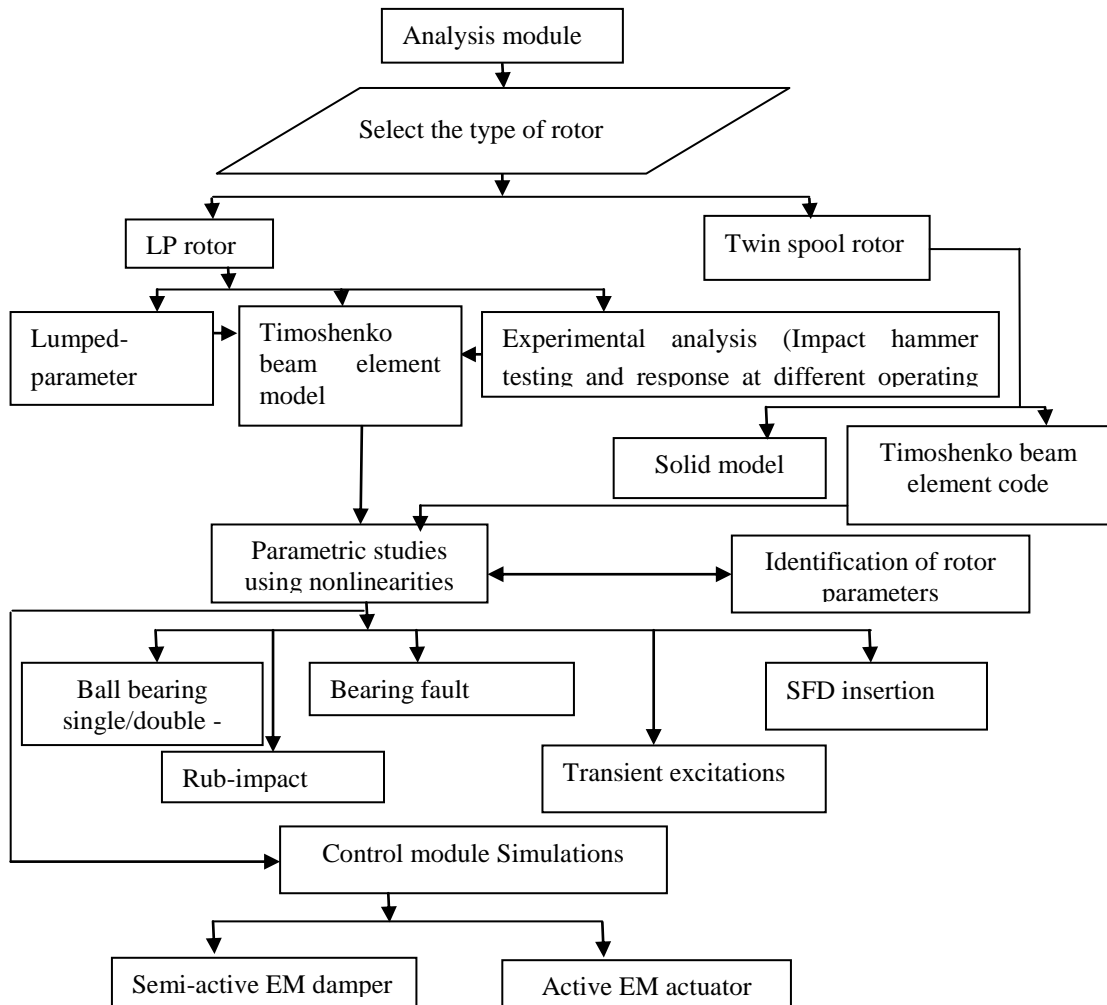
Figure 6.1: The Schematic of various studies carried-out

The experimental responses of the system were used in identifying the effective parameters of the system. Different ball bearing considerations such as variations in double row bearings, ball bearings supported over squeeze-film dampers, as well as bearing faults are accounted. The external nonlinear forces such as gas force transients idealized by Muszynska's model, rub-impact forces modelled by point contact force model are employed to study their effects on dynamic response of rotor. By using this data, the parameters are identified from known dynamic responses using inverse modelling and with the help of neural networks.

Finally, control results of the dual-disk rotor bearing system using a semi-active magnetic actuation approach and active electro-magnetic actuator are presented for attenuation of the critical response amplitudes. The chapter is classified into primary and secondary studies. While the primary studies deal with the linear models and used to validate the finite element model, the secondary studies describe effects of various parameters and their identification from a given vibration responses by considering the real-time nonlinearities at bearings and forces.

6.2 Preliminary modelling of rotor bearing system

Present study considers the finite element modelling of the rotor using Timoshenko beam theory. Disks are considered as a rigid, while the flexible shaft model accounts two bending deflections. Computer programs are developed for assembling the element matrices and also their sizes are reduced to eliminate the rotational degrees of freedom. In the primary case, the bearings are idealized as spring-dashpot models with different stiffness cases. In other words, the bearing stiffness is considered as static and time invariant idealising as a complete linear model. User of the present program can select two cases of rotors.

6.2.1 Dual disk LP rotor

Figure 6.2 shows a simplified LP aero-engine rotor model having a turbine and compressor disks supported on rolling element bearings in between the disks.

Finite element modelling of the rotor system is the first step. A convergence study for optimum number of elements is carried out and it was found that six elements are giving relatively constant results for the first four modes. Each of the three segments is divided into two equal elements. Thus, the model having six element and seven nodes is employed through-out the work.
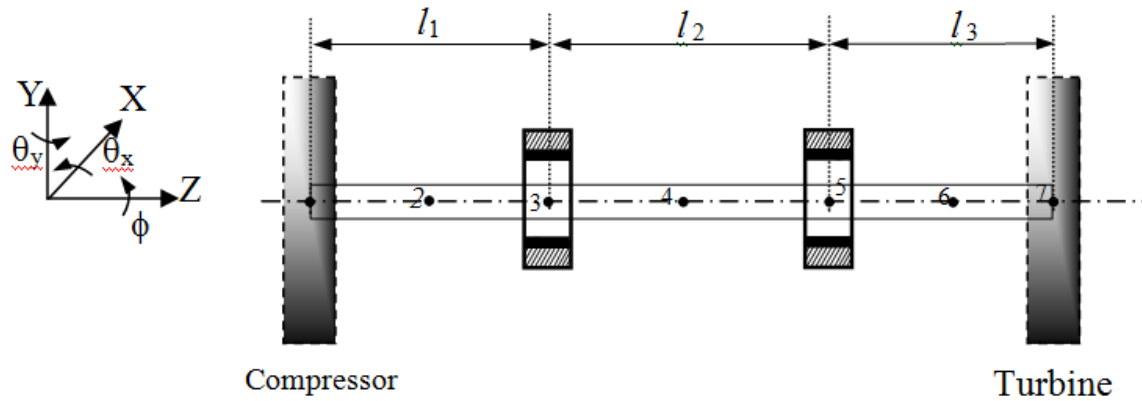
Figure 6.2: Finite element model of a two disk rotor

Two disks are located at node 1 and 7. The bearings are located at nodes 3 and 5. The system has in total 28 degrees of freedom represented by q=[v_1 w_1 θ_{x1} θ_{y1} ………. . v_7 w_7 θ_{x7} θ_{y7}]^T. The reduced matrices are used in computing the eigenvalue problem which results in a set of complex conjugate eigenvalues. At different speeds of the operation of the rotor, these eigenvalues are recorded. Campbell diagrams are plotted and critical speeds of operation are initially computed for three different bearing stiffness conditions. The bearing damping is not considered and the system damping is expressed in terms of modal damping factor of 0.001. Table 6.1 depicts the dimensions of the rotor-bearing system and its material properties.

Table 6.1: Material properties and geometric parameters of rotor and bearings

Parameter	Dimension
Shaft diameter (mm)	20
Disk diameters (mm)	110(R), 90(L)
Disk thickness (mm)	10
Density of shaft and disk (kg/m^3)	2700
Elastic modulus (GPa)	70
Shear Modulus (GPa)	27
Total shaft length (mm)	650

For analysis consideration, the segmental lengths considered as l_1=200 mm, l_2=250 mm, l_3=200 mm. Table 6.2 shows the first six natural frequencies in comparison with the commercial FE program Ansys corresponding to bearing stiffnesses $k_{xx}=k_{yy}=1\times10^7$ N/m. Program is written in batch mode using ANSYS (v13) APDL environment by considering 3-D beam elements (BEAM188), 3-D mass elements (MASS21) and bearing elements (Combi214) is chosen. Combi214 has springs and dampers in four different directions

(xx, yy, xy and yx). The spring and damper constants are declared by real constants in Ansys.

Table 6.2: First six natural frequencies (Hz)

S.No	Present Finite element analysis	Ansys (1-D)
1	80.66	82.44
2	106.92	109.69
3	734.74	759.94
4	845.86	878.49
5	934.29	974.23
6	1721.17	1755.62

The natural frequencies obtained from present code are slightly smaller compared to Ansys values as the approach considers the shear deformation and rotary inertia effects. Figure 6.3 shows the corresponding unbalance response at the bearing node obtained by solving the linear system of differential equations. As the bearing dynamics is not included, the resulting peaks are due to rotor natural frequencies only without any sub-harmonics.
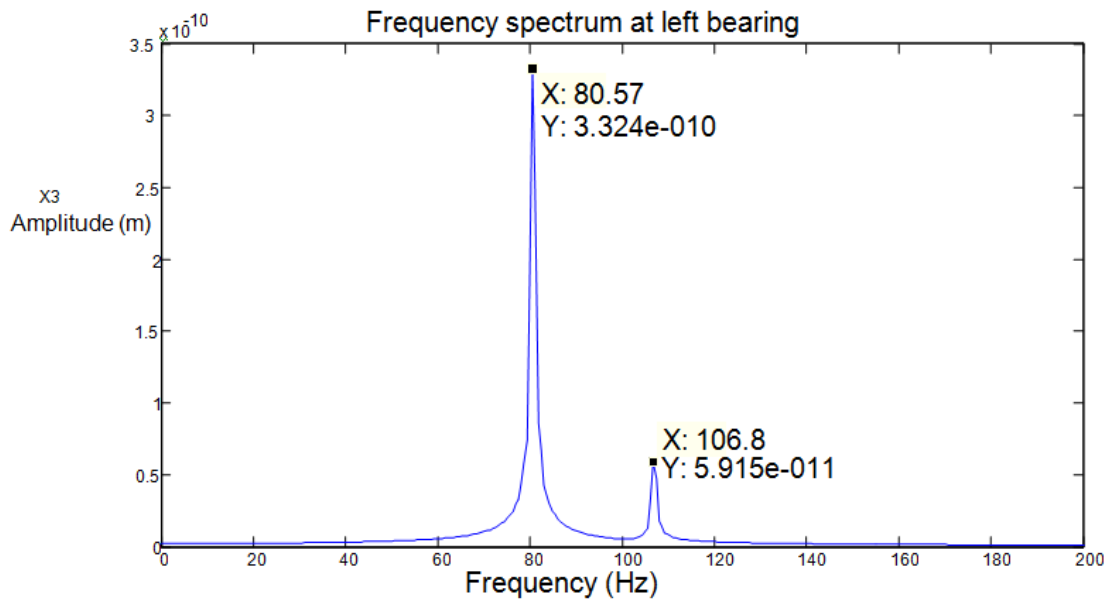
Figure 6.3: Unbalance response

Figure 6.4 shows the mode shapes of the dual disk rotor bearing system at different natural frequencies obtained from Ansys.
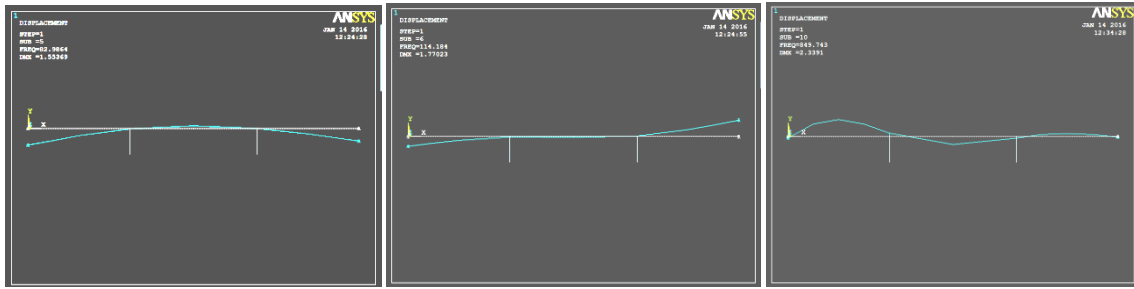
(a) First mode   (b) Second mode   (c) Third mode
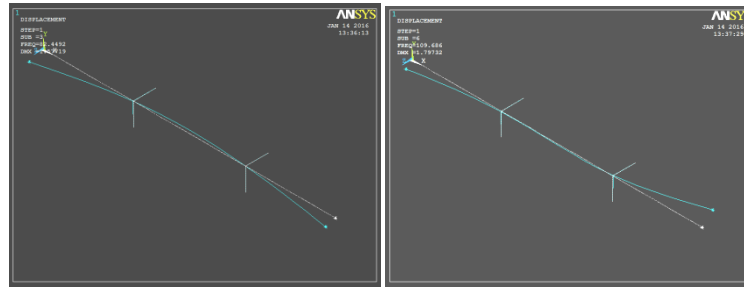
(d) Fourth mode   (e) Fifth mode

Figure 6.4: Mode shapes of the dual disk rotor bearing system in Ansys

Figure 6.5 shows the mode shapes of a dual disk rotor bearing system using present finite element analysis code. As seen, symmetrical modes are found in two bending directions.
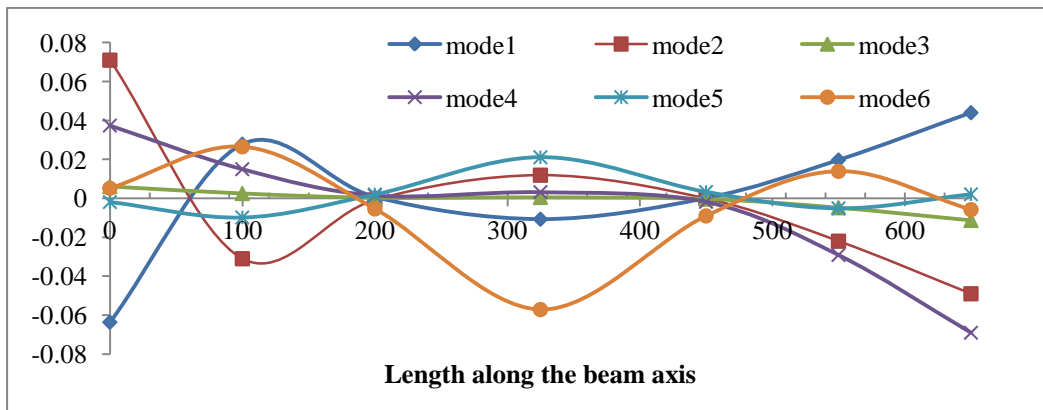
Figure 6.5: Mode shapes of the dual disk rotor bearing system using FEA

Figure 6.6 shows the Campbell plots obtained for three different bearing stiffness values.
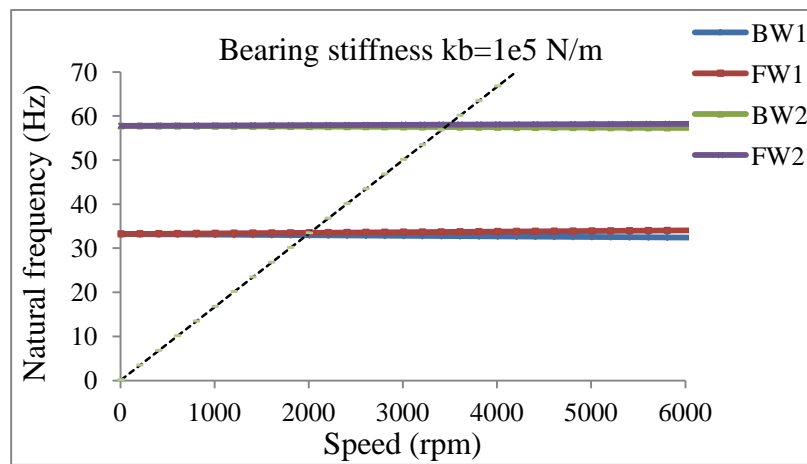
(a) Bearing stiffness values of k_b=1e5N/m.
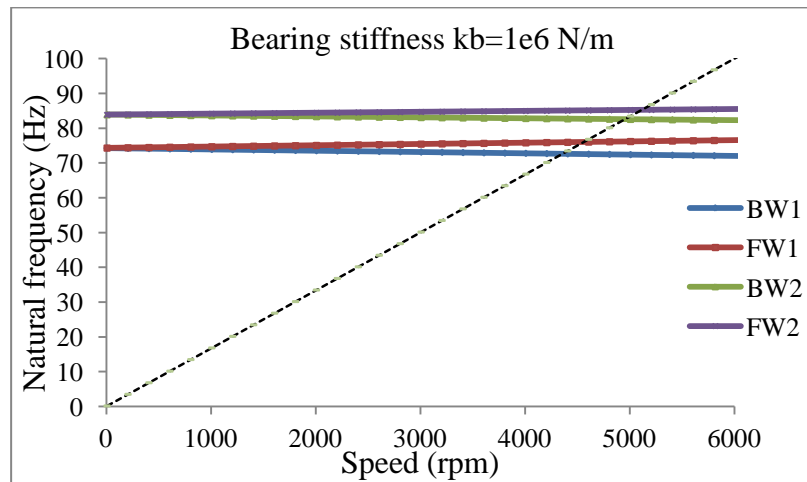
(b) Bearing stiffness values k_b=1e6 N/m.
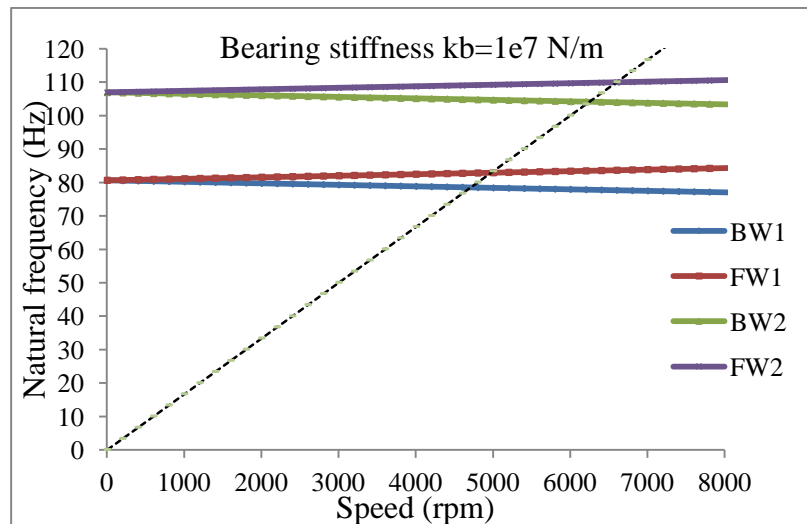
(c) Bearing stiffness values k_b=1e7 N/m.

Figure 6.6: Campbell diagrams from beam element analysis.

It is observed that at the bearing stiffness k_b=1e5N/m, the first backward whirl (BW) speed is approximately at 1900 rpm and the first forward whirl (FW) speed at 2000 rpm and the second backward whirl is at approximately 3500 rpm and the second forward whirl speed is at approximately 3600rpm. Likewise, at the bearing stiffness k_b=1e6N/m, the first BW speed is at 4200 rpm and the first FW speed is at 4500 rpm and the second BW is at 5000 rpm and the second FW speed is at 5200rpm. Also, at the bearing stiffness k_b=1e7 N/m, the first BW speed is at 4800 rpm and the first FW speed at 5000 rpm and the second BW speed is at 6400 rpm and the second FW speed is at 6900rpm. There is 42% and 44% of increase in the backward whirl speed and forward whirl speed due to increase the bearing stiffness value k_b from 1e5 to 1e6 N/m. Also, there is 82% and 91% of increase in backward whirl and forward whirl speeds due to the change in the stiffness value from 1e5 to 1e7 N/m. It is concluded that, due to increase in the bearing stiffness there is a significant increase in critical speeds of operation.

For further validation, using Ansys software, the dual disk rotor is analysed by meshing with 3-D brick elements (20-noded 3 degree of freedom per node) (SOLID187) and the bearing nodes are connected with spring-damper elements (COMBIN14) to the ground. Figure 6.7 shows the 3-D finite element model of rotor system. The resultant first few natural frequencies (evaluated for k_{xx}=k_{yy}=1.75e7N/m) are 67.872 Hz, 74.019 Hz, 139.62 Hz, 155.02 Hz, 363.89 Hz and 602.01 Hz. This model cannot give torsional frequencies of rotor. Moreover, the 3-D FE analysis consumed numerous computational times to get the final results.
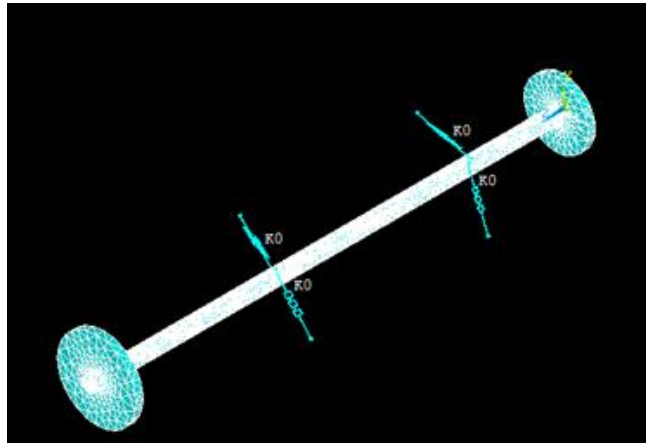
Figure 6.7: 3D finite element model

6.2.2 Two-spool rotor model

Like an LP rotor model, the support effects on a twin-spool rotor are next presented. Figure 6.8 shows a simplified finite element model of the twin-spool rotor assembly [100]. It consists of four bearings and four disks, two each on inner and outer spools respectively. As seen in figure, the node 4 of inner spool and node 10 of outer spool are

connected by the intermediate fourth bearing element. It has total 10 nodes and 40 degrees of freedom. Variable speed ratios are considered.
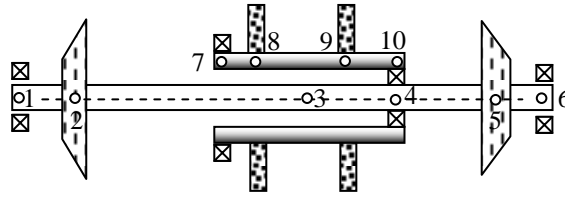
Figure 6.8: The finite element model of two-spool rotor system

Table 6.3 shows the dimensions of the two-spool rotor-bearing system and its material properties.

Table 6.3: Geometric and material data for rotor

Node	Axial dist. (mm)	d_{Inner} (mm)	d_{Outer} (mm)	Disc mass(kg)	I_P (kgm^2)
1	0	0	30.4	-	-
2	76.2	0	30.4	10.51	0.0859
3	323.85	0	30.4	-	-
4	406.4	0	30.4	-	-
5	457.2	0	30.4	7.01	0.0678
6	508	0	30.4	-	-
7	152.4	38.1	50.8	-	-
8	203.2	38.1	50.8	7.01	0.0429
9	355.6	38.1	50.8	3.5	0.0271
10	406.4	38.1	50.8	-	-

The material for the spools is steel with elastic modulus E=210 GPa and density ρ=7800 kg/m^3. All four disks have polar moment of inertia (I_P) twice the diametral mass moment of inertia (I_D). Further, an unbalance of 10 microns is considered in the disks. Initially the conventional problem with linear spring-damper bearing elements (with k_1=0.279e8 N/m, k_6=0.175e8 N/m, k_7=0.175e8 N/m and $k_{intermediate}$ =0.875e7 N/m) is attempted to know the approximate values of natural frequencies and corresponding unbalance response. The resultant stiffness, mass, damping (damping ratio of 0.01) and gyroscopic matrices are used and the set of first few natural frequencies are obtained. The proposed Matlab code simplifies the analysis procedure by reducing the size of the problem with the help of condensation through eliminating rotational degrees of freedom. Table 6.4 shows the comparison of first few modes obtained from present analysis along with Ansys results by employing BEAM188 element. Here, the gyroscopic and damping matrices are not considered. The corresponding mode shapes are shown in Figure 6.9.

Table 6.4: Natural frequencies (Hz) of twin spool rotor under consideration

Mode	Present code	Ansys (Beam model)	% deviation
1	90.7	91.945	1.354
2	217	186.75	16.19
3	227.9	---	---
4	277.2	270.73	2.389
5	280.1	---	---
6	378.5	321.47	17.74

It is seen that the first mode obtained using present code is well matching with Ansys result. At higher modes, the percentage deviations are relatively more. The possible reason for this may be due to the reduction process of matrix sizes by using static condensation scheme.

(a) First mode f_1=91.945 Hz   (b) Second mode f_2=186.75 Hz

(c) Third mode f_3=270.73 Hz   (d) Fourth mode f_4=321.47 Hz
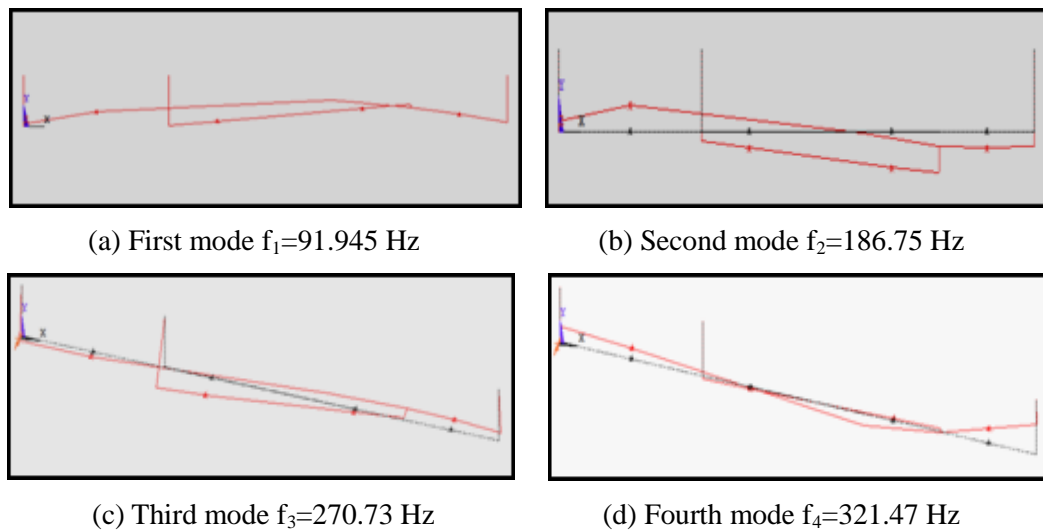
Figure 6.9: First four mode shapes of two-spool rotor

Figure 6.10 shows the Campbell diagram of the rotor obtained with a viscous damping (0.1%). The following Matlab code is employed for computing total damping:

Model code: Campbell diagram program

```
Aq=inv(Mr)*Kr;
[v2,w2]=eig(Aq);
mult=sqrt(v2'*Mr*v2);
for i=1:np
  omn(i)=sqrt(w2(i,i));
  Phi(:,i)=v2(:,i)/mult(i,i);
end
zi=0.001;
Cv=zeros(np,np);
for i=1:np
  Cv(i,i)=2*zi*omn(i);
end
Cq=inv(Phi')*Cv*inv(Phi); % CONSTANT DAMPING DUE TO RAYLEIGH
Ce=Gr+Cq; %The total damping with shaft, disk gyroscopic matrix
```
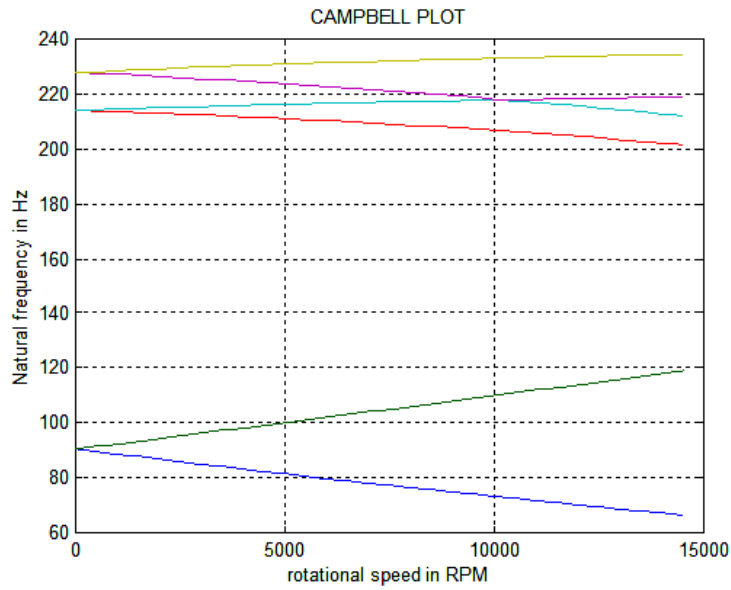
Figure 6.10: Campbell diagram of the rotor with bearings idealized as linear springs

It is seen that there is a vital effect of speed on the higher natural frequencies in this rotor even at lower operating range.

Figure 6.11(a) shows the unbalance response when eccentricity of 1 micron is considered in all the disks. A speed of 5000 rpm is considered. Results are validated with the harmonic analysis in Ansys as seen Figure 6.11 (b).
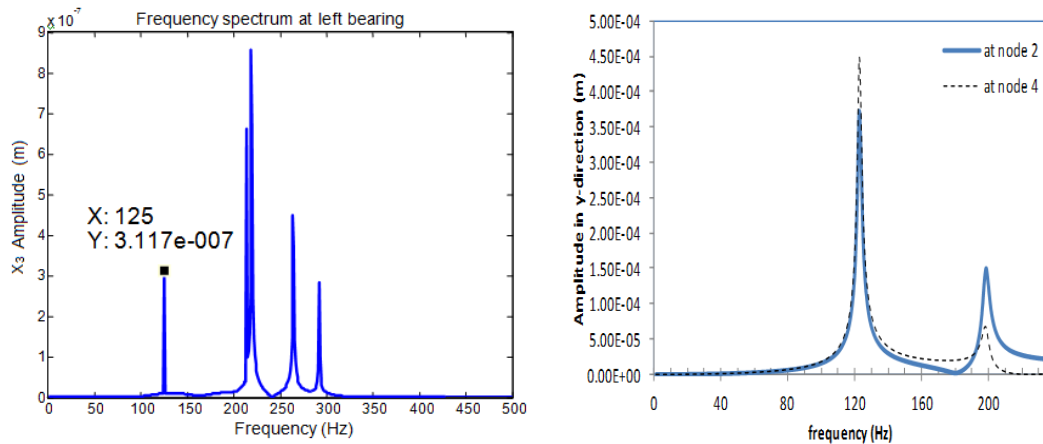
(a) Present program (ξ=0.001)   (b) ANSYS harmonic analysis

Figure 6.11: Unbalance response due to forces at all discs

Effect of multi-frequency unbalance forces on the dynamic response is in good agreement for this linear model indicating that the present code can be further used in nonlinear analysis. In above study, a speed-ratio of 1.5 is maintained.

For analyzing the rotor using 3-D modeling, the rotor configuration is developed in Ansys (as shown in Figure 6.12) and analyzed using 3-D solid elements (Solid 186-20

node element). At the bearing nodes, spring elements are considered. The above results are compared and there is a considerable coincidence of values.
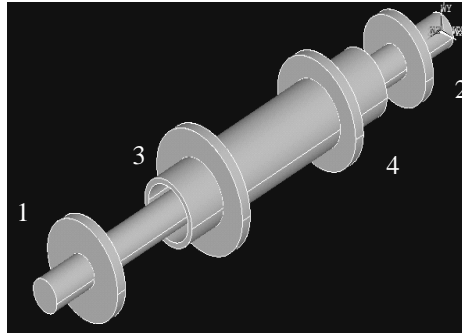
Figure 6.12: Two-spool rotors with compressor and turbine disks

The HP and LP stages are connected by means of intermediate bearing at node 4, the LP rotor supported at node 1 and node 2 and the HP rotor supported at bearing node 3 to the external stationary member.

6.3 Bearing nonlinear forces

Upon studying rotordynamic system using spring damper models, the finite element model of the rotor system is employed to study the effects of nonlinear bearing forces dynamic response of the system. There are four different case studies illustrated in order to understand the bearing parameter effects on dynamics. These are (i) Single row ball bearings (ii) Double row ball bearings (iii) Ball bearings with SFD (iv) Bearing fault modelling.

6.3.1 Single row ball bearing model

In order to illustrate the dynamics of single-row bearing, two cases are considered. In first case dual disk LP rotor and its experiment work is explained. This is followed by the numerical analysis if twin spool rotors. In addition to unbalance and gravity at the disks, the system is subjected to parametric bearing forces. Table 6.5 shows the bearing parameters considered in the analysis.

Table 6.5: Geometric details of ball bearing

Parameter	Dimension
Number of balls	8
Outer race radius(mm)	31.953
Inner race radius(mm)	20.046
Radial clearance (mm)	20e-3

(a) Dual disk LP rotor model

Unbalance response are studied at different speeds of operation, bearing contact stiffness values and radial clearances. Initially, a contact stiffness of k_b=3.527×10^9 N/m$^{3/2}$ is employed to know the effect of operating speeds on the unbalance response. A part of Matlab code for computing the ball bearing forces is given below.

Model code: Ball bearing force

```
R=31.953e-3;r=20.04681e-3;rc=20e-6;c1=3.527e9;Nb=8;
rb=(R-r-rc)/2;wc=r*omga/(R+r);
Fby1=0;Fbz1=0;
Fby2=0;Fbz2=0;
 for j=1:Nb
   th=wc*t+2*pi*(j-1)/Nb;
   y1=xx(6)+(r+2*rb)*sin(th);
   z1=xx(6)+(r+2*rb)*cos(th);
   delta1=sqrt(y1^2+z1^2)-R;
     if delta1>0
     Fby1=Fby1-c1*delta1^1.5*sin(th);
     Fbz1=Fbz1-c1*delta1^1.5*cos(th);
   else
     Fby1=Fby1;
     Fbz1=Fbz1;
    end
   end
```

Finite element model is used in the modelling of the rotor bearing system. By considering the rotor and disk configurations to be same as earlier LP rotor, replacing the spring model with bearing contact forces some studies are carried out first. Rayleigh's material damping parameters α=0.1485 and β=8.242×10^{-6} are considered in the analysis for computing the proportional damping matrix.

Figure 6.13-Figure 6.16 shows the effect of operating speeds on dynamic response, time histories and FFT plots in each case are obtained to analyse the system behaviour.
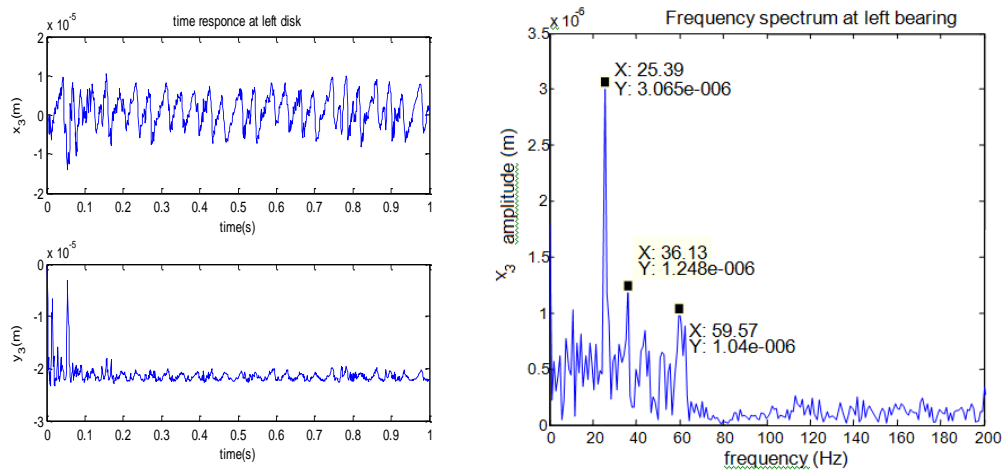
Figure 6.13: Time-response and frequency plot at the left bearing (500 rpm)
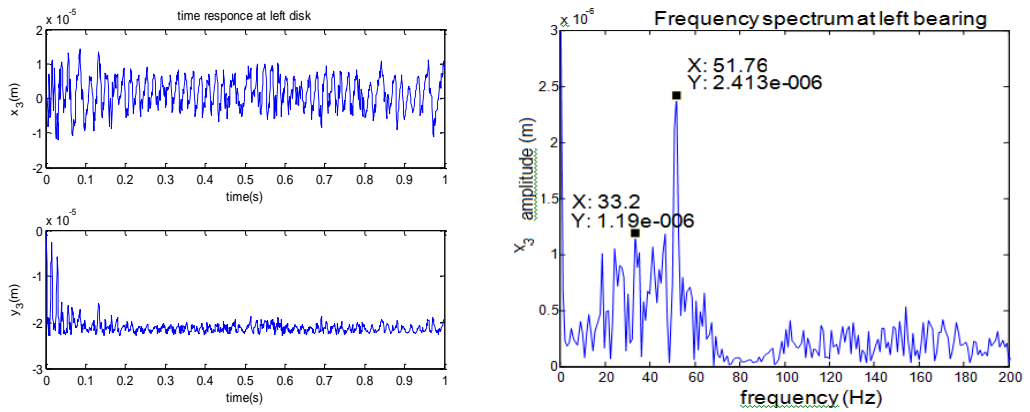
Figure 6.14: Time-response and frequency plot at the left bearing (1000 rpm)
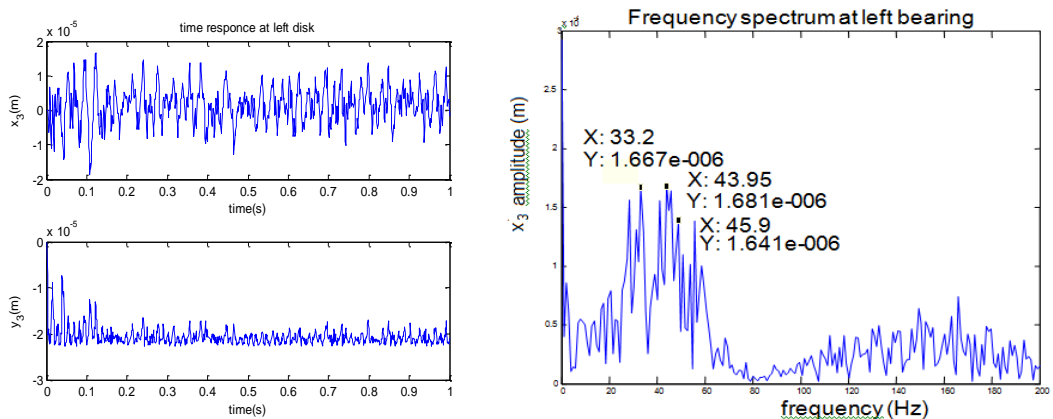
Figure 6.15: Time-response and frequency plot at the left bearing (1500 rpm)
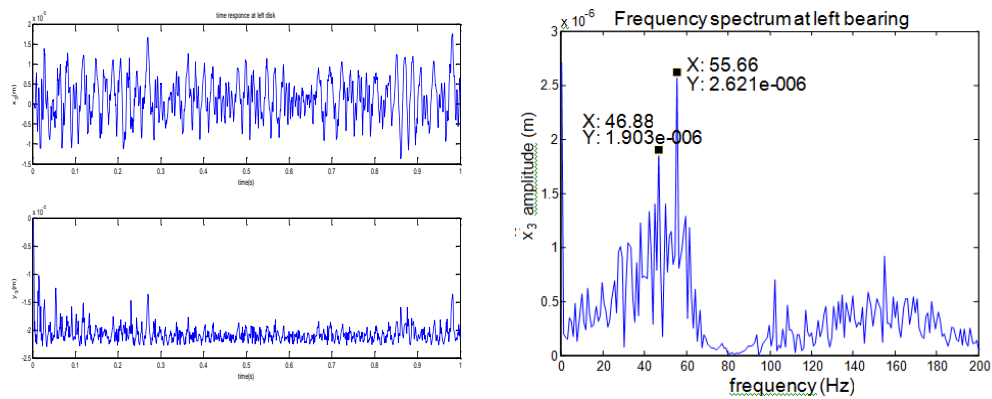
Figure 6.16: Time-response and frequency plot at the left bearing (2000 rpm)

It is seen from FFT plots that as the speeds increase from 500 to 2000 rpm, the peak resonance mode shifts from 25 Hz to 55Hz except at 1500 rpm where-in there is no appreciable peak observed. The effect of speed on stability of rotor is a highly nonlinear problem well studied in open literature. The stability at different operating speeds depends on the system rigidity and the stiffness. It can be observed that as the speed increases the frequencies are also increases as shown above.
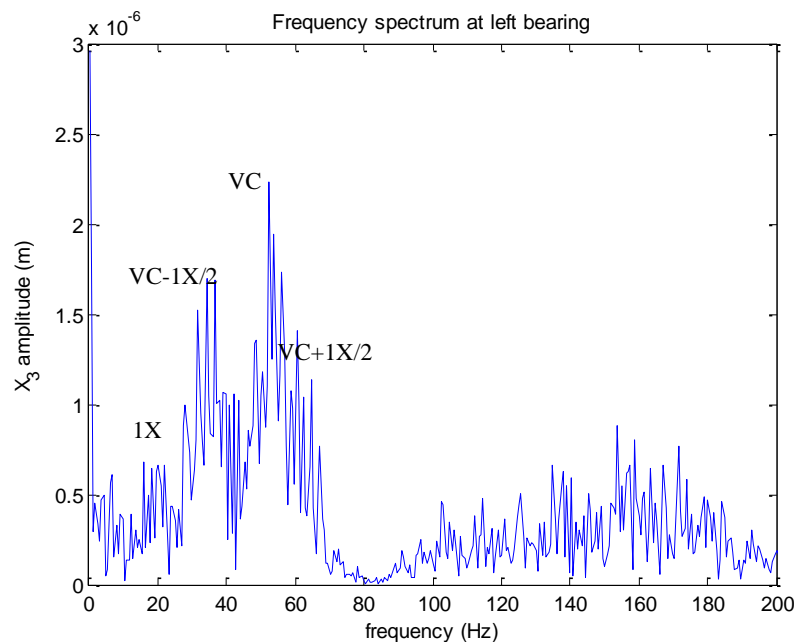
Figure 6.17: Frequency response of a single row ball bearing at a speed of 2000rpm

At a period of 2000 rpm, the presence of both the rotational speed (33Hz) and the varying compliance frequency (58Hz) are seen in the frequency spectrum and also interaction of these two frequencies produce sum and difference combination frequencies shown in Figure 6.17.

As another parameter of study, the contact stiffness between the ball and races is varied from 3.527×10^7 to 3.527×10^0 in three levels and are shown in Figure 6.18-Figure 6.20. These corresponds to rotor speed of 2000 rpm and $r_c = 20$ μm.
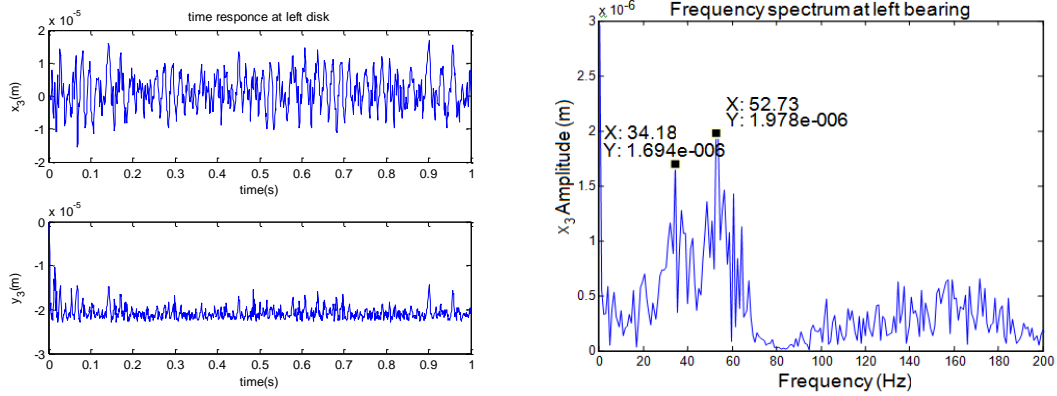
Figure 6.18: Time responses and FFT plot at left bearing (k_{bc}=3.527e7 N/m$^{1.5}$)
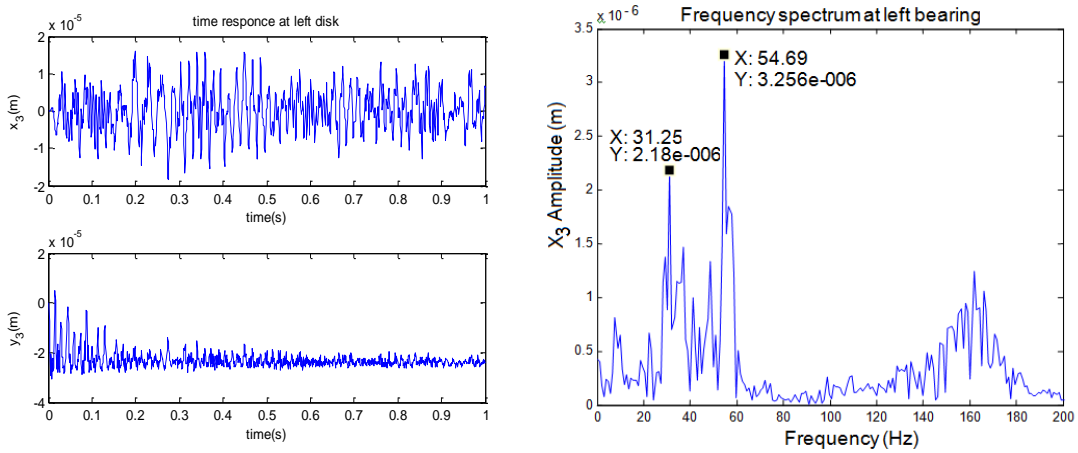
Figure 6.19: Time responses and FFT plot at left bearing (k_{bc}=3.527e8 N/m1.5)
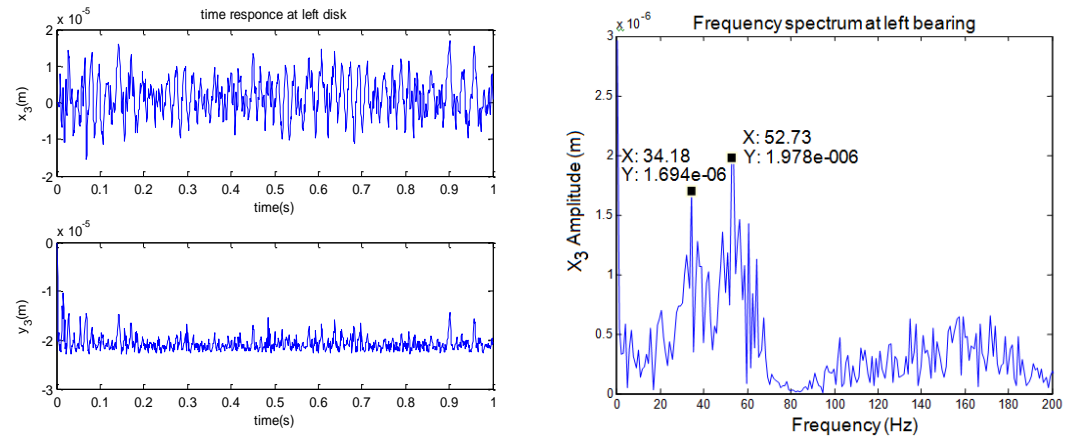
Figure 6.20: Time responses and FFT plot at left bearing (k_{bc}=3.527e9 N/m1.5)

As the contact stiffness k_{bc} depends on the geometric and material parameters of races, in practice, its value is required to be correctly predicted while designing a rotor bearing system. The stiffness of the system purely depends on the support bearings. The ball contact angular position is responsible for the stiffness of the system. As the contact stiffness increases the critical speeds also increases. From the above plots it can be clearly observed that, increase in the first natural frequency levels. In general, the bearing contact stiffness is varying as the ball moves in the groove with different angular positions and contact locations.

Next effect of internal radial clearance of ball bearings is studied on the rotor response. Figure 6.21-Figure 6.23 shows the dynamic response at three different values of r_c. Here, speed N=2000 rpm and k_{bc}=3.527×10^9 N/m$^{1.5}$ are employed.
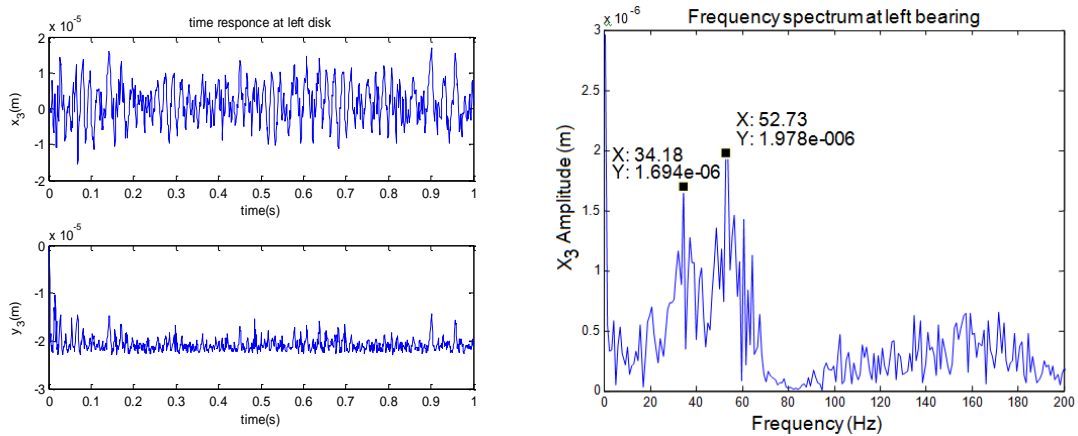
Figure 6.21: Time response and FFT plot at left bearing (r_c=20 μm)
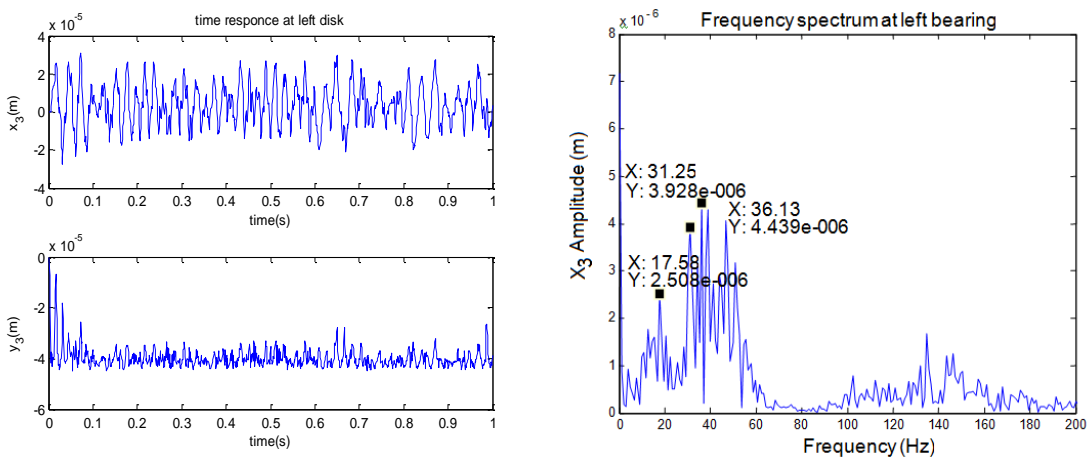
Figure 6.22: Time response and FFT plot at left bearing (r_c=40μm)

103
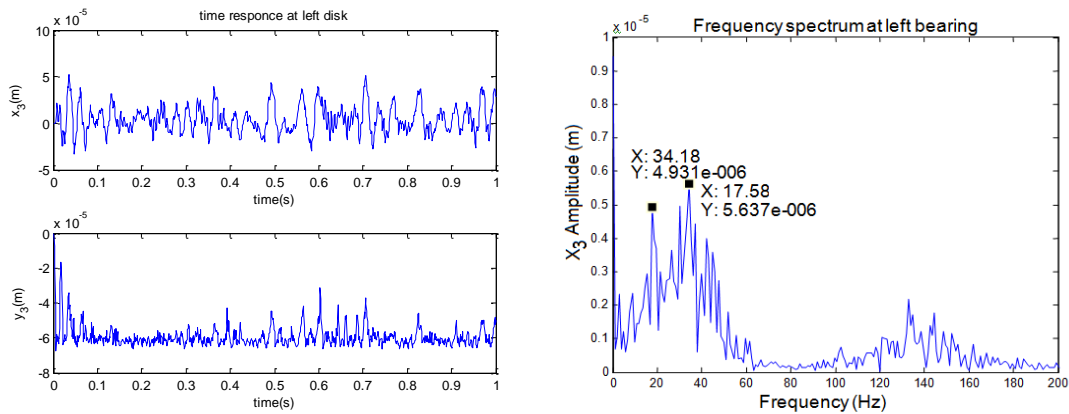
Figure 6.23: Frequency response of a left bearing at a rotor speed of 2000 rpm and at r_c=60e-6

Bearing radial clearance is the one of the key factors affecting the dynamic characteristics of the system responses. There is a significant influence of the bearing clearances on the overall dynamic characteristics of the rotor bearing system. From the above responses it is observed that as the radial clearance of ball bearings increases at the rotor support leads to decreases in the natural frequencies of the system which is also shown in the literature. From above plots, the maximum level of the amplitude and frequencies are recorded at different radial clearances. At the radial clearances r_c=20, 40 and 60μm the corresponding frequencies are 53.73Hz, 36.13Hz and 34.18 Hz. The critical speeds decreasing as the radial clearances increase in the system.

The single ball bearing forces are modelled by using lumped parameter modelling and the following Figure 6.24- Figure 6.28 shows the comparative frequency responses at the left bearing node when the rotor is operating at four different speeds (500, 1000, 1500 and 2000 rpm), the bearing radial clearance (r_c) is 20e-6 and the rolling element bearing contact stiffness is taken c_1=3.527e9. The masses of the disks are m_{D1}=4; m_{D2}=6 and the mass of the left bearing m_{B1}=0.25 and right bearing m_{B2}=0.25 and the stiffnesses of the shaft, bearing and the disk are k_{s1}=1e6, k_{s2}=0.25e6 and k_{s3}=2e6 respectively.
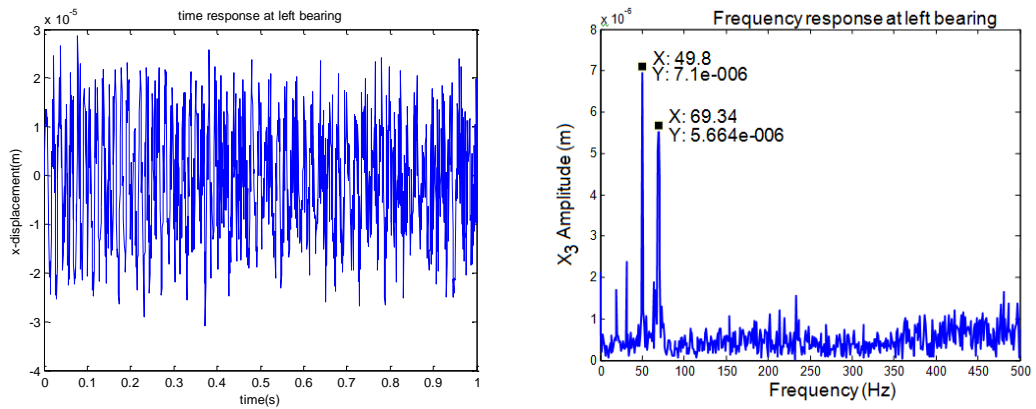
Figure 6.24: Time History and FFT at the left bearing at a rotor speed of 500 rpm
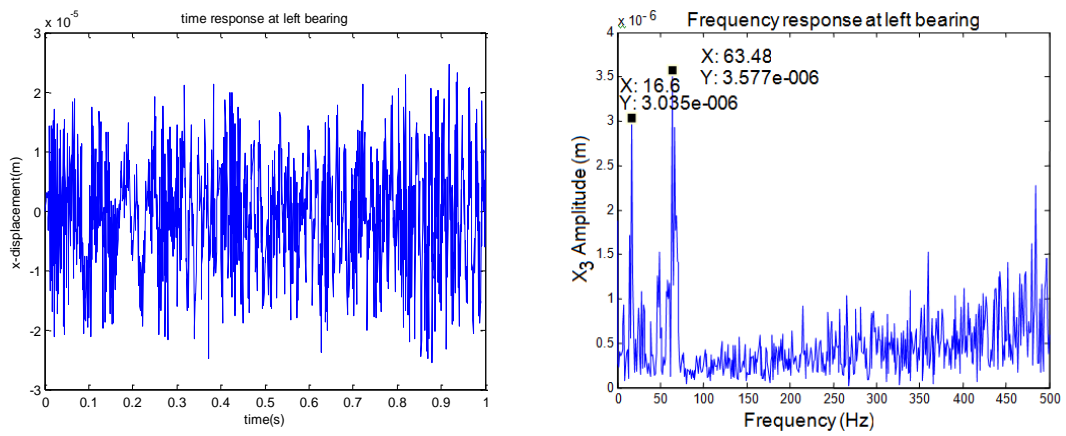
Figure 6.25: Time History and FFT at the left bearing at a rotor speed of 1000 rpm
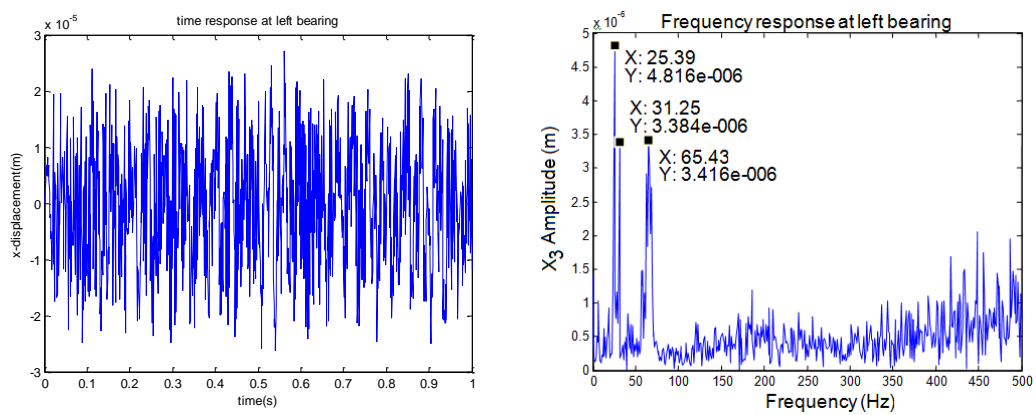
Figure 6.26: Time History and FFT at the left bearing at a rotor speed of 1500 rpm
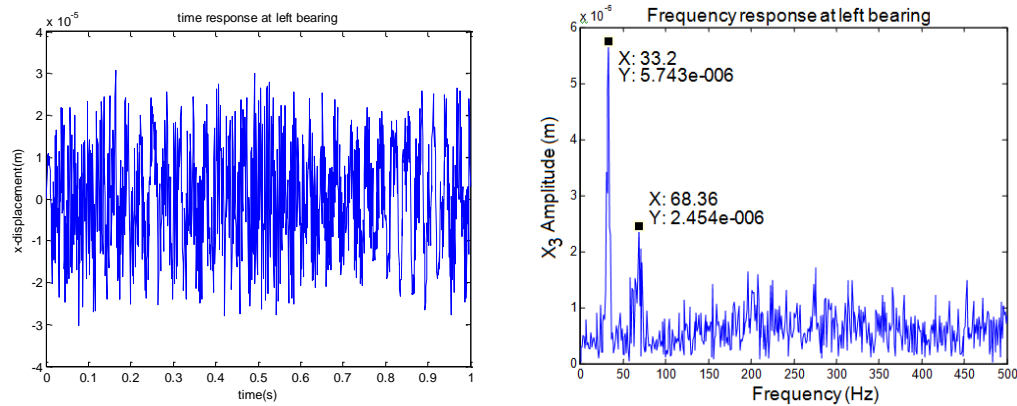
Figure 6.27: Time History and FFT at the left bearing at a rotor speed of 2000 rpm
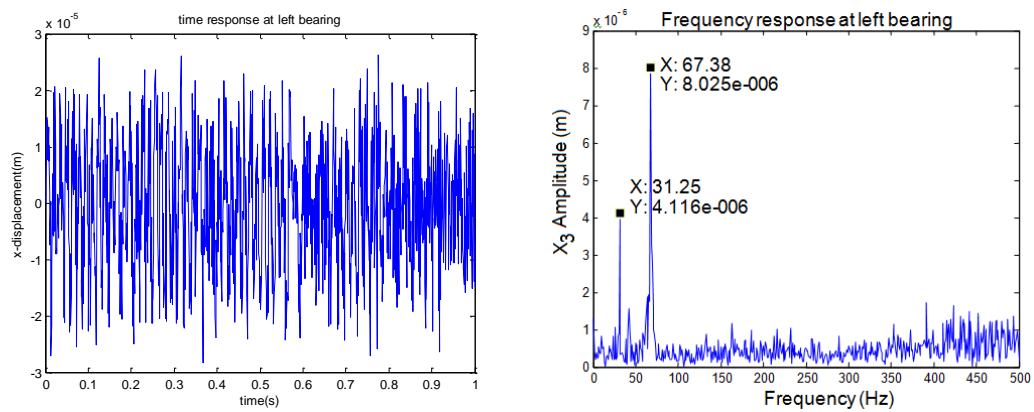
Figure 6.28: Time History and FFT at the left bearing at a rotor speed of 2500 rpm

It is seen from these simulations, as the speed increases amplitudes gradually increase along with formation of sub-harmonics and super-harmonics at the first mode of rotor found earlier. It is observed from above diagrams that both the time and frequency domains are sensitive to changes of the operational speeds.

(b) Experimental analysis

A scaled model of the rotor system is prepared for simulation. The compressor and the turbine are considered as disks installed on a rotor supported by ball bearings at the middle of the rotor.

A three phase AC induction motor was attached by coupling perfectly aligned to the rotor as shown in Figure 6.29 (a) and the schematic shown in Figure 6.29 (b). The dimensions of the rotor considered in present work are also shown.
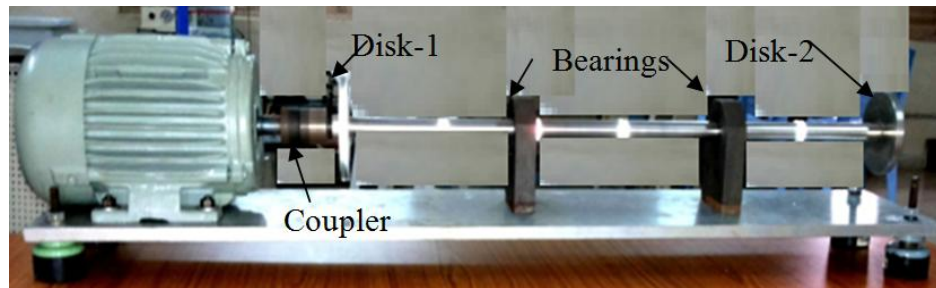
(a) Experimental set up
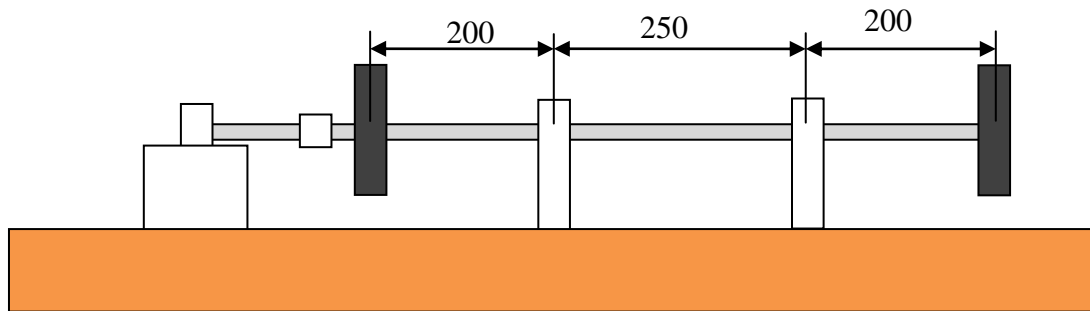
(b) Dimensional schematic

Figure 6.29: Experimental setup of a rotor with two discs

Technical specifications employed are as follows:

Three phase AC induction motor of 1HP power and 2820 rpm (Maximum speed), length of the shaft (L) = 650mm, diameter of shaft (d) = 20mm, Diameter of disc-1 (d_1) = 110mm, diameter of disc-2 (d_2) = 90mm, mass of disc-1(w_1) = 0.7kg, mass of disc-2(w_2) = 0.5kg, thickness of the discs = 10mm and the material is Aluminium alloy.

   A variable frequency drive is used to get different speeds of the rotor. Disk masses and diametral and polar moment of inertia of disks is computed based on diameter and thickness values.

   Modal analysis was carried out with an impact hammer having a load cell attached to its head and an output cable is connected to vibration analyzer through data acquisition (DAQ) system as shown in Figure 6.30.

   The laser-Doppler vibrometer, a precision optical transducer is used for determining vibration velocity and displacement at a fixed point. It has the specified velocity resolution of 0 to 22 kHz. The sampling frequency is set at 10 kHz during the experimentain and it is a single-point frequency analysis with VibSoft Data Acquisition Software. It calculates FFT with upto 12,800 lines of resolution and it can be extended resolution up to 8,19,200 lines. VibSoft Data processing exports data in ASCII and also provides direct access to binary data for processing in MATLAB and LabView using the PolyFile Access open data interface (Microsoft COM standard).
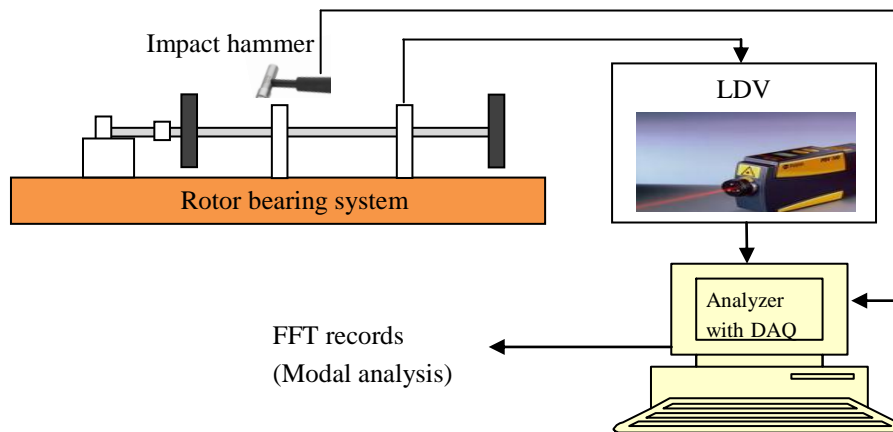
Figure 6.30: Experimental set up for Modal analysis

The impact generates an electric signal that is given to vibration analyzer with DAQ which analyzes the signal, compares with the signal received from Laser Doppler Vibrometer (LDV) focusing the laser beam at a point on the bearing location. Both force and response information are used to develop FRF (Frequency Response Function) and finally the natural frequencies of the structure are found.

In obtaining the response measurements along the rotor in all conditions, Polytec Laser Doppler Vibrometer (PDV-100) is employed (as shown in Figure 6.31) along with the post processing VibSoft software installed in a laptop. The acceleration, velocity and displacement histories are obtained in addition to their FFT plots at various locations along the shaft.

Figure 6.31: PDV-100 Portable Digital Laser Doppler Vibrometer

Table 6.6 shows the comparison between the experimental results of natural frequencies and in-house code values. It is seen from the table that, experimental values are matching closely to the results obtained from simulations in some modes.

Table 6.6: First five natural frequencies

S.No	Experimental	In-house code
1	23.42	24.56
2	40.98	-----
3	52.69	56.79
4	64.4	-----
5	81.97	87.42

Figure 6.32 shows the FRF plot obtained from the test, first five natural frequencies.
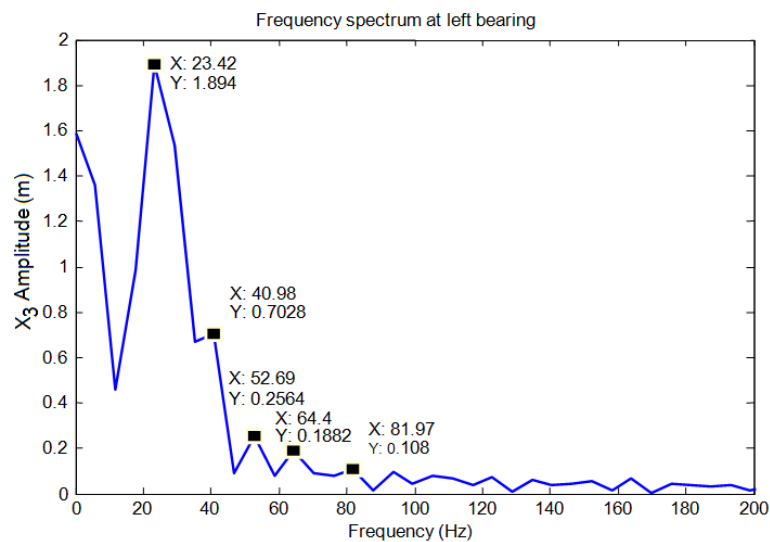
Figure 6.32: The FRF plot of modal test

In the next phase, a series of tests are carried out at variable speeds of the rotor in order to predict the response using LDV. Initially acceleration signals are obtained and the corresponding integrals namely velocity and displacement data are also recorded in the software and the data is imported into MS-Excel. The phase diagrams are then plotted. Figure 6.33-Figure 6.37 shows the FFT response and phase plane diagrams at different rotational speeds of the rotor from 500 rpm -2500 rpm taken at left bearing.
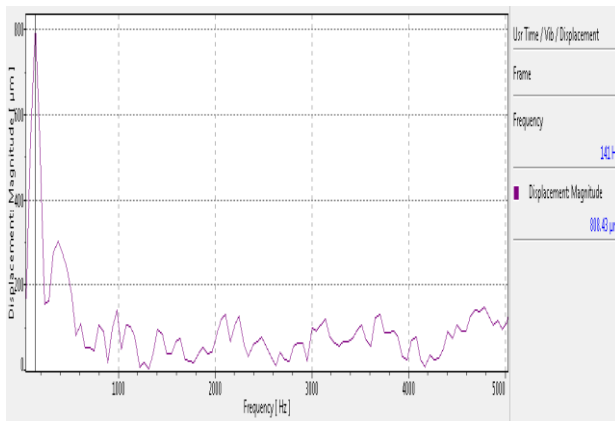
(a) Displacement FFT plot
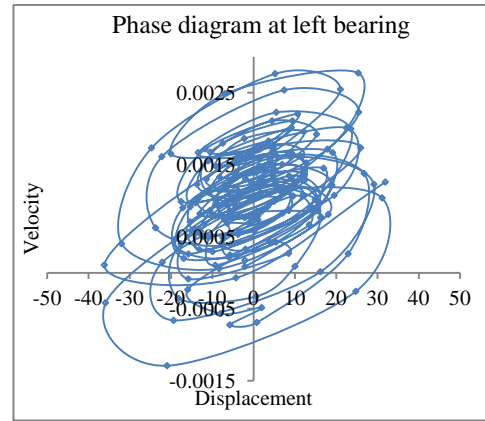
(b) Experimental Phase diagram

Figure 6.33: Records at left bearing (500rpm)
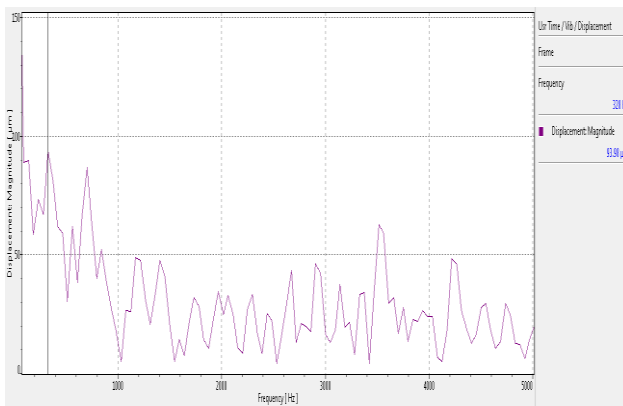
(a) Displacement FFT plot
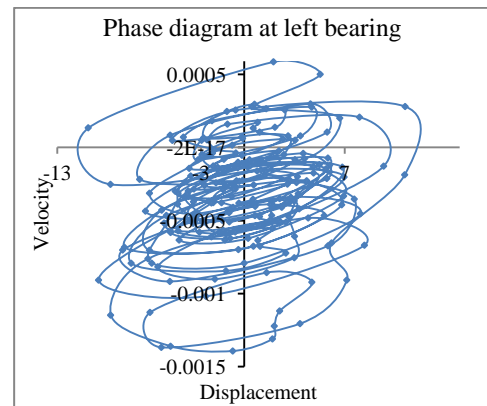
(b) Experimental Phase diagram

Figure 6.34: Records at left bearing (1000rpm)
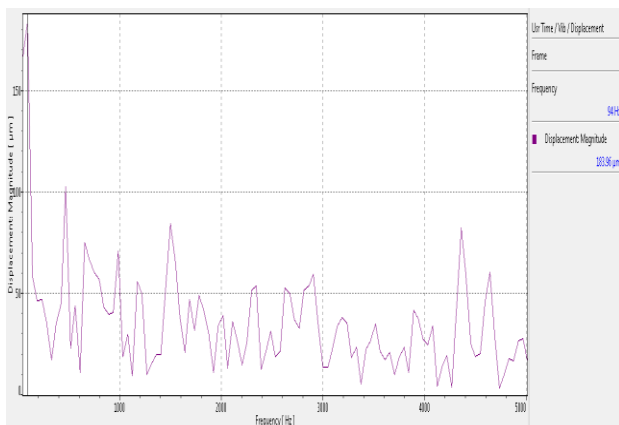
(a) Displacement FFT plot
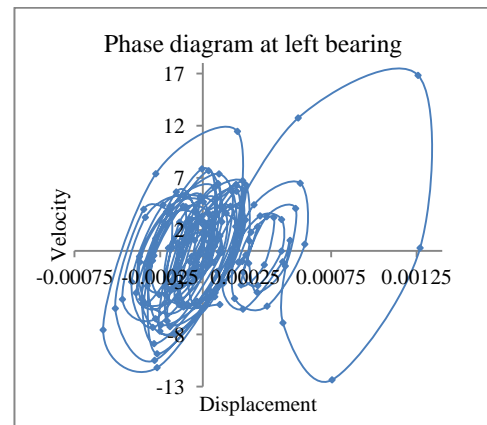
(b) Experimental Phase diagram

Figure 6.35: Records at left bearing (1500rpm)

(a) Displacement FFT plot   (b) Experimental Phase diagram
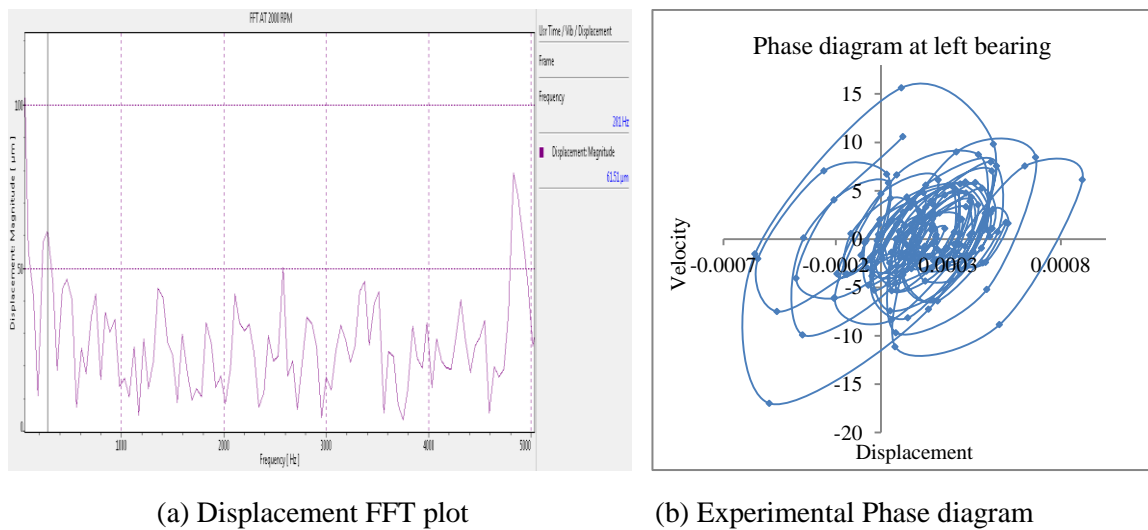
Figure 6.36: Records at left bearing (2000rpm)

(a) Displacement FFT plot   (b) Experimental Phase diagram
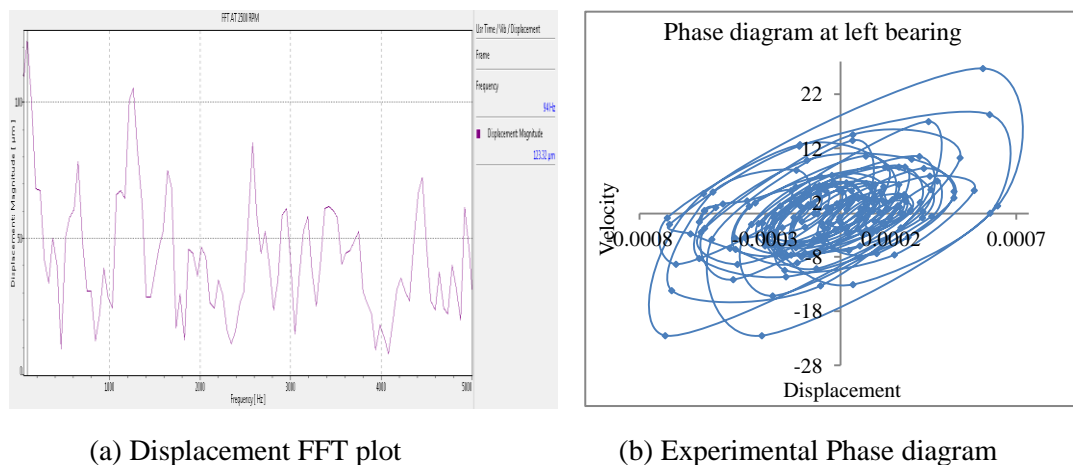
Figure 6.37: Records at left bearing (2500rpm)

The quasi periodic motions are identified from the projections of phase trajectories and FFT plots. The fractal structure is observed in the phase trajectory projections at the lower operation speeds (500 rev/min) and as speed increases the motion leads to more chaotic motion to chaotic motion and then stability motion.

As the next case, the experimental studies were conducted at a fixed speed of the rotor at 2000rpm and the laser was focused at different node locations along the rotor length and the FRF response using LDV with inbuilt Vibsoft software are plotted. Figure 6.38 (a)-(e) shows the FFT response at different nodes along the length.
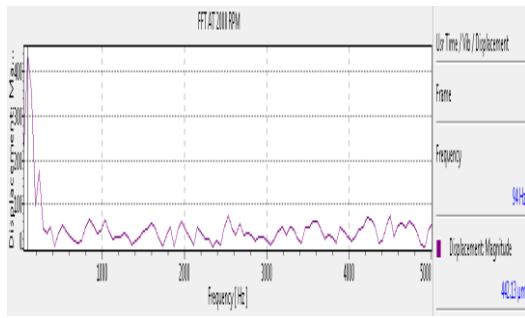
(a) Node 1
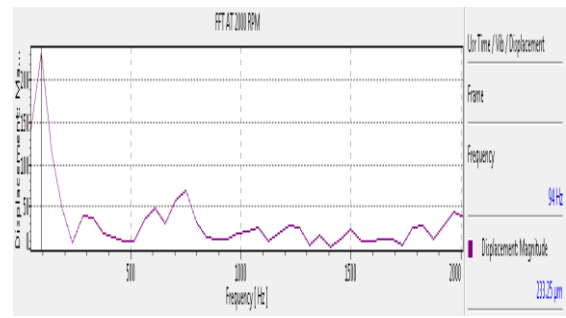
(b) Node 2
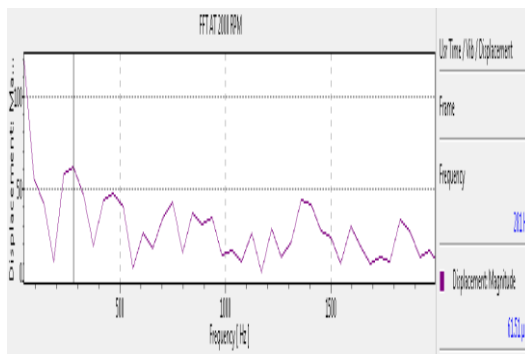
(c) Node 3
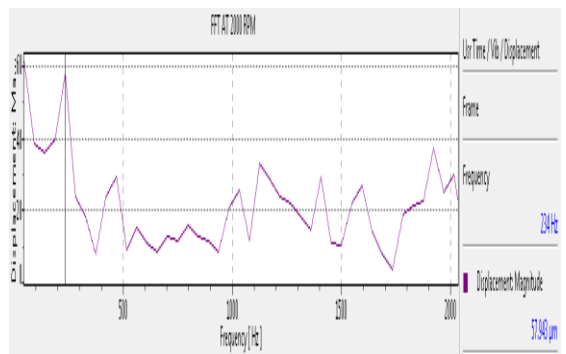
(d) Node 4
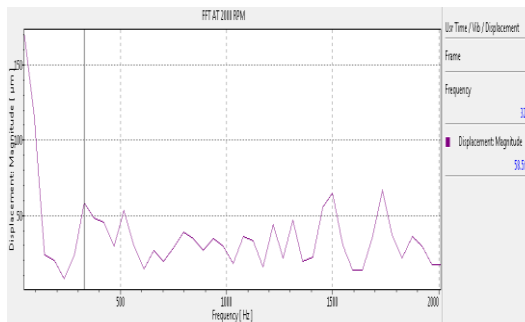
(e) Node 5
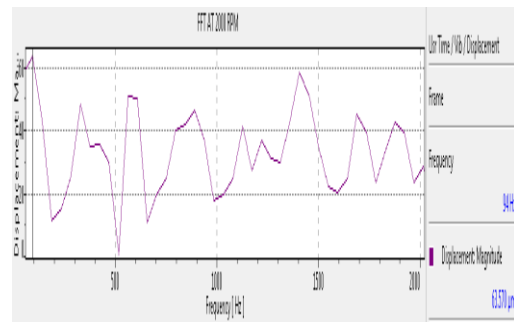
(f) Node 6
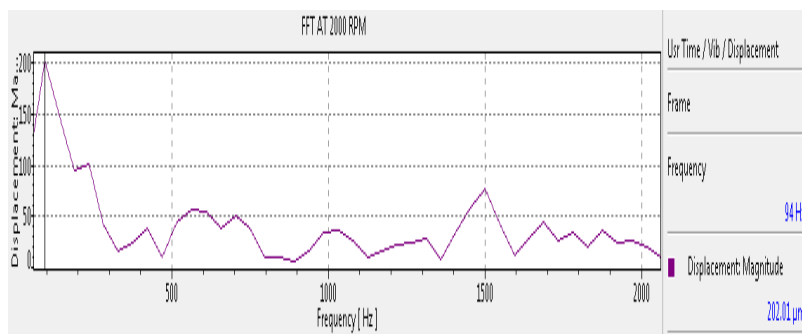
(g) Node 7

Figure 6.38: The FRF response at different nodes along the length

The responses of the rotor are shown in the form of FFT plots at a constant rotating speed along the length of the rotor at seven nodal positions. At bearing nodes 3 and 5, the frequency lower than other nodes due to rigidly supported by bearings and other nodes the frequency values are increased due to the boundary conditions.

(c) Twin spool

Bearing force effect is now illustrated with a twin spool rotor.

Speed ratio: An Aero-engine twin-spool rotor, consisting of high pressure and low pressure spools operating coaxially at different speeds. There is a fixed ratio of speeds to the high pressure spool to the low pressure spool. By rotating the model at different speed ratios, time response at the LP disk and HP disk and FFT are shown in Figure 6.39-Figure 6.44.
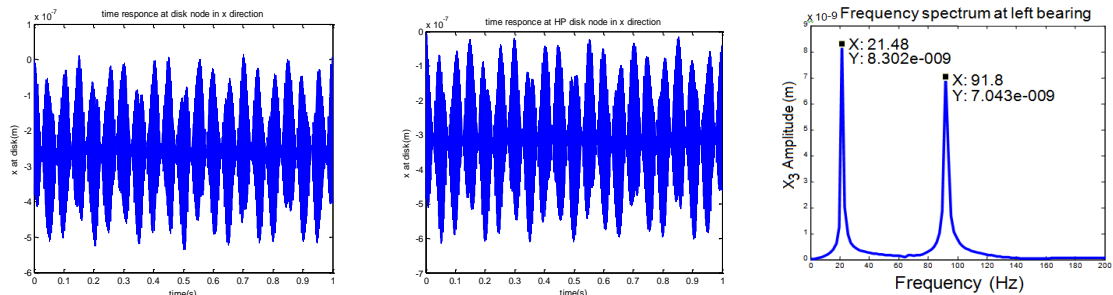
Figure 6.39: Time response at LP disk, HP disk and FFT at left bearing at a speed ratio of 1
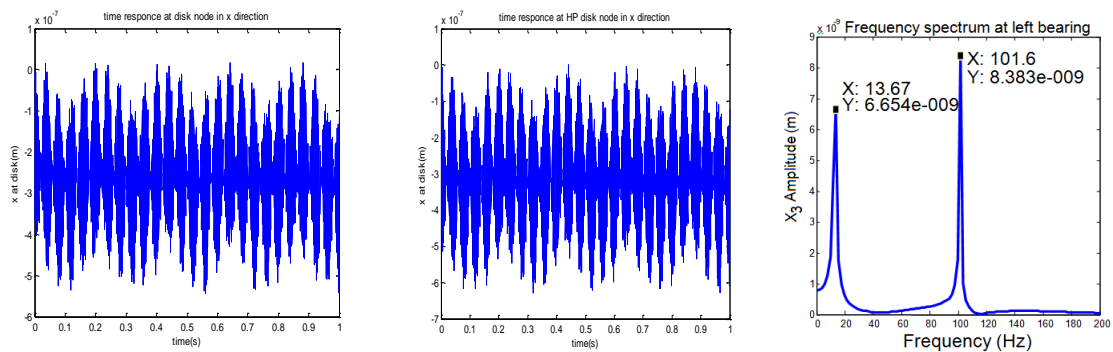
Figure 6.40: Time response at LP disk, HP disk and FFT at left bearing at a speed ratio of 1.5
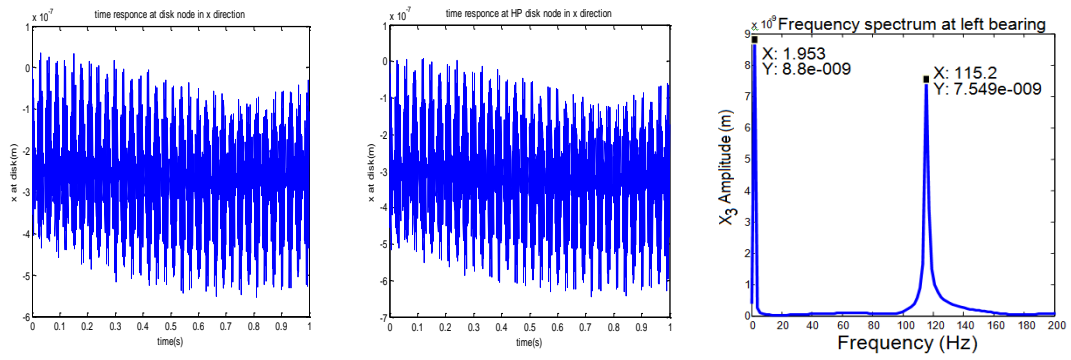
Figure 6.41: Time response at LP disk, HP disk and FFT at left bearing at a speed ratio of 2
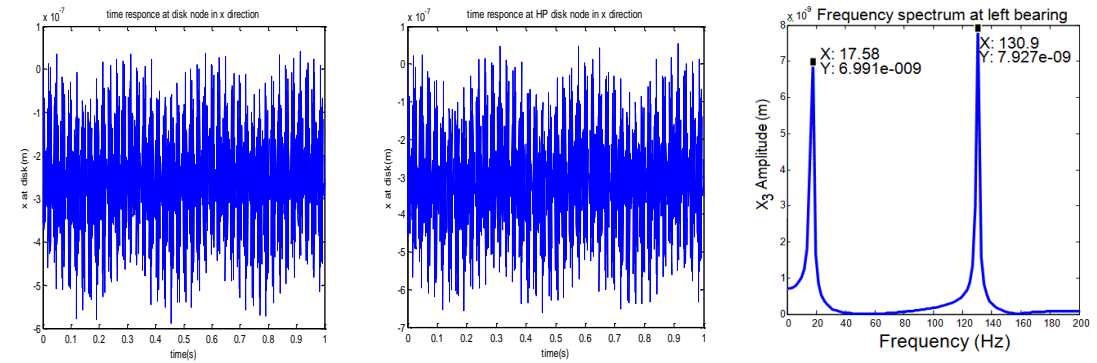
Figure 6.42: Time response at LP disk, HP disk and FFT at left bearing at a speed ratio of 2.5
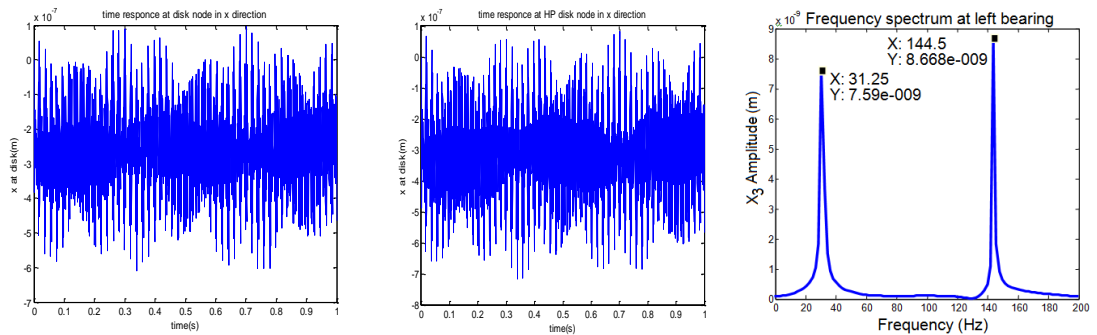
Figure 6.43: Time response at LP disk, HP disk and FFT at left bearing at a speed ratio of 3
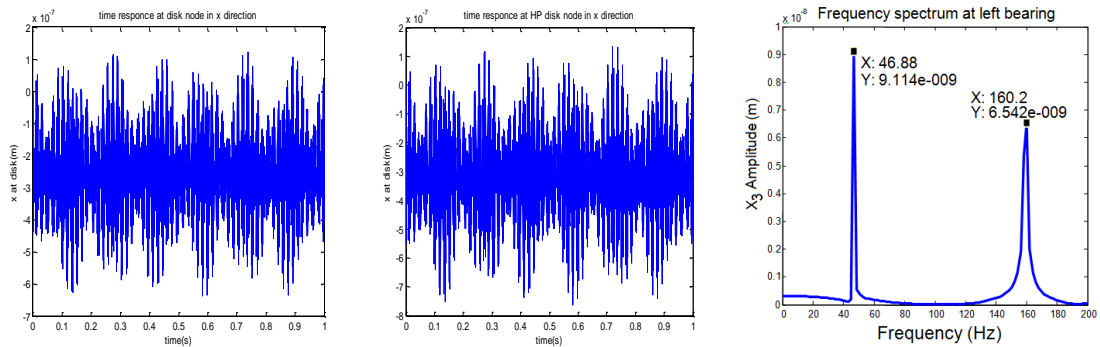
Figure 6.44: Time response at LP disk, HP disk and FFT at left bearing at a speed ratio of 3.5

From above responses it is observed that there is a significant influence of the spool speed ratios in the overall dynamics of the rotor system. Figure 6.44 shows the unbalance responses at the left bearing node, it is seen that due to multi-frequency unbalance forces, the response is shooting-up to a very high value. It is seen that there is a marked difference in amplitudes. As the speed ratio increases the frequency domain values are increasing. The LP rotor speed is fixed at 2000 (Rev/min) and the HP rotor speed is increasing with increasing the speed ratio. The responses are recorded at both LP and HP disks.

6.3.2 Double row ball bearing force modelling

For implementing the solution methodology, six second-order equations are decomposed into state-space form and the program is implemented such that in each time interval, the time dependant bearing forces and disc unbalance excitations are evaluated by separate function. Table 6.7 shows the dimensional parameters of the rotor-bearing system employed in present work for computation of dynamic response.

Table 6.7: Parameters of rotor-bearing system.

Parameter	Value	Parameter	Value
r_i	40 mm	K_b	13.34×10^9 N/m$^{3/2}$
r_o	64 mm	e	18.2mm
N_b	8	$\beta_x=\beta_y$	0
r_c	20 μm	A_0	0.65 mm

All the initial conditions are set close to zero and back to back configuration is considered in order to illustrate the effect of double-row bearing. The programs are simulated in a Matlab R2009a version software in Dell 2GB ram laptop. A part of Matlab code for computing the double row ball bearing forces is given below.

Model code: Double row ball bearing forces

```
    Fby1=0;Fbz1=0;
    Fby2=0;Fbz2=0;
    r=40e-3;R=64e-3;
    Nb=8;rc=20e-6;cb=13.34e9;g=9.81;
    wcage=omga*(r/(R+r));
     dz=18.20e-3;
     betax=0; betay=0;
     A0=0.65e-3; %unloaded distance between inner and outer race curvature centres%
     rb=(R-r-rc)/2;
     alpa=pi/6;%acos(1-rc/(r+R-2*rb)); %%35*pi/180;%unloaded contact angle%
     delz0=0;z=0;
    for i=1:2
      if i==1
         mu1=-1;
         nu=1;%back to back configuration%
      else
         mu1=1;
```

```
    nu=-1;
  end
  for j=1:Nb
    X2=xx(5);Y2=xx(6);
    X3=xx(9);Y3=xx(10);
    th1=wcage*t+(2*pi/Nb)*(j-1);
    X2d=X2+mu1*dz*betay;
    Y2d=Y2-mu1*dz*betax;
    X3d=X3+mu1*dz*betay;
    Y3d=Y3-mu1*dz*betax;
    delr1=(X2d*cos(th1)+Y2d*sin(th1)-rc*1e-3);
    delr2=(X3d*cos(th1)+Y3d*sin(th1)-rc*1e-3);
    delrstar1=delr1+A0*cos(alpa);delrstar2=delr2+A0*cos(alpa);
    delz1=z+(rb+r)*(betax*sin(th1)-betay*cos(th1));
    delz2=delz1;
    delzstar1=delz1+nu*(A0*sin(alpa)+delz0);
    delzstar2=delzstar1;
    alpa1=atan(delzstar1/delrstar1);%loaded contact angle%%
    alpa2=atan(delzstar2/delrstar2);%loaded contact angle%%
        Ab1=sqrt(delzstar1^2+delrstar1^2);
        Ab2=sqrt(delzstar2^2+delrstar2^2);
    del1=Ab1-A0;del2=Ab2-A0;
    if del1>0
      H1=1;
    else
     H1=0;
    end
    Fbz1=Fbz1-cb*del1^(3/2)*H1*cos(th1)*cos(alpa1);
    Fby1=Fby1-cb*del1^(3/2)*H1*sin(th1)*cos(alpa1);
        if del2>0
      H2=1;
    else
     H2=0;
    end
    Fbz2=Fbz2-cb*del2^(3/2)*H2*cos(th1)*cos(alpa2);
    Fby2=Fby2-cb*del2^(3/2)*H2*sin(th1)*cos(alpa2);
      end
      end
```

By considering the rotor and disk configurations to be same as earlier LP rotor, replacing the spring model with bearing contact forces some studies are carried out first. Rayleigh's material damping parameters $\alpha=0.1485$ and $\beta=8.242\times10^{-6}$ are considered in the analysis for computing the proportional damping matrix. Figure 6.45-Figure 6.47 shows the effect of operating speeds on dynamic response, time histories and FFT plots in each case are obtained to analyse the system behaviour
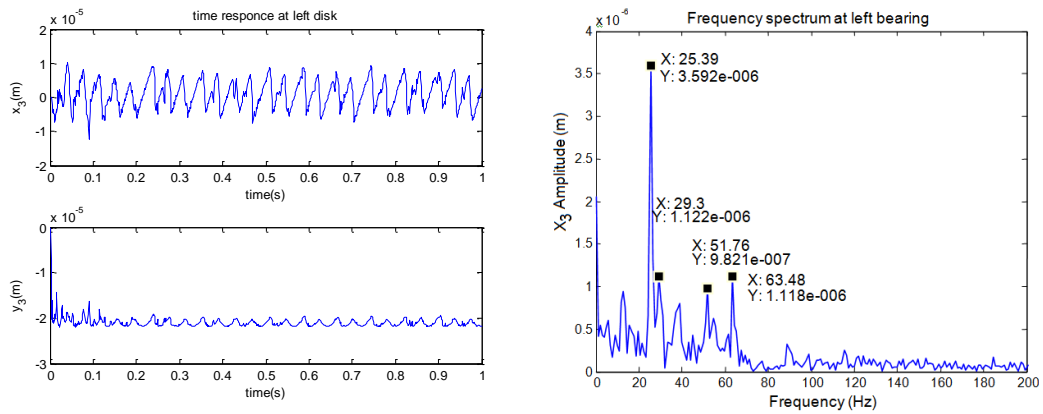
Figure 6.45: Plots of a left bearing at a rotor speed of 500 rpm, at r_c=20e-6
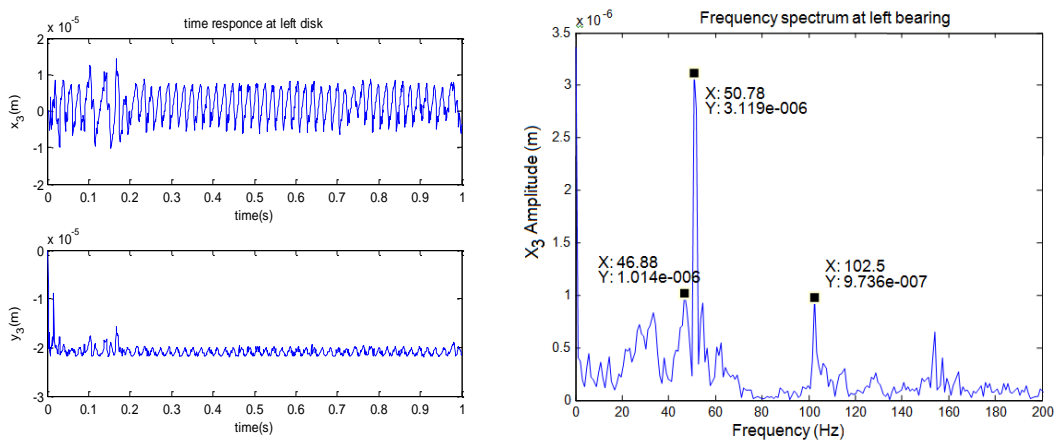
Figure 6.46: Plots of a left bearing at a rotor speed of 1000 rpm, at r_c=20e-6
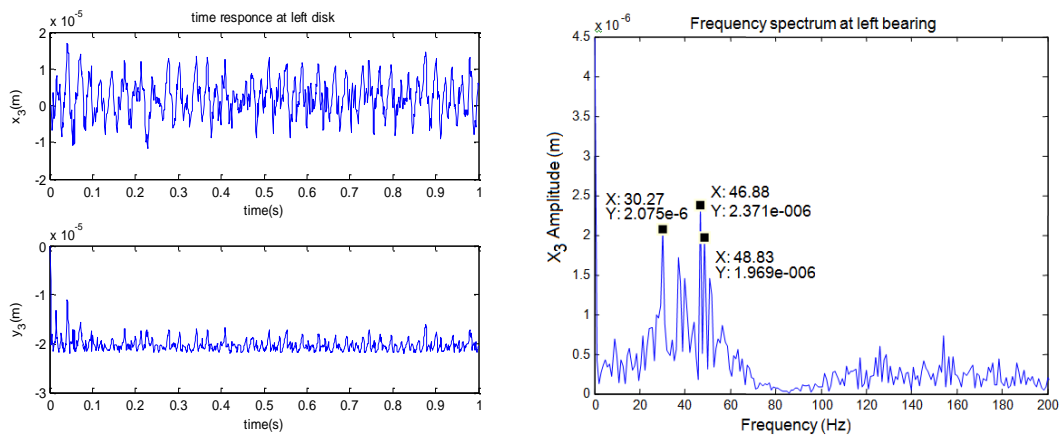

Figure 6.47: Plots of a left bearing at a rotor speed of 1500 rpm, at r_c=20e-6 m
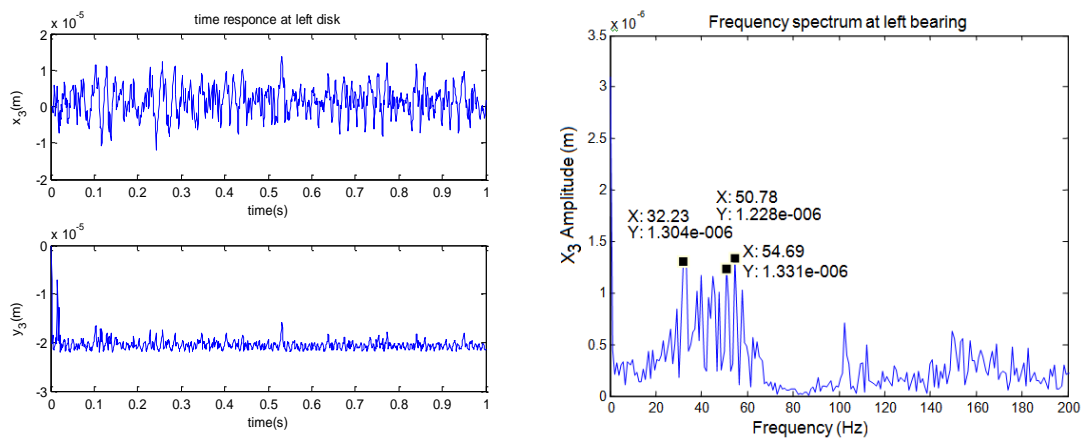
117

Figure 6.48: Plots of a left bearing at a rotor speed of 2000 rpm, at r_c=20e-6m

The vibration amplitude of the rotor increased with the increase of clearance, time and frequency domain projections becomes more and more complicated due to increase in rotating frequency of the rotor.

In the next simulation, the radial clearance of the bearing is varied in three steps (i.e 20e-6, 40e-6 and 60e-6mm) and the time histories and the Frequency responses are shown in the Figure 6.48-Figure 6.50.
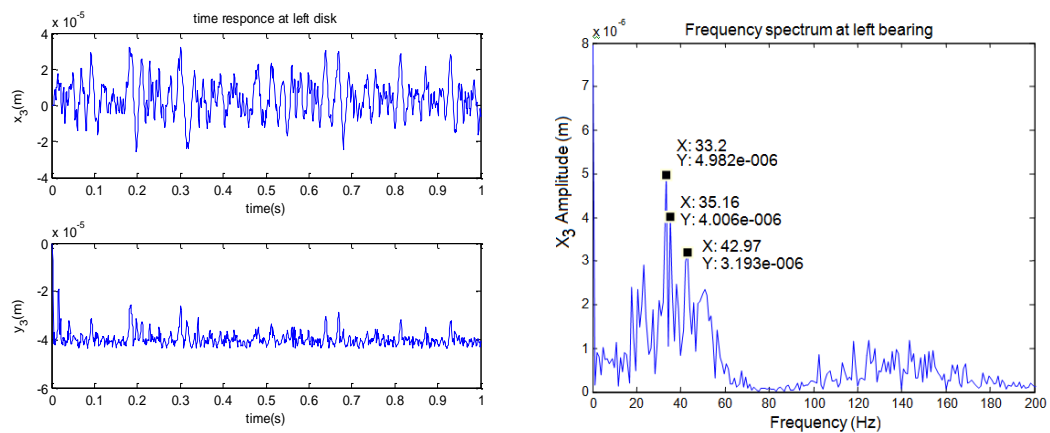
Figure 6.49: Plots of a left bearing at a rotor speed of 2000 rpm, at r_c=40e-6m

From the plots, it can be observed that the clearance of ball bearing plays very important role in the system life and this will increase the stiffness of the system.
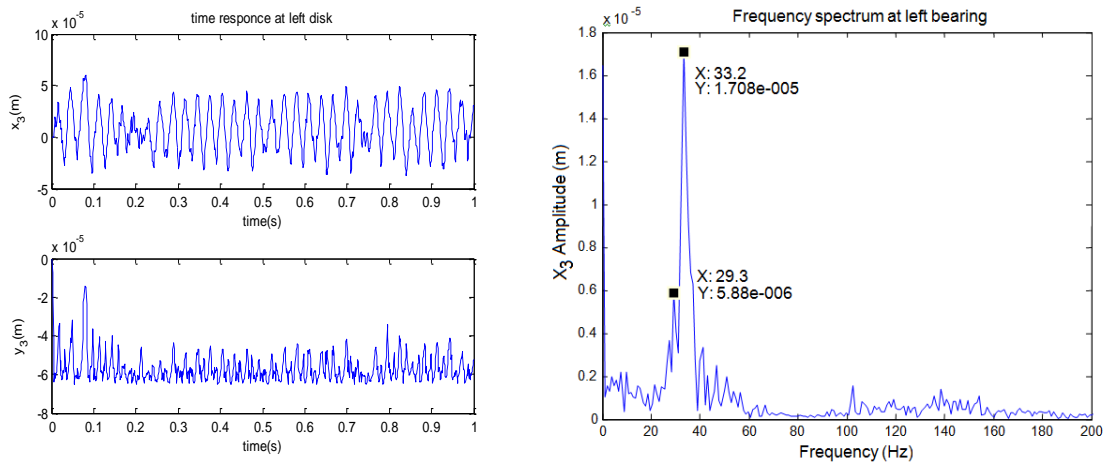
Figure 6.50: Plots of a left bearing at a rotor speed of 2000 rpm, at r_c=60e-6m

The radial clearance is an important parameter of study and the effect is studied in this section. For lower radial clearances, the lower amplitudes are identified. The super harmonics develops with the higher radial clearances. The reason behind this is the varying compliance frequency component develops strongly for higher internal clearances and it leads to higher values of amplitudes and frequencies

6.3.3 Single row with SFD Modelling

The nonlinear excitation force of squeeze film damper is introduced in the modelling. Generally the squeeze film dampers are lubricated elements providing viscous damping in the high speed engine rotors. To arrest the relative motion between the rotor and stator, a centralizing spring was used and different stiffness values of centralizing spring was studied.
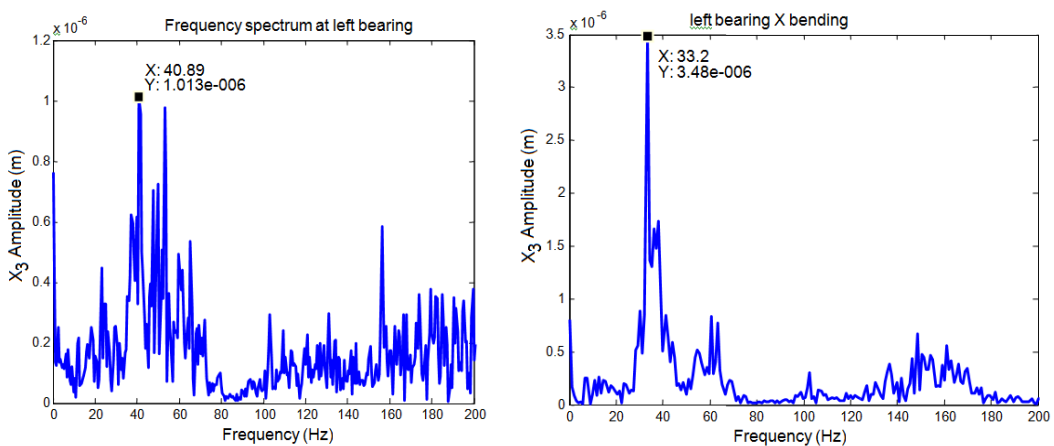
(a) No fault case   (b) with SFD force

Figure 6.51: Response of a single row ball bearing with and without SFD force (r_c=10e-6 mm)

Figure 6.51 shows the FFT responses of without SFD and with SFD modelling. The squeeze film dampers in high speed rotating engines reduce the amplitudes and also provide the required structural isolation to suppress the instability in the rotordynamic system.

Parametric studies are carried out at different stiffness values and various viscosity values. Figure 6.52-Figure 6.54 shows the responses at left bearing at a constant rotor speed of 2000 rpm and at centralizing spring stiffness of k_a=3e4, 3e5 and 3e6 respectively.
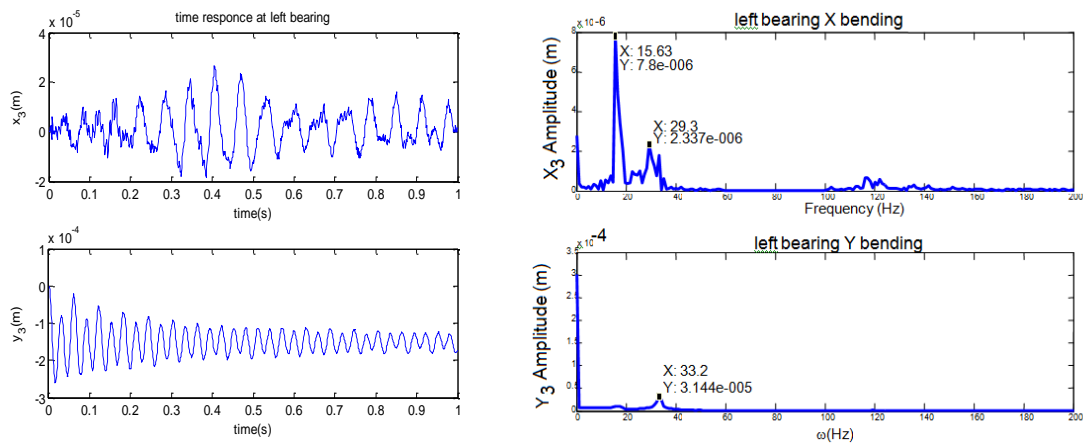
Figure 6.52: Responses at left bearing at a rotor speed of 2000 rpm and at k_a=3e4 N/m
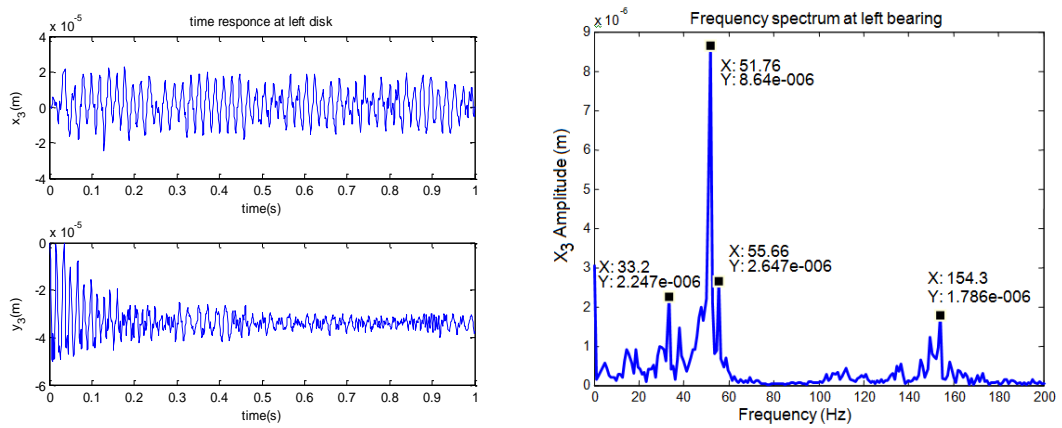
Figure 6.53: Responses at left bearing at a rotor speed of 2000 rpm and at k_a=3e5N/m
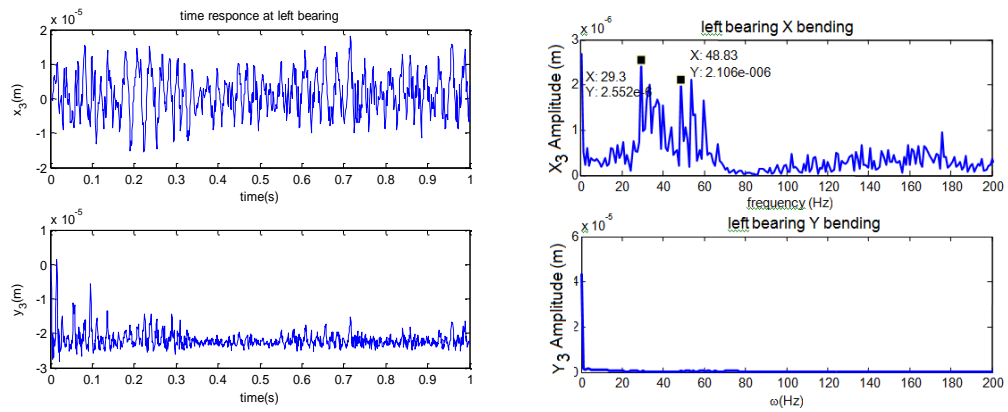
Figure 6.54: Responses at left bearing at a rotor speed of 2000 rpm and at k_a=3e6 N/m

The response of the system also studied of a LP rotor at different viscosity values as shown in Figure 6.55-Figure 6.57 . It can be observed above plots that the vibration energy dissipation as the amplitudes is decreasing as the stiffness values increasing and its leads to improve the dynamic stability.

These plots are taken at left bearing at a constant rotor speed of 2000 rpm and at different viscosity values of m_{u1}=2e-3,5e-3 and 10e-3 respectively.
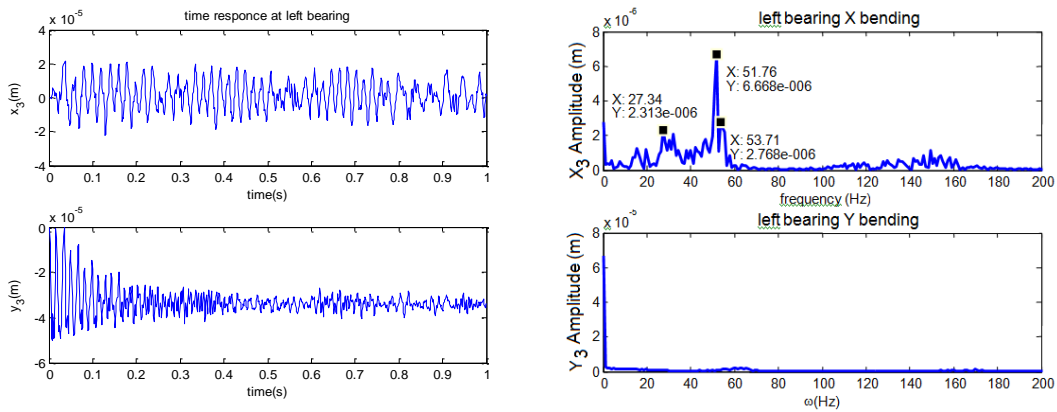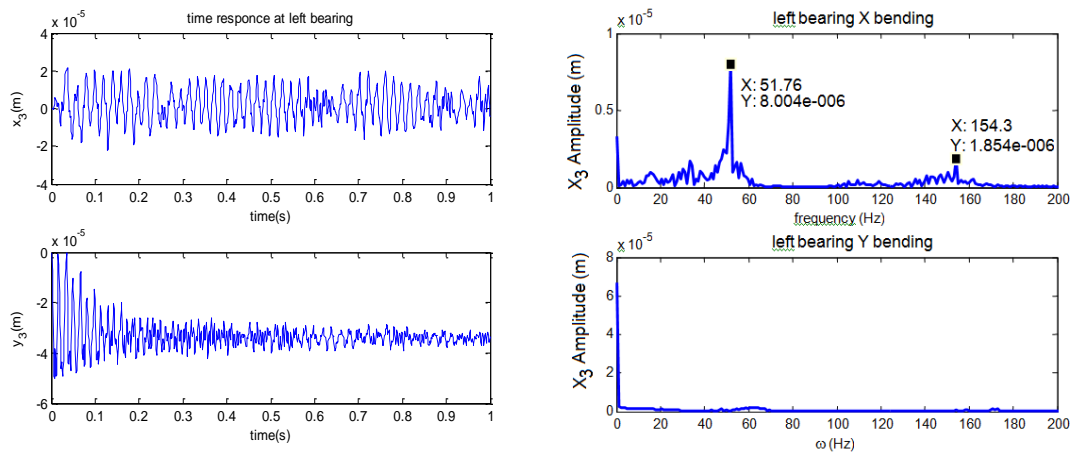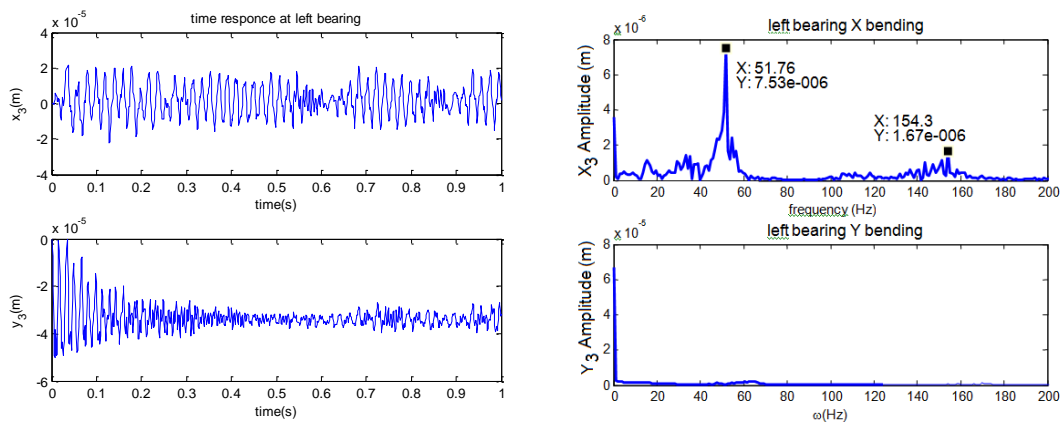

Figure 6.55: Responses at left bearing at m_{u1}=2e-3

Figure 6.56: Responses at left bearing at m_{u1}=5e-3

Figure 6.57: Responses at left bearing at m_{u1}=10e-3

The relative motion between the rotor and stator drags the lubricant by the aid of viscous forces into the converging gap between the moving and stationary surfaces. It is observed that at low viscous lubricants will lead to high frequencies. The effect of lubricant viscosity is mainly depends on the clearances between the surfaces in contact.

6.3.4 Ball bearings with faults

Two types of faults are found in the bearings as mentioned in the Chapter 3. Local and distributed faults are analyzed in the study. Frequency responses of inner and outer bearings at different waviness are plotted.

(a) Inner race waviness

Figure 6.58(a)–(c) shows FFT response of inner race waviness at different values of waviness configuration constant A=0.5e-6, 1e-6 and 1.5 e-6 m at a constant speed of 500rpm.
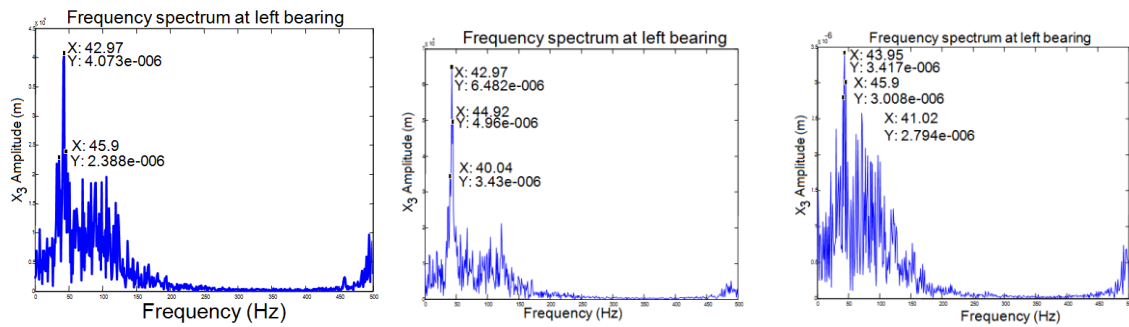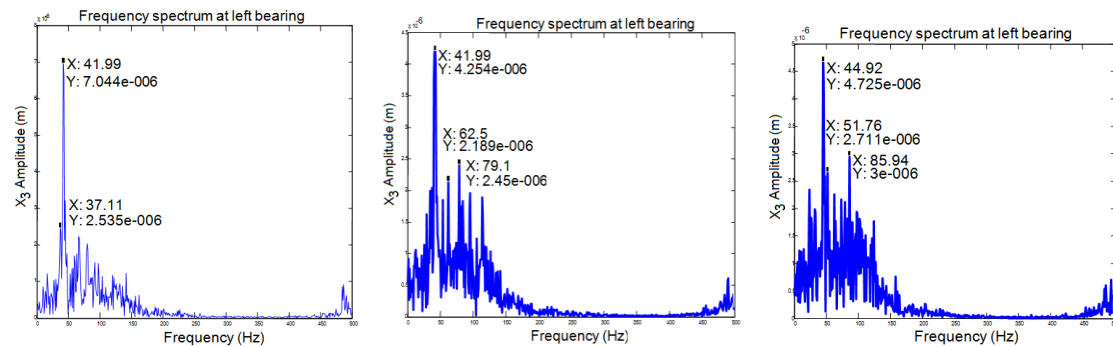
(a) A=0.5micron   (b) A=1micron   (c) A=1.5micron

Figure 6.58: Inner race waviness (m=1) on left bearing at a speed of 500 rpm
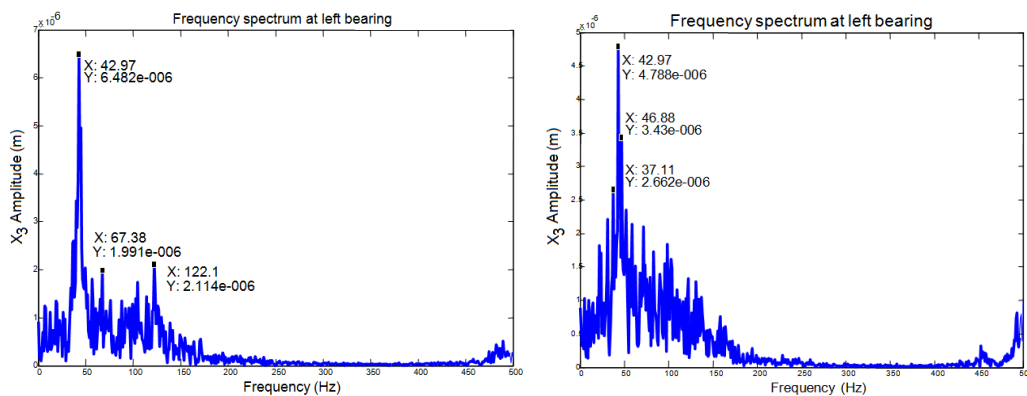
(b) Outer race waviness

Likewise, the effectiveness of this waviness on the outer race also considered and the responses are shown in the Figure 6.59(a)–(c) under same considerations.

(a) A=0.5micron   (b) A=1micron   (c) A=1.5micron

Figure 6.59: Outer race waviness (m=1) on left bearing at a speed of 500 rpm
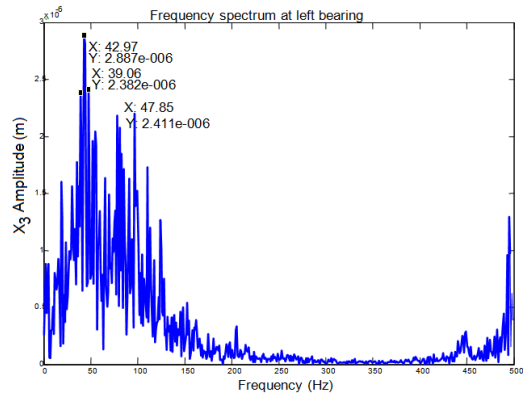
As the next phase of work, the effectiveness of the he waviness constant values (A=1) and (m=1) are studied at different speeds of the rotor and corresponding frequency responses are plotted from 500rpm - 2500 rpm as shown in Figure 6.60(a)–(e).

(a) At a rotor speed of 500 rpm   (b) At a rotor speed of 1000 rpm
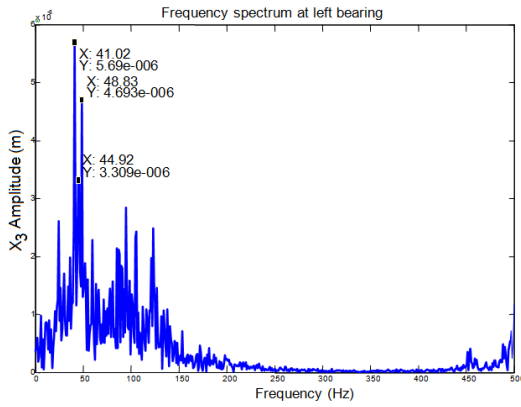
(c) At a rotor speed of 1500 rpm

(d) At a rotor speed of 2000 rpm

(e) At a rotor speed of 2500 rpm

Figure 6.60: Inner race waviness (A=1micron, m=1) on left bearing at different speeds

The frequency responses at outer waviness are plotted at different speeds of the rotor from 500rpm -2500 rpm as shown in Figure 6.61 (a) – (e).
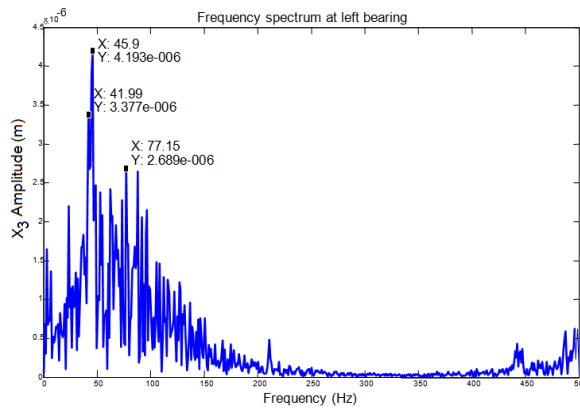

(a) At a rotor speed of 500 rpm

(b) At a rotor speed of 1000 rpm
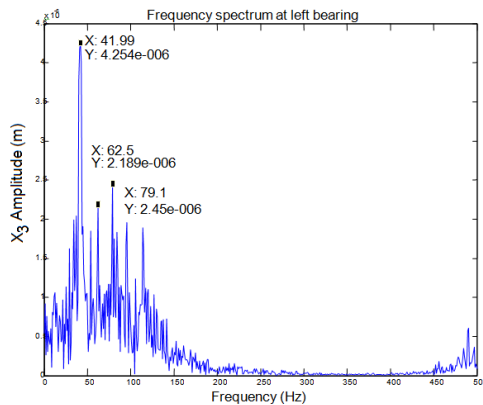
(c) At a rotor speed of 1500 rpm
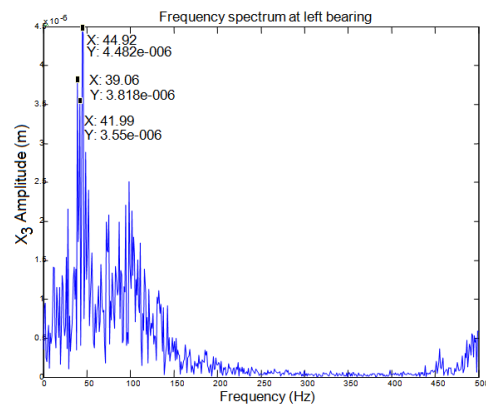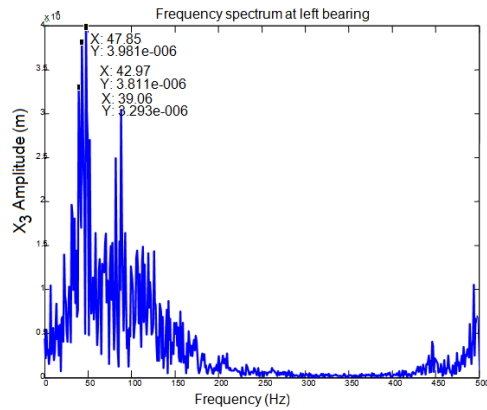
(d) At a rotor speed of 2000 rpm
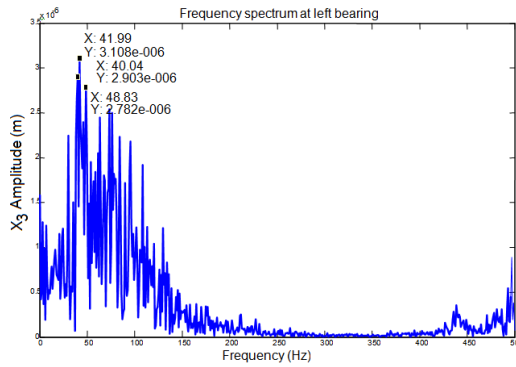
(e) At a rotor speed of 2500 rpm

Figure 6.61: Outer race waviness (A=1micron, m=1) on left bearing at various speeds

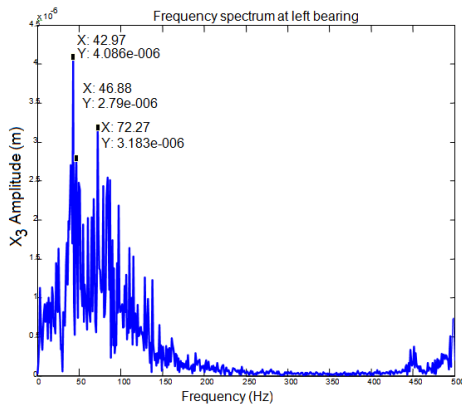Figure 6.62 and Figure 6.63 shows the FFT response of outer race waviness (A=1micron, m=1) on left bearing at a speed of 5000 rpm and 3000 rpm respectively.
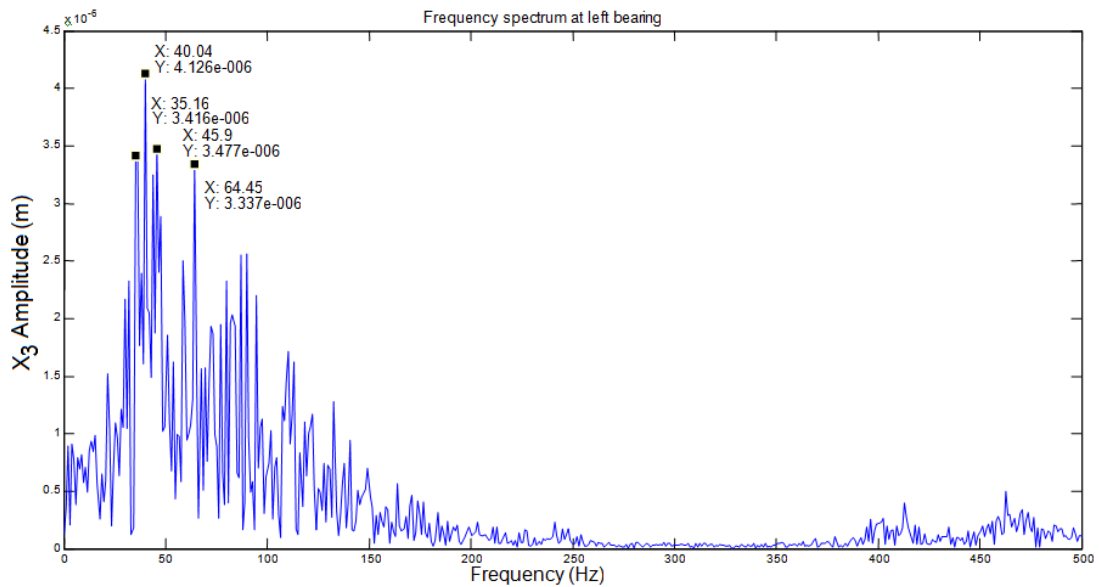
Figure 6.62: Outer race waviness (A=1micron, m=1) on left bearing at a speed of 5000 rpm
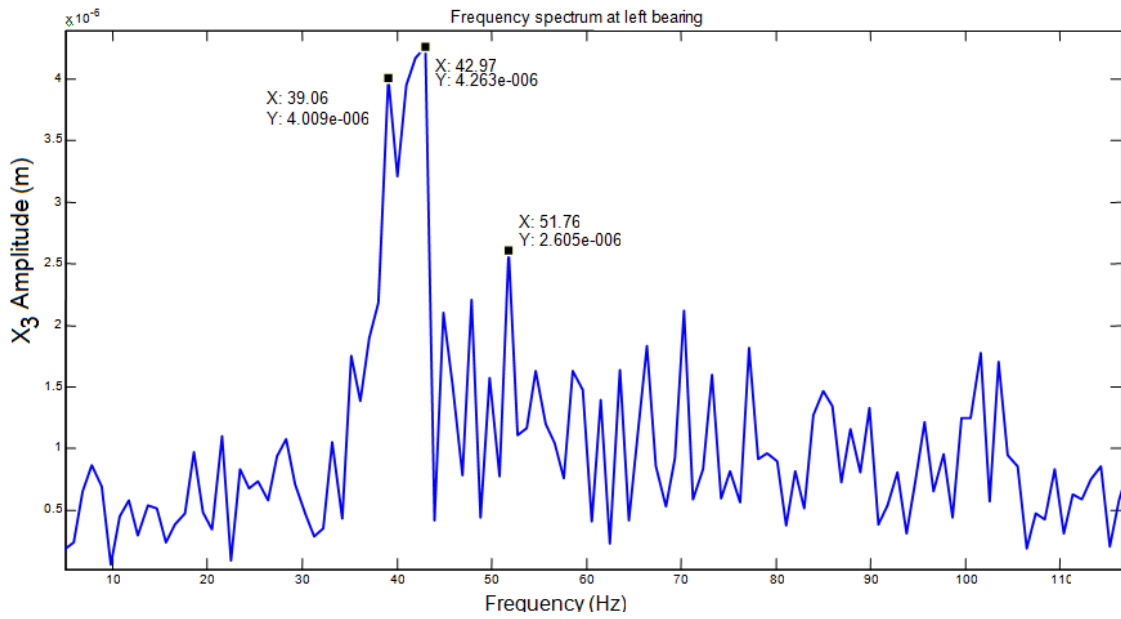
Figure 6.63: Outer race waviness (A=1micron, m=1) on left bearing at a speed of 3000 rpm

The effects of waviness on the overall dynamics of the system are shown. With the increase in the speed the amplitudes of the system are decreases.

(c) Inner race fault

The faults are studied in this section these are generally three types of localized faults are considered the system. They are outer race fault, inner fault and ball defects. The localized seeded defects are considered in the analysis with dent heights 1, 3 and 5 microns. Initially, The seeded defect of dent is analyzed in the inner race of the bearing, then the effects of the dent in the outer race and spall on the ball are illustrated in the frequency plots using in house Matlab codes.
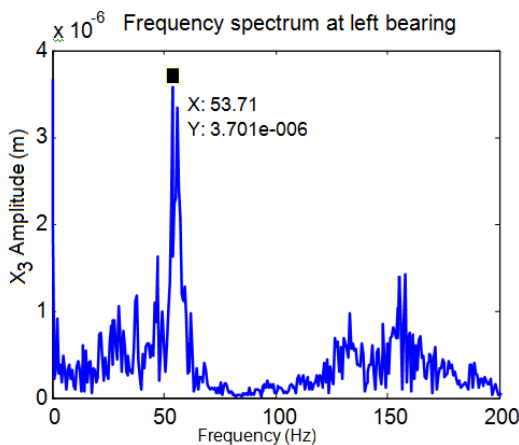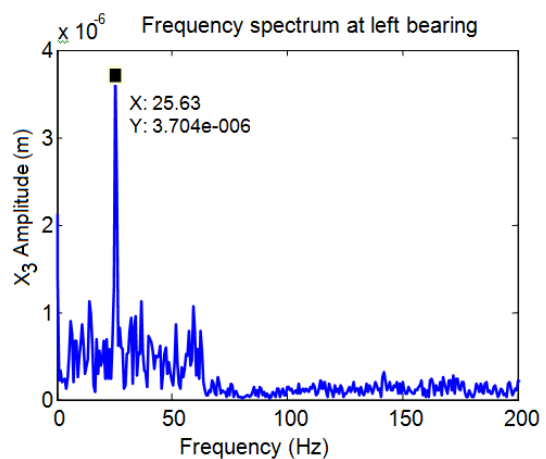
(a) Dent height he=1e-6   (b) Dent height he=3e-6
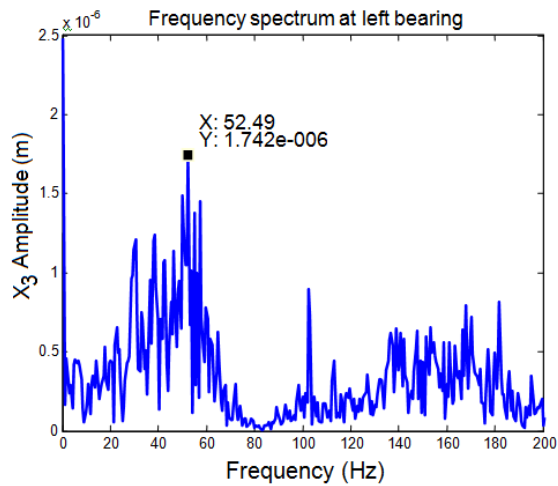
(c) Dent height he=5e-6

Figure 6.64: Inner race waviness (A=1micron, m=1) on left bearing at a speed of 2000 rpm

As the dent height increases the critical speeds operation. From the above Figure 6.64, it can be observed that the dent height is an important parameter effecting on the overall dynamic characteristics of the rotor bearing system.

(d) Outer race fault

The effect of the outer race dent height was analyzed with different dent heights at a constant rotor speed of a 2000 rpm. The response of the outer race dent height was shown in Figure 6.65(a)-(d).
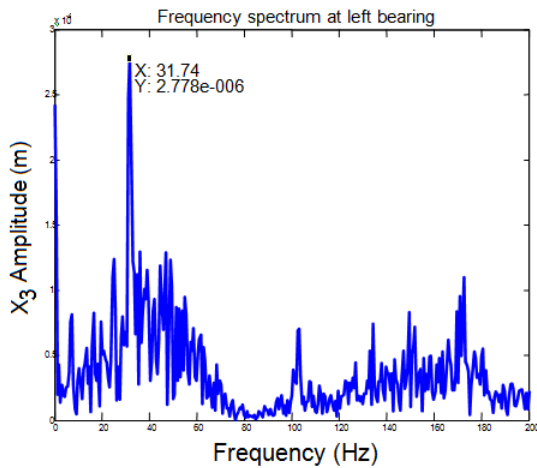
(a) Dent height he=1e-6m   (b)   Dent height he=3e-6m
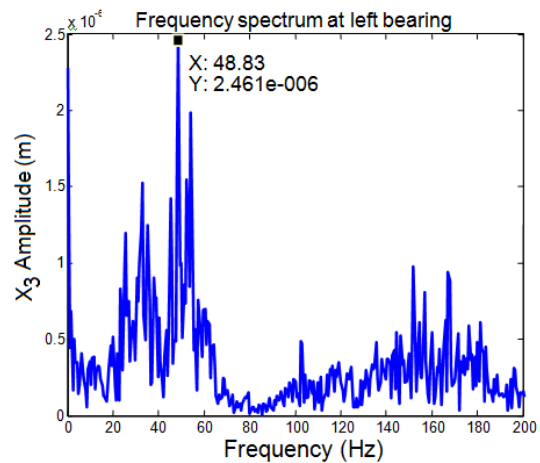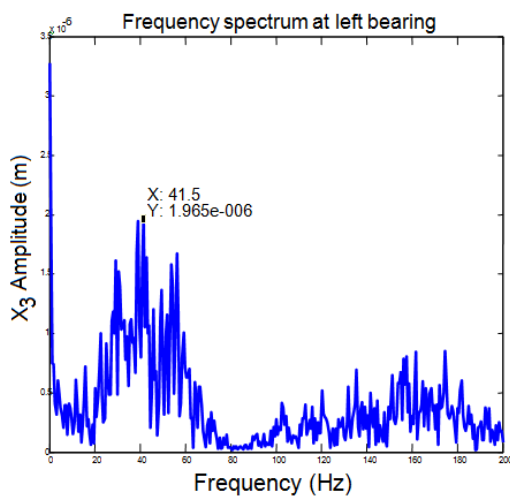
(c) Dent height he=5e-6m   (d) Dent height he=7e-6m
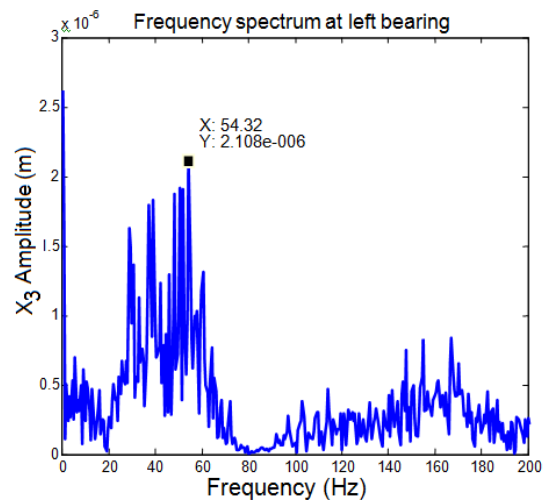
Figure 6.65: FFT response of an outer race fault with different dent heights at a constant speed of 2000 rpm

The dent height of the inner and outer races of the bearing plays very vital role on the overall dynamics of the system. The frequencies are increasing as the depth size increases.

(e) Ball fault

The stiffness of the bearing varies with the angular location of the ball in the ball bearing. The effect of the ball fault is twice the effect of inner or outer bearing faults as the ball hits inner and outer race in one revolution of the ball. Number of ball and the radial clearance of the bearings also important in the analysis of the ball fault.
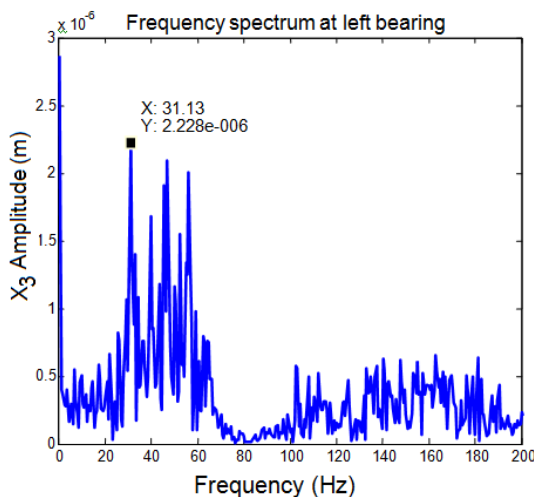
(a) Ball dent height 1e-6   (b) Ball dent height 3e-6
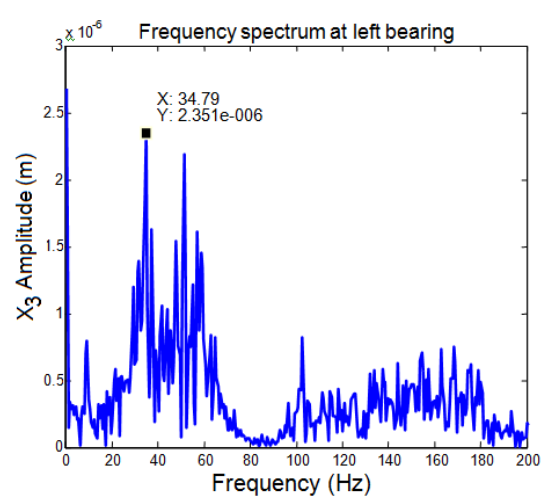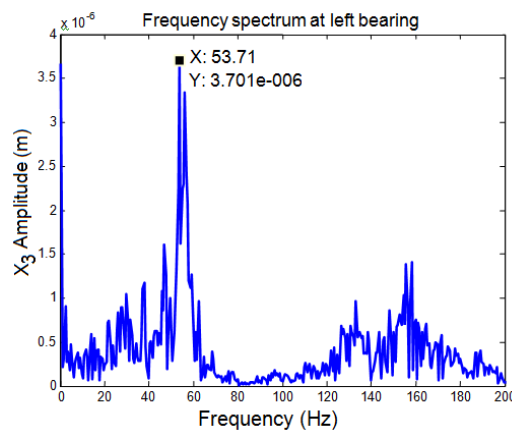
(c) Ball dent height 5e-6

Figure 6.66: FFT response at three sets ball dent heights

The ball bearing stiffness also depends on the load applied on the system. The variation in bearing stiffness due to the defect produces parametric excitations of the bearing assembly as shown in the Figure 6.66. The qualitative character of the vibration response correlates to the character of the stiffness variations.

6.4 Parameter prediction from inverse modelling

With various parametric studies, it was found that the bearing radial clearance, disc eccentricity along with stiffness coefficients of bearing and squeeze film damper have significant influence on the overall response within the operating speeds. So, these three input variables varied at three levels each are selected at different levels and the 27 design of experiments are carried out to obtain the fundamental frequency and corresponding amplitudes.

The bearing parameters like radial clearance of the ball bearings, mass eccentricity of the disk and the centralizing spring stiffness of the squeeze film damper play a very vital role in the stability and health of the system. From the analysis, it was found that the bearing radial clearance, disc eccentricity along with stiffness coefficients of bearing and squeeze film damper have significant influence on the overall response within the operating speeds.

The estimation of these parameters is attempted by taking 27 different experiment sets of values using inverse modelling approaches. The frequency responses and the amplitudes are used from the Matlab simulations.

Table 6.8 shows the data collected from FFT diagrams.

Table 6.8: Measured data from FE model

Exp No	Radial clearance (r_c) (μm)	Disc eccentricity (e) (μm)	Centralizing spring stiffness (k_a) (kN/m)	Natural frequency (Hz)	Amplitudes (dB)
1	**20**	**1**	**300**	**51.757813**	**-101.934218**
2	20	3	300	51.757813	-103.684734
3	20	5	300	51.757813	-104.374457
4	**20**	**1**	**600**	**33.200000**	**-111.800000**
5	20	3	600	51.757813	-111.088333
6	20	5	600	30.273438	-111.556593
7	20	1	900	31.250000	-111.687714
8	**20**	**3**	**900**	**53.710938**	**-111.189207**
9	20	5	900	54.687500	-114.927748
10	40	1	300	21.484375	-103.294575
11	**40**	**3**	**300**	**40.039063**	**-103.056293**
12	40	5	300	42.968750	-101.662825
13	40	1	600	26.367188	-102.340111
14	40	3	600	44.920000	-105.200000
15	40	5	600	23.437500	-104.781279
16	40	1	900	39.060000	-105.600000
17	**40**	**3**	**900**	**27.343750**	**-103.243682**
18	40	5	900	23.440000	-105.400000
19	60	1	300	22.460938	-97.8353140
20	60	3	300	20.510000	-100.800000
21	60	5	300	21.484375	-98.7253440
22	60	1	600	27.460938	-97.9027790
23	60	3	600	21.484375	-101.096655
24	60	5	600	41.020000	-101.900000
25	60	1	900	29.300000	-104.790000
26	60	3	900	31.250000	-102.500000
27	60	5	900	26.367188	-100.621837

Among 27 experimental sets, the first set is used as a basis for calculating average values. Four more experimental sets are reserved for testing. Learning rate = 0.4, along with 5000 epochs are taken. The best training performance of the three layer network (back-propagation) is shown in the Figure 6.67 for different values of hidden nodes.
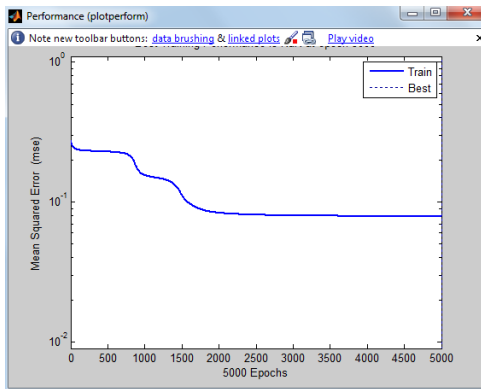
(a) Hidden nodes= 3 and the error 0.0791   (b) Hidden nodes= 4 and the error 0.0931
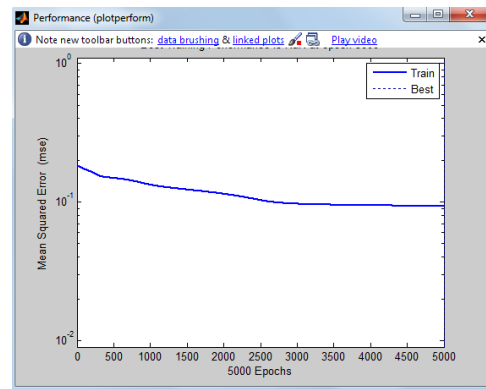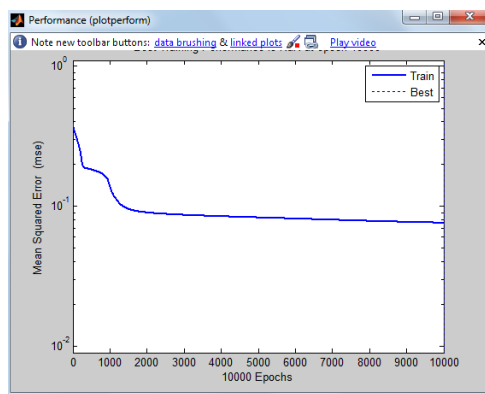
(c) Hidden nodes= 5 and the error 0.0759   (d) Hidden nodes = 6 and the error 0.0541
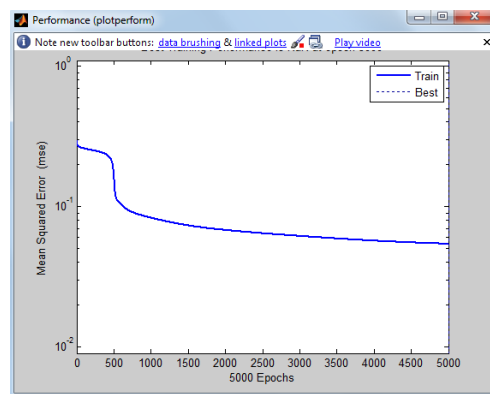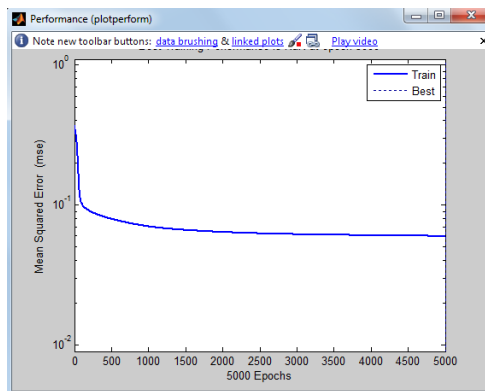
(e) Hidden nodes= 7 and the error 0.0598   (f) Hidden nodes= 8 and the error 0.0533
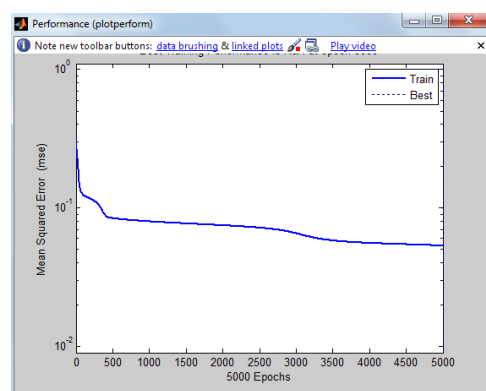
Figure 6.67: Performance graph

As seen, simulations are carried out by changing the hidden nodes and the error is identified in MLP neural network program and with hidden nodes = 8, lowest error is observed and the estimation of parameters are carried out using this architecture.

The performance of neural network on the four test patterns is shown in the bar charts (Figure 6.68 (a)-(c)).

131
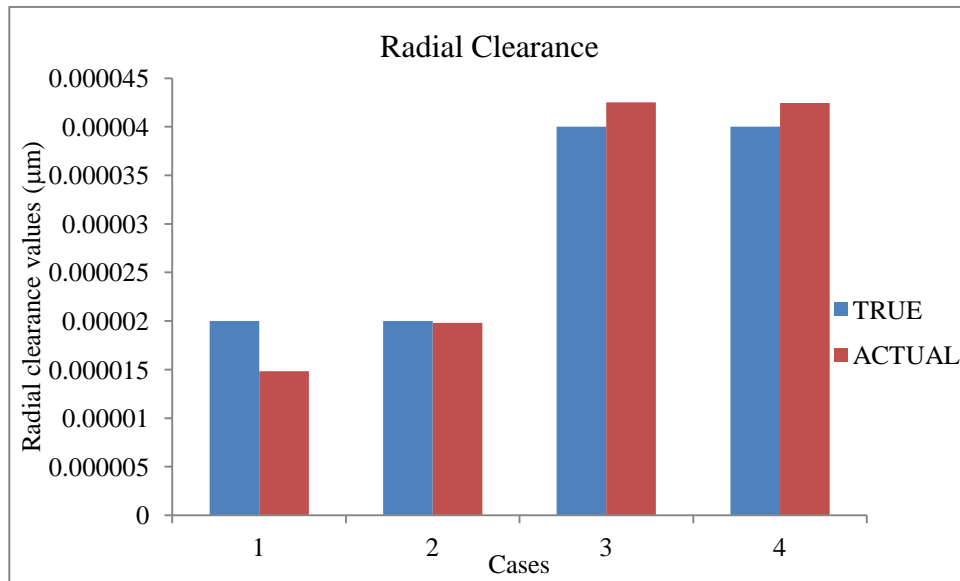
(a) Radial clearance estimation
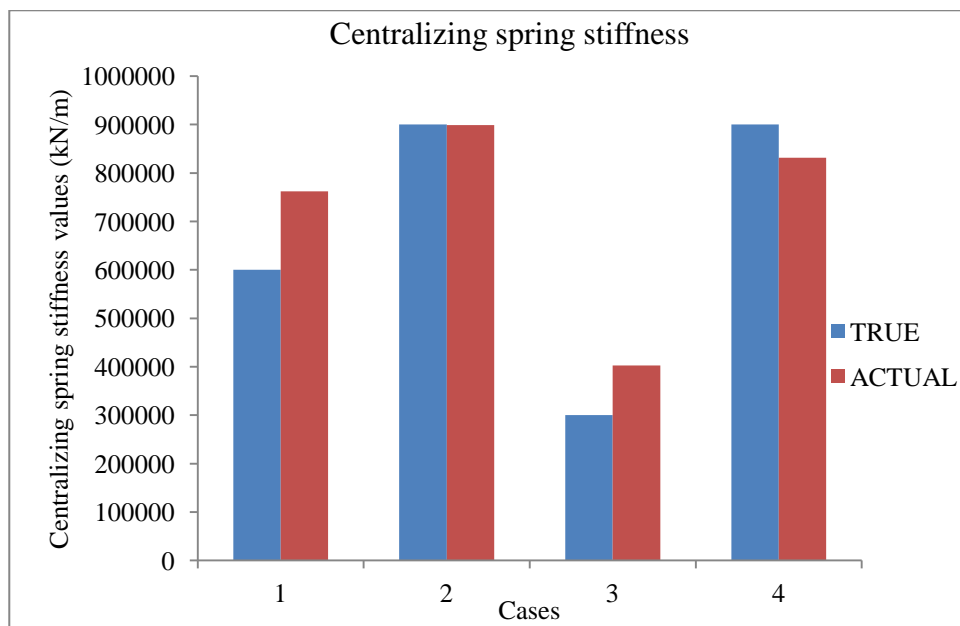
(b) Centralizing spring stiffness estimation
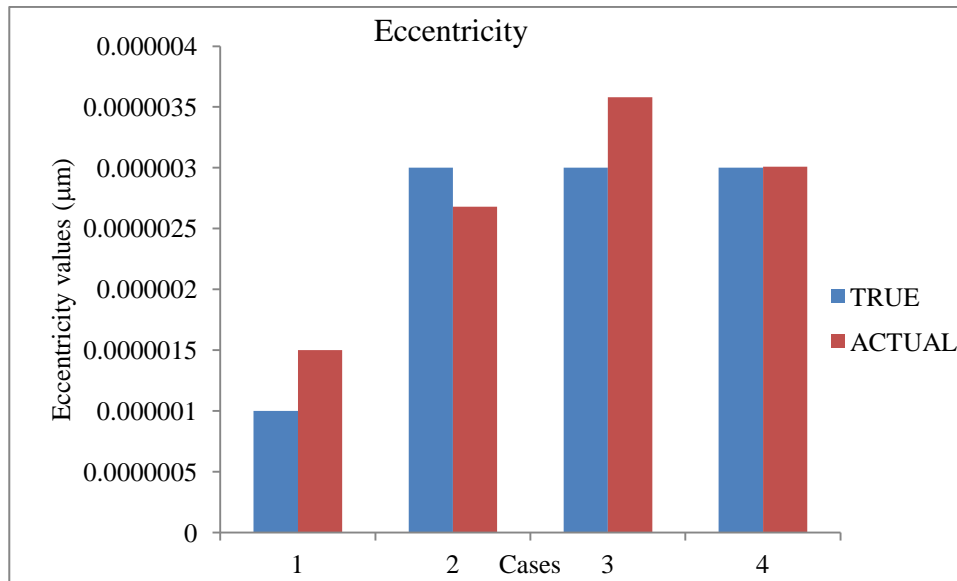
(c) Eccentricity estimation

Figure 6.68: The performance of neural network for test samples (two inputs)

In the above figures, true value refers to the target value specified corresponding to given input pattern. Actual values are the outputs obtained from the neural network after simulation with computed weights. It is observed that the actual values are matching with true values in all three parameters. The 3-layer back propagation neural network code written along with the neural network toolbox commands using MATLAB is given in Appendix. The parameters are also estimated by using radial basis function neural network code. The same 27 experimental sets data was used in this supervised network. There is a well agreement between true and actual values of these three parameters. From the above plots it is observed that the error between the true and the actual value is relatively small. The radial clearance estimated coincides with true value for all the samples except one. The centralizing spring stiffness is also estimated and is in good agreement and the same comparison is identified in the eccentricity values. Table 6.9 shows the comparison of true and actual values of bearing parameters.

Table 6.9: Comparison of true and actual values of neural networks

Case	Radial clearance (r_c)		Centralising spring stiffness (k_a)		Eccentricity	
	True	Actual	True	Actual	True	Actual
1	0.000020	0.00001966	600000	832470	0.000001	0.00000190
2	0.000020	0.00001956	900000	807940	0.000003	0.00000301
3	0.000040	0.00004531	300000	633030	0.000003	0.00000304
4	0.000040	0.00005044	900000	862330	0.000003	0.00000280

It is observed that the output errors of three layer back propagation network are much smaller compared to those obtained from RBF networks. This may be due to limited training features of RBF.

6.4.1 Bearing fault prediction

With different faults in one of the ball bearings, the dynamic response of the rotor is observed in time domain. Five cases are considered: one without fault and other four cases representing outer race waviness, outer race fault, inner race fault, and ball fault respectively. As the time responses and their FFT in all the cases are observed to be difficult to distinguish. Each time response is represented with statistical characteristics such as mean, variance and other higher order moments. Thus a single signal is equivalent to a finite number of statistical parameters. Corresponding to each fault a set of such statistical parameters is obtained at different operating speeds. Figure 6.69 shows the variation of four statistical parameters corresponding to different fault condition (Peak to peak-ptpx, Crest factor-cfx, Skewness -skewx and Kurtosis-Kurtox).

(a) No fault case   (b) outer waviness

(c) Inner fault case   (d) Inner case fault case
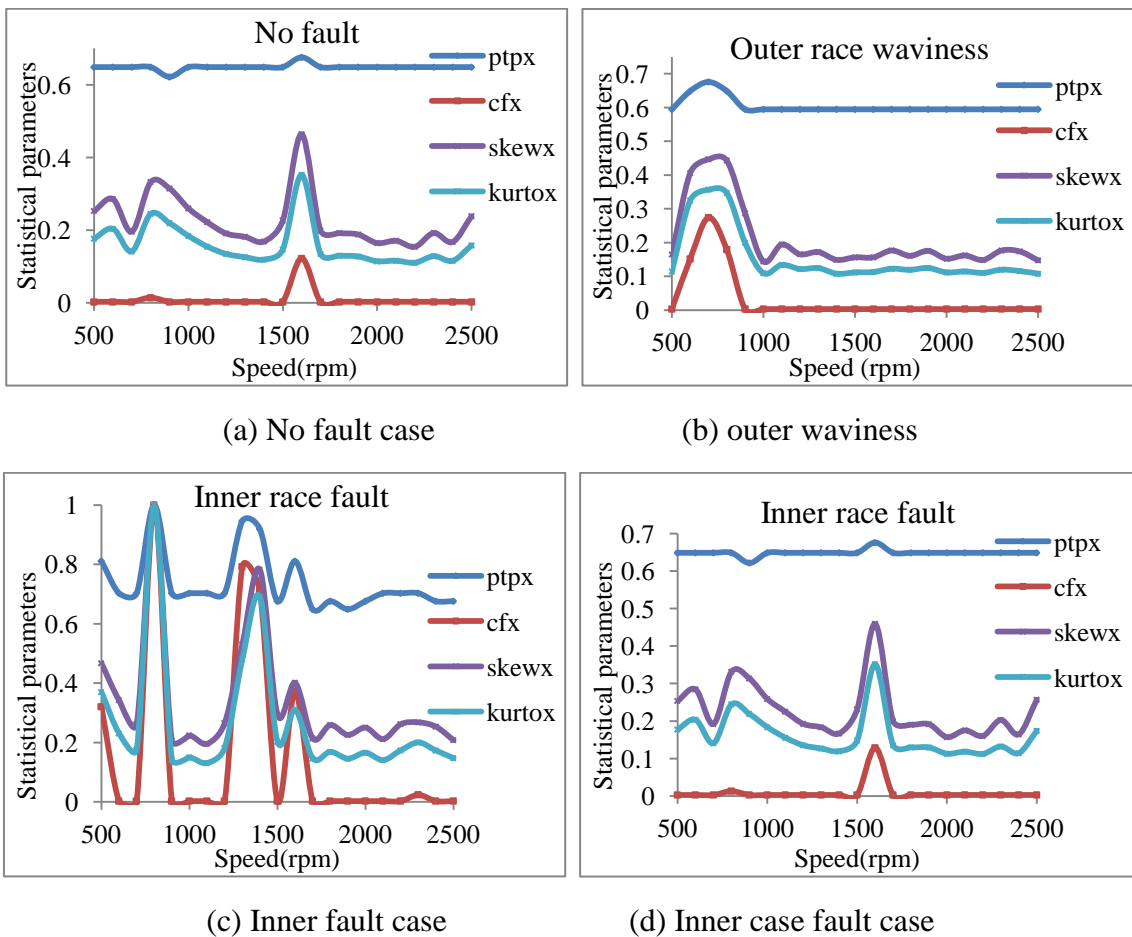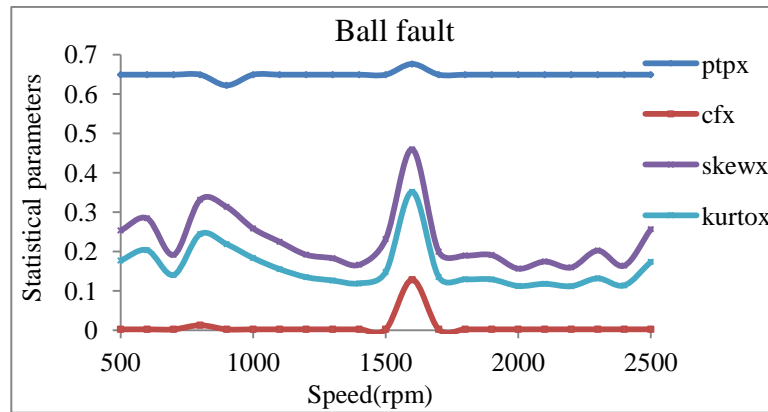
(e) Ball fault case

Figure 6.69: Variation of four statistical parameters corresponding to different fault condition

The number of hidden nodes is varied. The total 1005 samples are taken and some of the samples kept aside for predicting the outputs. After successful training of the neural network, it can identify the faults in the bearings.

In the next phase, identification studies are performed to quantify the faults in the system. Initially the response of a Matlab program is considered to calculate the faults at different speed of the rotor and the statistical quantities are identified and the plots are shown below. Figure 6.70 shows the statistical quantities of inner race fault, outer race fault and outer race waviness respectively.
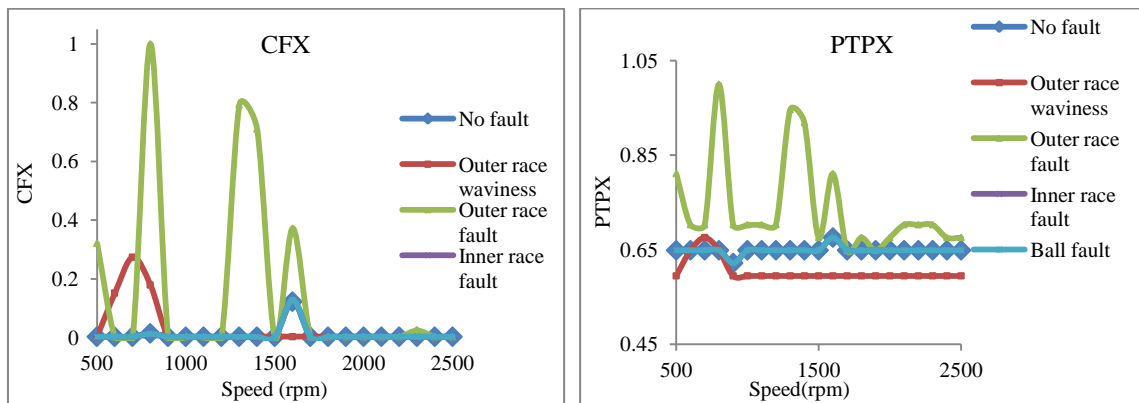
(a) Crest factor

(b) Peak to peak factor

(c) Skewness factor   (d) Kurtosis factor
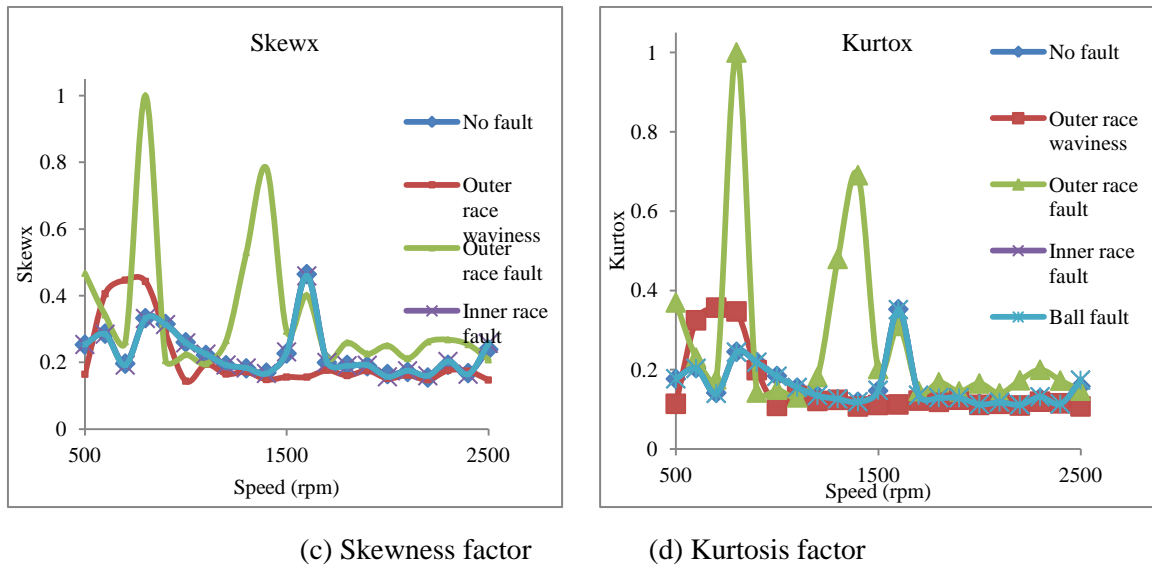
Figure 6.70: Statistical quantities

The four statistical parameters are considered in the analysis and the individual plots are shown in the plots. In Skewness and Kurtosis plots, the inner race fault and ball fault are coinciding. This might be due to very low effects of the inner race faults on the overall dynamics of the system.

A total number of 505 patterns with five classes are used in training and testing the neural networks. Unsupervised Kohonen's network and Probabilistic neural network are used to classify the patterns. The results of analysis are shown in the form of confusion matrix given in Table 6.10.

Table 6.10: PNN identification table (Confusion matrix)

	No fault	Outer race waviness	Outer race fault	Inner race fault	Ball fault
No fault	16	00	00	02	02
Outer race waviness	2	14	00	01	03
Outer race fault	00	02	12	02	04
Inner race fault	00	01	00	15	01
Ball fault	02	03	05	00	10

PNN is easy to train and it can be used in real-time applications. The best classification effect depends on the best input training data. The PNN is one of the best classifier which classifies the faults very efficiently and accurately. Same input values are provided to all the pattern layers. The output of each layer depends on the multiplication factor of previous weight vector and the input value. The faulty samples are randomly altered and

the given to the network to classify the faults. The fault classification is very effective in no fault, outer race waviness and ball faults and shown in the above table.

Along with the PNN, a self organized network is used to classify the faults in the bearings. A Kohonen's self organization network is used for fault classification without the target data. Outputs of Kohonen's self organization networks are also given in the Table 6.11 as a confusion matrix. The input nodes are taken as m=5 and output nodes are taken as n=6, number of epochs =500, number of patterns for training =100, Initial learning rate η_0=0.9.

Table 6.11: Kohonen's neural network outputs

	No fault	Outer race waviness	Outer race fault	Inner race fault	Ball fault
No fault	83	00	7	00	20
Outer race waviness	00	78	2	16	4
Outer race fault	15	5	64	6	10
Inner race fault	4	10	06	72	8
Ball fault	20	00	00	1	79

On running of different simulation the confusion table was prepared. The classification was done very nicely by Kohonen's network.

Figure 6.71 shows the convergence trend of mean error while training the Kohonen's network.
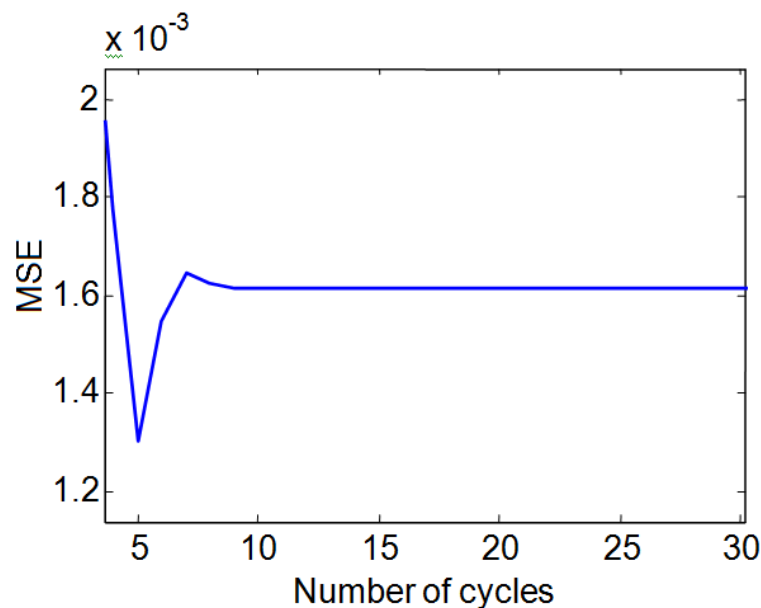
Figure 6.71: Convergence trend of Kohonen's network

6.5 Nonlinear transient excitation

This section deals with effect of nonlinear external forces on the dynamics of the rotor. Along with the regular bearing forces on the system, additional external excitations like Muszynska's forces and the rub forces are introduced in the system.

6.5.1 Muszynska's gas forces

Table 6.12 shows the parameters used in the Muszynska's gas force model in the Matlab simulation.

Table 6.12: Parameters of Muszynska's force model [185]

Parameter	Value	Parameter	Value
ξ	0.1	c_f	1.5mm
m_0	-0.25	n	2.5
R_f	43 mm	b	0.5
n_0	0.079	l_f	18 mm
Δp	0.1×10^5 Pa	V	$0.3 \times$omega
V	1.5×10^{-5}Pa S	τ	0.25

Matlab code to evaluate the external forces in the system is shown below:

Model code: External forces calculating program

```
%%% EXTERNAL FORCES %%%%%%
function [Fxg Fyg]=musz(x,y,xd,yd,xdd,ydd,t)
global N
m0=-0.25;
cseal=1.5e-3;
zeta=0.1;
Rs=43e-3;
eta=1.5e-5;
n0=0.079;
delp=0.1e5;
lseal=18e-3;
n3=2.5;n4=0.5;
tou0=0.25;
omega=2*pi*N/60;
v=0.3*omega;
Ra=(2*v*cseal)/eta;
Rv=(Rs*omega*cseal)/eta;
f=n0*Ra^m0*(1+(Rv/Ra)^2)^(1+m0)/2;
sigma=f*lseal/cseal;
Ea=(1+zeta)/(1+zeta+2*sigma)*0.5;
mu0=(2*sigma^2)/(1+zeta+2*sigma)*(Ea*(1-m0));
B=2-(Rv/Ra)^2-m0/(Rv/Ra)+1;
mu1=(2*sigma^2)*(Ea/sigma+B*(1/6+Ea)/2)/(1+zeta+2*sigma);
mu2=sigma*(1/6+Ea)/(1+zeta+2*sigma);
mu3=(pi*Rs*delp)/f;
```

```
k0=mu0*mu3;
caret=lseal/v;
d0=mu1*mu3*caret;
mf=mu2*mu3*caret^2;
e1=sqrt(x^2+y^2)/cseal;
   kf=k0*(1-e1^2)^-n3;
   df=d0*(1-e1^2)^-n3;
   tou=tou0*(1-e1)^n4;
   Fxg=(-kf+mf*tou^2*omega^2)*x-(tou*omega*df)*y-df*xd-2*tou*omega*mf*yd-mf*xdd;
   Fyg=(tou*omega*df)*x-(kf-mf*tou^2*omega^2)*y+2*tou*omega*mf*xd-df*yd-mf*ydd;
```

Figure 6.72 and Figure 6.73 shows FFT responses at a constant speed of 2000rpm with and without Muszynska's forces at right and left bearings respectively.

(a) With Muszynska's force   (b) Without Muszynska's force
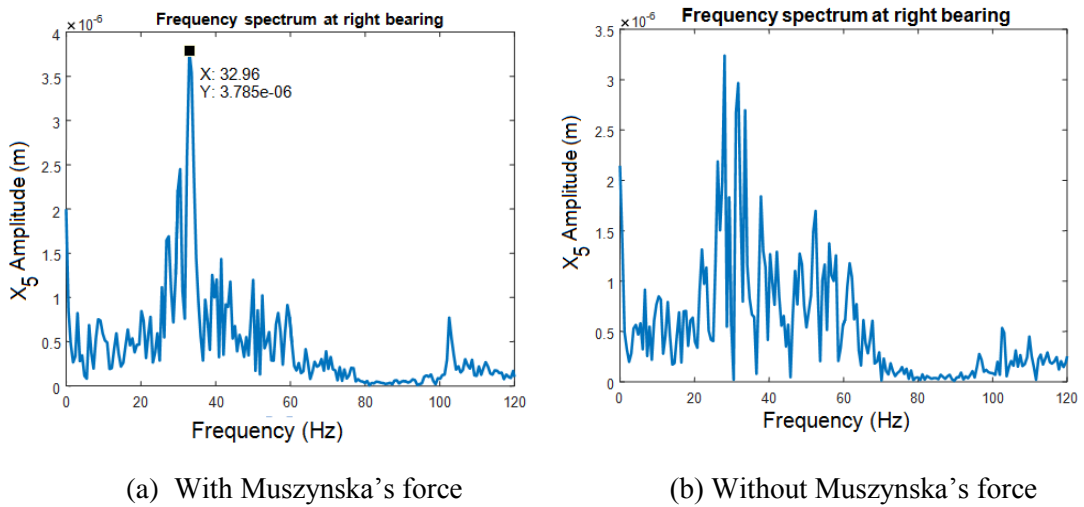
Figure 6.72: FFT responses at (2000rpm) right bearing

(a) With Muszynska's force   (b) Without Muszynska's force
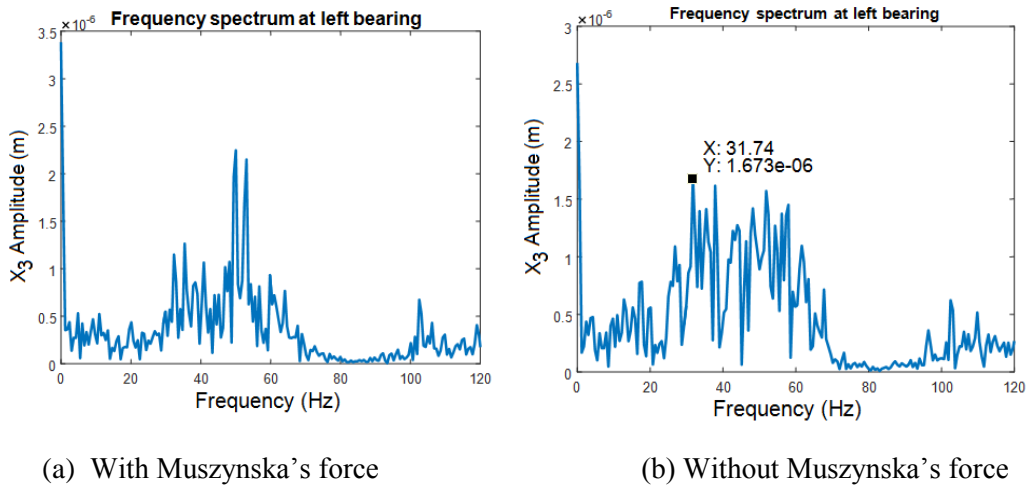
Figure 6.73: FFT responses at (2000rpm) left bearing

In addition to the ball bearing dynamic forces, an external excitation Muszynska's force is introduced in the system. The amplitudes are raised rapidly due to insertion this

force in the system. The external gas excitation forces are modelled as Muszynska's forces. It can be observed from the above plots that the effect of Muszynska's force will lead to system to unstable condition. At left and right bearings the recording are taken and the forces are acting at the disk nodes.

6.5.2 Rub impact effects

The solutions of equations of motion are obtained from MATLAB ode45 solver. All the initial conditions are set to zero and damping at the bearings is ignored.

A part of the Matlab code for computing the rub force on a disk is given below.

Model code: Rub forces computing program

```
function [frx,fry]=rub(x,y,t)
delx=1e-6;dely=1e-6;%Distance between rotor and stator centres
del4=50e-6;ks=45e6;mu=0.1;%del4 is nominal clearance, ks is rub stiffness, mu is the coefficient of friction
 rg1=sqrt((x-delx)^2+(y-dely)^2);
cp1=((x-delx)/rg1);sp1=((y-dely)/rg1);
if rg1<=del4
   Fn1=0;
else
   Fn1=ks*(rg1-del4);
end
Ft1=mu*Fn1;
frx=(-Fn1*cp1+Ft1*sp1);
fry=(-Fn1*sp1-Ft1*cp1);
```

Figure 6.74-Figure 6.76 shows the FFT diagrams at different rub stiffness values of stator at a constant speed of 2000rpm.
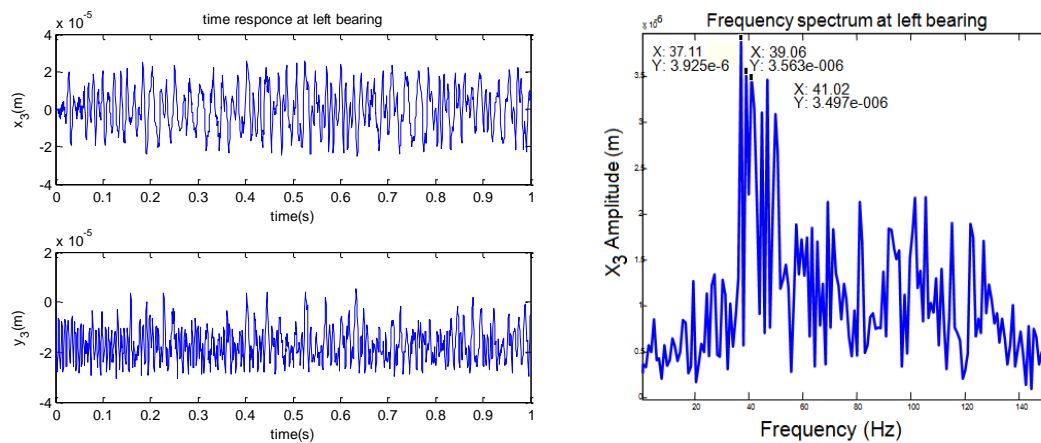
Figure 6.74: Rub response when the stiffness is k_s=5e6 N/m
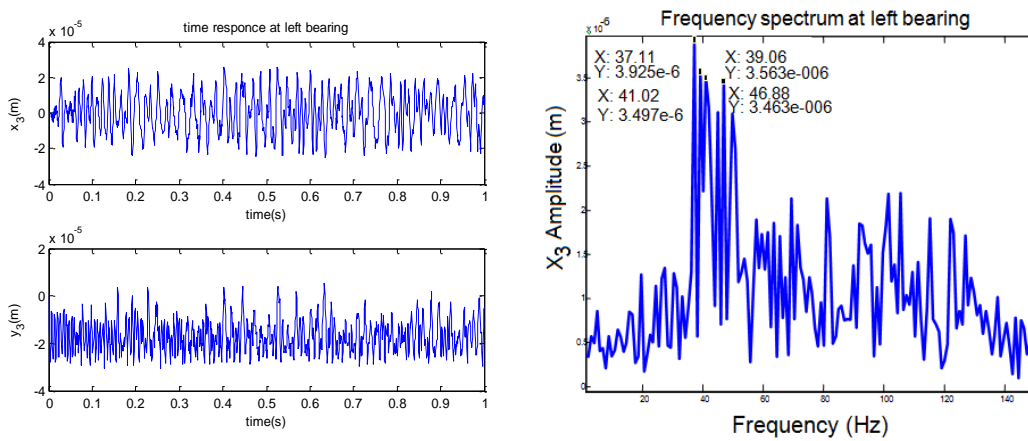
Figure 6.75: Rub response when the stiffness is k_s=45e6N/m.

(a) k_s=100e6 N/m   (b) k_s=1000e6 N/m
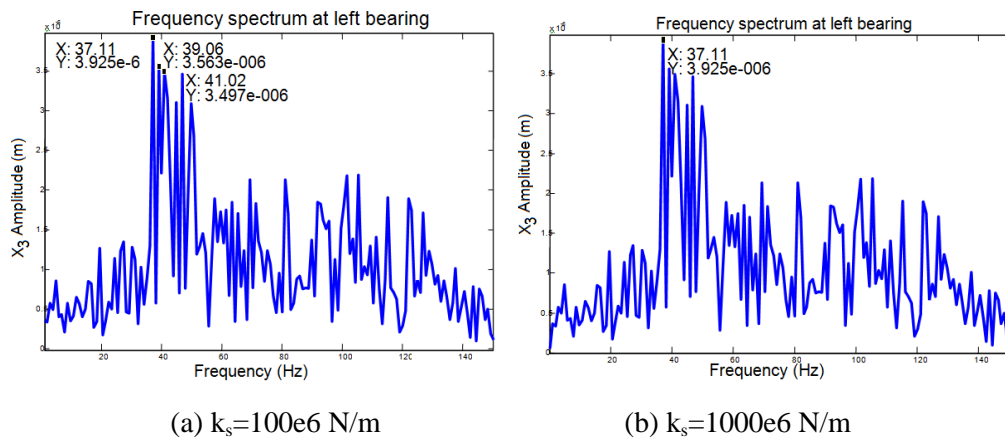
Figure 6.76: FFT responses at rub forces at different stiffness values

Due to the excessive unbalance in the system the rotor may hit the stationary casing. The unbalance may be due to misalignment or separation of one of the wanes of the rotor. Due to hitting of rotor, a huge force will act on the system. At that point where rub is taking place large stiffness will be introduced in the system. Due to increase in the stiffness at a particular point leads to quasi-periodic motion of the system can be observed from the above plots. As the stiffness increases amplitudes of the motion also increase.

Figure 6.77 (a) and (b) are showing the FFT responses at clearance value of 120e-6 mm and 50e-6 mm and at a constant rub stiffness of 45e6 N/m and the response is from both left and right bearing nodes.

(a) k_s=45e6N/m, clearance 120e-6m

(b) k_s= 45e6N/m, clearance=50e-6m
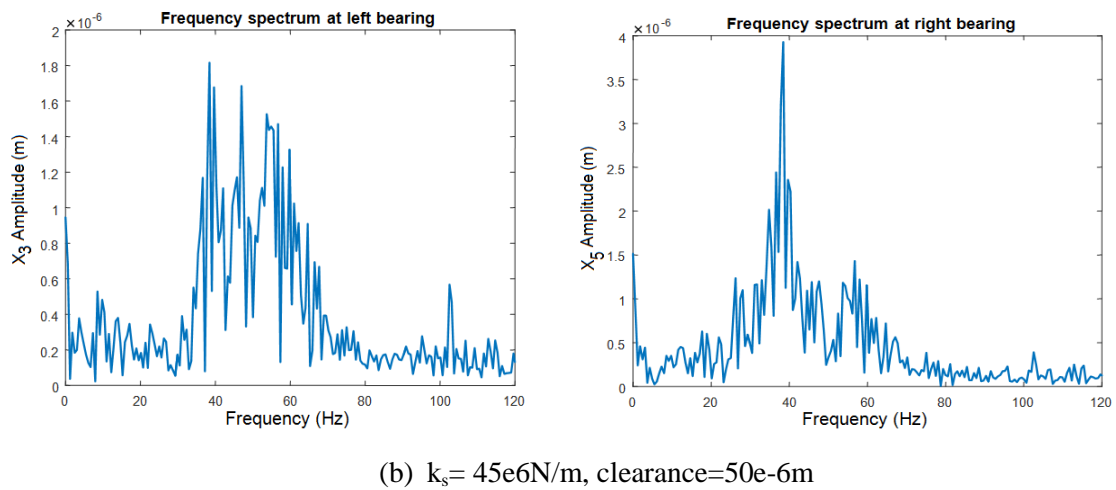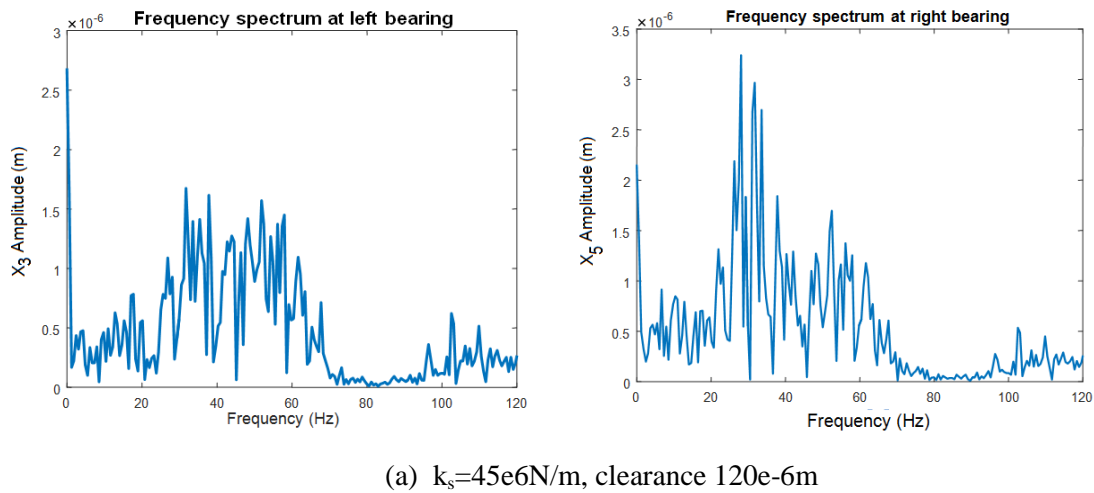
Figure 6.77: FFT responses at rub forces at different clearance values

As the clearance decreases at a constant stiffness value the system becomes unstable. The amplitudes are increasing by reducing the radial clearance and the chance of rub is very obvious when there is a very small clearance between rotor and stator.

6.5.3 Rub- Experiment

The experiment is carried out by setting up the vibrometer and giving the node at distinct positions on the rotor. The vibrometer records the transverse vibrations of the rotor in x-direction and y- direction of the rotor at each node. The rubbing positions of the disc have been set up as shown in the Figure 6.78.

Figure 6.78: Experimental rub-impact setup

Figure 6.79 shows the rub inducing set up. A combination of nut and bolt are used to induce the rub on the disk by changing the angular positions of the screw. The rub of the rotor has been intentionally induced at various positions on circumference of the disc, the time velocities and FFT's are recorded by vibrometer. The rotor with rub impact setup is analyzed at the different rotor speeds starting from 500rpm to 2500rpm.
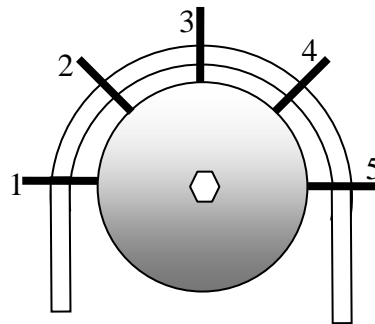
Figure 6.79: Rub induced positions of the disc

The rub is induced at various positions and FFT and phase diagrams are plotted at each angular position. Figure 6.80-Figure 6.84 shows the FFT and phase diagrams at each rubbing position on the disk at a constant speed of 2000rpm.
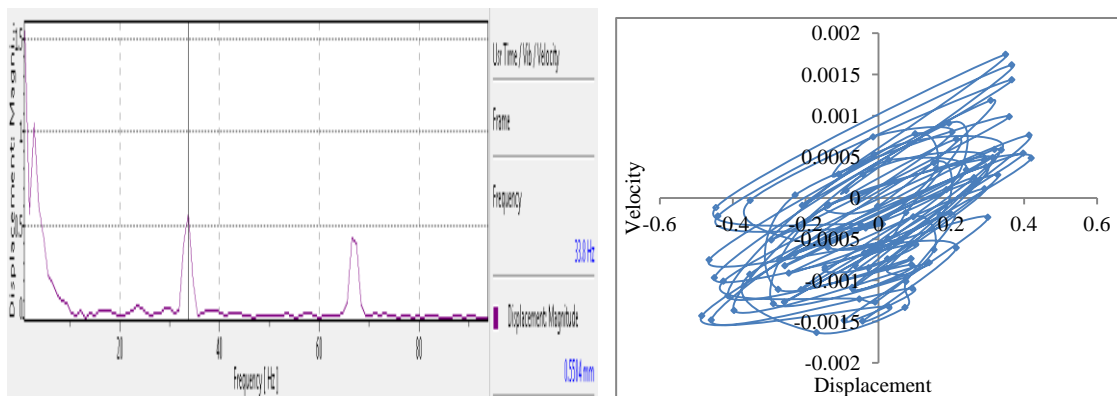
(a) Displacement FFT plot   (b) Experimental Phase diagram

Figure 6.80: Records at a disk of rub position 1 (2000rpm)
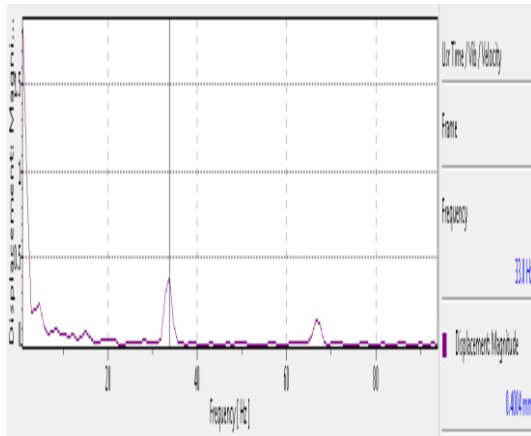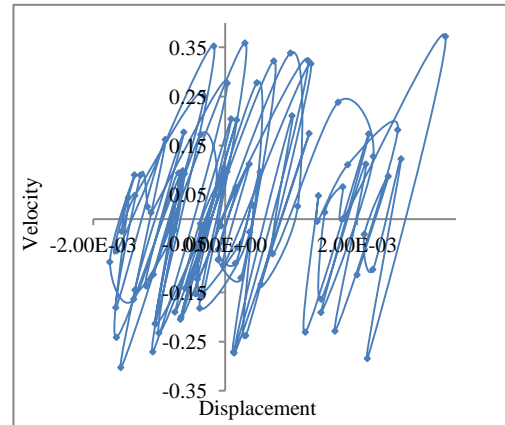
(a) Displacement FFT plot   (b) Experimental Phase diagram

Figure 6.81: Records at a disk of rub position 2 (2000rpm)
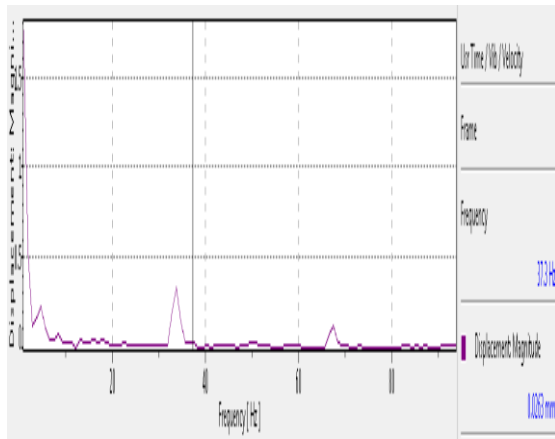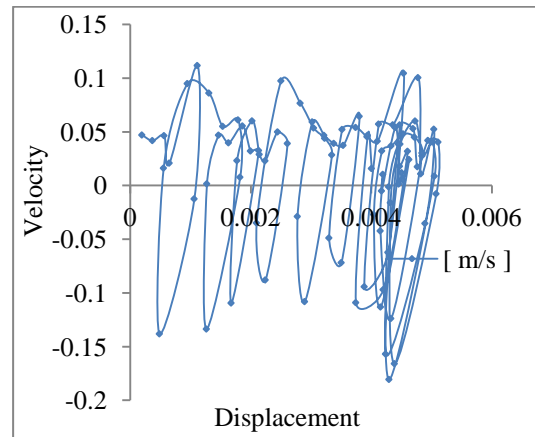
(a) Displacement FFT plot   (b) Experimental Phase diagram

Figure 6.82: Records at a disk of rub position 3 (2000rpm)

At a rub position 4, we can observe the maximum frequency form the plots. At different locations the rub responses differently, it may appear as 2 dimensional but in fact the effect of rub will be in 3 dimensional one. For this reason, the response may differ due to the locations of the rub.
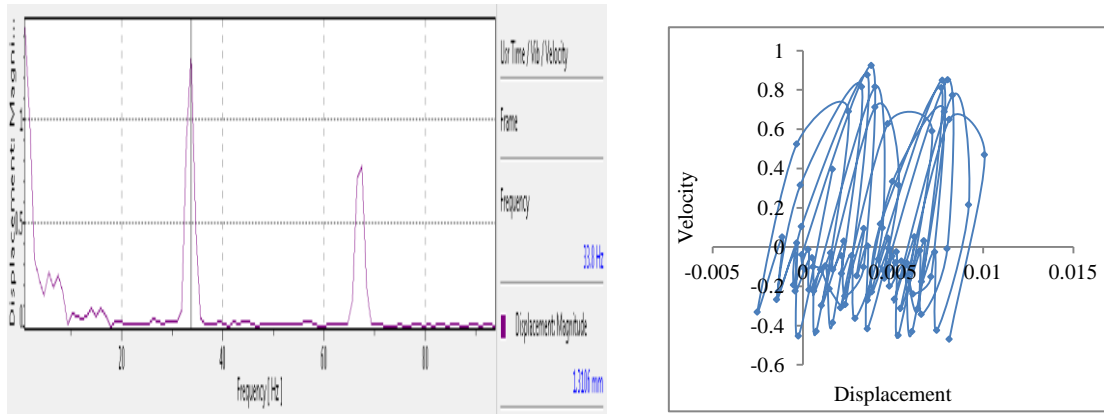
(a) Displacement FFT plot   (b) Experimental Phase diagram
Figure 6.83: Records at a disk of rub position 4 (2000rpm)
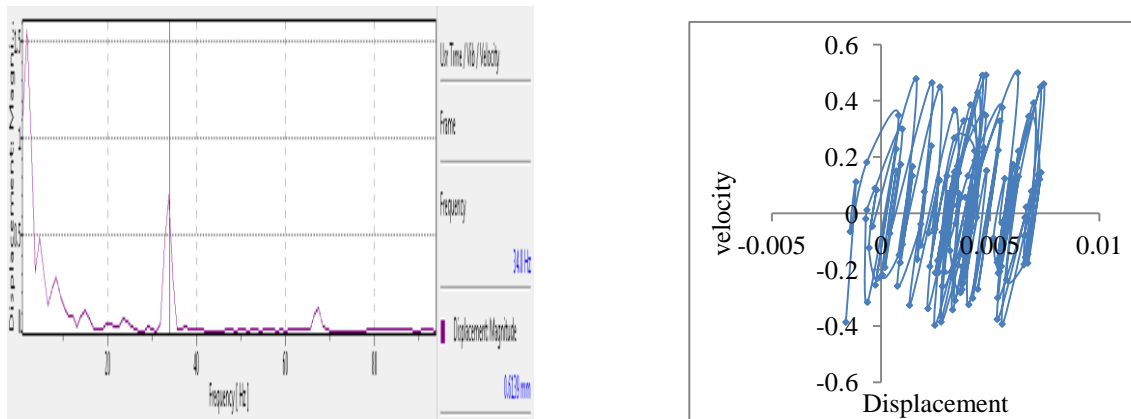
(a) Displacement FFT plot   (b) Experimental Phase diagram

Figure 6.84: Records at a disk of rub position 5 (2000rpm)

Even though the rotor is rotating at constant speed the response is different in different rub locations. At the location 4 small increment of the rub will leads to unstable condition of the system.

6.5.4 Identification of added stiffness

The vibration response of the system was recorded initially with rub forces on the left disk at different speeds of operation. In the next step, without rub forces and with randomly added stiffness and damping to the shaft the response data is collected in frequency domain in both X and Y directions. The resultant error between the original response and actual response by adding random stiffness and damping is minimized over a frequency range. This is done with particle swarm optimization method.

The following variable constraints are selected $X(1)=\Delta k \in [1000,1e6]$N/m, $X(2)=\Delta c \in [100,1e4]$ Ns/m.

145

The diagonal matrices with Δk and Δc as diagonals are added to the original stiffness and damping matrices of the shaft, so as to get equivalent stiffness and damping due to rub effect. Six different speeds at which the rubbing excitation acting on the system are considered during the estimation of Δk and Δc. Figure 6.85 shows the rub effect on amplitudes of response at left bearing node in different speeds.
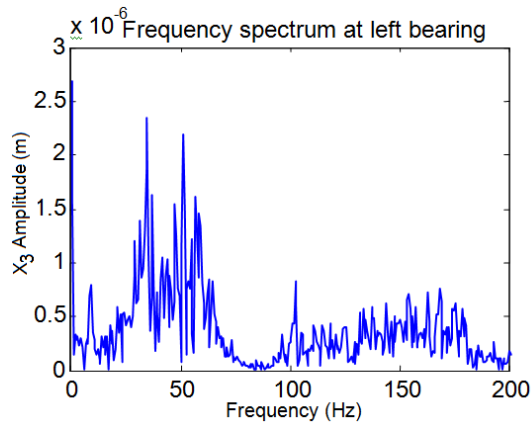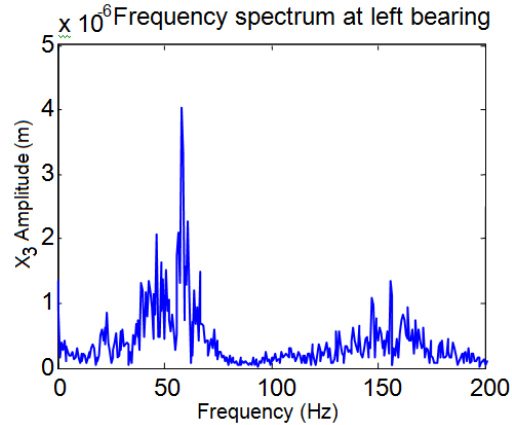
(a) 2000 rpm   (b) 4000 rpm
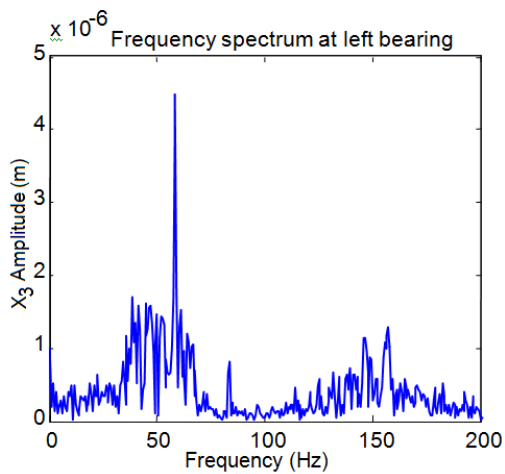
(c) 5000 rpm   (d) 5500 rpm
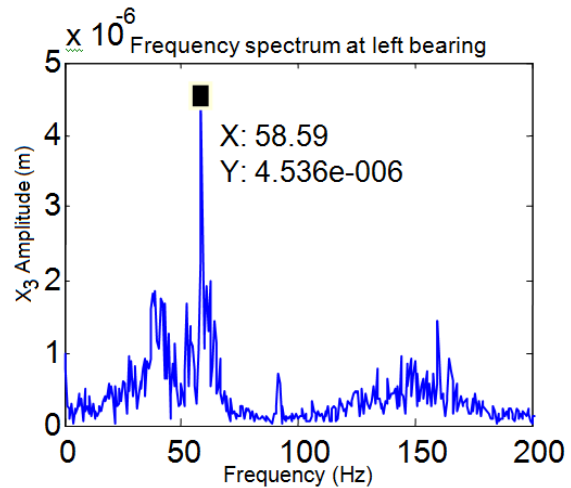
(e) 6000 rpm (f) 7000 rpm
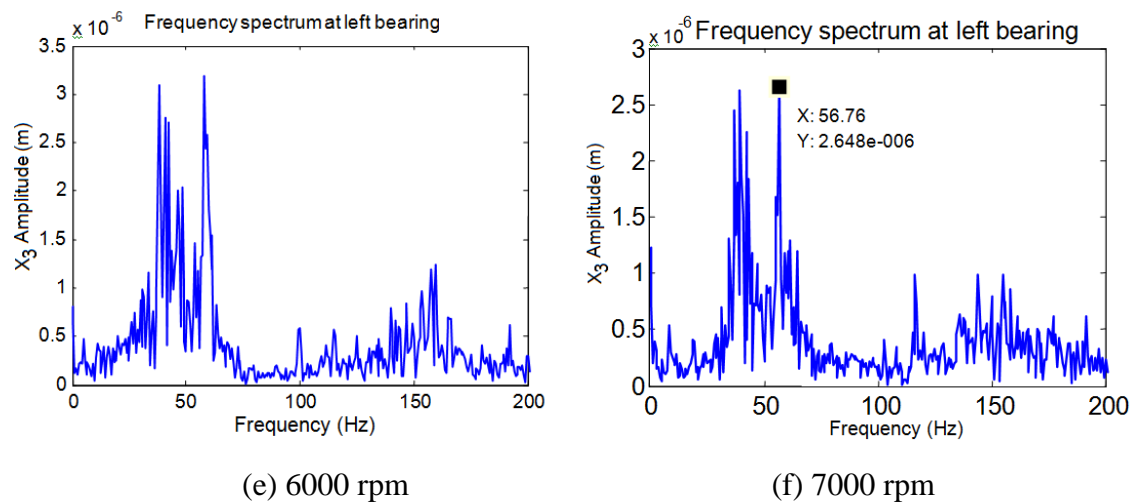
Figure 6.85: Effect of rub

Figure 6.86 shows the peak amplitude variation as a function of speed during rub impact.
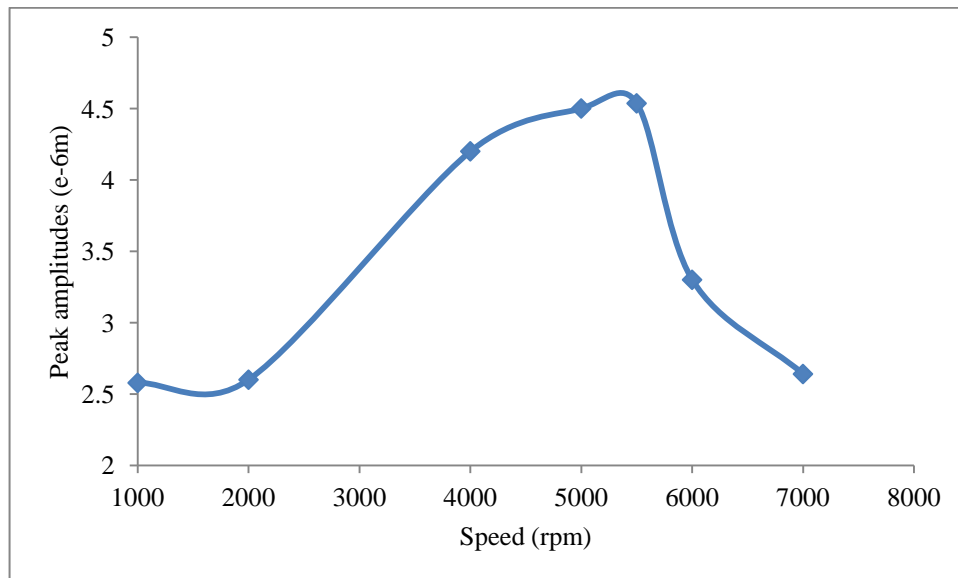
Figure 6.86: Peak amplitude variation in different speeds of operations.

It is seen that, the maximum amplitudes increase from 4000 rpm to 6000 rpm and decreases thereafter. Hence, the shaft stiffness will be added during this region only. While optimizing the difference between the radial deflection at left bearing node with and without rub forces, the following PSO parameters are considered.

Number of variables=2, Swarm size=10, Number of generations =50. Figure 6.87(a) shows the convergence graph during PSO at 4000 rpm rotor speed. At each speed the error is minimized separately and altogether six speeds are considered and corresponding identified added stiffness is shown in the Figure 6.87(b).

147

(a) Fitness convergence trend in PSO   (b) Identified added stiffness
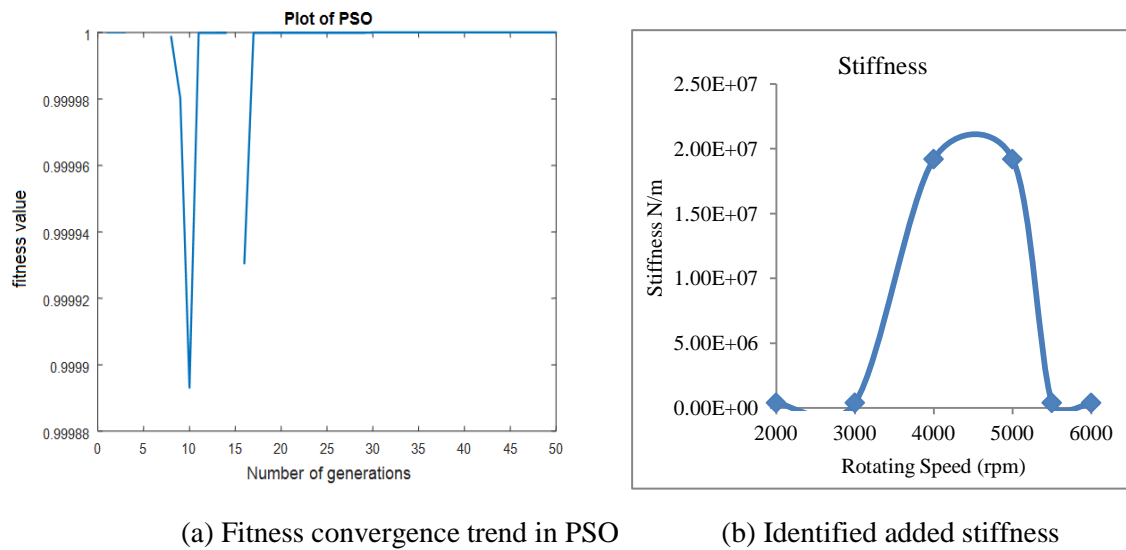
Figure 6.87: Convergence trend and Identified added stiffness in PSO

Likewise, the damping can also be identified.

6.6 Control studies

In this section two types of control strategies are used to attenuate the critical speeds of operations. Semi-active and active controls are used in the simulation to reduce the amplitudes of high amplitude motions.

6.6.1 Semi-active electromagnetic damper

The entire finite element analysis process starting from generation of nodal connectivity and element matrices, assembly together with static condensation for elimination of rotational degrees of freedom and posing boundary conditions is performed by an interactive computer program written in MATLAB. Further, the Campbell diagram for the rotor illustrating variation of its natural frequencies as a function of speed Ω and time-domain characteristics using Wilson-theta implicit time-integration scheme (with step size=1e-4 s) are obtained for the reduced-order system before and after implementing the proposed electromagnetic damper. Main parameters of rotor considered include:

Rotor Shaft:

Outer diameter =25 mm, Inner diameter =15 mm, Material (alloy steel): Elastic modulus E=207 GPa, density ρ=7840 kg/m^3, Poisson ratio μ=0.3, eccentricity of centre of masses (e)=10 microns, shear correction factor k=0.65.

Ball bearings for LPT and LPC sides:

148

Number of ball N=8, radial clearance r_c=20 microns, inner race radius r=20.046 mm, outer race radius R=31.95 mm, contact stiffness at balls C_b=3.527×10^9 N/m$^{3/2}$, ball radius r_b=(R-r-r_c)/2=5.94 mm

Stiffness at both rotor supports on casing=300 kN/m.

Other geometrical data of rotor rig is depicted in Table 6.13.

Table 6.13: Data for the rotor dynamic rig under consideration (+ bearing nodes)

Node Number	Axial distance (mm)	Disk dimensions(mm)	
		Diameter	Thickness
1	0	--	--
2 (LPT disk)	10	150	10
3$^+$	70	--	--
4	195	--	--
5$^+$	320	--	--
6 (LPC disk)	390	150	10
7	400	--	--

Figure 6.88 shows the Campbell diagram of the rotor supported on the casing. As can be seen, the first two critical speeds (about 2684 rpm and 3767 rpm) are in the operating range, while the third is far above.
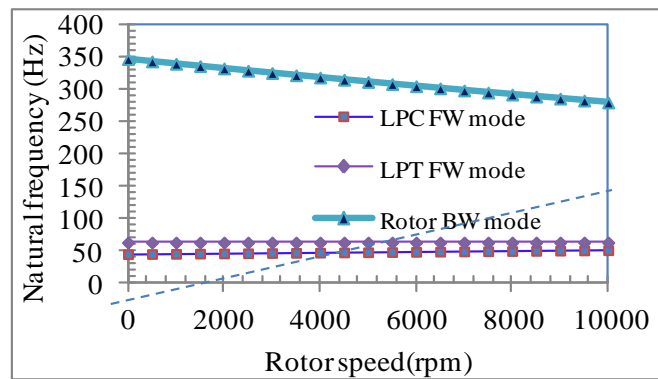
Figure 6.88: Campbell Diagram for supported rotor

Figure 6.89 shows the unbalance response of rotor at the LPT and LPC disks in x and y directions respectively. Figure 6.90 shows the corresponding frequency response curve at the LPT disk in the zone under consideration.

4.1 Electromagnetic Damper Design

During the design of actuators, the following parameters are taken as inputs:

Resonant frequencies at which the dampers should be effective=2500 rpm to 4000 rpm,

Supporting stiffness k_s=300 kN/m

LPC support Damper

Total resistance R=1.1 ohms

Air gap G=0.5 mm,

Number of turns N_t=345,

Wire diameter=0.5 mm,

Coil inductance at nominal air gap/electromagnet L_0=2.5 mH

$\therefore$ ω_{RL}=electromechanical pole frequency=1.1×10^3/2.5=440 rad/s (~ 4201 rpm)

Equivalent damping ratio= 0.0043

Support mass of LPC side m_c=0.287 kg,

Damping coefficient c_c=0.0043 $\sqrt{300\times10^3 / 0.287}$ =4.396 Ns/m.

Mechanical stiffness k_m=$c_c\omega_{RL}$=1934.24 N/m

Supply voltage V=0.2 volts
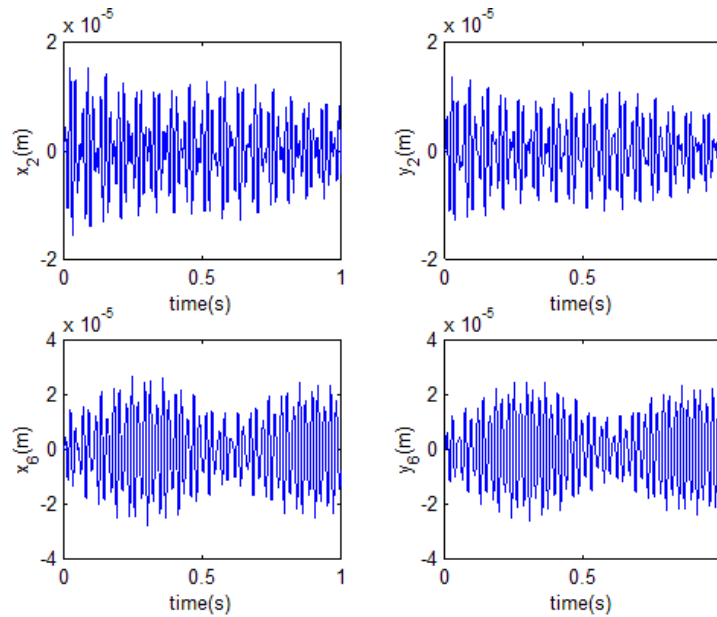
Figure 6.89: Time histories at turbine (suffix 2) and compressor disks (suffix 6) under 2680 rpm
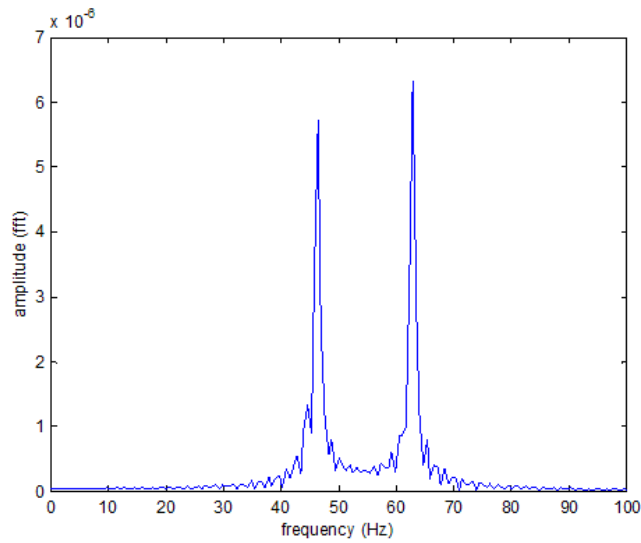
Figure 6.90: Frequency spectrum before application of actuators

Zero frequency $\omega_z = \omega_{RL}\left(1 - \dfrac{2V^2}{R\omega_{RL}G^2 k_m}\right) = 258$ rad/s (~2463 rpm)

LPT support damper

Total resistance R=1.85 ohms

Air gap G=0.5 mm,

Number of turns N_t=352,

Wire diameter=0.5 mm,

Coil inductance at nominal air gap/electromagnet L_0=3.7 mH

$\therefore$ ω_{RL}=electromechanical pole frequency=$1.85 \times 10^3/2.5$=500 rad/s (~ 4774 rpm)

Equivalent damping ratio= 0.003

Support mass m_t=0.19 kg,

Damping coefficient $c_t = 0.003\sqrt{300 \times 10^3 / 0.19}$ =3.7696 Ns/m.

Mechanical stiffness $k_m = c_t \omega_{RL}$=1884.84 N/m

Supply voltage V=0.242 volts

Zero frequency $\omega_z = \omega_{RL}\left(1 - \dfrac{2V^2}{R\omega_{RL}G^2 K_m}\right) = 365$ rad/s (~3485 rpm)

Activating the two damper systems in respective speed ranges, an unbalance response as shown in Figure 6.91 is obtained. It is seen that outside the selected region,

the amplitudes are not much affected. Figure 6.92 shows the time-varying damping forces acting on the supports so as to attenuate the vibration amplitudes in first two critical speeds regions.
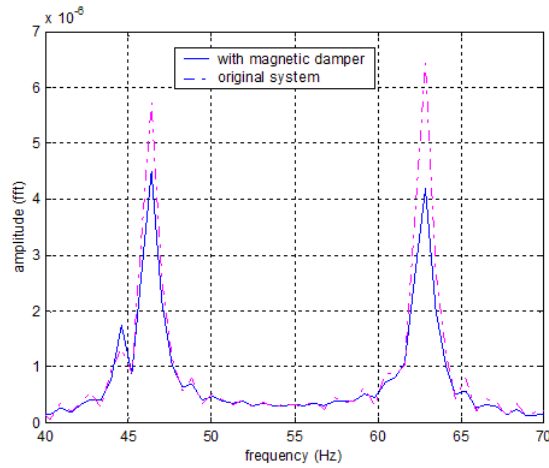
Figure 6.91: Unbalance response with the actuator system
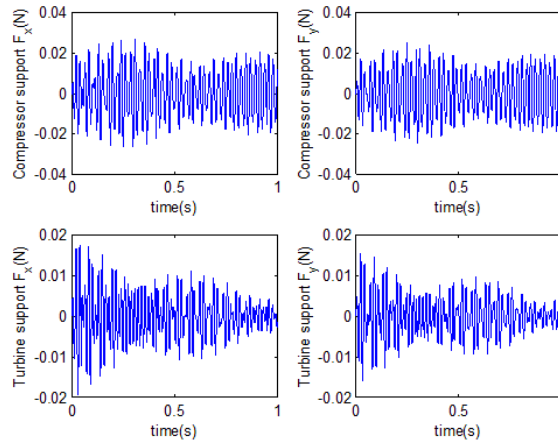
Figure 6.92: Corresponding damping forces

The system is under the action of equivalent spring k_{eq} from 0 to ω_Z rad/s and under the mechanical stiffness k_m in the range beyond ω_{RL}. The spring forces can also be likewise plotted to show their effective ranges.

6.6.2 Active EM actuator

The dimensional properties of the rotor used in the analysis shown in Table 6.14. The material for the spools is steel with elastic modulus E=210 GPa and density ρ=7800 kg/m^3. All four disks have polar moment of inertia (I_P) twice the diametral mass moment of inertia (I_D). Further, an unbalance of 10 microns is considered in the disks. The

resultant stiffness, mass, damping (damping ratio of 0.01) and gyroscopic matrices are used. The values of ω is set as 200 rad/s and angular acceleration α is varied.

Table 6.14: Geometric and material data for rotor

Node	Axial dist.(mm)	d_{outer} (mm)	d_{inner} (mm)	Disc mass(kg)	IP (kg-mm2)
1	0	30.4	0	-	-
2	76.2	30.4	0	4.904	0.02712
3	323.85	30.4	0	-	-
4	406.4	30.4	0	-	-
5	457.2	30.4	0	4.203	0.02034
6	508	30.4	0	-	-
7	152.4	50.8	38.1	-	-
8	203.2	50.8	38.1	3.327	0.01469
9	355.6	50.8	38.1	2.227	0.0972
10	406.4	50.8	38.1	-	-

Figure 6.93 shows the frequency response plot for the system with and without considering ball bearing forces. It is seen that there are multiple ball passing frequencies (VC) along with harmonics in the system.
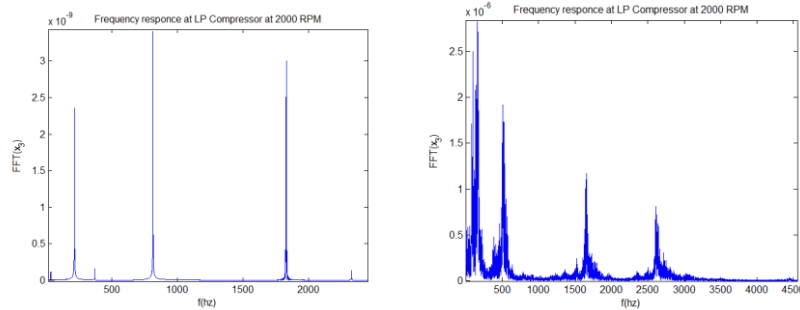
(a) Bearings as spring damper system [22]   (b) Bearings with forces considered

Figure 6.93: Frequency response of the rotor at 2000 rpm

Figure 6.94 shows the transient analysis results at different acceleration conditions in terms of frequency responses. It is obvious that there are multiplicities of ball passing frequencies increase with acceleration of rotor. This may be due to a randomly changing bearing excitation. In order to minimize the amplitude levels, the following electromagnetic actuator parameters are considered: A_g=240 mm^2, N=106, α=22.5°, G=0.9 mm and I_b=3 A. The instantaneous current components i_1 and i_2 depend on the displacements x and y at the disk node-1.
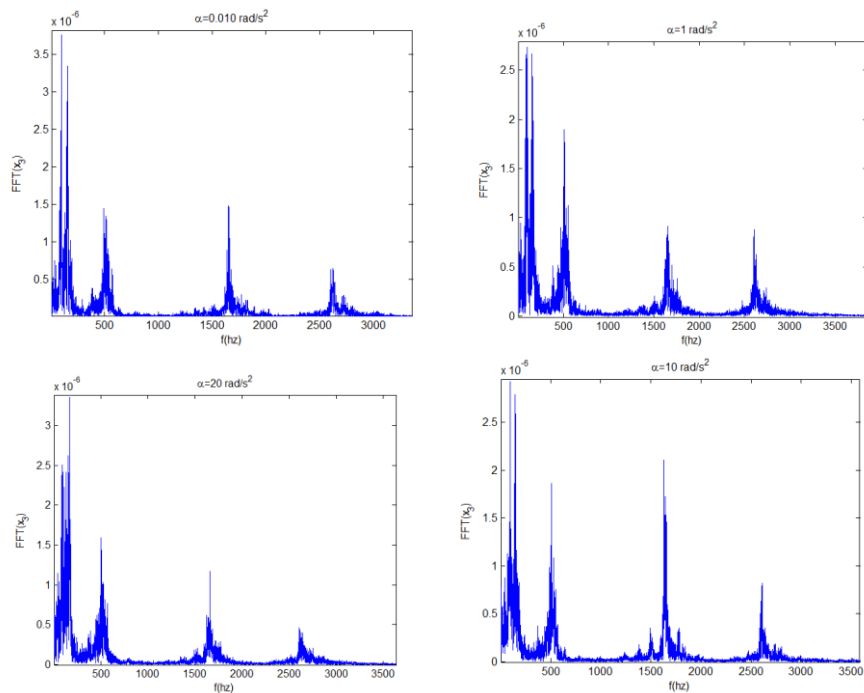
Figure 6.94: Effect of acceleration of rotor at LP compressor disk

Computer program is modified such that the right hand side force vector carries additional magnetic force compoents at the disk-1 node. Figure 6.95 shows the frequency response of the rotor computed with and without control. It indicates that the amplitudes from second mode have reduced drastically and the ball passing frequency amplitudes have been dropped. The methodology can be extended for other nodes of interest also.
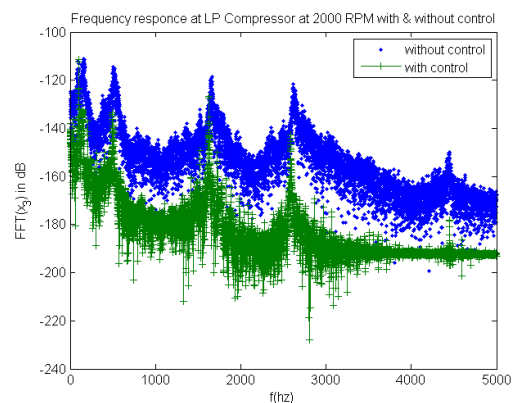
Figure 6.95: Amplitude reduction with controller

Linearly predicted unstable modes are helpful to obtain deeper insights into the nonlinear simulated results.

Figure 6.96 shows the multi-frequency unbalance response as the phase-diagram and Poincare map at compressor disk node, when the rotor is running at 500 rpm. It is seen that the motion is of period 3 non-synchronous vibratory nature.
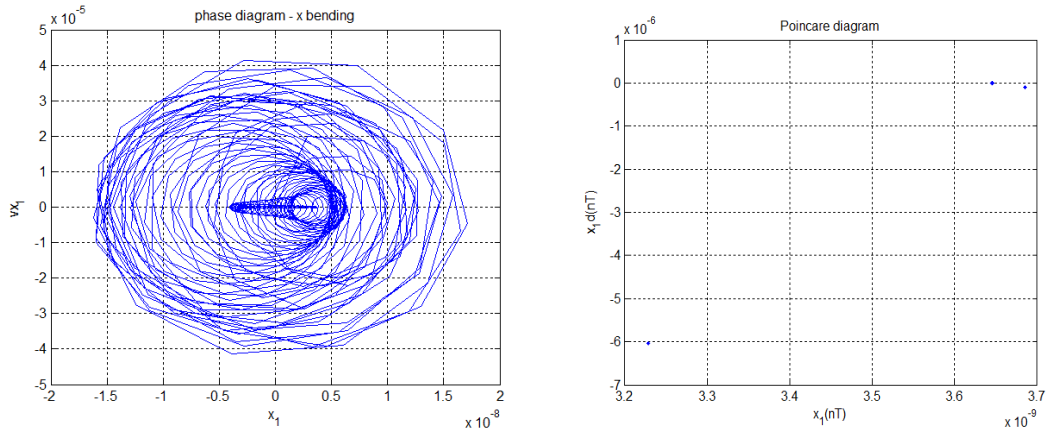
Figure 6.96: Phase diagram and Poincare map at compressor disk node (Ω=500 rpm)

As the rotor speed increases the motion becomes multi-periodic as seen in Figure 6.97. The motion becomes of quasi-period as the rotor speed reaches 40000 rpm as seen from Figure 6.98.

In order to minimize the vibration amplitudes at the compressor disk over the entire operating speed range, electromagnetic actuator is designed such that a null value of displacement and velocity should be achieved at the node. Here all the initial conditions are taken zero and static condensation is employed to eliminate the rotational degrees of freedom. Effect of axial deformation is not considered during modeling.

(a) 2000 rpm   (b)20000 rpm
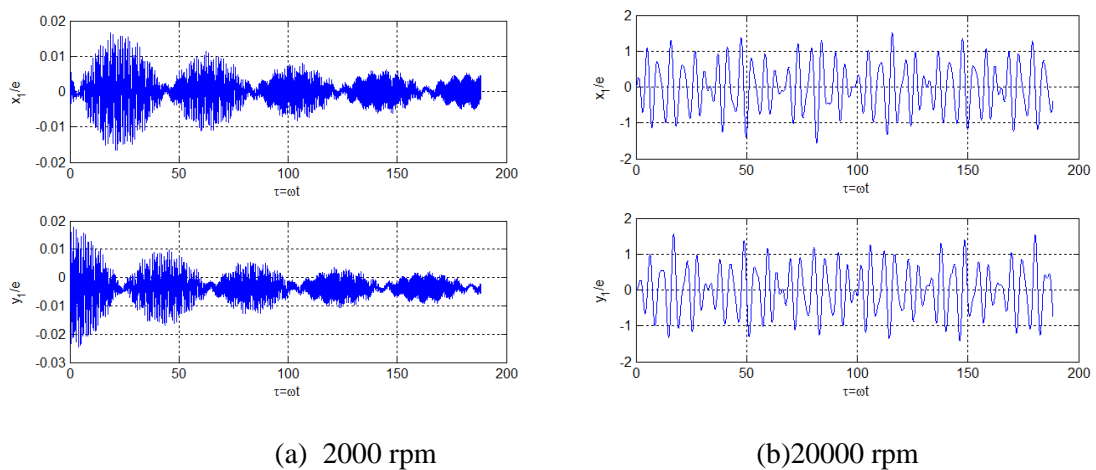
Figure 6.97: Time domain response at compressor (left) disk node
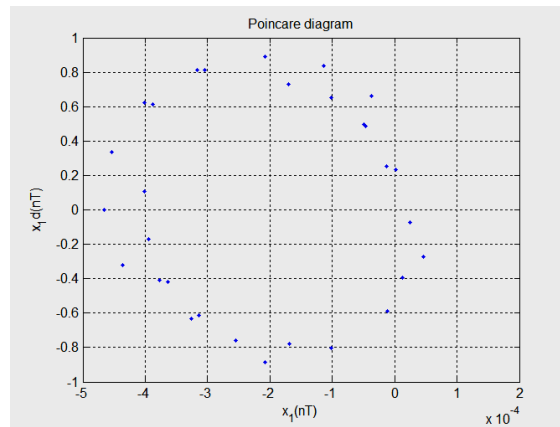
Figure 6.98: Poincare map (closed curve) at node 1 in x-direction (40000 rpm)

Figure 6.99 shows the block diagram of control system logic.
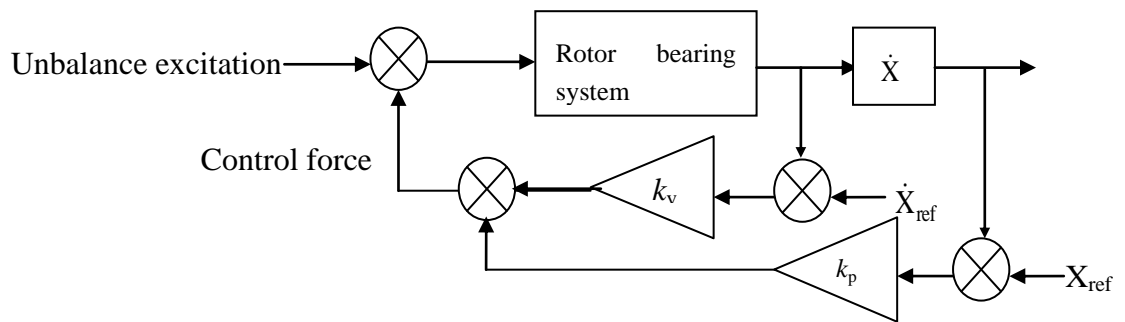
Figure 6.99: Proportional-Derivative control strategy for controlling vibrations at a disk

Here the proportional and derivative gains k_p and k_v are selected as 10 and 0.1 respectively.   Other parameters include: A_g=240 mm^2, N=106, α=22.5^o, G=0.9 mm and I_b=3 A. The instantaneous current components i_1 and i_2 depend on the displacements x and y at the disk node-1. Computer program is modified such that the right hand side force vector carries additional magnetic force compoents at the disk node.

(a) Before   (b) after
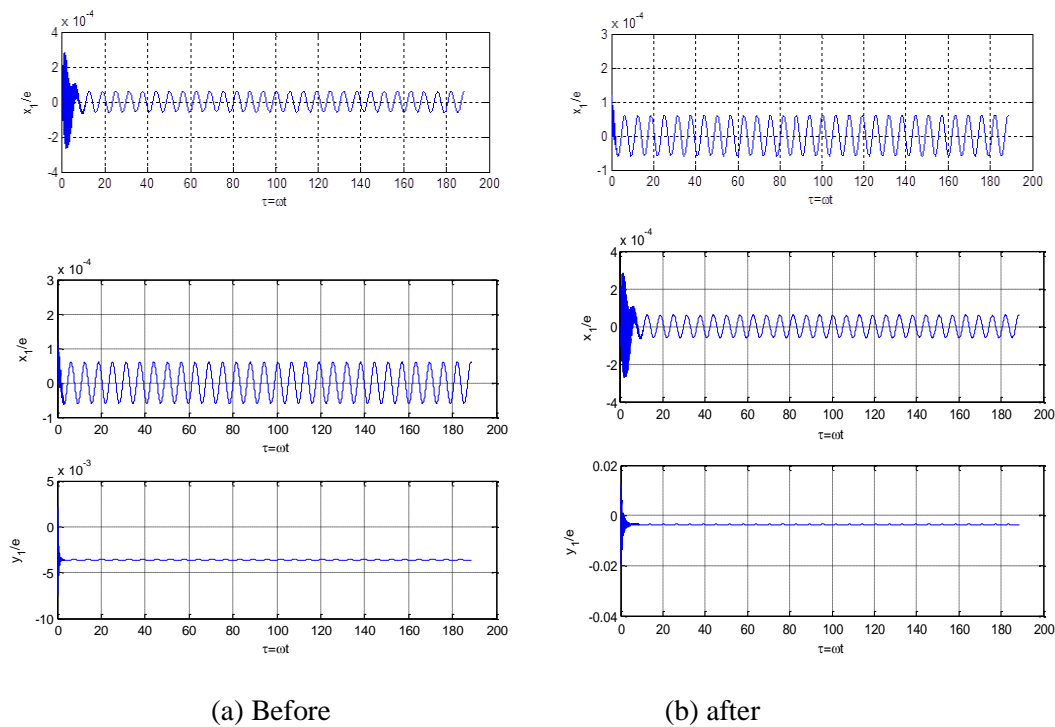
Figure 6.100: Time histories before and after control

Figure 6.100 shows the non-dimensional time response at the compressor node in the x-direction with and without control. It is seen that initial chaotic motion has reduced in addition to amplitude reduction.

Figure 6.101 shows the corresponding frequency response of the rotor computed with and without control. In absence of control, it is obvious that the rotor resonates at 450 Hz and after that the unstable motion persists due to the rotary force generated by internal damping of the shaft.
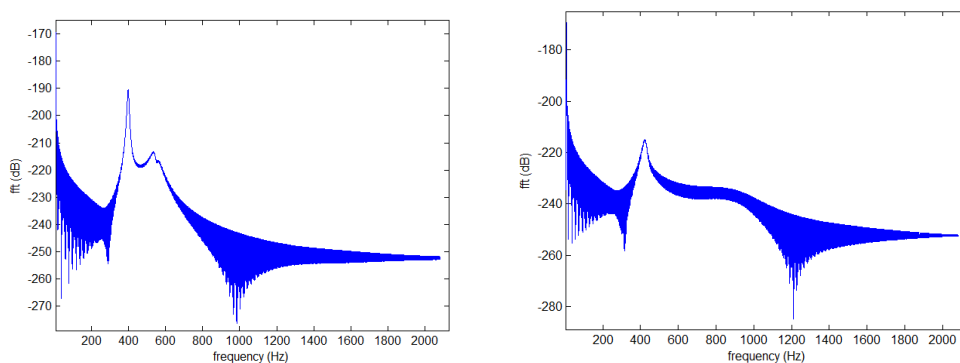
Figure 6.101: Amplitude reduction at critical speed without and with controller

From the above plots, it can be observed that with the aid of proportional derivative the high amplitudes are reduced to the reasonable levels. The main advantage of control is

to attenuate high amplitudes in the operations and to prevent the rotor from the dangerous damaging conditions.

6.7 Concluding remarks

Dynamic modelling of a rotor supported over ball bearings presented initially and the disk- shaft bearing system has been analyzed using Timoshenko beam elements by considering ball bearing contact forces and Muszyska's force at seal disk interface and the model was simulated as a real time system. Gyroscopic effects due to both shaft and disks were taken into account and unbalance was considered for both the disks. Secondly, a hollow aero- engine rotor supported over engine housing with compressor and turbine was modelled and a semi active technique for vibration attenuation through electromagnetic actuator has been presented.

Chapter 7

Conclusions and Future scope

Dynamic analysis of low pressure and twin spool rotors supported over the bearings is presented using finite element modelling. The results are presented in terms of natural frequencies, mode shapes and Campbell diagram plots and these results are compared with the Ansys models. The nonlinear dynamic Hertzian contact bearing forces and the squeeze film damping forces were accounted in the modelling.

A scaled prototype of low pressure rotor supported over ball bearing system is fabricated and its modal characteristics were obtained using impact hammer test. The responses of this scaled rotor were compared with the nonlinear single row ball bearing model at various speeds and the single row ball bearing with SFD model is further simulated to carry out parametric studies. After validating these results, this model was further extended to double row ball bearing nonlinear force model. A rub inducing set up was prepared on scaled rotor. The simulation of this rub was performed by advancing the nut and bolt mechanism at different angular positions around the left disk. The nonlinear Muszynska's gas excitation forces are also introduced in the system at disk locations. The simulation of this rub was performed by advancing the nut and bolt mechanism at different angular positions around the left disk.

As next piece of work, different faults are considered in the modelling the bearings. Two types of faults considered in the modelling. Firstly, local faults like dents and spills in the bearings and races and secondly, distributed waviness of the races also considered in the modelling. Parameter identification of rotor carried out by taking frequency and the time history of the rotor as inputs and the radial clearance, unbalance and centralising spring stiffness as the output parameters. Bearing fault classification was also carried out in the research. Additional stiffness of rotor due to rub was identified through optimization scheme.

Finally, control of the rotor was performed by two approaches in the work. First one is Semi active magnetic damper (SAMD) and the other is active magnetic control. The effectiveness of different parameters of EM damper was studied on control using electromagnetic excitation. User-interactive programs developed in this work help in selecting the condition of the rotor bearing systems and allow in incorporating appropriate control scheme for the rotor.

7.1 Summary

Following brief conclusions are drawn out of the work

- The effect of bearing clearance, disc eccentricity and centralizing spring stiffness of SFD have marked effect on the dynamic response of rotor.
- The rubbing of the rotor with the stator was modelled as nonlinear excitation forces in the model.
- The nonlinear Muszynska's gas excitation forces are also introduced in the system at disk locations.
- In active control methodology, an existing proportional-derivative (PD) control approach is studied and a neural network based controller for prediction of electromagnetic actuator coil currents is designed and tested for twin-spool rotor system.
- Of all the neural network models used for bearing fault identification, the PNN and self organization map networks have given reliable results.
- Identification of shaft stiffening due to rub impact by the proposed optimization has given interesting results.
- The control schemes proposed can be applied any kind of rotors using simple simulation codes.
- A user-interactive program has been developed to incorporate the nonlinear bearing forces.

7.2 Future Scope

As a future scope of the work, 3D modelling of rub impact using contact theory may be attempted to validate the present results. Further, the gas forces effect on a disc (rotor as a whole) has to be studied experimentally by injecting high pressure compressed air on to the disc surface on the fabricated model. Also, as a last study the active magnetic exciter system studied theoretically in this work must be fabricated and mounted over the rotor surface to see the controlled responses in the rotor.

References

[1]   C. S. Sunnersjo, "Varying compliance vibrations of rolling bearings," *J. Sound Vib.*, vol. 58, no. 3, pp. 363–373, 1978.

[2]   H. T. S Fukata, E HGad, T Koudou, T Ayabe, "On the radial vibration of ball bearings," *Bull. JSME*, vol. 28, no. 239, pp. 899–904, 1985.

[3]   T. A. Harris, *Rolling Bearing Analysis*, 1st ed. New York: Wiley, 1966.

[4]   A. Palmgren, *Ball and Roller Bearing Engineering*, 3rd ed. Philadelphia, 1959.

[5]   T. C. Lim and R. Singh, "Vibration transmission through rolling element bearings, part I: Bearing stiffness formulation," *J. Sound Vib.*, vol. 139, no. 2, pp. 179–199, 1990.

[6]   T. C. Lim and R. Singh, "Vibration transmission through rolling element bearings, part II: System studies," *J. Sound Vib.*, vol. 139, no. 2, pp. 201–225, 1990.

[7]   T. C. Lim and R. Singh, "Vibration transmission through rolling element bearings. Part III. Geared rotor system studies," *J. Sound Vib.*, vol. 151, no. 1, pp. 31–54, 1991.

[8]   T. C. Lim and R. Singh, "Vibration transmission through rolling element bearings, part IV: statistical energy analysis," *J. Sound Vib.*, vol. 153, no. 1, pp. 37–50, 1992.

[9]   B. Mevel and J.L.Guyader, "Bearing 1993 Mavel.PDF." Journal of sound and Vibration, pp. 471–487, 1993.

[10]   D. Han, S. Choi, Y. Lee, and K. Kim, "The nonlinear and ball pass effects of a ball bearing on rotor vibration," *J. Mech. Sci. Technol.*, vol. 12, no. 3, pp. 396–404, 1998.

[11]   M. Tadina and M. Boltezar, "Improved model of a ball bearing for the simulation of vibration signals due to faults during run-up," *J. Sound Vib.*, vol. 330, no. 17, pp. 4287–4301, 2011.

[12]   K. G. and O. P. M. Tiwari, "Experimental study of a rotor supported by deep groove ball bearing," *Int. J. Rotating Mach.*, vol. 8, no. 4, pp. 243–258, 2002.

[13]   S. P. Harsha, "Nonlinear dynamic response of a balanced rotor supported by rolling element bearings due to radial internal clearance effect," *Mech. Mach. Theory*, vol. 41, no. 6, pp. 688–706, 2006.

[14]   X. Qing-yu, Zhang Xiao-long, B Chang-qing, "Nonlinear Stability of Balanced Rotor Due To Effect of Ball Bearing Internal Clearance," *Appl. Math. Mech.*, vol. 27, no. 2, pp. 175–186, 2006.

[15]   M. Tiwari, K. Gupta, and O. Prakash, "Dynamic Response of an Unbalanced Rotor Supported on Ball Bearings," *J. Sound Vib.*, vol. 238, no. 5, pp. 757–779, 2000.

[16]   Y. Kang, C.C. Huang, C.S. Lin, P.C. Shen, and Y.P. Chang, "Stiffness determination of angular-contact ball bearings by using neural network," *Tribol. Int.*, vol. 39, no. 6, pp. 461–469, 2006.

[17] Z. Kiral and H. Karagülle, "Simulation and analysis of vibration signals generated by rolling element bearing with defects," *Tribol. Int.*, vol. 36, no. 9, pp. 667–678, 2003.

[18] G. H. Jang and S. W. Jeong, "Nonlinear excitation model of ball bearing waviness in a rigid rotor supported by two or more ball bearings considering five degrees of freedom," *J. Tribol. Asme*, vol. 124, no. 1, pp. 82–90, 2002.

[19] S. P. Harsha and P. K. Kankar, "Stability analysis of a rotor bearing system due to surface waviness and number of balls," *Int. J. Mech. Sci.*, vol. 46, no. 7, pp. 1057–1081, 2004.

[20] S. P. Harsha, K. Sandeep, and R. Prakash, "Non-linear dynamic behaviours of rolling element bearings due to surface waviness," *J. Sound Vib.*, vol. 272, no. 3–5, pp. 557–580, 2004.

[21] G. Jang and S. W. Jeong, "Vibration analysis of a rotating system due to the effect of ball bearing waviness," *J. Sound Vib.*, vol. 269, no. 3–5, pp. 709–726, 2004.

[22] K. C. Panda and J. K. Dutt, "Optimum support characteristics for rotor-shaft system with preloaded rolling element bearings," *J. Sound Vib.*, vol. 260, no. 4, pp. 731–755, 2003.

[23] J. J. Sinou, "Non-linear dynamics and contacts of an unbalanced flexible rotor supported on ball bearings," *Mech. Mach. Theory*, vol. 44, no. 9, pp. 1713–1732, 2009.

[24] C. V. S. Villa, "Investigation of a Rotor- Bearing System with Bearing Clearances and Hertz Contact by Using a Harmonic Balance Method," vol. XXIX, no. 1, pp. 14–20, 2007.

[25] X. Shen, J. Jia, M. Zhao, and J. Jing, "Experimental and numerical analysis of nonlinear dynamics of rotor–bearing–seal system," *Nonlinear Dyn.*, vol. 53, no. 1–2, pp. 31–44, 2007.

[26] M. Cao and J. Xiao, "A comprehensive dynamic model of double-row spherical roller bearing-Model development and case studies on surface defects, preloads, and radial clearance," *Mech. Syst. Signal Process.*, vol. 22, no. 2, pp. 467–489, 2008.

[27] P. M. Hai and P. Bonello, "An impulsive receptance technique for the time domain computation of the vibration of a whole aero-engine model with nonlinear bearings," *J. Sound Vib.*, vol. 318, no. 3, pp. 592–605, 2008.

[28] X. Wenhui, T. Yougang, and C. Yushu, "Analysis of motion stability of the flexible rotor-bearing system with two unbalanced disks," *J. Sound Vib.*, vol. 310, no. 1–2, pp. 381–393, 2008.

[29] P. Bonello and P. Minh Hai, "A receptance harmonic balance technique for the computation of the vibration of a whole aero-engine model with nonlinear bearings," *J. Sound Vib.*, vol. 324, no. 1–2, pp. 221–242, 2009.

[30] G Chen, "Study on Nonlinear Dynamic Response of an Unbalanced Rotor Supported on Ball Bearing"," *J. Vib. Acoust.*, vol. 131, no. 1, pp. 1–9, 2009.

[31] G. Chen, "A New Rotor-Ball Bearing-Stator Coupling Dynamics Model for Whole Aero-Engine Vibration," *J. Vib. Acoust.*, vol. 131, no. 6, pp. 061009–9, 2009.

[32] E. Laniado-Jcome, J. Meneses-Alonso, and V. Diaz-Lpez, "A study of sliding between rollers and races in a roller bearing with a numerical model for mechanical event simulations," *Tribol. Int.*, vol. 43, no. 11, pp. 2175–2182, 2010.

[33] A. Rafsanjani, S. Abbasion, A. Farshidianfar, and H. Moeenfard, "Nonlinear dynamic modeling of surface defects in rolling element bearing systems," *J. Sound Vib.*, vol. 319, no. 3–5, pp. 1150–1174, 2009.

[34] M. C. Ricci, "Internal loading distribution in statically loaded ball bearings subjected to an eccentric thrust load," *Math. Probl. Eng.*, vol. 2009, no. 471804, p. 36, 2009.

[35] C. Bai, H. Zhang, and Q. Xu, "Experimental and Numerical Studies on Nonlinear Dynamic Behaviour of Rotor System Supported by Ball Bearings," *J. Eng. Gas Turbines Power*, vol. 132, no. 8, p. 082502, 2010.

[36] S. H. Ghafari, E. M. Abdel-Rahman, F. Golnaraghi, and F. Ismail, "Vibrations of balanced fault-free ball bearings," *J. Sound Vib.*, vol. 329, no. 9, pp. 1332–1347, 2010.

[37] M. S. Patil, J. Mathew, P. K. Rajendrakumar, and S. Desai, "A theoretical model to predict the effect of localized defect on vibrations associated with ball bearing," *Int. J. Mech. Sci.*, vol. 52, no. 9, pp. 1193–1201, 2010.

[38] R. Tomovic, V. Miltenovic, M. Banic, and A. Miltenovic, "Vibration response of rigid rotor in unloaded rolling element bearing," *Int. J. Mech. Sci.*, vol. 52, no. 9, pp. 1176–1185, 2010.

[39] M. Abbes and T. Hentati, "Dynamic analysis of helical gears supported by rolling elements bearings," *J. Theor. ...*, vol. 41, no. 1, pp. 33–50, 2011.

[40] A. Ashtekar and F. Sadeghi, "Experimental and Analytical Investigation of High Speed Turbocharger Ball Bearings," *J. Eng. Gas Turbines Power*, vol. 133, no. 12, p. 122501, 2011.

[41] A. Aram, A. Hosseinzadeh, and M. S. Foumani, "Analytical approach to dynamic and vibration analysis of a spherical ball under contact stress," *Sci. Iran.*, vol. 18, no. 6, pp. 1306–1312, 2011.

[42] T. Gupta, K. Gupta, and D. Sehgal, "Instability and chaos of a flexible rotor ball bearing system: an investigation on the influence of rotating imbalance and bearing clearance," *J. Eng. gas turbines ...*, vol. 133, no. 8, p. 082501, 2011.

[43] P. K. Kankar, S. C. Sharma, and S. P. Harsha, "Fault diagnosis of ball bearings using machine learning methods," *Expert Syst. Appl.*, vol. 38, no. 3, pp. 1876–1886, 2011.

[44] P. K. Kankar, S. C. Sharma, and S. P. Harsha, "Fault Diagnosis of High Speed Rolling Element Bearings Due to Localized Defects Using Response Surface Method," *J. Dyn. Syst. Meas. Control*, vol. 133, no. 3, p. 031007, 2011.

[45] K. Kappaganthu and C. Nataraj, "Nonlinear modeling and analysis of a rolling

element bearing with a clearance," *Commun. Nonlinear Sci. Numer. Simul.*, vol. 16, no. 10, pp. 4134–4145, 2011.

[46] C. Nataraj, "Vibration-based diagnostics of rolling element bearings : state of the art and challenges," in *13thWorld Congress in Mechanism and Machine Science, Guanajuato,M´exico, 19-25 June, 2011*, 2011, p. A17_603.

[47] W. Li, Y. Yang, D. Sheng, and J. Chen, "A novel nonlinear model of rotor/bearing/seal system and numerical analysis," *Mech. Mach. Theory*, vol. 46, no. 5, pp. 618–631, 2011.

[48] M. Nakhaeinejad and M. D. Bryant, "Dynamic Modeling of Rolling Element Bearings With Surface Contact Defects Using Bond Graphs," *J. Tribol.*, vol. 133, no. 1, pp. 041103(1–8), 2010.

[49] R. B. Randall and J. Antoni, "Rolling element bearing diagnostics-A tutorial," *Mech. Syst. Signal Process.*, vol. 25, no. 2, pp. 485–520, 2011.

[50] N. Sawalhi and R. B. Randall, "Vibration response of spalled rolling element bearings: Observations, simulations and signal processing techniques to track the spall size," *Mech. Syst. Signal Process.*, vol. 25, no. 3, pp. 846–870, 2011.

[51] J. Zapoměl and P. Ferfecki, "A computational investigation on the reducing lateral vibration of rotors with rolling-element bearings passing through critical speeds by means of tuning the stiffness of the system supports," *Mech. Mach. Theory*, vol. 46, no. 5, pp. 707–724, 2011.

[52] W. J. Chen, "Rotordynamics and bearing design of turbochargers," *Mech. Syst. Signal Process.*, vol. 29, pp. 77–89, 2012.

[53] A. Gunduz, J. T. Dreyer, and R. Singh, "Effect of bearing preloads on the modal characteristics of a shaft-bearing assembly: Experiments on double row angular contact ball bearings," *Mech. Syst. Signal Process.*, vol. 31, pp. 176–195, 2012.

[54] P. K. Kankar, S. C. Sharma, and S. P. Harsha, "Nonlinear Vibration Signature Analysis of a High Speed Rotor Bearing System Due to Race Imperfection," *J. Comput. Nonlinear Dyn.*, vol. 7, no. 1, p. 11014, 2011.

[55] L. X. Xu, Y. H. Yang, Y. G. Li, C. N. Li, and S. Y. Wang, "Modeling and analysis of planar multibody systems containing deep groove ball bearing with clearance," *Mech. Mach. Theory*, vol. 56, pp. 69–88, 2012.

[56] L. X. Xu and Y. G. Li, "An approach for calculating the dynamic load of deep groove ball bearing joints in planar multibody systems," *Nonlinear Dyn.*, vol. 70, no. 3, pp. 2145–2161, 2012.

[57] F. Cong, J. Chen, G. Dong, and M. Pecht, "Vibration model of rolling element bearings in a rotor-bearing system for fault diagnosis," *J. Sound Vib.*, vol. 332, no. 8, pp. 2081–2097, 2013.

[58] K. H. Groves and P. Bonello, "Empirical identification of squeeze-film damper bearings using neural networks," *Mech. Syst. Signal Process.*, vol. 35, no. 1–2, pp. 307–323, 2013.

[59] A. Gunduz and R. Singh, "Stiffness matrix formulation for double row angular

contact ball bearings: Analytical development and validation," *J. Sound Vib.*, vol. 332, no. 22, pp. 5898–5916, 2013.

[60] P. K. Kankar, S. C. Sharma, and S. P. Harsha, "Fault diagnosis of rolling element bearing using cyclic autocorrelation and wavelet transform," *Neurocomputing*, vol. 110, pp. 9–17, 2013.

[61] S. Lahriri and I. F. Santos, "Experimental quantification of dynamic forces and shaft motion in two different types of backup bearings under several contact conditions," *Mech. Syst. Signal Process.*, vol. 40, no. 1, pp. 301–321, 2013.

[62] B. Muruganatham, M. A. Sanjith, B. Krishnakumar, and S. A. V Satya Murty, "Roller element bearing fault diagnosis using singular spectrum analysis," *Mech. Syst. Signal Process.*, vol. 35, no. 1–2, pp. 150–166, 2013.

[63] J. Takabi and M. M. Khonsari, "Experimental testing and thermal analysis of ball bearings," *Tribol. Int.*, vol. 60, pp. 93–103, 2013.

[64] L. Tian, W. J. Wang, and Z. J. Peng, "Nonlinear effects of unbalance in the rotor-floating ring bearing system of turbochargers," *Mech. Syst. Signal Process.*, vol. 34, no. 1–2, pp. 298–320, 2013.

[65] Z. Ye, L. Wang, L. Gu, and C. Zhang, "Effects of tilted misalignment on loading characteristics of cylindrical roller bearings," *Mech. Mach. Theory*, vol. 69, no. 92, pp. 153–167, 2013.

[66] X. Zhang, Q. Han, Z. Peng, and F. Chu, "Stability analysis of a rotor-bearing system with time-varying bearing stiffness due to finite number of balls and unbalanced force," *J. Sound Vib.*, vol. 332, no. 25, pp. 6768–6784, 2013.

[67] W. Harrer, M. Deluca, and R. Morrell, "Failure analysis of a ceramic ball race bearing made of Y-TZP zirconia," *Eng. Fail. Anal.*, vol. 36, pp. 262–268, 2014.

[68] W. Jacobs, R. Boonen, P. Sas, and D. Moens, "The influence of the lubricant film on the stiffness and damping characteristics of a deep groove ball bearing," *Mech. Syst. Signal Process.*, vol. 42, no. 1–2, pp. 335–350, 2014.

[69] G. Kogan, R. Klein, A. Kushnirsky, and J. Bortman, "Toward a 3D dynamic model of a faulty duplex ball bearing," *Mech. Syst. Signal Process.*, vol. 54, pp. 243–258, 2015.

[70] A. V. Korolev, A. A. Korolev, and R. Krehel, "Character of distribution of the load between the balls in the ball bearings under the action combined of external load," *Mech. Mach. Theory*, vol. 81, pp. 54–61, 2014.

[71] F. Nonato and K. L. Cavalca, "An approach for including the stiffness and damping of elastohydrodynamic point contacts in deep groove ball bearing equilibrium models," *J. Sound Vib.*, vol. 333, no. 25, pp. 6960–6978, 2014.

[72] D. Petersen and C. Howard, "Bearing defect size estimation for extended raceway defects," in *inter.noise 2014,Melbourne, Australia*, pp. 1–10.

[73] D. S. Shah and V. N. Patel, "ScienceDirect A Review of Dynamic Modeling and Fault Identifications Methods for Rolling Element Bearing," *Procedia Technol.*, vol. 14, pp. 447–456, 2014.

[74]   X. Sheng, B. Li, Z. Wu, and H. Li, "Calculation of ball bearing speed-varying stiffness," *Mech. Mach. Theory*, vol. 81, pp. 166–180, 2014.

[75]   S. Singh, U. G. Köpke, C. Q. Howard, and D. Petersen, "Analyses of contact forces and vibration response for a defective rolling element bearing using an explicit dynamics finite element model," *J. Sound Vib.*, vol. 333, no. 21, pp. 5356–5377, 2014.

[76]   H. L. Zhou, G. Q. Feng, G. H. Luo, Y. T. Ai, and D. Sun, "The dynamic characteristics of a rotor supported on ball bearings with different floating ring squeeze film dampers," *Mech. Mach. Theory*, vol. 80, pp. 200–213, 2014.

[77]   Y. Zhuo, X. Zhou, and C. Yang, "Dynamic analysis of double-row self-aligning ball bearings due to applied loads, internal clearance, surface waviness and number of balls," *J. Sound Vib.*, vol. 333, no. 23, pp. 6170–6189, 2014.

[78]   Q. Han and F. Chu, "Nonlinear dynamic model for skidding behaviour of angular contact ball bearings," *J. Sound Vib.*, vol. 354, pp. 219–235, 2015.

[79]   A. Moazen Ahmadi, D. Petersen, and C. Howard, "A nonlinear dynamic vibration model of defective bearings - The importance of modelling the finite size of rolling elements," *Mech. Syst. Signal Process.*, vol. 52–53, no. 1, pp. 309–326, 2015.

[80]   E. Kurvinen, J. Sopanen, and A. Mikkola, "Ball bearing model performance on various sized rotors with and without centrifugal and gyroscopic forces," *Mech. Mach. Theory*, vol. 90, pp. 240–260, 2015.

[81]   Y. Li, H. Cao, L. Niu, and X. Jin, "A General Method for the Dynamic Modeling of Ball Bearing–Rotor Systems," *J. Manuf. Sci. Eng.*, vol. 137, no. 2, p. 21016, 2015.

[82]   D. Petersen, C. Howard, N. Sawalhi, A. Moazen Ahmadi, and S. Singh, "Analysis of bearing stiffness variations, contact forces and vibrations in radially loaded double row rolling element bearings with raceway defects," *Mech. Syst. Signal Process.*, vol. 50–51, pp. 139–160, 2015.

[83]   X. Zhang, Q. Han, Z. Peng, and F. Chu, "A new nonlinear dynamic model of the rotor-bearing system considering preload and varying contact angle of the bearing," *Commun. Nonlinear Sci. Numer. Simul.*, vol. 22, no. 1–3, pp. 821–841, 2015.

[84]   H. D. Nelson, "A Finite Rotating Shaft Element Using Timoshenko Beam Theory," *J. Mech. Des.*, vol. 102, no. 4, pp. 793–803, 1980.

[85]   A. Muszynska, "Whirl and whip-Rotor/bearing stability problems," *J. Sound Vib.*, vol. 110, no. 3, pp. 443–462, 1986.

[86]   V. Ramamurthi, "Finite element calculation of critical speeds of rotation of shafts with gyroscopic action of discs," *J. Sound Vib.*, vol. 117, no. 3, pp. 578–582, 1987.

[87]   A. Muszynska and D. E. Bently, "Frequency-swept rotating input perturbation techniques and identification of the fluid force models in rotor/bearing/seal systems and fluid handling machines," *J. Sound Vib.*, vol. 143, no. 1, pp. 103–124, 1990.

[88]   Y.-B. Kim and S. T. Noah, "Quasi-Periodic Response and Stability Analysis for a

Non-Linear Jeffcott Rotor," *J. Sound Vib.*, vol. 190, no. 2, pp. 239–253, 1996.

[89]   cheng X. M. Qing Hua Qin, "Coupled torsional-flexural vibration of shaft systems in mechanical engineering-II. FE-TM impedance coupling method," *Comput. Struct.*, vol. 58, no. 4, pp. 845–849, 1996.

[90]   H. Q. Qing and X. M. Cheng, "Coupled torsional-flexural vibration of shaft systems in mechanical engineering - I. Finite element model," *Comput. Struct.*, vol. 58, no. 4, pp. 835–843, 1996.

[91]   R. Tiwari and N. S. Vyas, "Stiffness estimation from random response in multi-mass rotor bearing systems," *Probabilistic Eng. Mech.*, vol. 13, no. 4, pp. 255–268, 1998.

[92]   I. Nagasaka, J. Liu, and Y. Ishida, "Forced Vibrations of a Very Slender Continuous Rotor With Geometrical Nonlinearity (Harmonic and Subharmonic Resonances)," *J. Vib. Acoust.*, vol. 132, no. 2, pp. 021004–9, 2010.

[93]   M. Tiwari, K. Gupta, and O. Prakash, "Effect of Radial Internal Clearance of a Ball Bearing on the Dynamics of a Balanced Horizontal Rotor," *J. Sound Vib.*, vol. 238, no. 5, pp. 723–756, 2000.

[94]   R. Ganguli, "A fuzzy logic system for ground based structural health monitoring of a helicopter rotor using modal data," *J. Intell. Mater. Syst. Struct.*, vol. 12, no. 6, pp. 397–407, 2001.

[95]   S. Zhou and J. Shi, "Identification of non-linear effects in rotor systems using recursive QR factorization method," *J. Sound Vib.*, vol. 270, no. 1–2, pp. 455–469, 2004.

[96]   S. Zhou, S. W. Dyer, K. Shin, J. Shi, and J. Ni, "Extended Influence Coefficient Method for Rotor Active Balancing During Acceleration," *J. Dyn. Syst. Meas. Control*, vol. 126, no. March, pp. 219–223, 2004.

[97]   Y. Qiu and S. S. Rao, "A fuzzy approach for the analysis of unbalanced nonlinear rotor systems," *J. Sound Vib.*, vol. 284, no. 1–2, pp. 299–323, 2005.

[98]   B. Yang and C. S. Suh, "On fault induced nonlinear rotary response and instability," *Int. J. Mech. Sci.*, vol. 48, no. 10, pp. 1103–1125, 2006.

[99]   P. Lou, G.-L. Dai, and Q.-Y. Zeng, "Finite-Element Analysis for a Timoshenko Beam Subjected to a Moving Mass," *Proc. Inst. Mech. Eng. Part C J. Mech. Eng. Sci.*, vol. 220, no. 5, pp. 669–678, 2006.

[100]   A. Shanmugam and C. Padmanabhan, "A fixed-free interface component mode synthesis method for rotordynamic analysis," *J. Sound Vib.*, vol. 297, no. 3–5, pp. 664–679, 2006.

[101]   M. Cheng, G. Meng, and J. Jing, "Numerical and experimental study of a rotor-bearing-seal system," *Mech. Mach. Theory*, vol. 42, no. 8, pp. 1043–1057, 2007.

[102]   D. Peters, C. Kaletsch, and R. Nordmann, "Test Rig for a Supercritical Rotor of an Aero Engine," *12th IFToMM World Congr.*, 2007.

[103]   O. De Santiago and L. S. Andrés, "Experimental Identification of Bearing Dynamic Force Coefficients in A Flexible Rotor—Further Developments," *Tribol.*

Trans., vol. 50, no. 1, pp. 114–126, 2007.

[104] M. Cheng, G. Meng, and J. Jing, "Numerical analysis of nonlinear rotor-bearing-seal system," *J. Shanghai Jiaotong Univ.*, vol. 13, no. 4, pp. 418–425, 2008.

[105] G. Sun, A. Palazzolo, A. Provenza, C. Lawrence, and K. Carney, "Long duration blade loss simulations including thermal growths for dual-rotor gas turbine engine," *J. Sound Vib.*, vol. 316, no. 1–5, pp. 147–163, 2008.

[106] J. Yao, J. Gao, Y. Zhang, and W. Wang, "The Dynamic Analysis of Two-Rotor Three-Bearing System," *Int. J. Rotating Mach.*, vol. 2015, no. 342636, pp. 1–15, 2015.

[107] P. K. Kankar, S. P. Harsha, P. Kumar, and S. C. Sharma, "Fault diagnosis of a rotor bearing system using response surface method," *Eur. J. Mech. A/Solids*, vol. 28, no. 4, pp. 841–857, 2009.

[108] A. W. Lees, J. K. Sinha, and M. I. Friswell, "Model-based identification of rotating machines," *Mech. Syst. Signal Process.*, vol. 23, no. 6, pp. 1884–1893, 2009.

[109] Y. J. Lu, R. Dai, D. Hei, Y. F. Zhang, H. Liu, and L. Yu, "Stability and bifurcation of a non-linear bearing-flexible rotor coupling dynamic system," *Proc. Inst. Mech. Eng. Part C J. Mech. Eng. Sci.*, vol. 223, no. 4, pp. 835–849, 2009.

[110] H. Z. Q. X. Bai, Changqing, "Subharmonic resonance of a symmetric ball bearing–rotor system," *Int. J. Non. Linear. Mech.*, vol. 50, pp. 1–10, 2013.

[111] G. Ying, G. Meng, and J. Jing, "Turbocharger rotor dynamics with foundation excitation," *Arch. Appl. Mech.*, vol. 79, no. 4, pp. 287–299, 2009.

[112] U. Hamdi, Taplak, Selcuk Erkaya, İbrahim, "Experimental analysis on fault detection for a direct coupled rotor-bearing system," *Measurement*, vol. 46, no. 1, pp. 336–344, 2013.

[113] G. Genta, C. Feng, and A. Tonoli, "Dynamics behaviour of rotating bladed discs: A finite element formulation for the study of second and higher order harmonics," *J. Sound Vib.*, vol. 329, no. 25, pp. 5289–5306, 2010.

[114] M. Karlberg, "Approximated stiffness coefficients in rotor systems supported by bearings with clearance," *Int. J. Rotating Mach.*, vol. 2010, 2010.

[115] J. J. . Moore, G. . Vannini, M. . Camatti, and P. . Bianchi, "Rotordynamic analysis of a large industrial turbocompressor including finite element substructure modeling," *J. Eng. Gas Turbines Power*, vol. 132, no. 8, pp. 1–9, 2010.

[116] H. S. Yang, G. D. Chen, S. E. Deng, and S. Li, "Rigid-flexible coupled dynamic simulation of aeroengine main-shaft high speed cylindrical roller bearing," *ICACTE 2010 - 2010 3rd Int. Conf. Adv. Comput. Theory Eng. Proc.*, vol. 4, pp. 31–35, 2010.

[117] Z. Wang and H. Jiang, "Robust incipient fault identification of aircraft engine rotor based on wavelet and fraction," *Aerosp. Sci. Technol.*, vol. 14, no. 4, pp. 221–224, 2010.

[118] D. K. S. T. C. Gupta, K. Gupta, "Nonlinear Dynamics and Chaos of an Unbalanced Flexible Rotor Supported by Deep Groove Ball Bearings with Radial Internal

Clearance," in *IUTAM Symposium on Emerging Trends in Rotor Dynamics*, 2010, vol. 1011, pp. 321–333.

[119] P. M. Hai and P. Bonello, "A Computational Parametric Analysis of the Vibration of a Three-Spool Aero-Engine Under Multifrequency Unbalance Excitation," *J. Eng. Gas Turbines Power*, vol. 133, no. 7, p. 072504, 2011.

[120] I. Jansson, H. O. Akerstedt, J. O. Aidanpaa, and T. S. Lundstrom, "The effect of inertia and angular momentum of a fluid annulus on lateral transversal rotor vibrations," *J. Fluids Struct.*, vol. 28, pp. 328–342, 2012.

[121] W. Li, Y. Yang, D. Sheng, J. Chen, and Y. Che, "Nonlinear dynamic analysis of a rotor/bearing/seal system," *J. Zhejiang Univ. Sci. A*, vol. 12, no. 1, pp. 46–55, 2011.

[122] M. Cheng, G. Meng, and J. Jing, "Non-linear dynamics of a rotor-bearing-seal system," *Arch Appl Mech*, vol. 76, pp. 215–227, 2006.

[123] D. J. Rodrigues, A. R. Champneys, M. I. Friswell, and R. E. Wilson, "Experimental investigation of a single-plane automatic balancing mechanism for a rigid rotor," *J. Sound Vib.*, vol. 330, no. 3, pp. 385–403, 2011.

[124] J. T. Sawicki, M. I. Friswell, Z. Kulesza, A. Wroblewski, and J. D. Lekki, "Detecting cracked rotors using auxiliary harmonic excitation," *J. Sound Vib.*, vol. 330, no. 7, pp. 1365–1381, 2011.

[125] G. N. D. S. Sudhakar and A. S. Sekhar, "Identification of unbalance in a rotor bearing system," *J. Sound Vib.*, vol. 330, no. 10, pp. 2299–2313, 2011.

[126] C. K. Babu, N. Tandon, and R. K. Pandey, "Nonlinear Vibration Analysis of an Elastic Rotor Supported on Angular Contact Ball Bearings Considering Six Degrees of Freedom and Waviness on Balls and Races," *J. Vib. Acoust.*, vol. 136, no. 4, p. 044503, 2014.

[127] C. Bai and H. Zhang, "Almost sure asymptotic stability of rotor systems subjected to stochastical axial loads," *Mech. Mach. Theory*, vol. 58, pp. 192–201, 2012.

[128] S. G. Barad, R. P.V., G. R.K., and K. G., "Neural network approach for a combined performance and mechanical health monitoring of a gas turbine engine," *Mech. Syst. Signal Process.*, vol. 27, pp. 729–742, 2012.

[129] J. Didier, J. J. Sinou, and B. Faverjon, "Study of the non-linear dynamic response of a rotor system with faults and uncertainties," *J. Sound Vib.*, vol. 331, no. 3, pp. 671–703, 2012.

[130] M. Lal and R. Tiwari, "Multi-fault identification in simple rotor-bearing-coupling systems based on forced response measurements," *Mech. Mach. Theory*, vol. 51, pp. 87–109, 2012.

[131] A. Almeida Goncalves Siqueira, R. Nicoletti, N. Norrick, K. Lucchesi Cavalca, H. Fiori De Castro, J. Bauer, and F. Dohnal, "Linear parameter varying control design for rotating systems supported by journal bearings," *J. Sound Vib.*, vol. 331, no. 10, pp. 2220–2232, 2012.

[132] H. Taplak, S. Erkaya, and I. Uzmay, "Passive balancing of a rotating mechanical

system using genetic algorithm," *Sci. Iran.*, vol. 19, no. 6, pp. 1502–1510, 2012.

[133] Z. Wan, J.-P. Jing, G. Meng, Y. Yang, and H.-Y. Bai, "Theoretical and experimental study on the dynamic response of multi-disk rotor system with flexible coupling misalignment," *Proc. Inst. Mech. Eng. Part C J. Mech. Eng. Sci.*, vol. 226, no. 12, pp. 2874–2886, 2012.

[134] Q. Han and F. Chu, "Dynamic response of cracked rotor-bearing system under time-dependent base movements," *J. Sound Vib.*, vol. 332, no. 25, pp. 6847–6870, 2013.

[135] B. Riemann, E. Araujo Perini, K. Lucchesi Cavalca, H. Fiori De Castro, and S. Rinderknecht, "Oil whip instability control using mu-synthesis technique on a magnetic actuator," *J. Sound Vib.*, vol. 332, no. 4, pp. 654–673, 2013.

[136] J. K. Sinha and K. Elbhbah, "A future possibility of vibration based condition monitoring of rotating machines," *Mech. Syst. Signal Process.*, vol. 34, no. 1–2, pp. 231–240, 2013.

[137] J. Sopanen, J. Heikkinen, and A. Mikkola, "Experimental verification of a dynamic model of a tube roll in terms of subcritical superharmonic vibrations," *Mech. Mach. Theory*, vol. 64, pp. 53–66, 2013.

[138] H. Taplak, S. Erkaya, and I. Uzmay, "Experimental analysis on fault detection for a direct coupled rotor-bearing system," *Meas. J. Int. Meas. Confed.*, vol. 46, no. 1, pp. 336–344, 2013.

[139] Z. N. Sadough Vanini, K. Khorasani, and N. Meskin, "Fault detection and isolation of a dual spool gas turbine engine using dynamic neural networks and multiple model approach," *Inf. Sci. (Ny).*, vol. 259, pp. 234–251, 2014.

[140] M. H. Jalali, M. Ghayour, S. Ziaei-Rad, and B. Shahriari, "Dynamic analysis of a high speed rotor-bearing system," *Measurement*, vol. 53, pp. 1–9, 2014.

[141] J. Lee, F. Wu, W. Zhao, M. Ghaffari, L. Liao, and D. Siegel, "Prognostics and health management design for rotary machinery systems - Reviews, methodology and applications," *Mech. Syst. Signal Process.*, vol. 42, no. 1–2, pp. 314–334, 2014.

[142] C. Li, S. Zhou, S. Jiang, H. Yu, and B. Wen, "Investigation on the stability of periodic motions of a flexible rotor-bearing system with two unbalanced disks," *J. Mech. Sci. Technol.*, vol. 28, no. 7, pp. 2561–2579, 2014.

[143] H. N. O. O.Ozsahin and E. Budak., "Analytical modeling of asymmetric multi-segment rotor - Bearing systems with Timoshenko beam model including gyroscopic moments," *Comput. Struct.*, vol. 144, pp. 119–126, 2014.

[144] L. Cui, X. Chen, and S. Chen, "Dynamics Modeling and Analysis of Local Fault of Rolling Element Bearing," *Adv. Mech. Eng.*, vol. 262351, pp. 1–10, 2016.

[145] E. Tang, J. Fang, and B. Han, "Active Vibration Control of the Flexible Rotor in High Energy Density Magnetically Suspended Motor With Mode Separation Method," *J. Eng. Gas Turbines Power*, vol. 137, no. 8, p. 082503, 2015.

[146] B. Ghalamchi, J. Sopanen, and A. Mikkola, "Modeling and Dynamic Analysis of

Spherical Roller Bearing with Localized Defects : Analytical Formulation to Calculate Defect Depth and Stiffness," *Shock Vib.*, vol. 2016, no. 2106810, pp. 1–11, 2016.

[147] S. J. Kim, Heung Soo, Cho, Maenghyo, Song, "Stability Analysis of a Turbine Rotor System With Alford forces," *J. Sound Vib.*, vol. 260, pp. 167–182, 2003.

[148] S. Li, Q. Xu, and X. Zhang, "Nonlinear dynamic behaviours of a rotor-labyrinth seal system," *Nonlinear Dyn.*, vol. 47, no. 4, pp. 321–329, 2007.

[149] C. Nataraj and S. P. Harsha, "Nonlinear Vibration Analysis of an Unbalanced Rotor on Rolling Element Bearings Due to Cage Run-out," *Nolinear Sci. Complex.*, pp. 213–221, 1999.

[150] Y. Wang and X. Wang, "Nonlinear vibration analysis for a Jeffcott rotor with seal and air-film bearing excitations," *Math. Probl. Eng.*, vol. 2010, pp. 1–4, 2010.

[151] M. Cheng, G. Meng, and B. Y. Wu, "Nonlinear dynamics of a rotor-ball bearing system with Alford force," *J. Vib. Control*, vol. 18, no. 1, pp. 17–27, 2012.

[152] V. C. R Tiwari, "Simultaneous identification of residual unbalances and bearing dynamic parameters from impulse responses of rotor–bearing systems," *Mech. Syst. Signal Process.*, vol. 20, no. 7, pp. 1590–1614, 2006.

[153] J. Liu, Y. Shao, and T. C. Lim, "Vibration analysis of ball bearings with a localized defect applying piecewise response function," *Mech. Mach. Theory*, vol. 56, pp. 156–169, 2012.

[154] A. Moazenahmadi, D. Petersen, and C. Howard, "A nonlinear dynamic model of the vibration response of defective rolling element bearings," in *Proceedings of acoustics*, 2013, no. 1, pp. 1–7.

[155] S. Singh, U. Köpke, C. Howard, and D. Petersen, "Impact generating mechanisms in damaged rolling element bearings," in *Proceedings of acoustics 2013-Victor Harbor*, 2013, no. 2, pp. 1–7.

[156] F. Chu and Z. Zhang, "Bifurcation and Chaos in a Rub-Impact Jeffcott Rotor System," *J. Sound Vib.*, vol. 210, no. 1, pp. 1–18, 1998.

[157] F. Chu and W. Lu, "Determination of the Rubbing Location in a Multi-Disk Rotor System By Means of Dynamic Stiffness Identification," *J. Sound Vib.*, vol. 248, no. 2, pp. 235–246, 2001.

[158] Q.S. Lu, Q.H. Li, and E. H. Twizell, "The existence of periodic motions in rub-impact rotor systems," *J. Sound Vib.*, vol. 264, no. 5, pp. 1127–1137, 2003.

[159] F. Wan, Q. Xu, and S. Li, "Vibration analysis of cracked rotor sliding bearing system with rotor-stator rubbing by harmonic wavelet transform," *J. Sound Vib.*, vol. 271, no. 3–5, pp. 507–518, 2004.

[160] Q. Han, T. Yu, H. Li, Z. Qin, Z. Zhang, and B. Wen, "Hybrid Model Based Identification of Local Rubbing Fault in rotor systems," vol. 294, pp. 355–364, 2005.

[161] J. Hua, S. Swaddiwudhipong, Z. S. Liu, and Q. Y. Xu, "Numerical analysis of nonlinear rotor-seal system," *J. Sound Vib.*, vol. 283, no. 3–5, pp. 525–542, 2005.

[162] T. Inoue and Y. Ishida, "Chaotic Vibration and Internal Resonance Phenomena in Rotor Systems," *J. Vib. Acoust.*, vol. 128, no. 2, p. 156, 2006.

[163] X Y Shen, J. H. Jia, M. Zhao, and J. P. Jing, "Numerical and experimental analysis of the rotor—bearing—seal system," *Proc. Inst. Mech. Eng. Part C J. Mech. Eng. Sci.*, vol. 222, no. 1, pp. 1435–1441, 2008.

[164] C. W. Chang-Jian and C. K. Chen, "Chaos and bifurcation of a flexible rub-impact rotor supported by oil film bearings with nonlinear suspension," *Mech. Mach. Theory*, vol. 42, no. 3, pp. 312–333, 2007.

[165] P. Pennacchi and A. Vania, "Analysis of rotor-to-stator rub in a large steam turbogenerator," *Int. J. Rotating Mach.*, vol. 2007, 2007.

[166] T. H. Patel and A. K. Darpe, "Vibration response of a cracked rotor in presence of rotor-stator rub," *J. Sound Vib.*, vol. 317, no. 3–5, pp. 841–865, 2008.

[167] M. Z. Shen, Xiaoyao, "Effect of the Seal Force on Nonlinear Dynamics and Stability of the Rotor-bearing-seal System," *J. Vib. Control*, vol. 15, no. 2, pp. 197–217, 2009.

[168] H. F. Wang and G. Chen, "Certain Type Turbofan Engine Whole Vibration Model with Support Looseness Fault and Casing Response Characteristics," *Shock Vib.*, vol. 2014, no. 368469, pp. 1–23, 2014.

[169] J. Der Jeng, Y. Kang, and Y. P. Chang, "An alternative Poincare section for high-order harmonic and chaotic responses of a rubbing rotor," *J. Sound Vib.*, vol. 328, no. 1–2, pp. 191–202, 2009.

[170] T. H. Patel and A. K. Darpe, "Study of coast-up vibration response for rub detection," *Mech. Mach. Theory*, vol. 44, no. 8, pp. 1570–1579, 2009.

[171] T. H. Patel and A. K. Darpe, "Coupled bending-torsional vibration analysis of rotor with rub and crack," *J. Sound Vib.*, vol. 326, no. 3–5, pp. 740–752, 2009.

[172] G. Chen, C. G. Li, and D. Y. Wang, "Nonlinear Dynamic Analysis and Experiment Verification of Rotor-Ball Bearings-Support-Stator Coupling System for Aeroengine With Rubbing Coupling Faults," *J. Eng. Gas Turbines Power*, vol. 132, no. 2, p. 022501, 2010.

[173] F. Chu and W. Lu, "Stiffening effect of the rotor during the rotor-to-stator rub in a rotating machine," *J. Sound Vib.*, vol. 308, no. 3–5, pp. 758–766, 2007.

[174] H. Ma, X. Y. Tai, H. L. Yi, S. Lv, and B. C. Wen, "Nonlinear dynamic characteristics of a flexible rotor system with local rub-impact," *J. Phys. Conf. Ser.*, vol. 448, p. 012015, 2013.

[175] S. Ziaei-Rad, E. Kouchaki, and M. Imregun, "Thermoelastic Modeling of Rotor Response With Shaft Rub," *J. Appl. Mech.*, vol. 77, no. 6, p. 061010, 2010.

[176] S. Roques, M. Legrand, P. Cartraud, C. Stoisser, and C. Pierre, "Modeling of a rotor speed transient response with radial rubbing," *J. Sound Vib.*, vol. 329, no. 5, pp. 527–546, 2010.

[177] Z. Shang, J. Jiang, and L. Hong, "The global responses characteristics of a rotor/stator rubbing system with dry friction effects," *J. Sound Vib.*, vol. 330, no.

10, pp. 2150–2160, 2011.

[178] J. Cao, C. Ma, Z. Jiang, and S. Liu, "Nonlinear dynamic analysis of fractional order rub-impact rotor system," *Commun. Nonlinear Sci. Numer. Simul.*, vol. 16, no. 3, pp. 1443–1463, 2011.

[179] F. Cong, J. Chen, G. Dong, and K. Huang, "Experimental validation of impact energy model for the rubimpact assessment in a rotor system," *Mech. Syst. Signal Process.*, vol. 25, no. 7, pp. 2549–2558, 2011.

[180] H. M. Khanlo, M. Ghayour, and S. Ziaei-Rad, "Chaotic vibration analysis of rotating, flexible, continuous shaft-disk system with a rub-impact between the disk and the stator," *Commun. Nonlinear Sci. Numer. Simul.*, vol. 16, no. 1, pp. 566–582, 2011.

[181] W. Zhou, X. Wei, X. Wei, and L. Wang, "Numerical analysis of a nonlinear double disc rotor-seal system," *J. Zhejiang Univ. A(Applied Phys. Eng.*, vol. 15, no. 1, pp. 39–52, 2014.

[182] J. Zapome and P. Ferfecki, "A Computational Investigation of the Disk-Housing Impacts of Accelerating Rotors Supported by Hydrodynamic Bearings," *J. Appl. Mech.*, vol. 78, no. March 2011, pp. 1–13, 2011.

[183] S. Lahriri, H. I. Weber, I. F. Santos, and H. Hartmann, "Rotor-stator contact dynamics using a non-ideal drive-Theoretical and experimental aspects," *J. Sound Vib.*, vol. 331, no. 20, pp. 4518–4536, 2012.

[184] S. Lahriri and I. F. Santos, "Theoretical modelling, analysis and validation of the shaft motion and dynamic forces during rotor-stator contact," *J. Sound Vib.*, vol. 332, no. 24, pp. 6359–6376, 2013.

[185] H. Ma, H. Li, H. Niu, R. Song, and B. Wen, "Nonlinear dynamic analysis of a rotor-bearing-seal system under two loading conditions," *J. Sound Vib.*, vol. 332, no. 23, pp. 6128–6154, 2013.

[186] N. Olgac, U. Zalluhoglu, and A. S. Kammer, "On blade/casing rub problems in turbomachinery: An efficient delayed differential equation approach," *J. Sound Vib.*, vol. 333, no. 24, pp. 6662–6675, 2014.

[187] H. Ma, Q. Zhao, X. Zhao, Q. Han, and B. Wen, "Dynamic characteristics analysis of a rotor-stator system under different rubbing forms," *Appl. Math. Model.*, vol. 39, no. 8, pp. 2392–2408, 2015.

[188] H. Ma, X. Tai, Q. Han, Z. Wu, D. Wang, and B. Wen, "A revised model for rubbing between rotating blade and elastic casing," *J. Sound Vib.*, vol. 337, pp. 301–320, 2015.

[189] B. K. Weaver, Y. Zhang, A. F. Clarens, and A. Untaroiu, "Nonlinear Analysis of Rub Impact in a Three-Disk Rotor and Correction Via Bearing and Lubricant Adjustment," *J. Eng. Gas Turbines Power*, vol. 137, no. 9, p. 092504, 2015.

[190] I. Redmond, "Study of a misaligned flexibly coupled shaft system having nonlinear bearings and cyclic coupling stiffness-Theoretical model and analysis," *J. Sound Vib.*, vol. 329, no. 6, pp. 700–720, 2010.

[191] M. A. Rezvani and E. J. Hahn, "An experimental evaluation of squeeze film dampers without centralizing springs," *Tribol. Int.*, vol. 29, no. 1, pp. 51–59, 1996.

[192] A. Khajepour and M. F. Golnaraghi, "Experimental Control of Flexible Structures Using Nonlinear Modal Coupling: Forced and Free Vibration," *J. Intell. Mater. Syst. Struct.*, vol. 8, no. 8, pp. 697–710, 1997.

[193] M. Chinta, "Stability and Bifurcation of Rotor Motion in a Magnetic Bearing," *J. Sound Vib.*, vol. 214, no. 5, pp. 793–803, 1998.

[194] R. C. Smith, "A Nonlinear Optimal Control Method for Magnetostrictive Actuators," *J. Intell. Mater. Syst. Struct.*, vol. 9, no. 6, pp. 468–486, 1998.

[195] Z. Yu, L. T. Meng, and L. M. King, "Electromagnetic bearing actuator for active vibration control of a flexible rotor," *Proc. Inst. Mech. Eng. Part C J. Mech. Eng. Sci.*, vol. 212, no. 8, pp. 705–716, 1998.

[196] M. M. Elmadany and Z. Abduljabbar, "Controller Design for High-Performance Thrbomachines," *J. Vib. Control*, vol. 6, no. 8, pp. 1205–1223, 2000.

[197] J. M. Vance and J. L. Ying, Daniel , Nikolajsen, "Actively controlled bearing Dampers for Aircraft Engine applications," *J. Eng. Gas Turbines Power*, vol. 122, no. July, pp. 467–472, 2000.

[198] R.F. Fung, J.H. Sun, and S.-M. Hsu, "Vibration Control of the Rotating Flexible-Shaft/Multi-Flexible-Disk System With the Eddy-Current Damper," *J. Vib. Acoust.*, vol. 124, no. 4, p. 519, 2002.

[199] J. C. Ji, "Dynamics of a Jeffcott rotor-magnetic bearing system with time delays," *Int. J. Non. Linear. Mech.*, vol. 38, no. 9, pp. 1387–1401, 2003.

[200] Y. K. Ahn, J.-Y. Ha, and B.-S. Yang, "A New Type Controllable Squeeze Film Damper Using an Electromagnet," *J. Vib. Acoust.*, vol. 126, no. 3, p. 380, 2004.

[201] P. Bonello, M. J. Brennan, and R. Holmes, "The prediction of the non-linear dynamics of a squeeze-film damped aero-engine rotor housed in a flexible support structure," *Proc. Inst. Mech. Eng. Part G J. Aerosp. Eng.*, vol. 218, no. 3, pp. 213–230, 2004.

[202] D. J. Clark, M. J. Jansen, and G. T. Montague, "An Overview of Magnetic Bearing Technology for Gas Turbine Engines_NASA-TM—2004-213177," no. August, 2004.

[203] H.-G. Horst, "Active Vibration Control of a High Speed Rotor Using PZT Patches on the Shaft Surface," *J. Intell. Mater. Syst. Struct.*, vol. 15, no. 9–10, pp. 721–728, 2004.

[204] P. Anusonti-Inthra and F. Gandhi, "Cyclic modulation of semi-active controllable dampers for tonal vibration isolation," *J. Sound Vib.*, vol. 275, no. 1–2, pp. 107–126, 2004.

[205] M. E. F. Kasarda, H. Mendoza, R. G. Kirk, and A. Wicks, "Reduction of subsynchronous vibrations in a single-disk rotor using an active magnetic damper," *Mech. Res. Commun.*, vol. 31, no. 6, pp. 689–695, 2004.

[206] S. L. Chen, S. H. Chen, and S. T. Yan, "Experimental validation of a current-

controlled three-pole magnetic rotor-bearing system," *IEEE Trans. Magn.*, vol. 41, no. 1 I, pp. 99–112, 2005.

[207] S. J. Shin, "System Identification Technique for Active Helicopter Rotors," *J. Intell. Mater. Syst. Struct.*, vol. 16, no. 11–12, pp. 1025–1038, 2005.

[208] C. Zhu, "Dynamic Performance of a Disk-type Magnetorheological Fluid Damper under AC Excitation," *J. Intell. Mater. Syst. Struct.*, vol. 16, pp. 449–461, 2005.

[209] Z. Changsheng, "Experimental Investigation on the Dynamic Behaviour of a Disk-type Damper based on Magnetorheological Grease," *J. Intell. Mater. Syst. Struct.*, vol. 17, no. 8–9, pp. 793–799, 2006.

[210] Y.-Y. He, S. Oi, F.L. Chu, and H.X. Li, "Vibration control of a rotor–bearing system using shape memory alloy: II. Experimental study," *Smart Mater. Struct.*, vol. 16, no. 1, pp. 122–127, 2007.

[211] J. I. Inayat-Hussain, "Chaos via torus breakdown in the vibration response of a rigid rotor supported by active magnetic bearings," *Chaos, Solitons and Fractals*, vol. 31, no. 4, pp. 912–927, 2007.

[212] A. Tonoli, "Dynamic characteristics of eddy current dampers and couplers," *J. Sound Vib.*, vol. 301, no. 3–5, pp. 576–591, 2007.

[213] N. Amati, X. De Lépine, and A. Tonoli, "Modeling of Electrodynamic Bearings," *J. Vib. Acoust.*, vol. 130, no. 6, p. 061007, 2008.

[214] A. S. Das, M. C. Nighil, J. K. Dutt, and H. Irretier, "Vibration control and stability analysis of rotor-shaft system with electromagnetic exciters," *Mech. Mach. Theory*, vol. 43, no. 10, pp. 1295–1316, 2008.

[215] J. Ji, C. Hansen, and A. Zander, "Nonlinear dynamics of magnetic bearing systems," *J. Intell. Mater. ...*, vol. 19, no. 12, pp. 1471–1491, 2008.

[216] M. Lallart, A. Badel, and D. Guyomar, "Nonlinear Semi-active Damping using Constant or Adaptive Voltage Sources: A Stability Analysis," *J. Intell. Mater. Syst. Struct.*, vol. 19, no. 10, pp. 1131–1142, 2008.

[217] A. Tonoli, N. Amati, and M. Silvagni, "Transformer Eddy Current Dampers for the Vibration Control," *J. Dyn. Syst. Meas. Control*, vol. 130, no. 3, p. 031010, 2008.

[218] A. Bonfitto, X. De Lépine, M. Silvagni, and A. Tonoli, "Self-Sensing Active Magnetic Dampers for Vibration Control," *J. Dyn. Syst. Meas. Control*, vol. 131, no. 6, p. 061006, 2009.

[219] C. R. Burrows, P. S. Keogh, and M. N. Sahinkaya, "Progress towards smart rotating machinery through the use of active bearings," *Proc. Inst. Mech. Eng. Part C J. Mech. Eng. Sci.*, vol. 223, no. 12, pp. 2849–2859, 2009.

[220] C. C. Fan and M. C. Pan, "Active elimination of oil and dry whips in a rotating machine with an electromagnetic actuator," *Int. J. Mech. Sci.*, vol. 53, no. 2, pp. 126–134, 2011.

[221] S. Jiffri and S. Garvey, "Controlling rotordynamic response without squeeze-film dampers (SFDs)," *J. Phys. Conf. Ser.*, vol. 181, p. 012022, 2009.

[222] A. Bouzidane and M. Thomas, "Nonlinear Dynamic Behaviour of a flexible shaft supported by smart Hydrostatic Squeeze Film Dampers," *J. Tribol.*, vol. 135, no. 4, p. 041102, 2008.

[223] X. Chen, J. Zhou, J. Xiao, X. Zhang, H. Xiao, W. Zhu, and W. Fu, "Fault diagnosis based on dependent feature vector and probability neural network for rolling element bearings," *Appl. Math. Comput.*, vol. 247, pp. 835–847, 2014.

Appendix

This appendix provides the computer program written in Matlab for 3-layer back propagation neural network. The code requires input-target patterns in normalized form supplied from a text or data file. User specifies the epochs and number of hidden nodes, so that the trained weights and error convergence graph come as outputs.

%%%%%%%%%%%%%%%%%%%%%%%%%%%%%%

```
m=4; % Number of inputs
n=8; % Number of hidden nodes
p=3; % Number of outputs
MAX=500; % Maximum cycles
PAT=25; % Number of patterns or examples presented
%% INITIALIZATION OF WEIGHTS
for i=1:m
   for j=1:n
      w(i,j)=rand;
   end
end
for i=1:n
   for j=1:p
      v(i,j)=rand;
   end
end
%%%%%%%%%%%%%%%%
for epoch=1:MAX
   fid=fopen('Input.txt','r');
   error=0;
   for pat=1:PAT
      for k=1:m
         I(k)=fscanf(fid,'%f',1);
      end
      for k=1:p
         T(k)=fscanf(fid,'%f',1);
      end
  % Input at the Hidden layer
   for j=1:n
   K(j)=0;
   for i=1:m
      K(j)=K(j)+w(i,j)*I(i);
   end
   end

   for j=1:n
   H(j)=tanh(-K(j)); %%% SIGMOID FUNCTION 1/(1+exp(-K(j)));
   end
   for j=1:p
   S(j)=0;
   for i=1:n
      S(j)=S(j)+v(i,j)*H(i);
   end
   end
   for j=1:p
```

```
   Y(j)=tanh(-S(j)); %%%% SIGMOID FUNCTION 1/(1+exp(-S(j)));
   end

   E=(T-Y);
   beta=0.3;
  % Adjustment of connection weights between hidden & output layer
   for i=1:n
   for j=1:p
      v(i,j)=v(i,j)+beta*Y(j)*E(j)*H(i);
   end
   end

   for i=1:n
   sig(i)=0;
   for j=1:p
      sig(i)=sig(i)+E(j)*v(i,j);
   end
   end
   for i=1:n
   sigma(i)=sig(i)*H(i)*(1-H(i));
   end
   alpha=0.3;
% Adjustment of connection weights between input and hidden layers
   for i=1:m
   for j=1:n
      w(i,j)=w(i,j)+alpha*sigma(j)*I(i);
   end
   end

% Error
for i=1:p
   error=error+0.5*E(i)*E(i);
end

end
fclose(fid);
err(epoch)=error/PAT;
fprintf('\n\n');
end
fprintf('Actual outputs:\n');
disp(Y);
fprintf('Target outputs:\n');
disp(T);

q=1:MAX;
plot(q,err);
xlabel('Number of cycles');
ylabel('MSE');
%%% RESULTANT WEIGHT MATRICES
disp(w);
disp(v);
%%% Training is completed  %%%%

%%%% Testing with obtained weights
```

```
%%%%%%%%%%%%%%%%%%%%%%%%%%%%%%%%%%%%%%%
```

The Matlab code with neural network toolbox functions is given below:

```
%%%%%%%%%%%%%%%%%%%%%%%%%%%%%%%%%%%%%
clc; clear all; close all;
% Training data: input patterns and output patterns
%%% enter x and y as patterns
% Create a NN and initialize weights
net=newff(minmax(x),[8 3],{'tansig','tansig'},'traingdx');
% Training functions: traingd, traingdm, traingda, traingdx
% output of NN with initial weights
ycap1=sim(net,x);

% Train the NN
net.trainparam.goal=0.005;
net.trainparam.epochs=500;
net.trainparam.show=50;
net.trainparam.lr=0.01;
[net,tr]=train(net,x,y);
% Output of NN
% Generalization : input vector is different
% from the one used for training
%% Enter test input x2
ycap2=sim(net,x2);

% Weights and Biases of the trained network
w=net.IW{1,1}
bw=net.b{1}
v=net.LW{2,1}
bv=net.b{2}
%%%%%%%%%%%%%%%%%%%%%%%%%%%%%%%%%%%%%%
```

Dissemination

Journal Articles

1. M. Rajasekhar and J. Srinivas "Active Vibration Control in Engine Rotors using Electromagnetic Actuator System" Journal of Mechanical Design and Vibration, 2014, Vol. 2, No. 1, 25-30.

2. M. Rajasekhar and J. Srinivas "Investigation of Transient Response of an Unbalanced Aero-Engine Rotor with Semi-Active Damper System" International Journal of Engineering Research & Technology, Vol. 3, Issue 1, January – 2014, 2862-2867.

3. M. Rajasekhar , J. Srinivas and G.N.Chaitanya "Vibration Response of Rotor-Bearing seal system subjected to Non-Linear parametric Excitations" IRACST – Engineering Science and Technology: An International Journal, 721-726, Vol.2, No. 4, August 2012.

Conference Presentations

1. M. Rajasekhar, J. Srinivas and CV Gopinath "Numerical Analysis of Rotor Bearing Seal system subjected to Nonlinear Parametric Excitations" XVII National Seminar on Aerospace Structures (NASAS), IIT Kanpur (22-24 September 2011).

2. M. Rajasekhar and J. Srinivas "Experimental Identification of Bearing Stiffness in a Rotor Bearing System" National Symposium on Rotor Dynamics (NSRD 2011), 359-366, IIT Madras (19th - 21st December, 2011).

3. M. Rajasekhar and J. Srinivas "Vibration control in aero-engine rotors using semi-active damper system" National Symposium on Rotor Dynamics (NSRD 2011), 370-376, IIT Madras, (19th - 21st December, 2011).

4. M. Rajasekhar and J. Srinivas "Dynamic analysis of rotor supported over double row ball bearings with squeeze film dampers", National Conference on Advances in Modelling and Analysis of Aerodynamic Systems (AMAAS-2013), National Institute of Technology- Rourkela, Rourkela, Orissa (March 1-2, 2013).

5. M. Rajasekhar and J. Srinivas "Dynamic Analysis of Aero-engine Rotors Supported on Ball bearing system ", 1st International and 16th National Conference on Machines and Mechanisms (iNaCoMM2013), Indian Institute of Technology Roorkee, India, (December 18-20 2013).

6. M. Rajasekhar and J. Srinivas "Vibration Analysis of Engine Rotor under Multi-Frequency Unbalance Forces" International Conference on Computer Aided Engineering (CAE-2013), Indian Institute of Technology, Madras (December 19-21, 2013).

7. M. Rajasekhar and J. Srinivas "Active Vibration Control In high-speed engine Rotors Using Electromagnetic actuator System", Third National Symposium on Rotor Dynamics (NSRD-2014), Dr. Ambedkar Institute of Technology, Bangalore (February 12-14, 2014).

8. M. Rajasekhar and J. Srinivas "Dynamic modelling of rotors mounted on ball bearings with elastohydrodynamic point contacts" NSRD 2016, National Institute of Technology, Rourkela (January 7-9, 2016).

Vitae

Experience

1) Working as Assistant Professor in the Department of Mechanical Engineering, GIT, Visakhapatnam, Andhra Pradesh since 8th June 2012

2) Worked as Assistant Professor in the Department of Mechanical Engineering, Chaitanya Engineering College, Visakhapatnam since 7th June 2007 to 2012.

Subjects taught

Dynamics of Machinery, Kinematics of Machinery, Engineering Drawing, Machine drawing, Production Technology, Engineering Graphics, Automobile Engineering, Power Plant Engineering, Mechatronics, Management Science, Metrology and surface engineering Etc.

Workshop/Faculty Development Programs attended

1) MISSION -10X in GVPCOE, VSP. Sponsored by Wipro Technologies.
2) AICTE Sponsored SDP on CAD and Precision Mfg in GIET, Rajahmundry.
3) International Interactive Workshop on ANSYS workbench and Multiphysics suite in CEC, VSP
4) Workshop on MODELING AND ANALYSIS OF DYNAMIC SYSTEMS 05th - 07th December, 2011, NIT-Rourkela.
5) Faculty Development Programme, 21st Dec 2012-10th Jan 2013, GITAM UNIVERSITY.
6) Two day faculty orientation programme on Basics of Pedagogy, 5th - 6th May 2014, GITAM UNIVERSITY.

Personal Profile

Name	: Medidi Rajasekhar.
Date of Birth	: 16th November 1979.
Father's Name	: Medidi Anjaneyulu,
Mother's Name	: Medidi Sundaramanikyam
Gender	: Male
Marital Status	: Married
Language Known	: English, Telugu, Hindi.
Nationality	: Indian